University of Modena and Reggio Emilia

INDUSTRIAL INNOVATION ENGINEERING
XXXII cycle – Academic Year 2018/2019

Ph. D. THESIS

in SOLID MECHANICS (ICAR/08)

Advanced inorganic composite materials for structural purposes

Enhancement of the interphase adhesion

Defended by
Cesare SIGNORINI

Thesis Advisor: Prof. Enrico RADI
School Coordinator: Prof. Franco ZAMBONELLI

"No one can whistle a symphony. It takes a whole orchestra to play it"

[Halford E. Luccock]

To my beloved family

Contents

Abstract

Building materials have experienced an extraordinarily fast development in the last decades, extending the possibilities for new innovative constructions, with outstanding properties such as high mechanical performance, audacious architecture and low energy consumption. On the other hand, also traditional materials, like cementitious and lime-based systems, are worthy of accurate investigation in order to take advantage of their benefits, which have been exploited for centuries and are still largely employed in contemporary structures. In the context of seismic retrofitting and structural rehabilitation, nowadays the techniques based on Fibre Reinforced Polymers (FRP) are firmly established and very reliable, and yet they present some critical issues, as far as some specific physical and thermal requirements are not fully accomplished. For these reasons, Textile Reinforced Mortar (TRM) or Fibre Reinforced Cementitious Mortar (FRCM) composites have encountered increasing interest in the scientific community as well as in the technical one. The innovation is the partial or complete substitution of the organic binder with lime-based and/or cementitious mortars, which play the role of embedding medium. The porous texture and the hydraulic nature of these inorganic mortars, besides a low elastic modulus result in high thermal stability, reversibility, high permeability to water vapour and good compatibility with masonry substrates. The main drawback associated with lime and cement matrices is their intrinsic poor adhesion at the fabric-to-matrix interphase. The poor impregnation quality of the fabrics yarns is responsible for triggering undesirable failure modes (i.e. telescopic failure or interphase sliding), which lead to unreliable design values. In the first part of the present work, several techniques based on the deposition of engineered coatings for multifilament fabrics are proposed and extensively described and tested in order to improve the interphase adhesion and, at the same time, to strengthen the core filaments bond in the yarn bundles to avoid telescopic failure. Both inorganic and organic coatings on synthetic fibres are discussed and optimized. Special attention is paid to alkali resistant (AR) glass fabrics, which are the prevalent reinforcement for masonry panels due to their good mechanical properties combined with relatively low cost, which make them preferable to carbon or other synthetic fabrics, like PBO. Besides, some durability issues are thoroughly investigated for polymer-coated TRM. In fact, although two guidelines have been recently released, no exhaustive indications have been provided about the potential consequences of the exposure to aggressive environments on the mechanical response of TRM. To the aim, uni-axial tension and three-point bending tests were performed on TRM composites. In the second part of the work, the role of interphase adhesion is investigated in a different category of inorganic composite materials, namely in Fibre Reinforced Concrete (FRC), that is commonly employed in industrial pavements. Discontinuous polypropylene (PP) fibres are proposed as dispersed reinforcement. Since PP is characterized by an outstanding chemical inertness, no adhesion is possible with the conglomerate. Alongside the

chance of increasing the friction grip by wrinkling the fibres' surface, the adhesion can be increased through mechanical gripping by using PP fibres with a high surface roughness. Additionally, this research also proposes two experimental activities to enhance the interphase adhesion chemically. The mechanical behaviour of the FRC composites is assessed through three-point bending tests at different dimensional scales and through pull-out tests. The two proposed treatments, i.e. deposition of a silica nano-coating and etching with piranha solution, notably improve the toughness of the composite through the modification of the fibres' surface, activating hydrophilic functional groups that are able to bond to the water molecules in the cementitious conglomerate.

Part I

Continuous fibres Textile-Reinforced Mortar/Concrete (TRM/TRC) composite materials

Chapter 1

Introduction

Fabric Reinforced Cementitious Matrix (FRCM) composite stands out as a new class of material available to the structural engineer for designing reliable and cost-effective strengthening and retrofitting systems for concrete and masonry structures [Feo 2016]. The use of fabric to reinforce structural components has been a key driving technology in the last 20 years, for it reconciles ease of manufacturing with excellent anchorage at little cost [Mobasher 2006]. This appealing concept has been declined into several forms within the construction industry, ranging from textile reinforced concrete (TRC) or mortar (TRM), to fibre-reinforced polymers (FRP), from ferrocement (often labelled as Steel Reinforced Grout, SRG [Wobbe 2004, Barton 2005, Huang 2005, Thermou 2015, Ascione 2018]) to FRCM. Although the common ground for such acronyms is sometimes slippery, we may still group these technology according to the nature of the matrix which holds the reinforcement grids bonded together and, possibly, to the structural element (in the so-called strengthening system) and according to the nature of the fabric deployed. In the present document, the acronyms mainly preferred are TRM or FRCM. TRM combines the high strength of reinforcing fabrics, mainly made of carbon and alkali resistant glass (ARG) fibres, with the benefits offered by the inorganic binders out of the embedding media are made of. In particular, TRM reinforcement consists in continuous fibres, gathered together in woven fabrics through various thermo-welding techniques. On the other hand, matrices are basically composed by lime-based binder with fine aggregates, which are responsible for the compressive strength of the conglomerate. Most of commercially available mortars are hybrid, namely made of lime and Portland cement binders mixed together. In contrast with the well-established FRP composites, TRM takes advantage of the hydraulic nature of the binder that mainly enhances internal porosity. The presence of pores in the embodying matrix allows TRM composites to exhibit an outstanding resistance to fire and high temperatures. As an example, this aspect makes TRM suitable in strengthening public buildings sensitive to crowding (e.g. theatres, hospitals, cinemas etc.). In fact, the most thermal energy due to fire is employed as latent heat for water inside the conglomerate. Contrarily, organic resins adopted in FRP dramatically weaken once reached the relevant glass transition temperature, around $[60 \div 80]^{\circ}$C. Furthermore, porosity of hardened mortar favours a quick water vapour transportation, especially when considering low-cement content or lime-based mortars with no polymeric addition, and remarkable mechanical properties. Indeed, one crucial issue of polymeric matrices is related to the inability to carry the intrinsic humidity of masonry out. The stagnation of water droplets inside the structure may induce serious damages in historical masonry (e.g. frescoed vaults or panels) since colour pigments may detach. In this sense, TRM overcome the problem due to their porous texture. Besides, the hydraulic nature of the matrix and its hardening reactions are perfectly suitable with applications of repair and retrofit of structures in the presence of water, like in the case of hydraulic infrastructures, such as dams and pipes, even in the emergency of a water loss. In fact, polymerization of epoxy resin is not possible with water.

In the attempt to classify structural composite materials according to the nature of matrices, we may distinguish ductile organic matrices, which are most often constituted by polymeric materials and thereby falls in the FRP group, from brittle inorganic ones, composed of cement or lime-based materials, respectively under the heading of TRC or TRM (although the wording fabric-cement composite, FCC, is also in common use). Similarly, a wide variety of materials may be adopted for the reinforcing fabric which may be grouped under several criteria: conventional materials, such as steel or glass, high-modulus materials, such as aramidic fibers (Kevlar), carbon fibers or synthetic polymers (Zylon, better known as polyphenylene-benzobisoxazole or PBO), low-modulus (polypropylene) or even natural fibres (straw, cellulose, flax, hemp). All these technologies may be labelled together under the common heading of continuous fiber reinforcing material (CFRM), as opposed to randomly distributed discontinuous fiber reinforced materials, such as fiber reinforced concrete (FRC) [Bentur 2006, Lanzoni 2012]. While FRP possesses a substantial history of successful applications to its credit [Triantafillou 1998], growing interest has been recently attracted by cement-based composites, in light of some important advantages [Papanicolaou 2008, Bournas 2009]. Besides these several attractive features, TRM and TRC present some substantial disadvantages, especially when compared with the well-established technology of FRP or even when compared to SRG. Indeed, their performance is mainly driven by interphase compatibility, that is the surface adhesion between the matrix and the fabric reinforcement, and common fabric reinforcement materials present inadequate interphase compatibility with cement-based binders [Raoof 2016, Nadiv 2017]. As a result, delamination is the predominant failure mode and it is most often associated with large data scattering and a not entirely consistent performance [D'Antino 2017, Nobili 2017a]. Among TRM and TRC materials, Fabric Reinforced Cementitious Matrix (FRCM) composites attempt to bridge the performance gap with FRPs through modification of the inorganic binder with an organic component. In fact, the recently published guidelines [ICC AC434 2013, ACI 549.4R-13 2013] advocate, for FRCM materials, the adoption of a "polymer-modified cement-based binder (mortar)" as the composite inorganic matrix, given that this amount is not overcoming the weight ratio of 5% with respect to the overall mortar. Alternative to matrix modification, thermal and particularly chemical treatment of the reinforcement have been investigated in order to improve adhesion with the cementitious matrix. This part deals with the study of several strategies to enhance chemical and mechanical interaction at the fabric-matrix interphase in composite materials characterized by continuous fibres embedded in a lime-based mortar.

1.1 Reinforcing fabrics

Textiles in everyday activities find their origin very far in time, also for commonly used objects. The most immediate example is provided by clothing. This ancient idea is adopted in an innovative way to obtain lightweight materials with outstanding mechanical properties, not achievable by conventional materials. Indeed, massive carbon (in the form of graphite) presents Young's modulus and ultimate strength unacceptable for structural purposes. The same holds true for bulk glass, which is highly brittle and presents defects in its structure. Using glass and carbon in the form of fibres minimizes defects and optimizes the mechanical response. For this reason, textiles have been widely employed as reinforcement phase in composite materials since the half of twentieth century, expecially for automotive, nautical and aerospace applications. Only starting the 1990s, fibre reinforced polymers have been exploited for structural strengthening and seismic retrofit.

1.1.1 Nomenclature

Before detailing the main types of reinforcing fibres in TRC composites, the following list recalls the main definitions that apply [Mobasher 2011, CNR TD200-R1 2013]:

- *Continuous fibre or filament*: basic unit manufactured in the form of a single filament. Filaments are used for yarns, rovings, strands and fabrics in general. Average diameter around 10 µm
- *Tow*: bundle of filaments, ready to be kept together through weaving and twisting or chopped to work as discontinuous fibres.
- *Yarn*: twisted continuous monofilament or multifilament made of several fibres, intended to be assembled in a fabric.
- *Roving*: a number of yarns collected into a parallel bundle usually with little twist.
- *Fabric*: manufactured textile made of yarns assembled with a variety of techniques, especially weaving or knitting. Fabrics are tailored to comply with the purpose they are expected to fulfil.
- *Tex*: unit for fibre fineness. 1 Tex = 1 g/km = 9 Den, where Den stands for Denier.
- *Cross-section of a TRM laminate*: area of net fabric (in mm^2) that contributes to strength in the cracked stage. The fabric cross-section is evaluated through the customary formula [CNR TD200-R1 2013, §2.2.3.1]:

$$A_f = \frac{T_x N_f}{10^4 \rho_{fib}} b_f \tag{1.1}$$

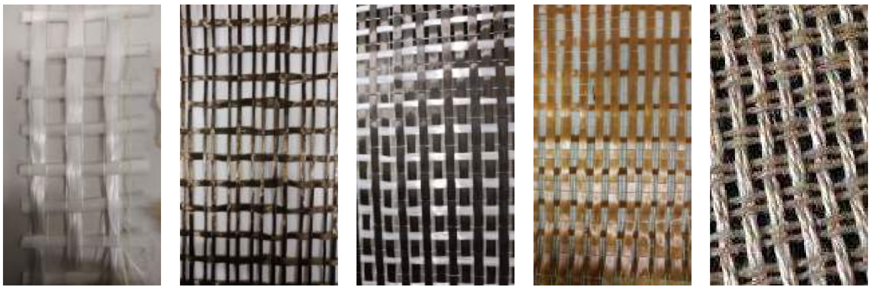

(a) AR-Glass (b) Basalt (pre-preg warp yarns) (c) Carbon (with AR-glass weft yarn) (d) PBO (e) Flax

Figure 1.1: Example of some typical reinforcing multifilament textiles for TRM

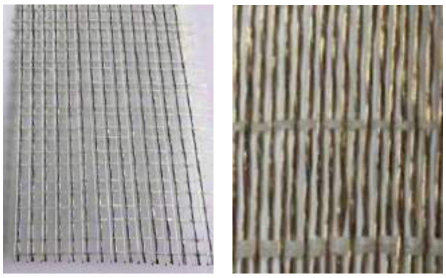

(a) Zinc-plated UHS steel (b) Brass-plated UHS steel

Figure 1.2: Example of some typical reinforcing steel textiles for TRM

1.1.2 Fibres

A great variety of fibres can be manufactured, which can be divided in natural or artificial ones. A complete overview is provided by [Mobasher 2011], who has classified fibres according to the raw materials employed for their production. Artificial fibres can be divided into organic (polymeric-based) and inorganic ones. Carbon fibres belong to the former group, whereas AR-glass belong to the latter. In the group of natural fibres, vegetable ones like flax, hemp and sisal are of particular interest to the research community from an environmental standpoint. Indeed, the production of traditional fibres has a deep impact in terms of energy consumption, since manufacturing processes attain extremely high temperatures [Triantafillou 2016]. The complete classification of fibres for structural purposes is represented in Fig.1.3. Some common reinforcing textiles are shown in Figures 1.1 and 1.2.

1.1.2.1 Glass Fibres

One of the cheapest and wide-spread solutions in textile-reinforced composite materials takes advantage of glass fibres. Over the last century, these fibres have been applied in several fields. In fact, glass fibres are transversally employed in naval applications, as well as in industrial ones. Indeed, contrarily to glass in bulk form,

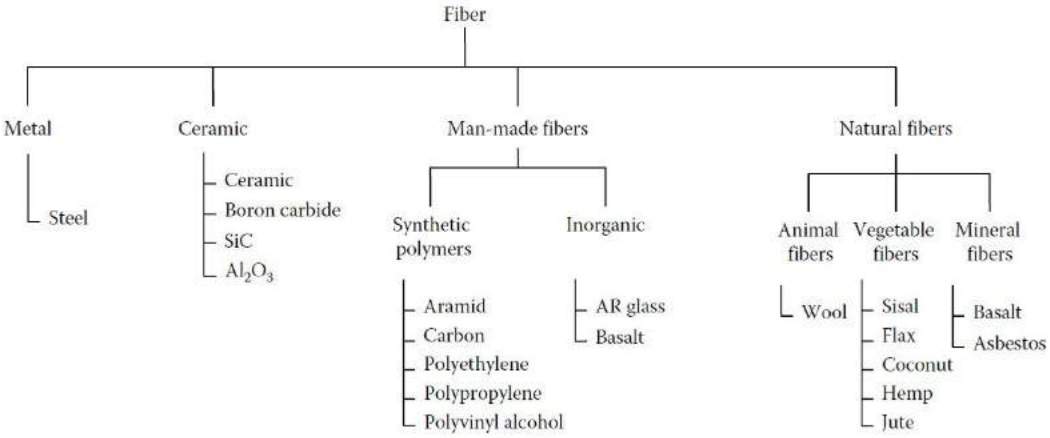

Figure 1.3: Types of commonly used fibres for composite materials [Mobasher 2011, §2.2].

which is characterized by high brittleness as a consequence of the presence of defects, fibres are manufactured with a negligible amount of defects. For this reason the tensile strength of glass fibres is very close to the nominal strength of the the Si−O covalent bond of silica.

The production chain of glass fibres consists in melting the glass from a proper mixture of sand, alumina and limestone in a furnace at around 1200°C and then extruding the molten glass into fibres, after collecting the extruded material in bushing plates [Lubin 1975]. Typical fibre diameters range from 10 to 15 µm.Within this particular device, made of platinum alloyed with rhodium, fibres are formed through nozzles that control the direction and the characteristics of the flow [Loewenstein 1973]. After drawing, a sizing is often applied in a glass-to-sizing ratio commonly ranging from 0.5 to 2.0%wt [Kumar 1997]. Then, fibres are wounded onto a bobbin at about 1 km/min and have a diameter ranging from 10 to 15 µm. Sizing may have a twofold benefit, both facilitating the manufacturing process and enhancing the compatibility with some resins, in view of a specific application in composites. The main constituent of glass fibres is silica (silicon dioxide) which softens at about 1200°C. The molten glass is generally extruded and cooled quickly, thus the formation of an ordered structure is hindered. Therefore, glass fibres are made of SiO_4 tetrahedral structural units mutually connected through the bridging oxygen atoms. Additives can be added to the molten material to confer some peculiar characteristics to the final glass fibres and to reduce the processing temperature. For example, the most common formulation for glass fibres is the so-called E-glass, an alkali-free alumino-borosilicate glass, commonly used for FRP composites. As a curiosity, the letter "E" traditionally used for these fibres derives from its initial application in the electrical field. Besides, C-glass consists of a material with high resistance to chemical attacks and S-glass presents an enhanced mechanical performance ("S" stands for strength). Some other glass formulations are adopted in niche application fields, like D-glass, with low dielectric constant and R-glass, characterized by high mechanical resistance. The latter differs from S-glass because of the absence of MgO, with high tensile strength. Both S- and R-glasses are CaO-free [Fitzer 2000]. Finally, T-glass presents elevated thermal insulation properties. In the most recent applications of glass fibres in the framework of inorganic matrix composite materials, a novel category of fibres has been developed, whose composition is characterized by the presence of zirconia (zirconium oxide, ZrO_2). Zirconia provides the glass with resistance to alkaline environments, like cementitious or lime-based environments, typical of the embedding media in FRCM. Alkali resistant (AR) glass fibres require a minimum amount of zirconia of 16%wt, according to European guidelines [UNI EN 15422 2008]. Glass fibres in general have a Young modulus around 70 GPa, which is lower than carbon fibres and suffer creep, fatigue and abrasion.

1.1.2.2 Carbon Fibres

Carbon fibres have raised an astonishing interest for their outstanding mechanical properties combined with a notable chemical inertness and durability. Carbon fibres present a diameter around 5-10µm and higher tensile strength ($\simeq 3500 \div 4800$MPa) and modulus ($\simeq 240 \div 600$GPa) with respect to glass, aramid and basalt fibres. If the field of civil engineering is considered, carbon fibres exhibit a slightly lower tensile strength than PBO fibres. On the other hand, PBO fibres are much more expensive. Furthermore, carbon fibres offer good creep behaviour, as well as good resistance to cyclic loading and to abrasion. The crystalline configuration of graphite is responsible for an extremely high degree of anisotropy, since covalent bonds within the single planes are stronger than Van der Waals bonds in the orthogonal direction. Carbon fibres are also characterized by an almost perfect pureness (graphite content $\geq 99\%$) due to their manufacturing process, which comprises pyrolysis at extremely high temperatures, up to 3000°C [Bunsell 2005]. The main steps of the production process include:

- **Stabilization (200-240°C)**: a carbon-based precursor (like polyacrylonitrile fibers (PAN) or rayon fibres) is subjected to an initial thermal treatment for 24 hours. This preliminary stage aims to orient the molecular structure according to the applied load.

- **Carbonization (1500°C)**: the material is deprived of impurities in an inert atmosphere.

- **Graphitization (3000°C)**: carbonized fibres are treated at ultra-high temperature to obtain a fully crystalline net, thus reducing defects.

Analogously to glass fibres, polymeric sizing (such as polyethylene oxide (PEO) or polyvinyl alcohol (PVA)) are often applied during the spinning process to protect the fibres and, if required, to increase their adhesion to the surrounding matrix in composite materials. As expected, all these thermal treatments have a strong energetic cost and environmental impact and therefore new fibres are sought after in order to reduce the impact of the production chain. For structural purposes, several kinds of carbon fibres are commercially available. They are arranged in thermo-welded textiles, ranging from high tenacity (HT) to high modulus (HM) and ultra-high modulus (UHM) systems, depending on the specific application.

1.2 Application of TRC and FRCM in Civil Engineering

Textile reinforced composites are extremely attractive to solve practical problems of civil engineering, for they offer a remarkable strength-to-weight ratio if compared to other construction materials. This feature is advantageous for the reinforcement of existing structures originally designed without taking into account seismic loading configurations. For seismic retrofitting casuistry, several applications are involved, namely unreinforced masonry panels or bearing walls, reinforced concrete beams and columns, wooden slabs and so on [Mayrhofer 2002]. The virtue of TRM lies in its extreme versatility of design and application, which can cover almost all structural problems in rehabilitation [Peled 2003]. Indeed, in-plane and out-of-plane forces induced by seismic events may trigger dramatic crack patterns and injuries to masonry, which exhibits a fairly low response in traction. Traditionally, techniques adopted for refurbishment range from jacketing, insertion of steel bars as transversal link to mortar injection. All these solutions may have a strong impact on the serviceability of the building [Galano 1998]. Moreover, it is often inevitable to consider the aesthetic impact of such techniques, which may compromise the originality of the prior look of the building. This issue is carefully taken into account in Italy, whose architectural heritage should be protected ensuring the structural integrity and safety and also preserving the historical fashion, given by valuable materials and adornments (i.e. frescoes, facade bas-reliefs etc.). When a layer of grout is cast to stiffen a slab or a wall, the benefit for the element is drastically reduced or even nullified by the increase of weight, which shortens the oscillation period of the structure resulting in amplified seismic forces and in reduced ductility. Thin composite materials are able to provide an optimized mechanical behaviour with no additional weight on the structure, already subjected to damage [Prota 2006]. Among the various refurbishment needs for the existing architectural heritage, FRCM may offer good and versatile solutions for interventions on reinforced concrete and masonry structures. Focusing on masonry elements, the bearing capacity of panels against shear and compressing-bending actions can be notably enhanced through the application of bi-axial meshes and/or uni-axial strips on both faces of the walls. The use of composite connectors is strongly recommended to transfer solicitations and to confer higher transversal strengthening, especially in the presence of walls characterized by poor texture of the clay-bricks [Babaeidarabad 2013]. The application on masonry panels relies on an increasing amount of experimental studies [Faella 2010, Balsamo 2016] and new analytical and numerical models have been proposed for practitioners and scientists [Lignola 2009, Cascardi 2016, Lignola 2019]. In the last years, the sensibility towards green application has aimed to lower energy consumption and natural materials have been increasingly explored and promoted. Indeed, composites

Figure 1.4: Extrados reinforcement of a cross vault through uni-axial fabric strips embedded in a cement-based mortar. (Courtesy of [CNR DT215 2018])

combining an inorganic matrix with natural fibres (N-FRCM) are attracting the attention of the scientific community. [Menna 2015]. Another field of application of textile-reinforced composites consists of masonry arches and vaults, whence the intrinsic low tensile strength of bricks may trigger collapses through the formation of hinges, which induce unexpected/undesired mechanisms. The main potentiality offered by FRCM relies in the chance to strengthen vaulted structures both at the intrados and at the extrados, without loading the structure additionally. In analogy with the in-plane reinforcement of walls, intervention on vaults can be designed either in a diffuse way (i.e. bi-axial fabric embedded in a thin mortar layer over the whole area) or through uni-axial strips laminated on the edge arches and along the diagonals, as illustrated in a common application in Fig.1.4. Form the aesthetic viewpoint, the extrados intervention is preferable when the intrados should be preserved because of the presence of valuable artistic or architectonic works. In general, the main reinforcing pattern should be connected with the bearing masonry walls through properly designed connectors. Again, a common weakness for masonry buildings, especially historical ones, consists in their poor "box" action, which is necessary to face seismic dynamic loading successfully. This can be ascribed to a poor interconnection set-up between horizontal and vertical elements. For the best resistance to earthquakes, it is fundamental that the whole structure behaves like a box, namely displacements of the external walls and of the plane slabs move consistently. A schematic of the difference in the behaviour of masonry structures without and with rigid slabs and good connections between elements is represented in Figure 1.5. A promising technique to favour the box action of masonry buildings and increase the collapse multipliers against rigid rotation of walls consists in confining the outer walls with composite strips or ropes, properly overlapped to warrant an adequate stress transfer. These reinforcements should be designed at the floor slabs. Whence the complete reinforcement ring is not viable for technical or logistic reasons, external FRCM fabrics should be connected with the orthogonal main walls for an appropriate depth. An example of application of a PBO strengthening ring placed at the garret floor is displayed in Figure 1.6 ([CNR DT215 2018]). FRCM is also commonly adopted as non-invasive and reversible confinement for masonry piers and columns. This reinforcement strategy allows remarkable enhancements in

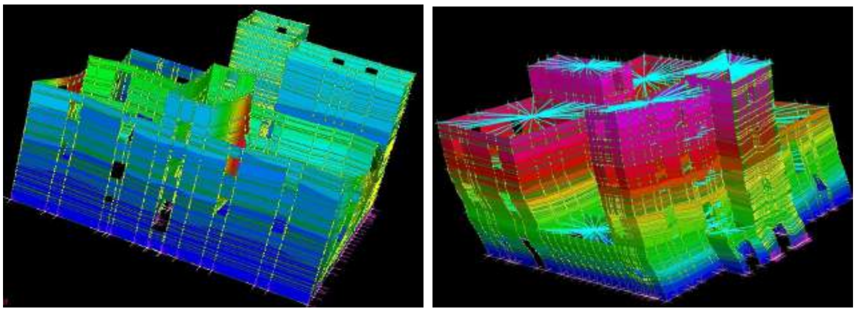

Figure 1.5: Different behaviour of a masonry building modelled without (left) and with (right) rigid slab, obtained through proper FRCM reinforcement.

Figure 1.6: PBO-FRCM strip applied at the garret floor of a masonry building. (Courtesy of [CNR DT215 2018])

terms of ductility as well as bearing capacity, in the presence of compression and bending loads. Also in this field, practitioners and scholars rely on a massive experimental [Mezrea 2016, Cascardi 2018] as well as analytical or numerical background [Cascardi 2017, Balsamo 2018], mainly developed in the very recent period. Moving to reinforced concrete elements, FRCM comprise several application fields, for instance the reinforcement of beams subjected to bending and shear. Continuous uni-axial strips can be applied in one ore more plies (up to an upper limit connected with the ring of fabric) on the edge in tension of beams, after an adequate restoration of the concrete cover. The experimental activity mainly carried out in the last decade [D'Ambrisi 2011, Babaeidarabad 2014] has depicted all the design criteria recalled in the more recent guidelines and constitute a set the basis for sound simulations of the mechanical behaviour, taking into account delamination and adhesion properties also in finite element modelling [Hashemi 2012]. Furthermore, also very recent industrial buildings, originally made of precast and pre-stressed reinforced concrete have urgently needed recover and seismic retrofitting, thus research interest is also devoted to that particular branch of concrete structures to define special design requirements for full-scale high strength precast beams [Pellegrino 2013]. Flexural reinforcement may also reduce the crack pattern and deflection under service loading, even if the stiffness increase is not substantial, due to the low thickness of the laminate. In analogy with FRP, shear reinforcement is performed through composite strips whose warp is oriented orthogonally to the main axis of the beam

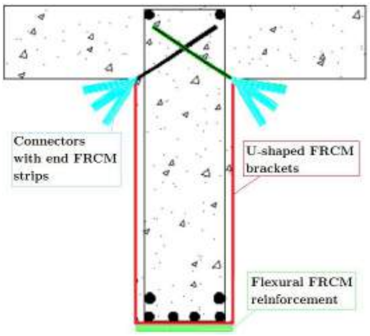

Figure 1.7: T-shaped beam of a road bridge reinforced with U-shaped brackets with connectors.

[Gonzalez-Libreros 2017]. FRCM brackets may be applied by juxtaposing fabrics (continuous reinforcement) or leaving a space between the strips (discontinuous reinforcement) and the optimal design condition consists in wrapping the beam with a ring bracket, when possible. If not all the edges of the beam can be reached, also a "U-shaped" confinement can be performed possibly transferring the loading within the beam core through connectors [D'Antino 2019]. It is usually the case of T-shaped beams whose upper flange is often unapproachable for complete wrapping. A possible technical solution for shear reinforcement is shown in Figure 1.7. Other applications for RC structures involve the enhancement of the bearing capacity and the ductility of columns, first by improving the compressive strength. Furthermore, instead of a perfect plastic behaviour (typically modelled for plain concrete), confinement trigger a further almost elastic trend [CNR TD200-R1 2013, §12, Fig.12-1], whose slope is governed by the configuration of the reinforcement (namely elastic modulus of the fabric), cross-sectional shape of the column and FRCM reinforcing system geometry [Arduini 2010, §5.4.1]. From the seismic standpoint, a decisive role is played by beam-column nodes. Strengthening nodes may provide the whole structure with a remarkable increase in terms of ductility, which improves the seismic response of the RC frame, combined with a negligible modification of the masses configuration. To the purpose, bi-axial, multi-axial and/or cross-placed uni-axial fabrics can be used in the actual node surface, in addition to a proper shear reinforcement on the edges of the elements converging towards the node. In Figure 1.8 (a) the wet lay-up of a PBO bi-axial textile embedded in a lime mortar is shown, while Figure (b) displays a similar application but with the use of a galvanized steel net within a cementitious mortar [CNR DT215 2018]. Concluding the scenario of applications regarding RC elements, FRCM can be effective in the shear reinforcement of concrete walls, in the strengthening of the intrados of floor slab beams, to prevent the concrete cover detachment. Furthermore, externally-bonded FRCM may be successfully employed to hinder the out-of-plane collapse of infill walls in RC frames, which can impair the safety in the service life of civil and industrial buildings [Koutas 2018]. Eventually, retrofitting of bridge beams and piers can be also performed, also in the presence of water.

(a.1) (a.2) (b.1) (b.2)

Figure 1.8: Reinforcement of RC nodes with PBO (a) and steel fabrics (b). Courtesy of [CNR DT215 2018]

1.3 Coatings on synthetic fibres in cementitious textile-reinforced composites: an overview

As already pointed out in the very introductory section, TRC and TRM, alongside the polymer-modified variation FRCM, is gaining ground as a viable alternative to more traditional composite materials [Bentur 2006, RILEM 232-TDT 2016], among which FRPs stand out for their importance. Indeed, compared to these, TRC exhibits interesting advantages, which are deeply connected to the adoption of a cementitious-based matrix: in particular we mention durability, fire resistance, reversibility and ease of intervention, compatibility with traditional building materials and water vapour permeability [Nobili 2016, Mechtcherine 2013, Nobili 2017a]. In contrast to FRPs, their performance is mainly driven by interphase compatibility, that is the surface adhesion between the matrix and the fabric reinforcement, and common fabric reinforcement materials present inadequate interphase compatibility with cement-based binders [Raoof 2016, Nadiv 2017]. It greatly hinders the full exploitation of the fibre mechanical strength [Mobasher 2011] and delamination is the predominant failure mode and it is most often associated with large data scattering and a not entirely consistent performance [D'Antino 2017, Nobili 2017a]. The qualitatively difference of impregnation between glass fibres embedded in a lime mortar with and without an adhesion promoter is as shown in Figure 1.9. Lack of adhesion plays a dramatic role when multifilament yarns are employed, because interior stands (the so-called core zone) can hardly be reached by the matrix, whose low penetrability affords contact only with the outer strands (the sleeve zone). As a consequence, failure occurs in a distinctive "telescopic pullout" manner, i.e. through sliding of inner over outer strands (just as in the unfolding of a telescope) [Cohen 2012, Butler 2011].

Among TRM and TRC materials, FRCM composites attempt to bridge the performance gap with FRPs through modification of the inorganic binder with an organic component. In fact, the recently published guidelines [ICC AC434 2013, ACI 549.4R-13 2013] advocates, for FRCM materials, the adoption of a “polymer-modified cement-based binder (mortar)” as the composite inorganic matrix. Al-

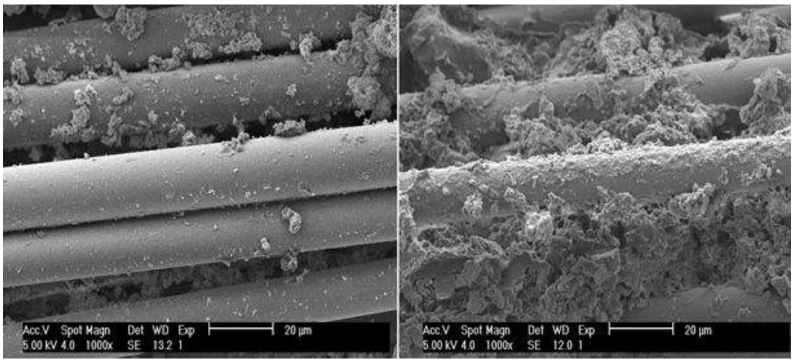

Figure 1.9: E-SEM image about fibre-to-matrix adhesion in a glass-FRCM yarn without the presence of an interphase coupling layer (left) and with a polymer interphase layer (right). Differences in the adhesion quality

ternative to matrix modification, thermal and particularly chemical treatment of the reinforcement have been investigated in order to improve adhesion with the cementitious matrix [Kim 1998]. One possible approach consists of developing a hydrophilic condition on the fiber surface [Fu 1996, Li 1997, Xu 1999], which increases wettability by the cementitious matrix and it leads to diffuse bond formation. As an example, cold gas plasma has been used to remove the hydrogen atoms from the polymer backbone of polyethylene fibers and to replace them by polar groups [Li 1996]. This approach may be extended and the specific polar group is connected to the adopted gas. The presence of polar functional chemical groups on the fiber surface increases reactivity and thus improves the reinforcement-to-matrix adhesion. In the case of carbon fibers, [Fu 1996] improved the surface bond strength with Portland cement by chemical oxidation of the reinforcement surface with ozone. This treatment leads to the formation on carbon fibers of oxygen-containing functional groups, which improve water wettability and, consequently, fiber/matrix bond. Surface bond enhancement with Portland cement is achieved in [Xu 1999] by performing silane and potassium dichromate treatment of carbon fibers. Results suggest that the hydrophilic nature of silane improves bond formation with cement. Moreover, similarly to ozone, dichromate treatment entails surface oxidation, which results in the appearance of oxygen-containing functional groups that enhance hydrophilicity, and consequently, adhesion. Coating and sizing have been recently proposed as a mean to provide improved strength, consistency as well as extended durability, respectively through interphase bond enhancement, defect healing and fabric protection. Through coating and sizing, fibre-matrix interphase modification is induced, taking advantage of polymer coatings, which comes as a natural choice to capitalize on the experience with FRPs [Kim 1998, Scheffler 2009].

In [Butler 2010], a polymeric surface coating is considered to protect glass fabric from deterioration in a highly alkaline environment, such is that associated with cementitious matrices. Indeed, in [Majumdar 1974] it is demonstrated that the quality of glass-to-cement bond changes in time, even for ARG fabric, owing to chemical and mechanical damage. Similar results are shown in

[Borri 2015, Nobili 2016, Micelli 2019, Nobili 2017b] in the framework of a wide spectrum durability analysis. The desire to streamline production, increase reproducibility and reduce labour-cost suggests to consider industrial coating for the fabric. Epoxy coating is already proven to contribute to defect healing and fabric durability [Gao 2007].

Remarkably, a small minority of studies is available in the literature assessing the role of epoxy coatings in improving mechanical performance of TRM, with special regard to coating formulation and thickness. Furthermore, existing studies consider out-of-the-box application of commercially available proprietary coatings, for which little data is accessible.

Mineral coating agents may be considered instead, such as silica, carbon nanotubes (CNT) and nanoclays, especially when fire resistance is a serious concern [Cohen 2012, Nadiv 2017, Signorini 2018b]. Polymer-based liquid impregnation agents can be employed at the lamination stage (wet phase) and their action mechanism is clearly related to their capacity to bridge the fabric-to-matrix interface [Nobili 2017a]. This bridging effect can be further improved adding fillers to the resin [Donnini 2016].

Recently, nano-structured coatings have been used to fill-in natural surface flaws in ARG fabric and thus fully deploy their expected mechanical performance [Gao 2007, Donnini 2016]. The same treatment is shown to possess a positive bearing on durability. The same approach is extended in [Scheffler 2009] to carbon fabric, where a polymer (epoxy resin) coating is considered, also in conjunction with Multi-Walled Carbon Nanotubes (MWCNT) and/or organoclays.

In [Cohen 2012], the role of organic and inorganic nanofillers on the mechanical performance of AR-glass TRC is investigated. Nanofillers act as an extra adhesion/frictional phase and they are applied to the glass bundles according to two different strategies: wet and dry. It is found that mechanical performance is strongly dependent on filler particle type and application strategy. In likewise manner, [Dvorkin 2013] investigates the effect of epoxy coated multifilament carbon fabric on the tensile, pull-out and fluid absorption capacity of TRC. Fabric is embedded in Portland cement and little details are available on the coating procedure. In [Donnini 2016], epoxy coating of carbon fabric in a cementitious matrix is investigated. Coating is performed by manual application with a brush or a spatula, which introduces large uncertainty on coating quality and thickness uniformity (see also [Nobili 2017a] for a case study example of data scattering connected to poor impregnation quality).

Chapter 2

General materials and methods

2.1 Materials

To better emphasize the role of the coatings proposed in the next chapters, pozzolan-based natural hydraulic mortars (NHL), adopted in [Nobili 2017a, Signorini 2018b, Signorini 2019c, Signorini 2019a], are employed as the inorganic binder for the composites.

These semi-hydraulic low-modulus mortars, whose mechanical properties are gathered in Tab.2.1, have proven particularly suitable in combination with synthetic fabrics in strengthening masonry panels. Both AR-Glass and carbon fabric reinforcements are considered and their main mechanical properties are gathered in Tab.2.2. Carbon reinforcement is a bi-axial (for traction tests described in Chapters 3 and 5, coded C1) or uni-axial (for bending tests described in Chapter 5, coded C2) open square-grid high-tenacity (HT) fabric, see Figs.2.1(a) and (b), respectively. Glass reinforcement is a bi-axial open square-grid fabric with a 19% weight content of ZrO_2 (Zirconium dioxide or Zirconia) to impart alkali resistance, Fig.2.1(c).

2.2 Mortars characterization

Three-point bending (3PB) tests are carried out on mortar prisms, according to the guidelines UNI EN 1015-07 [UNI EN 1015-11 2007], to precisely assess the mechanical performance of the lime-based mortar. Consequently, mortar specimens are cast in a 40 × 40 × 160 mm stainless steel mold and vibro-compacted. Specimen prisms are subjected to 7 day moist-curing and then stored to cure in a Memmert HP10 climatic chamber at 65% relative humidity (RH) for further 21 days. Tests are

Table 2.1: Lime mortars properties

Characteristic	Unit	HM5	M5	M15
Aggregate maximum size	mm	1	1	1.4
Density (fresh state, UNI 1015-6)	kg/dm^3	1.50	1.60	1.73
Min. compression strength (28 days)	MPa	5.0	6.5	15
Min. flexural strength (28 days) (EN 196/1)	MPa	1	3	3.4
Support adhesion strength after 28 days	MPa	0.4	1	1
Water content	%	21	23	21
Longitudinal elastic modulus (EN 13412)	GPa	—	6.0	9.0

Table 2.2: Fabric mechanical properties

Characteristic	Unit	C1	C2	ARG
Yarn count	tex	800	800	1200
Specific weight per unit fabric area	g/m^2	200	160	300
Fabric specific weight	g/cm^3	1.78	1.78	2.50
Grid spacing (warp)	mm	8	5	12
Fabric cross-sectional area (per unit width), A_f	mm^2/cm	0.56	0.88	0.60
Ultimate strength (warp, with epoxy)	N/cm	1800	1800	720
Elastic modulus	GPa	240	240	74

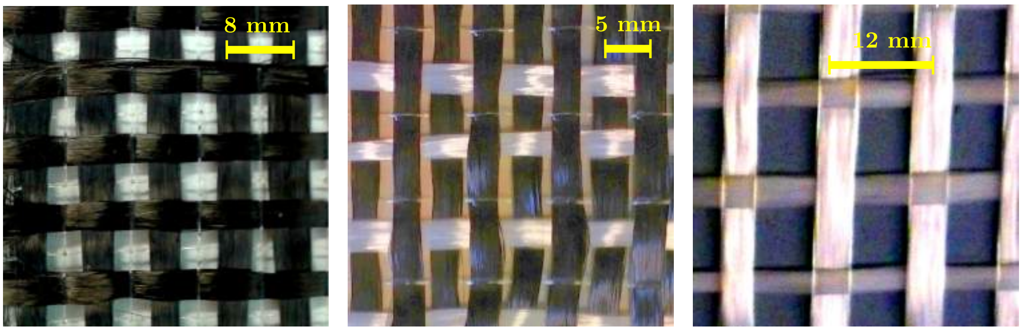

(a) C1 *(b) C2* *(c) ARG*

Figure 2.1: Fabrics used for TRM composite materials, labelled consistently with Table 2.2.

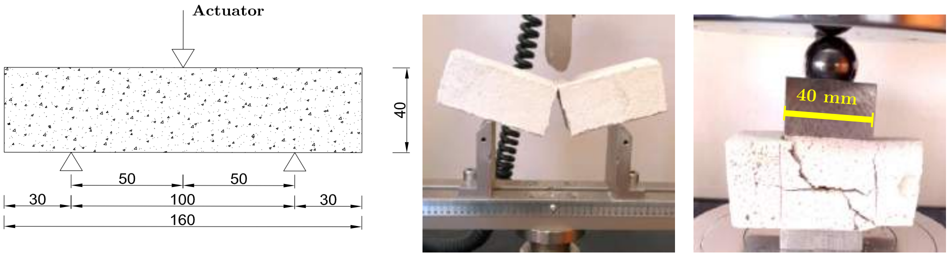

(a) *(b)* *(c)*

Figure 2.2: Three-point bending (test geometry (a), test set-up and failed specimen (b)) and compression test set-up (c) for mortar characterization

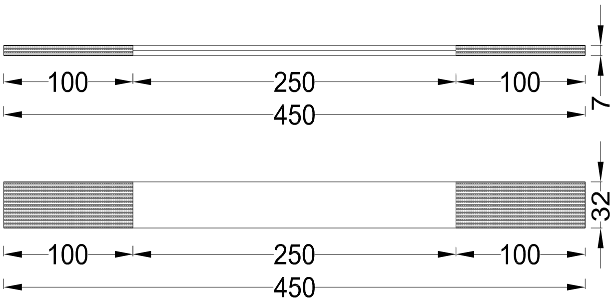

Figure 2.3: Typical composite coupon geometry. $w_g = 32\,\mathrm{mm}$ *is the width adopted for biaxial carbon fabric used in Chapters 3 and 5.*

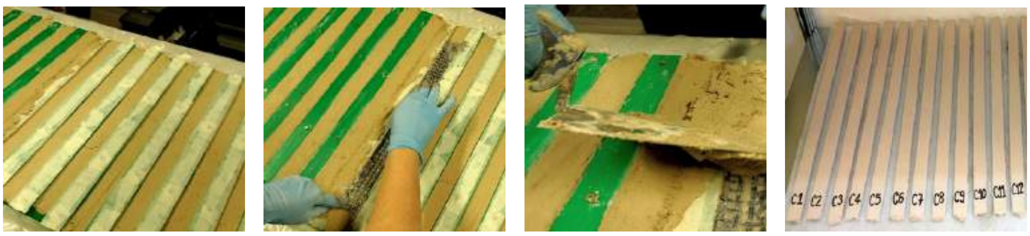

(a) *(b)* *(c)* *(d)*

Figure 2.4: Specimen manufacturing: (a) impregnated reinforcement placing (b) formwork upper piece and mortar second layer (c) coupons (d) coupons with tabs

performed through a Universal Testing Machine (UTM) at a nominal displacement rate of 1 mm/min (equivalent to $50 \div 100\ \mathrm{Ns}^{-1}$). The test geometry and set-up are shown in Fig.2.2(a-b). Monotonic compression tests are performed on failed specimens after 3PB: either specimen end is compressed between two 40×40 mm plates at a fixed displacement rate of 1 mm/min (equivalent to $50 \div 500\,\mathrm{Ns}^{-1}$). To rule out unwarranted bending effects which may arise owing to geometric irregularities in the specimen, a steel ball is placed right under the top steel plate of the UTM, see Fig.2.2 (c). Flexural and compression ultimate strength and elastic moduli are obtained from the experimental curves. At least 6 specimens are tested both in compression and in flexure.

2.3 Monotonic tensile tests of TRM laminates

2.3.1 Specimen manufacturing

Specimens for tensile tests are prismatic coupons of impregnated 1-ply TRM or FRCM with rectangular cross-section (Fig.2.3). The specimen nominal width is a multiple of the grid spacing and it accommodates an integer number of fabric strands [ICC AC434 2013]. Coupons are individually cast in a special purpose two-piece dismountable polyethylene formwork which provides reference for correct fabric reinforcement placing and allows easy and safe stripping. This procedure avoids cutting from a larger sheet, which might crack the fragile matrix and arguably

Figure 2.5: Test set-up for laminated coupons uni-axial tensile tests (gauge length $L_g = 250\,\mathrm{mm}$*)*

enhance the negative effect of aggressive environment exposition. Indeed, according to [ICC AC434 2013, A1.0], "poor material fabrication practices, lack of control in alignment of fiber grid, and damage induced by improper cutting and machining the coupons are known causes of high material data scatter". The manufacturing process comprehends the following stages:

1. a first 3-mm-thick mortar layer is cast onto the the lubricated formwork (which consists of the bottom piece only) and a scraper is used to level it up;
2. the fabric reinforcement is cut-to-size and optionally treated with dry or fresh coatings, laid on top of the mortar layer (Fig.2.4a);
3. the formwork is screw-fitted on top by the upper piece which constraints the grid reinforcement into its proper position;
4. a second 3-mm-thick mortar layer is cast in the surmounting formwork (Fig.2.4b) and a scraper is used to level it up;
5. the formwork is wrapped in a tight plastic sheet and, after 7-day moist curing (conditioning, see [ICC AC434 2013, A5.0]), it is disassembled and specimens are stripped (Fig.2.4c).

Specimens are cured for 28 or 60 days (including conditioning) in the laboratory environment. Successively, the specimen ends are fitted with 100 mm-long carbon or E-glass fabric tabs (the prescribed minimum tab length is 75 mm) which are glued to the coupon top/bottom surface with epoxy resin (Fig.2.4d). On the overall, at least four composite 1-ply coupons are fabricated for tensile testing experimental campaigns.

2.3.2 Test procedure

Coupon performance is assessed under uni-axial tensile testing. Traction tests are performed under displacement control at a constant elongation rate of 0.5 mm/min with an Instron 5567 Universal Testing Machine (UTM), with both an essentially stationary head and a movable head, equipped with a 30 kN load cell. According to [ICC AC434 2013, §A2.2], "each head of the testing machine shall carry one grip for holding the test specimen in coincident with the longitudinal axis of the specimen". Besides, the pair of wedge clamps, as again specified in [ICC AC434 2013, §A2.2], "shall apply sufficient lateral pressure to prevent slippage between the grip face and the coupon". Besides, rotationally self-aligning grips are adopted, "to minimize bending stresses in the coupon" (cf.[Hartig 2012] for some considerations on the importance of the test set-up). This nominal elongation rate amounts to the strain rate recommended in [RILEM 232-TDT 2016], i.e. $\dot{\varepsilon} = 2\,\mathrm{mstrain/min}$ (compare with $\dot{\varepsilon} = 3\,\mathrm{mstrain/min}$ in [Donnini 2016]). Grips are connected to the machine crosshead through a spherical hinge which allows rotation in three perpendicular planes. The test set-up is shown in Fig.2.5. Instead of transducers, the stress-strain response of the coupons are monitored by means of a stereoscopic 3 Mpixel Dantec Dynamics Q-400 Digital Imaging Correlation (DIC) system is adopted to fine measure the actual displacement field of the specimen surface, that is previously sprayed with a fine black speckled pattern onto a white background. DIC acquisition allows determining the influence of wedge grip elongation on the specimen end displacement induced by the traction machine. Fig.5.4 is representative of the comparison between the cross-head displacement, as measured by the traction machine, and the actual specimen-ends' relative displacement, digitally acquired on the end tabs. As specified in the following chapters when relevant, the theoretical ramp overestimates the actual specimen elongation rate by, roughly, $8 \div 10\%$, which brings in a displacement mismatch that is a linear function of time.

2.3.3 Elastic moduli calculation

The mean stress-strain curves allows determining the longitudinal elastic modulus for the uncracked, E_f^*, and the cracked, E_f, specimen [ICC AC434 2013, A7.5/6]. Such moduli are determined from the strength curve through linear-fitting of the conventional points given in [Arboleda 2014a, Nobili 2016]. In light of the matrix cross-sectional area $A = w_s h_s$ (here $h_s = 7$ mm is the specimen nominal thickness) being much larger than the fabric's $A_f w_s$, a corrected uncracked modulus is sometimes introduced [Arboleda 2014a]

$$E_1^* = E_f^* \frac{A_f w_s}{A} \tag{2.1}$$

which should better express the mechanical stiffness of the coupon before matrix cracking occurs.

Modulus after first cracking is evaluated by identifying two points, which are likely subsequent to the transition point.

$$E_f = \frac{\sigma_{@0.9f_u} - \sigma_{@0.6f_u}}{\varepsilon_{@0.9f_u} - \varepsilon_{@0.6f_u}}. \tag{2.2}$$

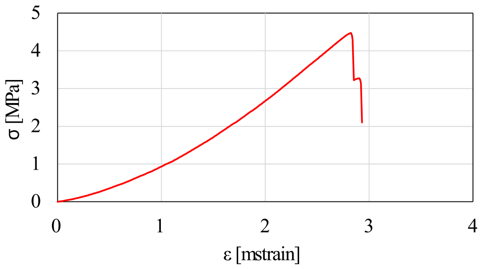

Figure 2.6: Mean strength curve of the clay brick (prior to lamination)

According to the experimentation conduced by [Arboleda 2014a, Arboleda 2014b], cracked elastic moduli is affected by clamping device. For wedge clamped specimen it may result higher than in the real application due to the fully constrained configuration of the laminate. Indeed, as Arboleda points out in her dissertation, "in repair applications, the fabric is not anchored, thus establishing the boundary condition which is represented by pin action type grips or any gripping that does not apply a clamping force". Anyway, for comparative purposes the variation of the modulus is considered, rather than its absolute value, which can properly scaled according to the findings available in the literature [Bianchi 2013, Carozzi 2017].

2.4 Three-point bending tests on brick supports

2.4.1 Specimen manufacturing

Three-point bending tests are performed on clay bricks following [ASTM C 947-03 2003]. Bricks are strengthened at the bottom surface by lamination of TRM composite material, see Fig.2.8. A minimum of 5 laminated bricks are considered for each test group.

The lamination geometry is illustrated in Fig.2.7 (a) and it appears that no provision against delamination is taken at the specimen ends. Indeed, the adopted mortar has already proven very effective in terms of bond formation with a clay substrate, see [Nobili 2017a]. Fig.2.7 (b) shows the clay brick substrate (Fornace Brioni Srl). In particular, the brick mean strength curve under three-point bending is presented in Fig.2.6.

Lamination is performed according to the following procedure:

1. the brick surface is levelled (yet surface should remain rough) and thoroughly wetted to warrant complete mortar-to-clay bond formation;
2. paper adhesive tape is located at the brick ends to protect the supported zone from the lamination material (Fig.2.8);
3. a 1-mm-thick layer of mortar is laid on the wetted brick surface. Levelling the brick surface averts the risk of obtaining areas where the laminate is excessively thick, which is undesirable on account of the small scale of the test (Fig.2.7(b));

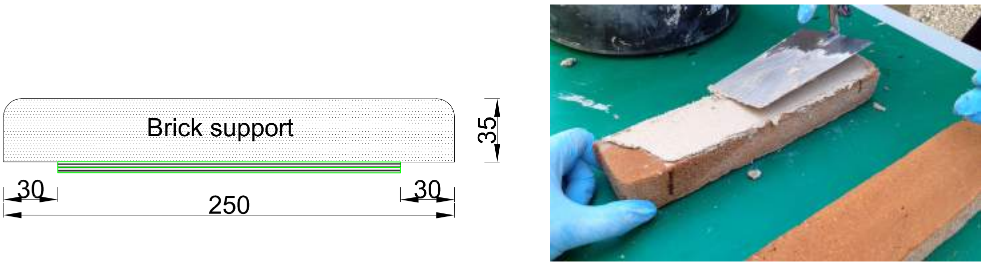

(a) (b)

Figure 2.7: Three-point bending of laminated bricks schematic (a) and clay-brick surface lamination (b): the first mortar layer is laid on the wetted specimen surface

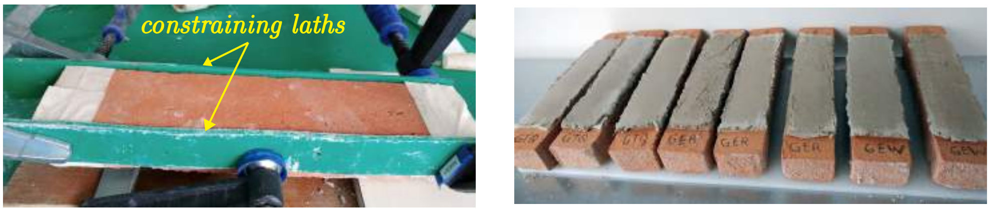

(a) (b)

Figure 2.8: Three-point bending test specimen manufacture: (a) brick support with constraining laths (b) laminated specimens

4. for polymer coating, impregnation takes place as for coupon manufacture;

5. cut-to-size fabric is laid and slightly pressed onto the fresh mortar. Air bubbles trapped at the mortar-to-fabric interface are eliminated through rolling;

6. a 3-mm-thick over-layer of mortar is applied and levelled by using a scraper.

A removable formwork provides a smooth and regular border for lamination. Conditioning and curing take place as per uni-axial traction tests (28 days on the overall).

Figure 2.9: Test set-up for laminated clay-bricks three-point bending test (support distance $d = 200\,\mathrm{mm}$)

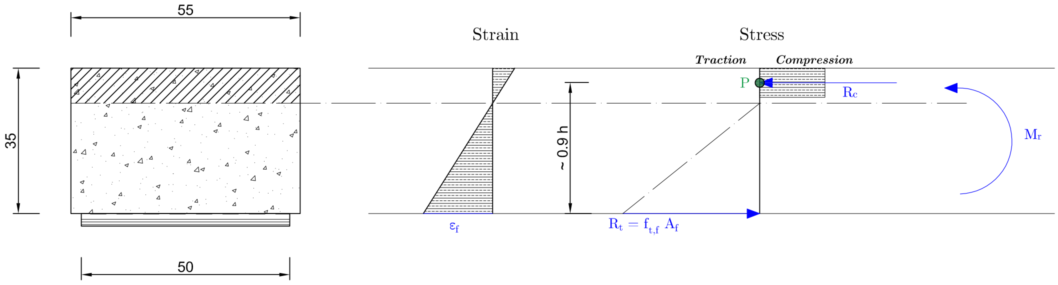

Figure 2.10: Schematic of the simplified model adopted to evaluate the maximum axial stress attained by laminated fabrics in bending. The hatched part of the section refers to its compressed portion.

2.4.2 Test procedure

Three-point bending is carried out in a Instron 5567 electromechanical Universal Testing Machine (UTM), equipped with a two-point support and a floating knife. The test set-up is shown in Fig.2.9(b). Bending test occurs under displacement control at 1 mm/min speed for the moving knife [ASTM C 947-03 2003]. To compute the axial stress to which fabrics are subjected after brick failure at the lower edge of the mid-span cross-section, a simplified model is considered, recalling the technical formulas of RC structures bending resistance. Indeed, at post-cracking stage, brick is assumed to provide only compressive stress and all the tensile component is demanded to the fabric. The arm of the two forces is assumed to be equal to the 90% of the beam height, as commonly assumed in estimating the ultimate limit state (ULS) resistance of a reinforced concrete cross-section. In the schematic of Figure 2.10 the simplified model is outlined. The maximum value of strength attained by the reinforcing fabric in bending, is given by

$$f_{t,f} = \frac{M_{max}}{0.9\ h\ A_f} \tag{2.3}$$

In Eqn.(2.3), $M_{max} = \frac{P_{max} L_s}{4}$ corresponds to the maximum bending moment acting on the mid-span cross-section of the brick, according to the simply supported static configuration. L_s is the span length, P_{max} the maximum load measured by the load cell, after the peak corresponding to the cracking of the support. Finally, h and A_f are the height of the brick cross-section and the net fibres cross-section, respectively.

Chapter 3

Inorganic and hybrid coatings for synthetic fibres

Contents

To enhance the interphase bond and increase the fabric-to-matrix compatibility, a hydrophilic SiO_2 nano-layer is proposed as a simple and relatively low-cost procedure to obtain interphase modification and functionalization of ARG and carbon fabric reinforcement in a cementitious (or lime-based) mortar. Although applications of silica coatings form a vast body of literature, to the best of the author's knowledge this is the first contribution investigating the effect of silica sol-gel deposition on the mechanical performance of continuous reinforcements for structural purposes [Signorini 2018b].

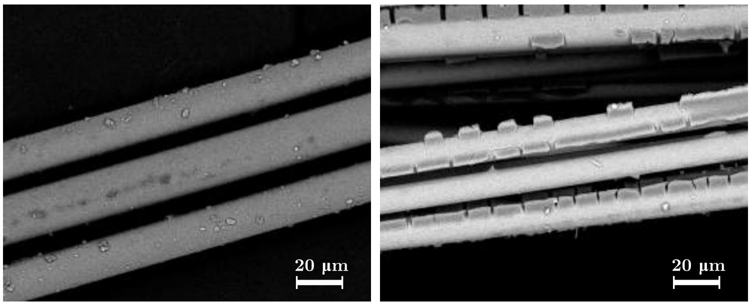

(a) Uncoated fibres *(b) Silica-coated fibres*

Figure 3.1: 2000x magnification FEG-SEM images of uncoated and silica coated fibres

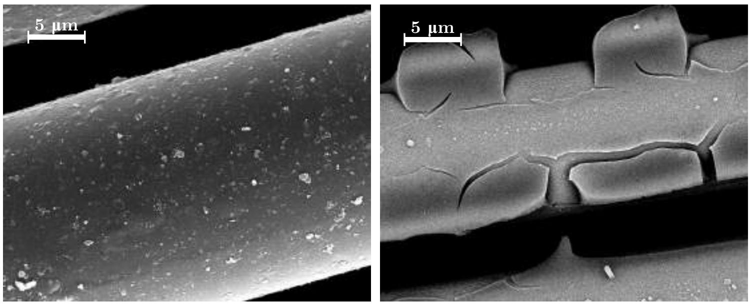

(a) Uncoated fibres *(b) Silica-coated fibres*

Figure 3.2: 10000x magnification FEG-SEM images of uncoated and silica coated fibres

3.1 Nano-silica coating

3.1.1 Coating procedure and characterization

SiO_2-coated fibres are prepared through a fast acid-catalysed sol-gel synthesis as reported by [Nikkanen 2015] in the context of photoactive and photoelectrochemical enhanced coated steel. First, tetraethyl orthosilicate (98% TEOS, Sigma-Aldrich Inc.) and isopropyl alcohol ($\geq$ 99.7% Sigma-Aldrich Inc.) are mixed together for 15 min and then deionized water and nitric acid (65% Carlo Erba Reagents Srl) are added. This solution is further stirred for 2 hrs in a magnetic stirrer. The solution $TEOS:C_3H_7OH:H_2O:HNO_3$ is in the molar ratio $1 : 4.5 : 5 : 0.16$. Coating is realized through dip-coating fibers in the obtained solution for 5 min, to ensure that the whole fibre surface is thoroughly wetted. After bathing, fibres are immediately air-dried at 110°C for 15 min in an oven. The coating on the fibres is assessed through a field emission gun scanning electron microscopy (FEG-SEM), which takes advantage of ultra-high resolution, ideal for studying materials on the nanometre scale.

Three different magnification levels for uncoated and silica-coated fibres are reported in Figures 3.1, 3.2 and 3.3, i.e. 2000×, 10000× and 20000×, respectively. The treatments reduce the actual cross-section of the fibres, that are covered by a non-uniform ultra-thin layer of silica gel. The distribution of the coating evidenced by the high-zoom images suggests that the interaction with the surrounding mortar

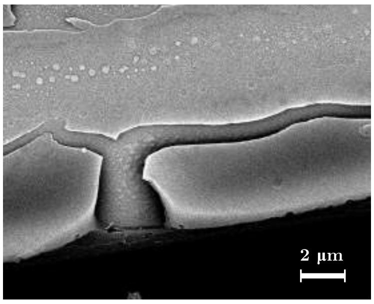

Figure 3.3: 20000x magnification (detail) FEG-SEM image silica coating on AR-glass fibres

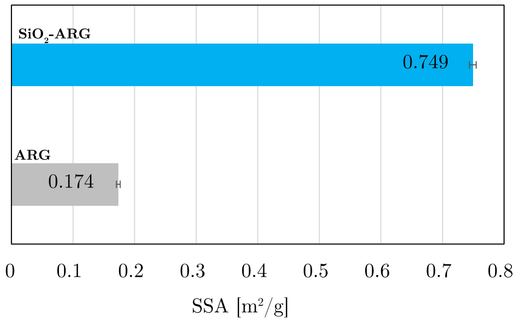

Figure 3.4: Specific Surface Area (SSA) for uncoated ARG vs. silica coated (SiO_2)-ARG) fibres.

relies upon both the enhanced chemical affinity (due to high hydrophilicity) and the roughness at micro-level on the fibres' surface. The confirmation of the increased hydrophilicity of the fibres is measured through a Brunauer-Emmett-Teller (BET) analysis [Brunauer 1938], which is the most commonly used technique to have a measurement of the specific (per unit mass) surface area (SSA) of a solid. BET analysis provides an accurate evaluation of SSA of materials by measuring nitrogen adsorption as a function of relative pressure. SSA is an indicator useful to investigate adsorption and reactive capability of a surface. SSA is evaluated by computing the adsorbate gas amount corresponding to a monomolecular layer on the surface of the material. The technique encompasses external area and pore area evaluations to determine the total specific surface area. The measurement is carried out with a Micromeritics porosimeter. Bar-chart of Figure 3.4 brings evidence of a remarkable enhancement in terms of surface area due to the nano-silica coating. Indeed, the increase of SSA is more than 4-fold with respect to plain ARG fibre. This can be ascribed to the increase of the surface micro roughness and to the functionalization induced by the hydroxyl molecules of amorphous silica (see Figure 3.5).

3.1.2 Specimens

3.1.2.1 Uni-axial tensile test

According to the nomenclature of Table 2.2, two reinforcement materials, namely AR-Glass (ARG) and bi-axial carbon fabric (C1), are investigated and, for each of

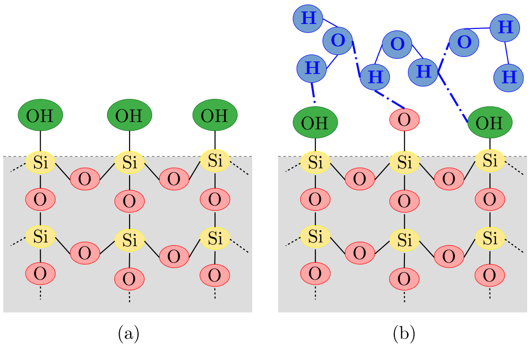

Figure 3.5: Schematic of the functionalization of the surface and the enhancement of its hydrophilic attitude. Dry (a) and hydrated silica-coated surface.

these, three test groups are considered, namely dry-fabric (UC, alias uncoated), silica coated (SC) and polymer coated (PC) fabric. Specimens are manufactured on an individual basis, in order to avoid cutting from a larger sheet following the procedure detailed in Sect.2.3.1. Six prismatic coupons are manufactured in each test group for a total of 36 coupons, having the dimensions displayed in Figure 2.3. Accordingly, specimens conform to the specifications of Annex A of [ICC AC434 2013] and, in particular, the coupon nominal width is chosen as a multiple of the fabric grid spacing [ICC AC434 2013, §A3.0]. Thus, with respect to ARG fabric reinforced specimens, the coupon width $w_{s,G} = 360\,\mathrm{mm}$ accommodates 3 strands, while, for carbon fabric reinforced specimens, the coupon width $w_{s,C} = 320\,\mathrm{mm}$ accommodates 4 strands.

After the initial moist-curing of the coupons, the formwork is dismounted and specimens are stripped for curing at the laboratory conditions (21 ± 2°C and 60–75% relative humidity). The total conditioning and curing time is 28 days. Finally, coupons are fitted with 100-mm-long carbon fabric tabs, which are glued at both ends through epoxy resin.

3.1.2.2 Three-point bending tests

For bending tests, the same six test groups mentioned for axial tensile tests are considered, namely ARG and C1 reinforcing fabrics and, for each of these, dry-fabric, silica coated and polymer coated fabric. In this case, the laminate sandwich is directly applied onto the brick support, following the procedure detailed in Section 2.4. Again, six laminated bricks are considered for each test group. No provisions against edge delamination are taken. Indeed, the adopted mortar has already proven very effective in terms of bond formation with a clay substrate, see [Nobili 2017a].

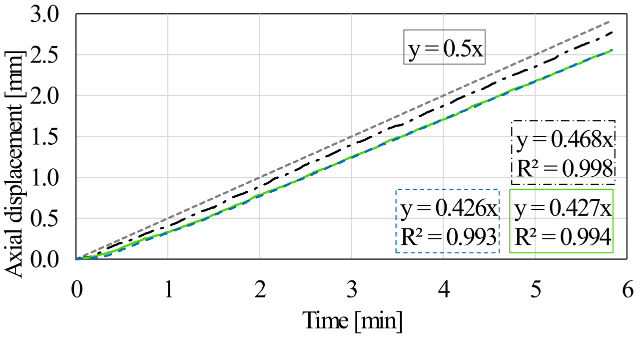

Figure 3.6: DIC estimated vs. prescribed (grey, short-dashed line) specimen end displacement curves for ARG coupons: uncoated (black, dash-dot), silica (green, solid line) and, almost superposed, polymer coated (blue, dashed line)

3.1.3 Experimental investigation

3.1.3.1 Uni-axial tensile test

Tensile tests on laminated coupons are carried out in accordance with the prescriptions provided by [ICC AC434 2013] and [RILEM 232-TDT 2016], as described thoroughly in Section 2.3.2, by means of a Instron 5567 UTM. A stereoscopic twin-camera 3 Mpixel Dantec Dynamics Q-400 Digital Imaging Correlation (DIC) system is adopted to capture the displacement field of the specimen surface, previously speckled, throughout the test. DIC investigation allows correcting the displacement ramp prescribed at the traction machine crosshead by the elongation taking place at the wedge grips and thus it provides the actual specimen deformation. This step is mandatory for a reliable evaluation of the ultimate strain [Hartig 2012]. Indeed, Fig.3.6 compares the specimen elongation for ARG coupons in the uncoated, silica and polymer coated groups with the prescribed ramp. Regression lines are shown together with the coefficient of determination R^2. It immediately appears that the regression line for silica coated specimens almost coincides with the corresponding regression line belonging to the polymer coated group.

3.1.3.2 Three-point bending test

Three-point bending test for laminated clay-bricks is performed following the procedure, properly detailed in Section 2.4.

3.1.3.3 Optical and scanning microscope investigation

In consideration of the strong connection between mechanical properties of the composite and interphase compatibility, a visual analysis is conducted using both optical and scanning electron microscopy (SEM). This analysis falls in line with the conditions of acceptance given in [ICC AC434 2013, §4.5.2]. To this aim, some specimens for each population have been observed after the failure occurred, in order to consider an inner random element of the lamina at the interlayer level. Figs.**??** and 3.7 show the fabric surface after failure at 8X magnification, respectively for ARG

(a) ARG, uncoated *(b) ARG, silica coated*

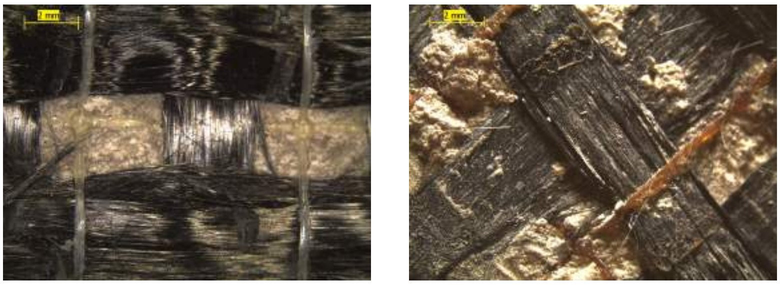

(c) C1, uncoated *(d) C1, silica coated*

Figure 3.7: Optical microscopy investigation at 8X magnification of ARG and C1 failed specimens (a,c) uncoated (b,d) silica coated

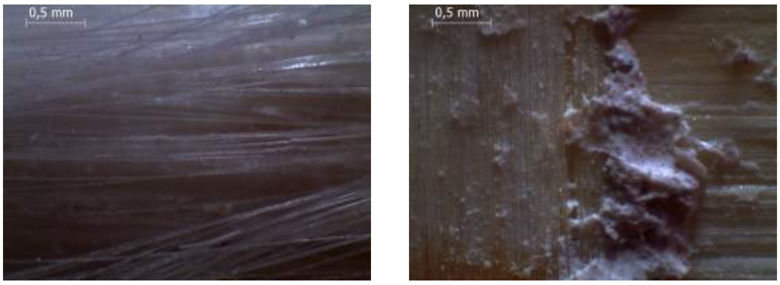

(a) *(b)*

Figure 3.8: Optical microscopy investigation at 35X magnification of ARG failed specimens (a) untreated (b) silica coated

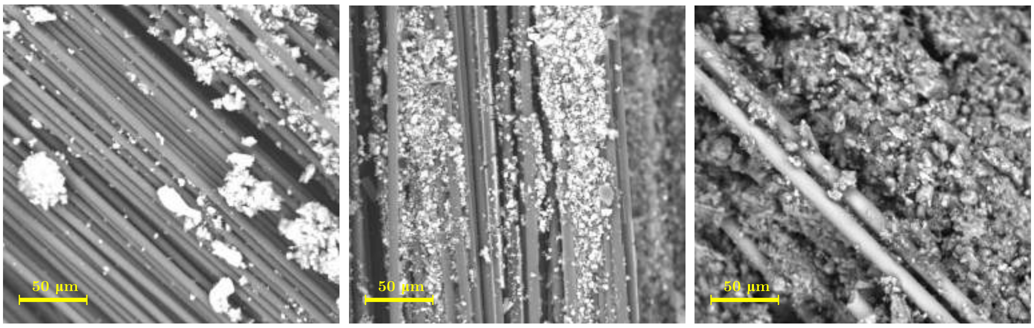

(a) *(b)* *(c)*

Figure 3.9: SEM investigation of C1 failed specimens at 1000X magnification: (a) uncoated (b) silica and (c) polymer coated

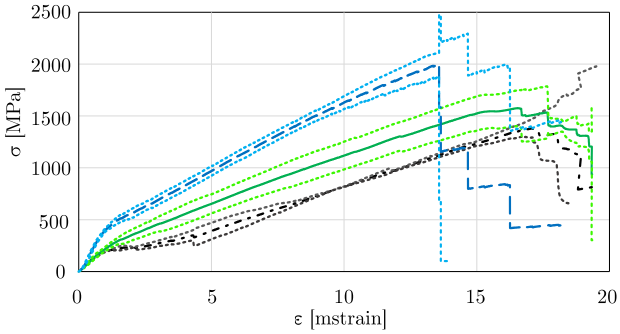

Figure 3.10: Mean stress-strain curves for uni-axial traction of C1 uncoated (black, dash-dotted) silica (green, solid) and polymer coated (blue, dashed) specimens. Confidence bands, in terms of $\mu \pm \varsigma$, are also given (dotted)

and C1 specimens. It appears that uncoated specimens show no evidence of mortar adhesion to the fabric surface, whereas silica and, even more so, polymer coated specimens present patches still bonded to the matrix. To better illustrate the point, Fig.3.8 presents a 35X comparison between uncoated and silica coated ARG failed specimens. It is seen that the silica coated specimen shows clear evidence of interphase bond enhancement and strong bond formation with the matrix. Conversely, the lime-based matrix possesses little compatibility with the uncoated fabric from which it detaches completely at failure, leaving an almost perfectly polished surface. In fact, in the lack of chemical adhesion, the major contribution to mechanical performance is given by the mechanical interlock occurring through the open square grid of the fabric. Similar observations are suggested by a SEM investigation at 1000X magnification for a C1 failed specimen (Fig.3.9). It can be observed that, for the uncoated specimen, only a few outmost fabric strands are adhered to by the mortar, whereas for silica coated and, to an even greater extent, for polymer coated specimens, uniformly diffuse bond formation appears.

3.1.4 Results and discussion

3.1.4.1 Carbon fabric

Fig.3.10 gathers the mean stress-strain curves and the confidence bands (i.e. mean stress-strain curve ± one-standard deviation) for uni-axial traction of C1 coupons in all test groups. Force is conventionally reported to the fabric cross-sectional area [ICC AC434 2013, Nobili 2017b]. Mean ultimate strength and strain are determined and they are collected in Tab.3.1 along with the standard deviation, ς, and the coefficient of variation, CV (also known as relative standard deviation).

Fig.3.11 presents a bar-chart comparison of mean ultimate values for all C1 groups tested in traction. It is observed that, although silica coating offers a mere 10% mean ultimate strength increase over the uncoated group, it conveys a 26% reduction of the standard deviation. This decrease of data dispersion is even more pronounced when expressed in terms of ultimate strain. Indeed, ultimate strain

Table 3.1: Mean ultimate tensile strength $\mu(f_{fu,t})$ and elongation $\mu(\varepsilon_{fu,t})$, together with corresponding standard deviation, ς, and coefficient of variation, CV, for uncoated (UC), silica (SC) and polymer coated (PC) C1 specimens in uni-axial traction

Group	$\mu(f_{fu,t})$ [MPa]	ς_f [%]	CV_f [%]	$\mu(\varepsilon_{fu,t})$ [%]	ς_ε [%]	CV_ε [%]
UC	1496	245	16	2.23	0.46	20
SC	1637	180	11	2.07	0.10	5
PC	2117	92	4	1.52	0.19	13

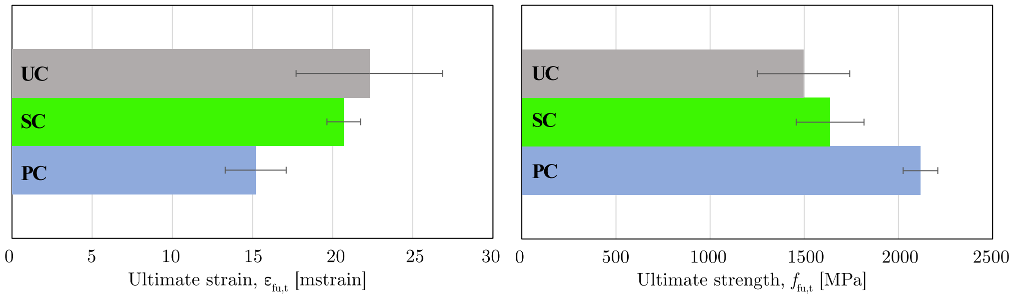

(a) *(b)*

Figure 3.11: Mean ultimate strain (a) and strength (b) for C1 coupons in uni-axial traction: uncoated (UC) silica (SC) and polymer coated (PC)

is reduced by 7% with respect to the uncoated group and yet the corresponding standard deviation is decreased by an impressive 78%, i.e. it is reduced to one fourth. Therefore, it appears that silica coated specimens become marginally stronger and more brittle than uncoated ones, however failure occurs consistently in terms of ultimate strain, which behaviour conveys a strong beneficial effect on design values. Indeed, according to [ICC AC434 2013], the ultimate strain is obtained by the so-called three-sigma rule,

$$\varepsilon_{fu} = \mu(\varepsilon_{fu,t}) - 3\varsigma_\varepsilon, \tag{3.1}$$

from which the design strain follows

$$\varepsilon_{fd} = 0.7\varepsilon_{fu} < 1.2\%. \tag{3.2}$$

From Tab.3.1, it is $\varepsilon_{fu} = 0.85\%$ for the uncoated group and $\varepsilon_{fu} = 1.77\%$ for the silica coated group, that gives a two-fold increase. Similarly, if characteristic values are considered as the basis from which design strain is determined (see the design considerations in [Nobili 2017b])

$$\varepsilon_{fuk} = \mu(\varepsilon_{fu,t}) - 1.96\varsigma_\varepsilon, \tag{3.3}$$

we find $\varepsilon_{fuk} = 1.33\%$ for the uncoated and $\varepsilon_{fuk} = 1.87\%$ for the silica coated group, which still brings a 41% increment. This substantial gain in the design strain reflects itself in an equally important benefit in terms of design strength, for

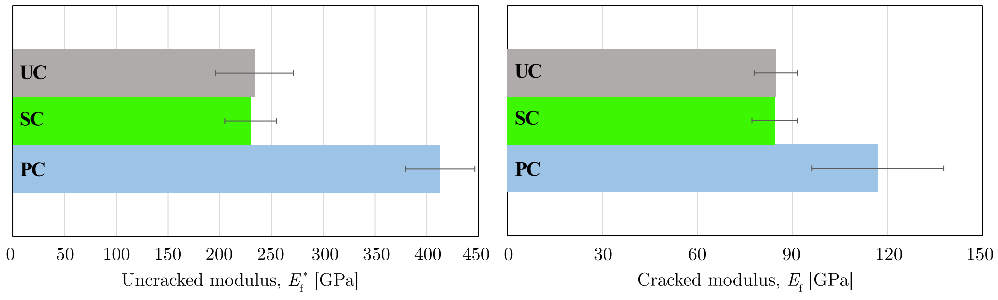

(a) *(b)*

Figure 3.12: Uncracked (a) and cracked modulus (b) for C1 coupons in uni-axial traction: uncoated (UC) silica (SC) and polymer coated (PC)

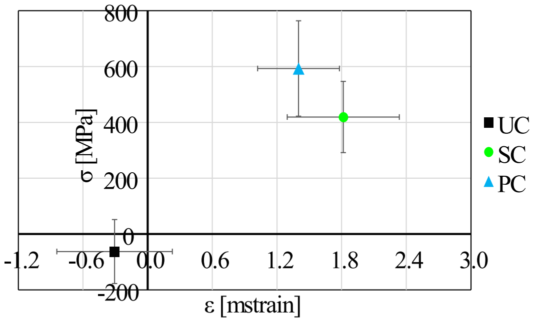

Figure 3.13: Transition point location and standard deviation bars for C1 coupons in uni-axial traction: uncoated (UC) silica (SC) and polymer coated (PC)

the latter is proportional to the former through E_f, the tensile modulus of elasticity of the cracked composite material.

Results for polymer coated specimens give a 42% and a 29% improvement of the mean ultimate strength over the uncoated and the silica coated groups, respectively. Such strength increment is accompanied by an impressive decease in the coefficient of variation, that is reduced to one-fourth of that pertaining to uncoated specimens. However, strength gain comes at a significant cost in terms of ductility, for mean ultimate strain is reduced by 32% as compared to the uncoated group.

In terms of design values, we have $\varepsilon_{fu} = 0.95\%$, which brings a small 11% increase over uncoated specimens, and yet it is nearly half the corresponding value for silica coating. Besides, when characteristic values are adopted, we find $\varepsilon_{fuk} = 1.15\%$, which is lower than the corresponding value in the uncoated group. It is concluded that, under the light of best design values, silica coating offers better performance over polymer coating.

Values of the cracked and of the uncracked moduli are presented in Tab.3.2 together with transition point locations. It is interesting to note that, for the uncoated and for the silica coated groups, uncracked and cracked moduli are nearly equal, whereas polymer coated specimens are substantially stiffer (Fig.3.12). This observation highlights the importance of interphase bond formation in determining tensile moduli. Transition points are determined as in [Nobili 2016] and they are

Table 3.2: Uncracked modulus, E_f^*, cracked modulus, E_f, and turning point location with corresponding standard deviations for uncoated (UC), silica (SC) and polymer coated (PC) C1 specimens in uni-axial traction

Group	E_f^* [GPa]	$\varsigma_{E_f^*}$ [GPa]	E_f [GPa]	ς_{E_f} [GPa]	ε_T [mstrain]	ς_ε [mstrain]	f_T [MPa]	ς_{f_T} [MPa]
UC	233	34	85	7	−0.3	0.5	−63	115
SC	230	25	84	7	1.8	0.5	419	128
PC	413	33	117	21	1.4	0.4	593	171

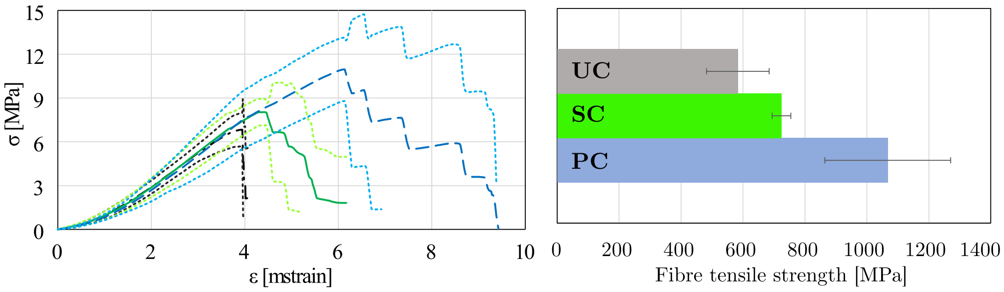

(a) *(b)*

Figure 3.14: Mean stress-strain curves for three-point bending tests of C2 uncoated (black, dash-dotted) silica (green, solid) and polymer coated (blue, dashed) specimens. Confidence bands, in terms of $\mu \pm \varsigma$, are also given (dotted) (a). Evaluation of the maximum axial tensile stress of the fabric (b)

plotted in Fig.3.13 along with confidence bars. In particular, it can be seen that the transition point for uncoated specimens is located in the third quadrant of the (σ, ε) plane.

Mean stress-strain curves and confidence bands for three-point bending of C2 coupons are presented in Fig.3.14, together with the corresponding maximum tensile stress attained by the fabric, according to the simplified model depicted in Figure 2.10 and relevant formula in Eqn.2.3. It is observed that confidence bands are considerably narrower in the uncoated and in the silica groups compared to the polymer coated group and this occurs for strain and strength alike. On the other hand, unlike traction, mean curves show remarkable correspondence until failure occurs. Tab.3.3 shows the mean ultimate values as determined through three-point bending tests. In contrast to traction, the coefficient of variation CV_f, relative to the ultimate mean strength of silica coated specimens in bending, is roughly one fifth than that for polymer coated specimens. The corresponding quantity relative to the ultimate strain, CV_ε, is 38% less than for polymer coated specimens, yet 68% grater than in the uncoated group. However, this apparently surprising outcome is expected, owing to the uncertainty connected to the determination of the ultimate deformation at failure of ductile, as opposed to brittle, specimens. Finally, Fig.3.15 gives a bar-chart illustration of ultimate strength and strain obtained in bending for all test groups.

Table 3.3: Mean ultimate flexural strength $\mu(f_{u,f})$ and elongation $\mu(\varepsilon_{u,f})$, together with corresponding standard deviation, ς, and coefficient of variation, CV, for uncoated (UC), silica (SC) and polymer coated (PC) C2 specimens in three-point bending of laminated clay bricks

Group	$\mu(f_{u,f})$ [MPa]	ς_f [MPa]	CV_f [%]	$\mu(\varepsilon_{u,f})$ [mstrain]	ς_ε [mstrain]	CV_ε [%]	$\mu(f_{t,f})$ [MPa]	$\varsigma(f_{u,f})$ [MPa]
UC	6.95	1.20	17	4.1	0.3	7	584	101
SC	8.62	0.36	4	5.7	0.7	12	724	30
PC	12.70	2.42	19	8.0	1.6	20	1067	203

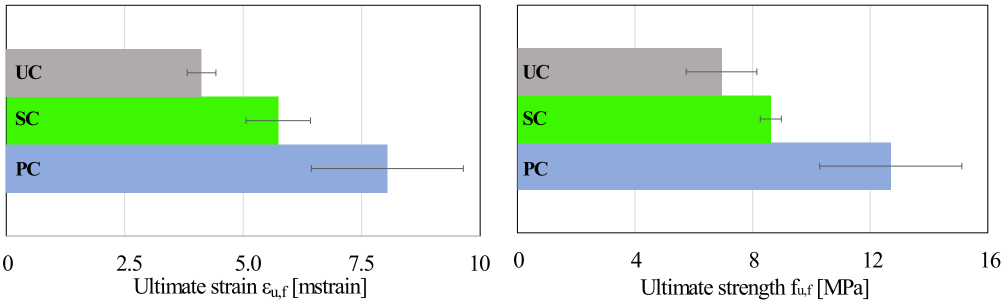

(a) *(b)*

Figure 3.15: Mean ultimate strain (a) and strength (b) for C2 laminated bricks in three-point-bending: uncoated (UC), silica (SC) and polymer coated (PC)

3.1.4.2 AR-Glass fibres response

Fig.3.16 presents the mean stress-strain curves for uni-axial traction of ARG coupons in all test groups. The corresponding ultimate stress and strain values are given in Tab.3.4.

The bar-chart comparison of Fig.3.17 indicates that silica and polymer coating of ARG induce a strong beneficial effect on the ultimate strength which, unlike carbon fabric, comes along with a relevant ductility increment. However, confidence bars still confirm that the best performance in terms of design strain is achieved by silica coating. Indeed, by Eq.(3.1), we have $\varepsilon_{fu} = 0.47\%$ for the uncoated group

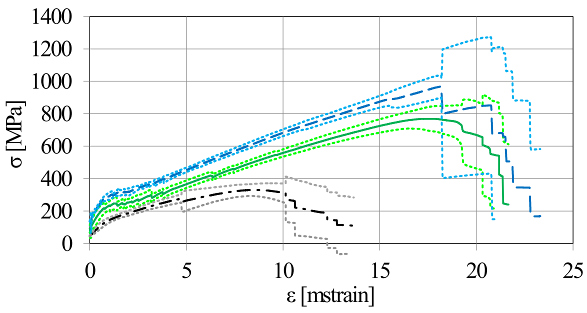

Figure 3.16: Mean stress-strain curves for uni-axial traction of ARG uncoated (black, dash-dotted) silica (green, solid) and polymer coated (blue, dashed) specimens. Confidence bands, in terms of $\mu \pm \varsigma$, are also given (dotted)

Table 3.4: Mean ultimate tensile strength $\mu(f_{fu,t})$ and elongation $\mu(\varepsilon_{fu,t})$, together with corresponding standard deviation, ς, and coefficient of variation, CV, for uncoated (UC), silica (SC) and polymer coated (PC) ARG specimens in uni-axial traction

Group	$\mu(f_{fu,t})$ [MPa]	ς_f [MPa]	CV_f [%]	$\mu(\varepsilon_{fu,t})$ [mstrain]	ς_ε [mstrain]	CV_ε [%]
UC	353	33	9	11.3	2.2	20
SC	786	74	9	19.6	1.1	6
PC	1042	47	4	23.1	1.9	8

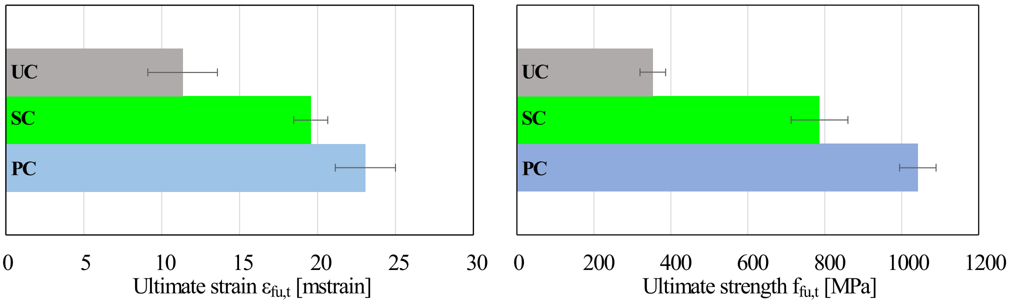

(a) *(b)*

Figure 3.17: Mean ultimate strain (a) and mean ultimate strength (b) for ARG specimens in uni-axial traction: uncoated (UC) silica (SC) and polymer coated (PC)

and $\varepsilon_{fu} = 1.63\%$ for the silica coated group, that is nearly a 3.5-fold increase, to be compared with 2.2-fold increase in the ultimate strength. For polymer coated specimens, we get $\varepsilon_{fu} = 1.74\%$, which is similar to the performance of the silica coated group (in fact, it displays a 6.7% increment), and it should be contrasted with 295% and 135% increments in terms of ultimate strength, with respect to the uncoated and the silica coated groups, respectively. When characteristic values are referred to, we get, according to Eq.(3.3), $\varepsilon_{fuk} = 0.70\%$, 1.74% and 1.93%, respectively for the uncoated, silica and polymer coated groups. Surprisingly, while adopting characteristic values, as opposed to the three-sigma-rule, has a marked effect on the design strain in the uncoated group, it determines little change on the design values of silica and polymer coated groups, the latter surpassing the former by 11%. These considerations show that the remarkable increment that polymer coating imparts on the ultimate strength, as compared to silica coating, is not matched by a parallel increment in design values, which, in fact, are very similar, whether they be calculated through the three-sigma-rule or through characteristic values. Conversely, the important ultimate strength increment obtained by silica coated specimens over uncoated ones appears even more pronounced when looked at in terms of design values. As a result, for designing purposes, polymer coating is equivalent to silica coating.

Tab.3.5 gathers uncracked and cracked moduli, turning point location and corresponding standard deviations. Fig.3.18 presents a bar-chart comparison of un-

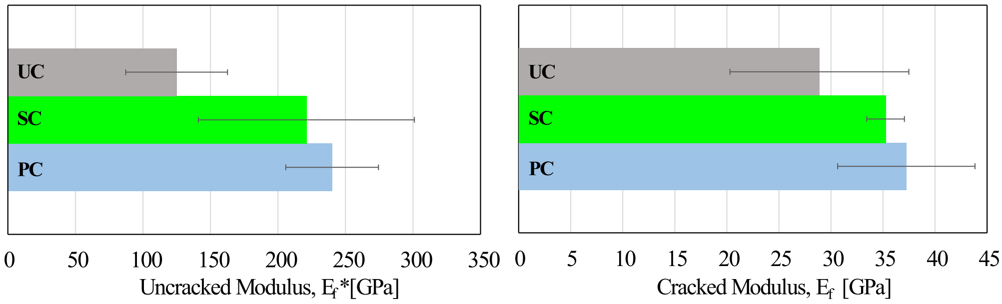

(a)

(b)

Figure 3.18: Uncracked (a) and cracked modulus (b) for ARG coupons in uni-axial traction: uncoated (UC) silica (SC) and polymer coated (PC)

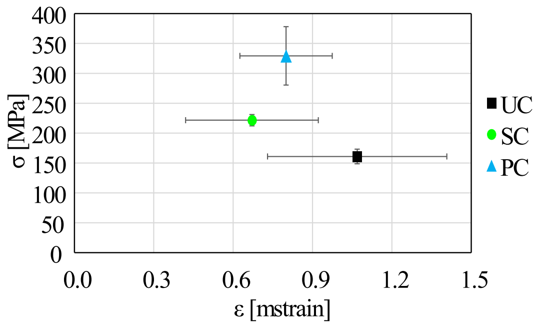

Figure 3.19: Transition point location and confidence bars for ARG coupons in uni-axial traction: uncoated (UC) silica (SC) and polymer coated (PC)

cracked and cracked moduli for ARG coupons, while Fig.3.19 illustrates the turning point location with confidence bars.

Fig.3.20 presents the mean strength curves for ARG laminated bricks in three-point bending tests and maximum tensile stress attained by the fabric (see again Eqn.(2.3)). Besides, Tab.3.6 gathers the mean ultimate strength and strain values determined accordingly. As expected, bending test results are more homogeneous across groups as compared to tensile tests. However, the result is retrieved that the standard deviation, and the coefficient of variation alike, associated with silica coated specimens, is the lowest among groups. Fig.3.21 present in bar-chart form

Table 3.5: Uncracked modulus, E_f^*, cracked modulus, E_f, and turning point location with corresponding standard deviations for uncoated (UC), silica (SC) and polymer coated (PC) ARG specimens in uni-axial traction

Group	E_f^* [GPa]	$\varsigma_{E_f^*}$ [GPa]	E_f [GPa]	ς_{E_f} [GPa]	ε_T [mstrain]	ς_ε [mstrain]	f_T [MPa]	ς_{f_T} [MPa]
UC	125	38	29	9	1.1	0.3	161	12
SC	221	80	35	2	0.7	0.3	222	9
PC	240	34	37	7	0.8	0.2	329	49

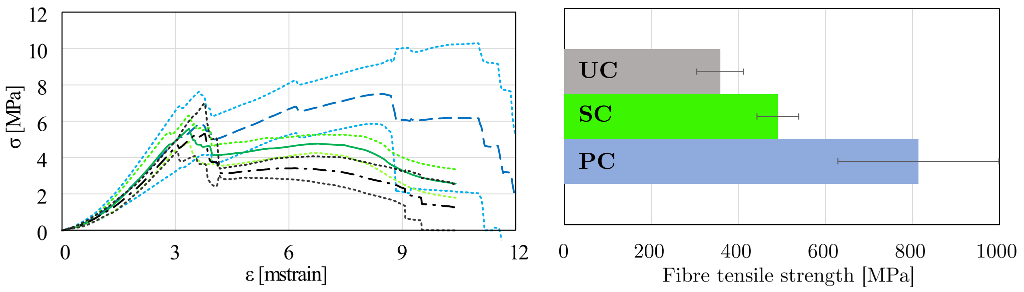

(a) *(b)*

Figure 3.20: Mean stress-strain curves for three-point bending tests of ARG uncoated (black, dash-dotted) silica (green, solid) and polymer coated (blue, dashed) specimens. Confidence bands, in terms of $\mu \pm \varsigma$, are also given (dotted) (a). Evaluation of the maximum axial tensile stress of the fabric (b)

Table 3.6: Mean ultimate flexural strength $\mu(f_{u,f})$ and elongation $\mu(\varepsilon_{u,f})$, together with corresponding standard deviation, ς, and coefficient of variation, CV, for uncoated (UC), silica (SC) and polymer coated (PC) ARG specimens in three-point bending of laminated clay bricks

Group	$\mu(f_{u,f})$ [MPa]	ς_f [MPa]	CV_f [%]	$\mu(\varepsilon_{fu})$ [mstrain]	ς_ε [mstrain]	CV_ε [%]	$\mu(f_{t,f})$ [MPa]	$\varsigma(f_{t,f})$ [MPa]
UC	6.06	0.80	13	8.7	2.6	30	358	53
SC	6.10	0.40	6	10.0	0.7	7	491	48
PC	8.54	1.31	15	11.3	2.1	19	813	185

ultimate strength and strain values as determined in bending for ARG laminated bricks.

3.1.5 Crack pattern and dissipated energy

The quality of interphase bond strength may be assessed through the analysis of the crack pattern evolution prior to failure and of the energy dissipated in crack formation and widening [Mobasher 2006, Nobili 2017b]. Fig.3.22 presents a DIC colour map display of ARG coupons longitudinal displacement field at $\varepsilon = 10\,\text{mstrain}$. Clearly, the displacement field is roughly piecewise constant and the number of uniformly coloured patches is strictly related to the crack density. Fig.3.23 (left) plots the evolution of the average crack spacing against the specimen elongation for ARG test groups. Similarly, Fig.3.23 (right) describes the average crack width against the specimen elongation. It can be observed that uncoated specimens display the largest crack spacing and the widest crack opening at (almost) all elongations. Indeed, crack width appears remarkably constant and crack spacing grows almost linearly with the elongation. In contrast, polymer coated specimens present diffuse and thin cracking (with the possible exception of the very early stage of deformation, when the effect of the gripping system is more evident), which slowly widens with the elongation. Silica coated specimens behave halfway in between the two groups. These plots provide evidence of interphase bond strengthening and, in fact,

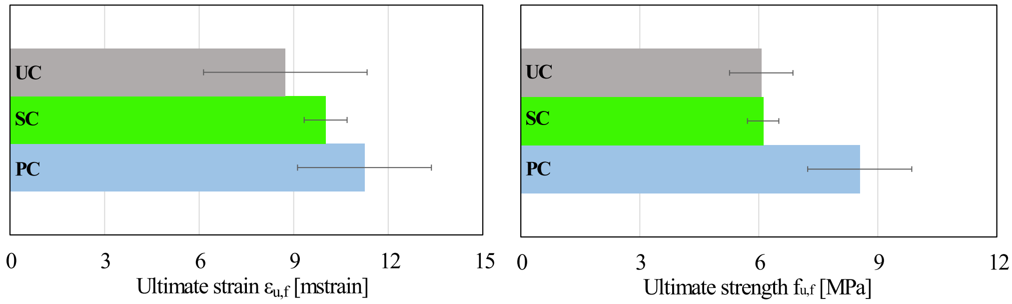

(a) *(b)*

Figure 3.21: Mean ultimate strain (a) and strength (b) for ARG laminated bricks in three-point-bending: uncoated (UC), silica (SC) and polymer coated (PC)

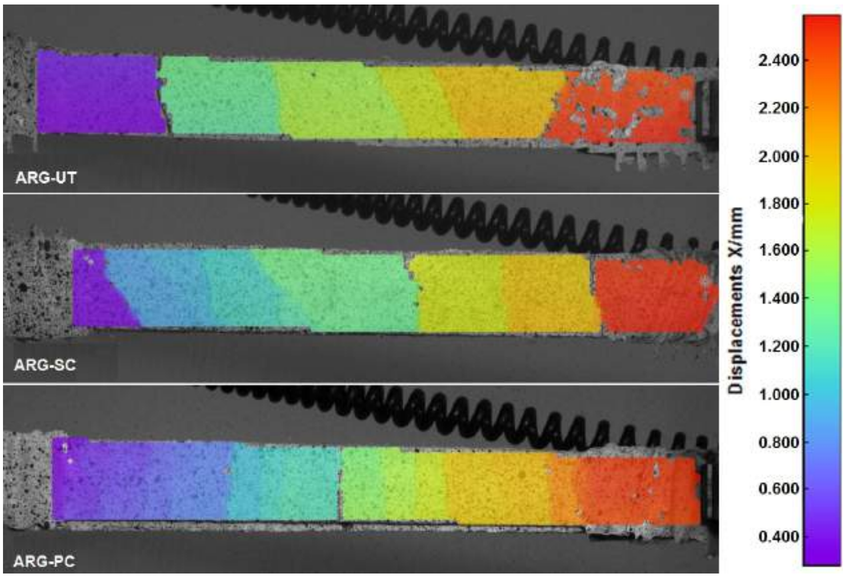

Figure 3.22: Longitudinal displacement field for ARG coupons at ε = 10 mstrain (from top to bottom: uncoated, silica and polymer coated)

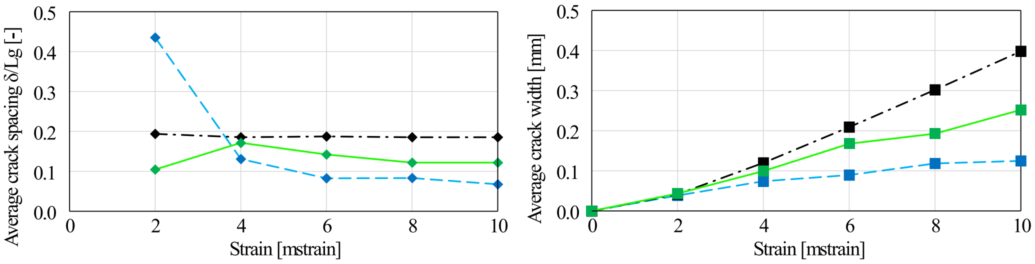

Figure 3.23: Average crack spacing (left) and crack width (right) vs. elongation ε for ARG specimens belonging to the uncoated (black, dash-dotted curve) silica (green, solid curve) and polymer coated (light blue, dashed curve) groups

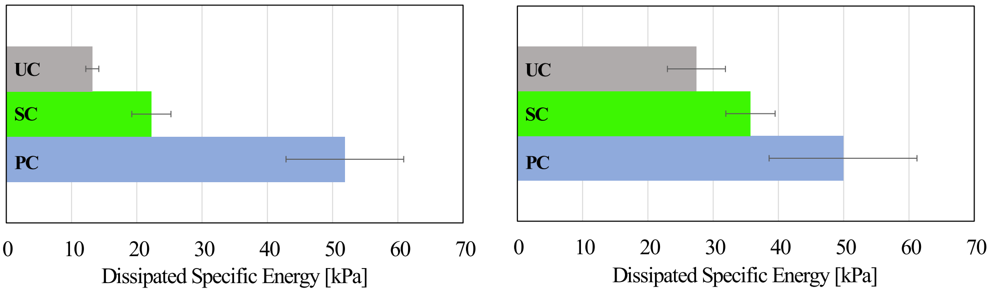

(a) *(b)*

Figure 3.24: Dissipated energy and one-standard-deviation bars for uni-axial tensile tests of C1 specimens (a) and ARG specimens (b) in all test groups: uncoated (UC) silica (SC) and polymer coated (PC)

they may be used as a mean to assess this enhancement.

Fig.3.24 compares energy dissipation, evaluated as the area under the stress-strain curve up to $\varepsilon = 1\%$, for C1 and ARG specimens in all test groups. It is seen that polymer coating is by far the most efficient in dissipating vast amounts of energy, especially in combination with carbon fabric. However, in line with the previous results, its performance is characterized by large data dispersion, to the extent that, for ARG fabric, confidence bands for polymer and silica coated specimens partially overlap and there is little statistical difference between the two populations.

3.1.6 Effects of the matrix binder on the mechanical response

The effects of the proposed nano-silica coating are also investigated taking into account the mortar kind. In this section, the mineralogical and mechanical characterization of composite coupons through tensile tests with the same reinforcing fabric and lay-up technique are discussed. Spotlight is now set on assessing the role of the matrix in taking full advantage of the enhanced interphase adhesion. Results obtained with M5 mortar and fully described in the previous sections are compared with new results achieved with M15 mortar, whose main properties are detailed in Table 2.1. Digital image correlation, electron scanning and optical microscopy provide evidence of improved interphase strength. X-ray diffraction of the anhydrous mortars brings out the role of the mineralogical composition of the embedding media on the overall bonding properties of the composites. Consideration of design limits and energy dissipation capabilities reveals the crucial role of matrix ductility in bringing the contribution of interphase enhancement to full effect.

3.1.6.1 Crystalline phases characterization

The crystalline phases in the mortars are determined through X-ray diffraction (XRD) in a Philips PW3710 diffractometer, using Cu-Kα radiation. The analysis is performed on fine powder obtained by hand-grinding in an agate mortar. Diffraction data are collected in the range from 5° to 70° in the angular variable 2θ, with 0.02° step size and 6 sec exposure rate. The XRD pattern for the two

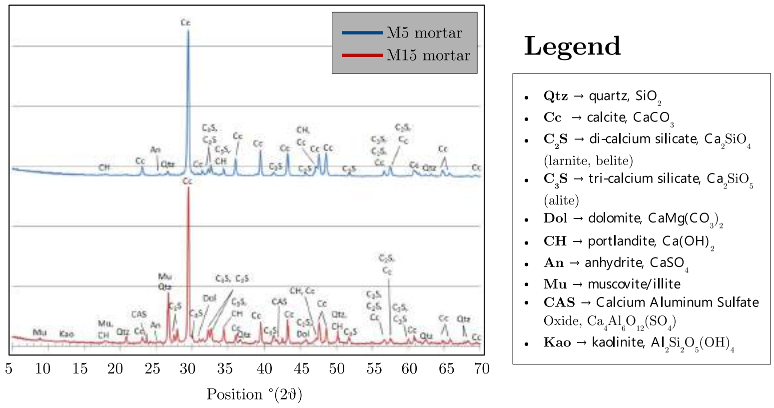

Figure 3.25: X-ray diffraction (XRD) of the anhydrous mortars (M5, top, M15, bottom panel)

lime mortars (namely M5 and M15) is shown in Figure 3.25. It immediately appears that calcite is by far the main component of both mortars, an outcome that is likely connected to the mineralogical composition of the fine aggregates employed in mortar manufacturing. Moreover, the presence of quartz and dolomite in mortar M15 suggests that quartzitic and dolomitic fine aggregates have been employed too. In contrast, only traces of quartz could be detected in M5. With respect to the binding properties, a small proportion of calcium-based precursor typical of lime binders appears in the form of portlandite (calcium hydroxide, $Ca(OH)_2$), while the hydraulic nature of the mortar reflects itself in the presence of Calcium Aluminum Sulfate Oxide (CAS) as well as calcium silicate. This XRD pattern is consistent to that presented in [Forster 2014] for NHL mortars and indeed, similarly to there, burnt lime (calcium oxide, CaO) is absent, as it is usually the case owing to its high reactivity in presence of humidity. As expected, a large proportion of calcite (calcium carbonate, $CaCO_3$) is detected. Mineralogical composition differs between the mortars owing to the presence of Calcium Aluminum Sulfate Oxide, muscovite/illite and kaolinite, that are observed only in M15. The presence of clay minerals (e.g. kaolinite, illite) as impurities may induce detrimental effects in terms of reactivity at the interphase with the fabric[Veniale 2001, Winnefeld 2006]. Indeed, clay mineral contents induce higher water demand in mortar setting and hardening that leads to a reduction of strength and durability. Moreover, clay tends to adhere strongly to the aggregates and thus decreases the surface area available to the hydrated binder. In addition, uncalcined clays release Al and Si ions and calcium hydroxide, calcium silicate hydrates and/or calcium aluminate hydrates may form. Owing to these, the sulphate resistance of the mortar may be negatively influenced. However, only traces of these minerals could be detected. In both mortars, the binder consists of natural hydraulic lime. No silica fume could be identified. Indeed, the XRD patterns reveal the presence of calcium silicates, as larnite (i.e. C_2S or belite) and alite (C_3S) and traces of anhydrite ($CaSO_4$). In addition, only a small amount of Portlandite ($Ca(OH)_2$) could be found, as a likely outcome of the carbonation process induced by air exposure.

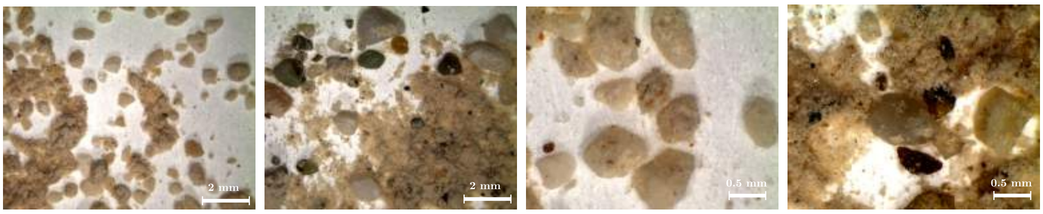

(a) M5, 8x magnification *(b) M15, 8x magnification* *(c) M5, 25x magnification* *(d) M15, 25x magnification*

Figure 3.26: 8x and 25x magnification optical microscopy images for anhydrous mortars.

3.1.6.2 Microscopy investigation and chemical analysis through X-ray spectroscopy

The two mortars (M5 and M15) are characterized through an optical stereomicroscope (EZ4D, Leica) and a scanning electron microscopy (Quanta-200, Fei Company) to qualitatively evaluate the mutual differences in terms of average grain size and composition. Furthermore, an energy dispersive X-ray microanalysis (EDX) is carried out to chemically assess the elemental analysis of the mortars samples. EDS is integrated in the electron microscope and it is a commonly employed analytical technique that relies on the interaction of the high-energy electron impinging ray and the elements involved in the sample subjected to the electron excitation. The ray is then reflected by the sample and the silicium detector converts X-ray energy into voltage signals and transmits the information to the pulse processor which correlates the signal to the emission spectrum of a particular element, which is unique, according to the fundamental principle of spectroscopy [Goldstein 2017]. Optical microscopy images of the anhydrous mortars are reported in Figure 3.26, at two different magnifications, while analogous pictures are taken at higher magnification through SEM investigation, reported in Figure 3.27(b-c). The most clear distinction detectable from the microscopy images is related to the different average grain size of the aggregates, indeed M5 mortar is finer and thus characterized by a lower nominal compressive strength. Moreover, M15 mortar presents aggregates with several different colours, as a first evidence of a wider range of mineral sources. This aspect is assessed in depth trough the quantitative chemical microanalysis provided by post processing of EDX characterization (Inca software) carried out on spectra captured in a wide area of the mortar samples, reported in Figure 3.27(a) (as an example, only for M5). The microanalysis outcome is detailed in Table 3.7, in the form of the weight ratio of oxides detected. The main difference emerged by the microanalysis concerns the higher purity grade of M5 in terms of calcium oxide in the binder (75% vs 60%). On the other hand, M15 mortar composition is characterized by the presence of more impurities (ferrous and potassium oxides), mainly due to the aggregates.

Table 3.7: Weight ratio [%] for oxides found in the samples of the two mortars

Oxides		Mortar	
		M5	M15
Sodium oxide	Na_2O	—	0.9
Magnesium oxide	MgO	2.2	1.9
Aluminium oxide	Al_2O_3	4.0	4.4
Silicon dioxide	SiO_2	15.2	27.3
Sulphur trioxide	SO_3	2.8	2.6
Potassium oxide	K_2O	0.3	1.0
Calcium oxide	CaO	75.0	60.2
Ferrous oxide	FeO	0.5	1.5

3.1.6.3 Mechanical tests

Fig.3.28 compares the mean stress-strain curve of the silica-coated (SC) group against the uncoated (UC) group for both mortar types. One standard deviation bands are also provided. While the mechanical behaviour observed in the UC group is little sensitive to the mortar type, the effect of the silica nano coating is remarkably affected by the mortar quality. Indeed, nano-silica is most effective with the weakest mortar M5. Fig.3.29 and 3.30 provides a bar-chart comparison of ultimate strength and ultimate elongation, respectively. It appears that, when strength is considered, the uncoated performance is dominated by the interphase bond, which is little affected by the mortar strength. In contrast, the ultimate strain performance in the uncoated group is adversely affected by the mortar strength, which is an expected outcome of the ductility loss associated with the stronger binder. In similar fashion, matrix fragility strongly hinders the performance of the silica nano-coating, especially in terms of strength, although a negative effect appears also in terms of ultimate strain. Indeed, it seems that interphase strength enhancement takes full effect only in ductile failure. This result may be explained in light of the fracture energy release pattern. In fact, for brittle failure, fracture energy is released in a single strong burst, which can be hardly absorbed by the interphase bond, although

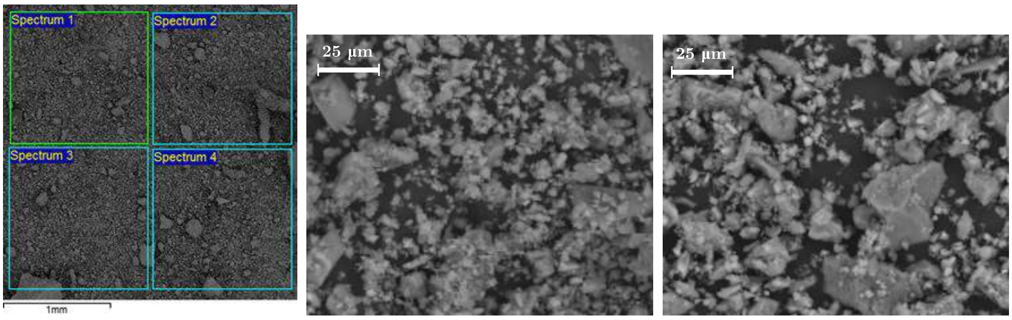

(a) EDX sample (M5) *(b) M5* *(c) M15*

Figure 3.27: 1500x magnification ESEM images for anhydrous mortars.

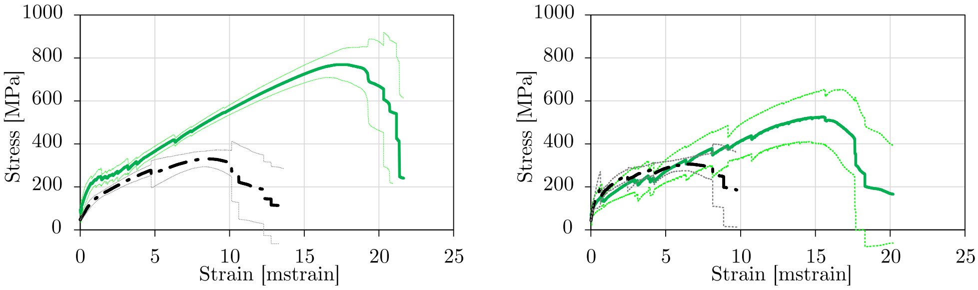

(a) M5 mortar *(b) M15 mortar*

Figure 3.28: Mean stress-strain curve and ±1 standard deviation bands for the uncoated (UC, black, dash-dotted line) and for the silica-coated (SC, dark green, solid line) group

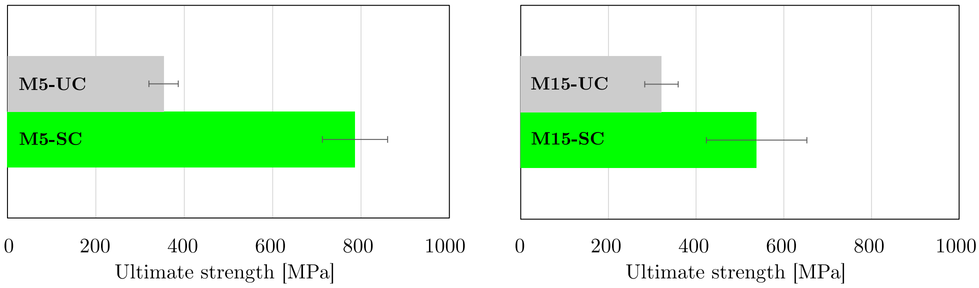

(a) M5 mortar *(b) M15 mortar*

Figure 3.29: Mean ultimate strength bar-chart comparison between the uncoated (UC) and the silica-coated (SC) groups

enhanced. Interestingly, the same trend applies to the standard deviation bar.

A bi-linear curve model is fitted to each strength curve and then the average bi-linear curve within every specimen group is considered (see [Nobili 2016] and [Nobili 2017b] for a discussion). The mean bi-linear curve characterizes two regimes: in the uncracked regime, the mechanical response is dominated by the matrix, while in the cracked regime the fabric plays the major role. The slopes of the bi-linear curve defines the uncracked and the cracked moduli, respectively E_f^* and E_f. Following [Arboleda 2014a], they are conventionally computed through the finite differences

$$E_f^* = \frac{\Delta\sigma^*}{\Delta\varepsilon^*} = \frac{\sigma_2 - \sigma_1}{\varepsilon_2 - \varepsilon_1} \tag{3.4}$$

and

$$E_f = \frac{\Delta\sigma}{\Delta\varepsilon} = \frac{\sigma_4 - \sigma_3}{\varepsilon_4 - \varepsilon_3} \tag{3.5}$$

In Eq.(3.4), we take $\sigma_1 = 0$, $\sigma_2 = 0.10\ f_{fu,t}$, whereas in Eq.(3.5) it is $\sigma_3 = 0.60\ f_{fu,t}$ and $\sigma_4 = 0.90\ f_{fu,t}$, with $f_{fu,t}$ being the ultimate strength, as already pointed out in Section 2.3.3. Deformation values are obtained from the strength curve at the corresponding stress level. The bi-linear model defines the so-called transition point T, which is located at the intersection of the uncracked to the cracked regime. The stress therein attained by the specimen is defined as the *first cracking strength*.

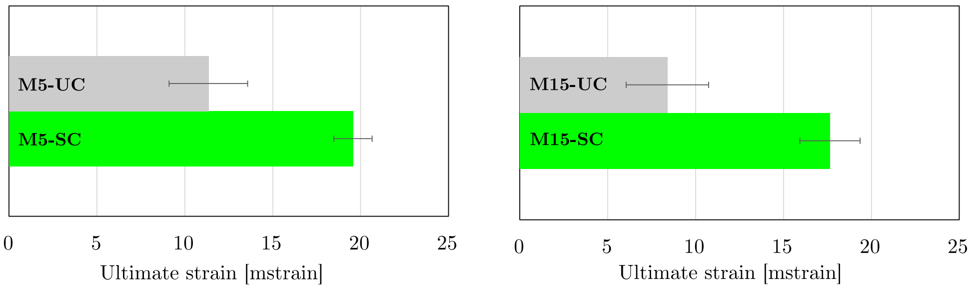

(a) M5 mortar *(b) M15 mortar*

Figure 3.30: Mean ultimate elongation bar-chart comparison between the uncoated (UC) and the silica-coated (SC) groups

Fig.3.31 shows the location of the transition point across the test groups with the corresponding one standard deviation bars. It appears that transition occurs in a narrow region around the first cracking strength, in the neighbourhood of 200 MPa, and that silica coated specimens crack consistently at $\varepsilon = 0.6$, regardless of the matrix. Tab.3.8 presents the mean uncracked and cracked moduli, together with the transition point location and information on data scattering. For easy comparison, moduli are displayed in bar-chart form in Fig.3.32. As it may be expected, uncracked moduli exhibit strong dependence on the mortar strength for the uncoated fabric, while they appear remarkably stable in the silica-coated groups. In contrast, the cracked modulus displays little variation between the uncoated and the coated groups, although it clearly decreases when moving to a fragile matrix, i.e. from M5 to M15. To investigate the statistical significance of the variation across the four groups, a one-way ANOVA (ANalysis Of Variance) test is performed on the cracked moduli [Nobili 2016, Kirkman 1996]. In this test, the null-hypothesis under scrutiny is that the cracked modulus E_f, evaluated across different groups of specimens (namely M5-UC, M15-UC, M5-SC, M15-SC), is a statistical variable pertaining to the same population. We then obtain the Fisher-Snedecor ratio F and the probability confidence P that the null-hypothesis holds

$$F_{(E_f)} = 1.389 \qquad P_{(E_f)} = 28\%, \tag{3.6}$$

from which we deduce that variation across has indeed statistical significance (i.e. the null hypothesis is negated 72% of the time).

3.1.6.4 Design considerations and remarks

As thoroughly discussed in [Signorini 2018b], performance comparison is best carried out in terms of design rather than ultimate values, for the former take into account data scattering. Following [ICC AC434 2013], data scattering is considered through the so-called "three-sigma-rule": given a statistical variable f with mean value $\mu(f)$ and standard deviation $\varsigma(f)$, we compute

$$f_{3\varsigma} = \mu(f) - 3\,\varsigma(f). \tag{3.7}$$

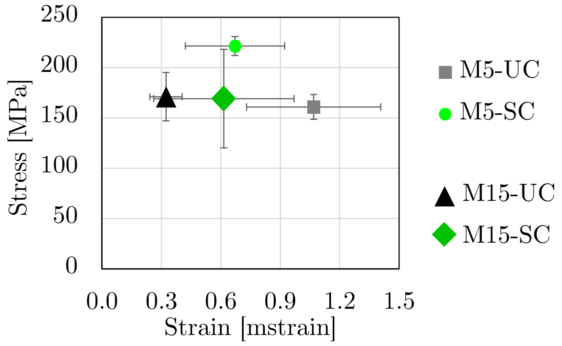

Figure 3.31: Transition point location for M5-UC (black, small square), M15-UC (black, big square), M5-SC (green, small circle) and M15-SC (green, big circle)

Table 3.8: Uncracked modulus, E_f^*, cracked modulus, E_f, turning point location and corresponding standard deviations ς for the uncoated (UC) and the silica coated (SC) groups

Mortar type	Group	E_f^*	$\varsigma_{E_f^*}$	E_f	ς_{E_f}	ε_T	ς_ε	f_T	ς_{f_T}
		[GPa]				[mstrain]		[MPa]	
M5	UC	125	38	29	9	1.1	0.3	161	12
	SC	221	80	35	2	0.7	0.3	222	9
M15	UC	439	72	32	13	0.32	0.08	171	24
	SC	252	125	27	7	0.62	0.35	169	49

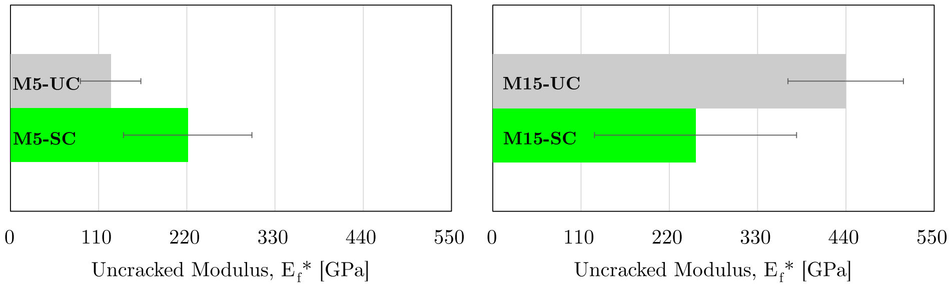

(a) M5 mortar

(b) M15 mortar

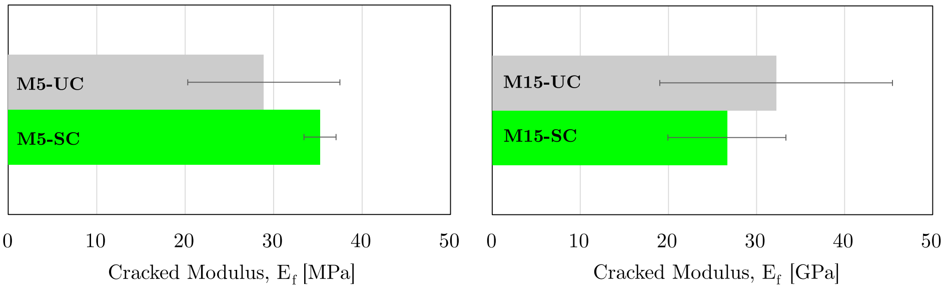

(c) M5 mortar

(d) M15 mortar

Figure 3.32: Mean uncracked and cracked elastic moduli for the uncoated (UC) and the silica coated (SC) groups

Table 3.9: Mean ultimate tensile strength, $\mu(f_{fu})$, standard deviation, ς_f, coefficient of variation, CV_f, 3-sigma rule $f_{fu,3\varsigma}$ and design ultimate strength $f_{fu,d}$ for all groups

Mortar	Group	Tensile strength				
		$\mu(f_{fu})$ [MPa]	ς_f [MPa]	CV_f [%]	$f_{fu,3\varsigma}$ [MPa]	$f_{fu,d}$ [MPa]
M5	UC	353	33	9	207	145
	SC	786	74	9	564	395
M15	UC	321	38	12	207	145
	SC	538	114	21	196	137

Table 3.10: Mean ultimate tensile strength, $\mu(\varepsilon_{fu})$, standard deviation, ς_ε, coefficient of variation, CV_ε, 3-sigma rule $\varepsilon_{fu,3\varsigma}$ and design ultimate elongation $\varepsilon_{fu,d}$ for all groups

Mortar	Group	Elongation				
		$\mu(\varepsilon_{fu})$ [mstrain]	ς_ε [mstrain]	CV_ε [%]	$\varepsilon_{fu,3\varsigma}$ [mstrain]	$\varepsilon_{fu,d}$ [mstrain]
M5	UC	11.3	2.2	20	4.7	3.3
	SC	19.6	1.1	6	16.3	11.4
M15	UC	8.4	2.3	28	1.5	1.1
	SC	17.6	1.7	10	12.5	8.8

Design values are calculated as a fraction thereof

$$f_d = 0.7\ f_{3\varsigma}. \tag{3.8}$$

Tables 3.9 and 3.10 gather mean ultimate strength and elongation respectively, for all groups as well as ”three-sigma-rule” and design values.

Under the standpoint of elongation design values, silica coating brings outstanding performance gains. Indeed, interphase strengthening leads to an increment of 245% for M5 and of a remarkable 700% for M15, with respect to the relevant uncoated group. Besides, the ultimate elongation for M15-SC is still 1.7-fold bigger than the corresponding limit for M5-UC, despite the much stronger binder. In fact, this performance gain should be weighted against the ultimate elongation available in the M15-UC group, that is one third of that achieved in M5-UC. We conclude that binder strength has a strong negative bearing on ductility and, nonetheless, this can be outweighed by interphase strengthening.

When design strength values are considered, we observe that binder strength brings no advantage in the uncoated groups and it is indeed clearly detrimental for silica coated specimens. In fact, the superior mechanical property of the mortar is offsetted against wider data scattering, in the so-called covariance effect [Nobili 2017b]. Undoubtedly, this offsetting is largely due to the strong bias put on data scattering by a three-sigma-rule, as opposed to a characteristic value approach (see [Signorini 2018b] for more details). Indeed, this offsetting may be seen in the M15 group, despite a promising increase in the mean performance when moving from UC to SC. Conversely, the M5-SC group stands out as a noticeable exception,

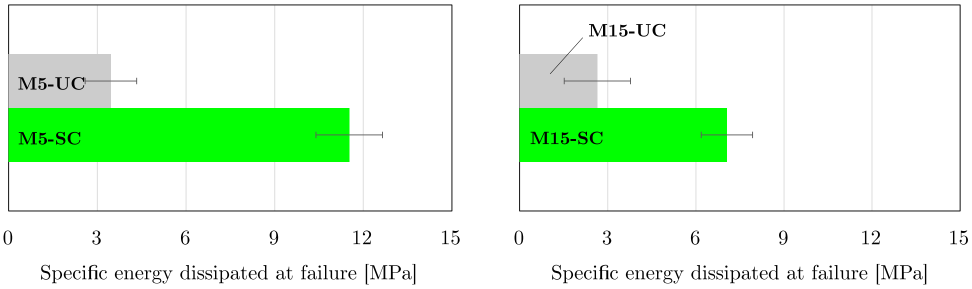

(a) M5 mortar *(b) M15 mortar*

Figure 3.33: Energy dissipated at failure per unit fabric volume in uni-axial tensile test

for it features a 172% enhancement of SC over UC. We therefore emphasise the role of matrix ductility in developing the benefits of interphase strengthening. Besides, ductility plays a major role in resisting aggressive environments [Nobili 2016].

Fig.3.33 presents a comparison of the deformation energy dissipated at failure per unit fabric volume across all groups. It is immediately observed that the pairing of good matrix ductility and interphase strengthening provides large energy dissipation capability. Indeed, energy dissipation in the SC group is 268% larger for M5 and 150% for M15 as compared to the corresponding UC group. Similarly, energy dissipated in the M5-SC group is 68% greater than in the M15-SC group.

Concluding this section, it is found that, despite remarkable performance gain in the mean mechanical properties, the actual design limits may be seriously impaired by lack of matrix ductility. Indeed, best composite performance is not tied to best performance of the single components: a concept which is often overlooked. Besides design limits, the importance of pairing interphase strength enhancement and adequate matrix ductility is clearly manifested through evaluation of the energy dissipation capability at failure. Therefore the best performance requires optimizing the pairing between fabric-to-matrix adhesion and matrix ductility.

3.1.6.5 Analysis of failure mode and optical investigation

All specimens failed by sliding at the matrix-to-fabric interface, although the contribution of telescopic failure within the yarns of the fabric could also be detected. Indeed, evidence of telescopic failure is presented in Fig.3.34, where it is clearly seen that individual yarns separate from the fabric strands in the uncoated group.

Fabric failure could never be reached, despite the increase in interphase adhesion through the silica coating. Evidence of the latter is given in Fig.3.35, which compares E-SEM images of the fabric after failure with and without silica coating. While diffuse patches of embedding matrix remain attached to the SC fabric, little mortar residues can be observed on the UC fabric. Optical microscopy of the mortar-to-fabric interphase is presented in Fig. 3.36. Remarkably, the mortar-to-fabric region is characterized by widely different macro-porosity, in dependence of the the

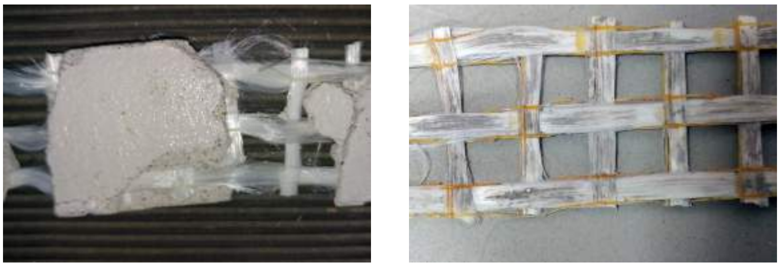

(a) M15-UC *(b) M15-SC*

Figure 3.34: Fabric after failure: yarn separation within the strand clearly manifests itself in the uncoated specimen (a), while no evidence of it appears in the silica-coated specimen (b)

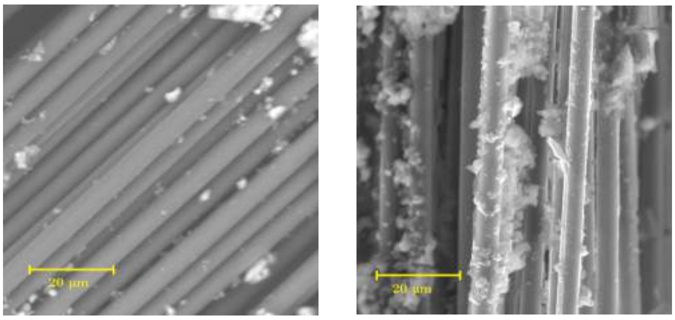

(a) M15 uncoated (UC) *(b) M15 silica coated (SC)*

Figure 3.35: E-SEM images at 1000X *magnification of fabric yarns of failed specimens*

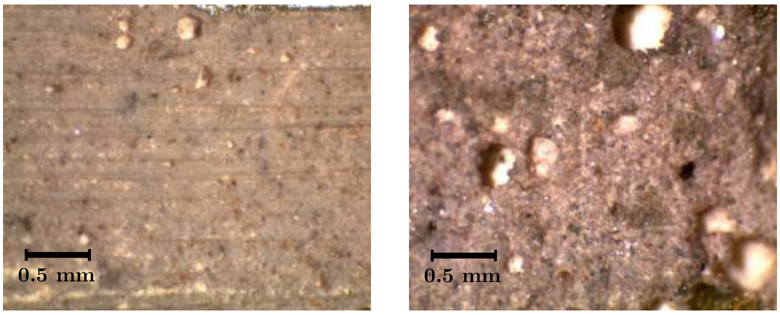

(a) M5-SC *(b) M15-SC*

Figure 3.36: Optical microscopy at 35x magnification of the mortar-to-fabric interphase: M5 mortar (a), M15 mortar (b).

embedding matrix. Indeed, for mortar M5, the size of macro-pores is generally small and it reaches a maximum value of about 0.17 mm; macro-pores are few and tend to cluster near the filaments (Fig.3.36(a)). For mortar M15, large macro-pores are detected, with a maximum diameter of about 0.38 mm; pores are homogenously distributed in the mortar, although they still abound near the filaments. As a consequence, the poor interphase adhesion demonstrated by mortar M15 may be ascribed to the diffuse formation of large macro-pores, which hinder the formation of a continuous bond between the reinforcing fabric and the matrix.

3.1.7 Conclusive remarks

In this section, a novel application of silica nano-coating is considered for interphase bond enhancement of alkali-resistant glass (ARG) and carbon fabric in Textile Reinforced Mortar composites. The effectiveness of the coating is assessed qualitatively through optical and electron microscopy and quantitatively through mechanical tests. Indeed, mechanical performance is determined both through uni-axial traction of rectangular coupons and through three-point bending of laminated clay bricks. Results for the silica coated group are measured against those pertaining to untreated specimens and against the performance of specimens coated through a partially organic impregnation agent (polymer coating). The following conclusions can be drawn:

- silica and polymer coatings determine remarkable gains in terms of mechanical performance for fabric reinforced composite materials;

- in particular, polymer coating brings the best performance in terms of *mean* ultimate strength, strain, diffuse cracking and energy dissipation for glass fabric specimens in traction and bending;

- the same holds true for carbon fabric, with the noticeable exception of the ultimate strain, which is reduced by the coating, i.e. specimens become more brittle;

- the performance gap with silica coating, however, is greatly mitigated, if not subverted, when design values are considered, for they take into consideration the dispersion of experimental data;

- indeed, polymer coating produces generally wider confidence bands and larger coefficients of variation for design values than silica coating;

- it can be argued, partially on the grounds of microscopy analysis, that this data dispersion is related to the polymeric agent affecting a thick layer of mortar around the fabric. Indeed, the thickness of this layer appears to vary greatly in dependence of many factors among which, in particular, the effectiveness of the impregnation;

- as a result, silica coating performs as well as, if not better than, polymer coating in terms of design values and this conclusion holds true regardless of whether a three-sigma-rule or characteristic values are adopted to incorporate standard deviation of data into design values.

Results support the important rationale behind material performance optimization, which is targeted at improving design limits rather than mean absolute performance [Gürdal 1999]. Finally, the great advantage, in terms of application ease, reproducibility and cost, of industrial pretreatment of the reinforcement fabric cannot be over-emphasized and it should be compared with the difficulty connected to in-situ impregnation of the fabric. When focus is set on assessing the role of the matrix properties on the overall mechanical performance, if a lime containing mortar is used, silica coating greatly enhances the matrix-to-fabric interphase bond and this is reflected in superior strength and elongation properties as well as energy dissipation capabilities and telescopic failure is hindered translating into higher elastic moduli. However, for design purposes, it is found that interphase strengthening is most beneficial when paired with adequate matrix ductility. Indeed, superior mean performance generally conveys wider data scattering (covariance effect), which impairs the design ultimate values. This negative bearing is mostly pronounced in brittle failure, whence the importance of matrix ductility. In addition, mortar composition plays an important role in supporting the effectiveness of the coating. Indeed, the presence of impurities (in particular clays) in the lime-based mortar may lead to the reduction of the active surface area of the aggregates available to the binder. Besides, the macro-porosity pattern of the hydrated mortar in the interphase layer seems to affect the bond strength to the fabric. In fact, small and scattered macropores correspond to an enhanced mechanical performance. Although fabric failure could never be reached, ultimate stress values suggest that silica coating alongside matrix ductility brings near-optimal performance.

3.2 Micro-silica coating

An experimental investigation on the mechanical behaviour of TRM laminates in uni-axial tensile tests is presented in this section. The performance of a micro-silica coating applied to two reinforcing fabrics, namely alkali resistant (AR) glass (G) and high-tenacity carbon with AR-glass weft (C), embedded in a single cement-lime hybrid mortar, is assessed and compared to the nano-silica coating presented in Section 3.1. The chosen mortar for the present study is the one labelled "M15" (Tab.2.1 in Sect.2). Preliminary design considerations are put forward through statistical analysis of the experimental evidence. The final goal is to promote wider acceptance of interphase-modified TRM composite materials in current engineering practice.

3.2.1 Coating procedure

Silica micro-particles (particle size $\sim 0.15\,\mu\text{m}$) are laid onto the fabric surface starting from a silica-fume dispersion (hereafter "microsilica", labelled "MS"). The suspension is obtained from a commercially available silica fume dry powder (Elkem Silicon Materials, Bluestar Company) with a minimum purity grade of 85%. In order to coat 450 cm^2 of glass fabric, 80 g of undensified silica-fume powder are gradually added to 80 ml of deionized water and stirred for 1 h in a lidded beaker at ambient temperature. The obtained suspension is sonicated for 10 min (Elmasonic S30H) immediately prior to fabric coating, partly following the guidelines provided by [Hommer 2009], although in a different context. Cut-to-size fabric is dipped in the suspension for 5 min. Finally, fabrics are left to dry at ambient conditions for 24 h, until complete evaporation of water occurs.

3.2.2 Results and discussion

3.2.2.1 Design considerations

Statistical analysis of the mechanical performance is carried out in order to evaluate characteristic values for ultimate strength and strain of uncoated and coated specimens. In particular, data scattering plays a crucial role when moving to design values. According to [ICC AC434 2013], when failure occurs in tension, the design tensile strain is given by

$$\varepsilon_{f,d} = 0.70\ \varepsilon_{fu,k} \leq 12\,\text{mstrain}, \tag{3.9}$$

where $\varepsilon_{fu,k}$ is the characteristic tensile strain of the TRM laminate

$$\varepsilon_{fu,k} = \mu(\varepsilon_{fu}) - 1.96\ \varsigma(\varepsilon_{fu}). \tag{3.10}$$

In Eqn.(3.10), $\mu(\cdot)$ and $\varsigma(\cdot)$ denote the mean and the standard deviation of the relevant quantity, respectively. This formula really yields a value for strain, that is the 2.5% fractile of the sample set, inasmuch as the latter follows a normal distribution. Indeed, 1.96 is the coefficient used in the construction of approximate 95% confidence intervals. The design ultimate strength at failure is evaluated according to

$$f_{f,d} = 0.70 f_{fu,k}, \tag{3.11}$$

where $f_{fu,k}$ is the characteristic ultimate strength, that may be computed from the characteristic ultimate strain via E_f, the cracked modulus of the TRM[Nobili 2017b],

$$f_{fu,k} = 0.85 E_f \varepsilon_{fu,k}. \tag{3.12}$$

3.2.2.2 Optical and SEM investigation

Representative 35x magnification pictures of the failed C-UC, C-NS (taken from a previous work[Signorini 2018b]) and C-MS specimens are reported in Fig.3.37 (a–c). Uncoated specimens present little evidence of mortar adhesion to the fibres'

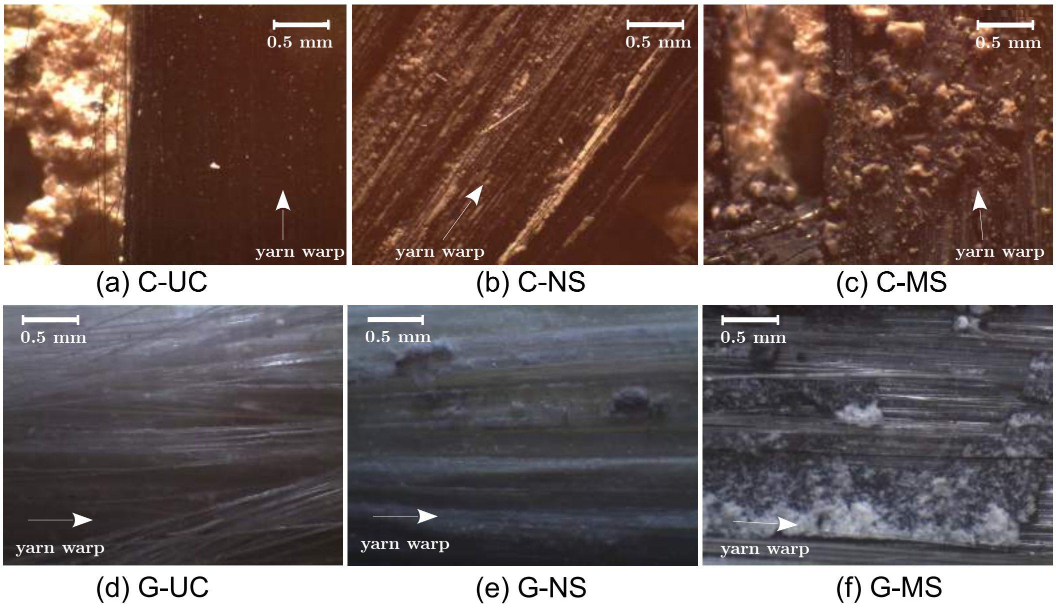

(a) C-UC (b) C-NS (c) C-MS

(d) G-UC (e) G-NS (f) G-MS

Figure 3.37: 35x magnification of the uncoated (UC), nanosilica (NS) and microsilica (MS) coated carbon, respectively Fig.(a),(b) and (c), and glass fabric, Fig.(d), (e) and (f), after failure.

surface, which appears completely clean. Conversely, both silica coatings seem to induce a strong coupling effect at the interphase, since mortar patches remain diffusely attached to the coated fabric after failure. Analogous considerations hold true for glass-fabric reinforced specimens, as shown in Fig.3.37 (d–f). To gain further insight into the adhesion enhancement provided by the coatings, SEM images are presented in Fig.3.38. The strong bond at the interphase may be ascribed to pozzolanic reactions occurring between the cementitious matrix and the finely dispersed silica particles[Sanchez 2010]. Pozzolanic activity is promoted by silica-rich precursors reacting with calcium hydroxide ($Ca(OH)_2$) and silicic acid ($Si(OH)_4$) to obtain calcium silicate hydrate ($CaH_2SiO_4 \cdot 2\,H_2O$), which presents good binding properties. The strongly alkaline environment of the cementitious matrix promotes pozzolanic reaction and its stability [Cherian 2015]. In fact, silica fume is largely employed as additive in high performance concrete because of its strong pozzolanic reactivity. Furthermore, silica fume enhances the compressive strength of concrete and mortar as well as the durability and rheology of the conglomerate[Qing 2007].

3.2.2.3 Mechanical tests

Fig.3.39 gathers the mean stress-strain curves evaluated for each specimen group and it appears that the improvement in terms of ultimate strain, due to coating, is remarkable for both fabrics. An equally impressive increase is seen for the ultimate stress for glass, while the beneficial effect for carbon is milder. Looking at the slope of the plots, we note little change in the uncracked (and, possibly, in the cracked) modulus of the coated groups, as compared to the relevant uncoated group. Indeed, in the first part of the stress-strain curve, the elastic (uncracked) modulus is

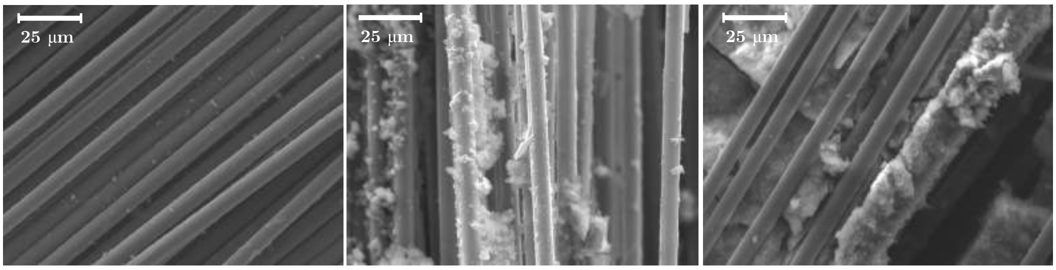

(a) C-UC (b) C-NS (c) C-MS

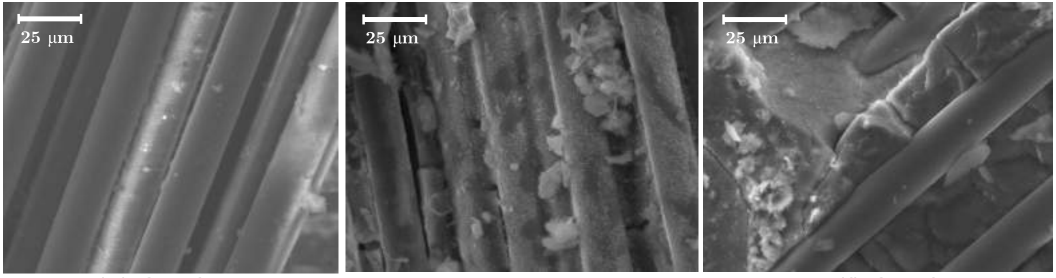

(d) G-UC (e) G-NS (f) G-MS

Figure 3.38: E-SEM images of uncoated (UC), nanosilica (NS) and microsilica (MS) coated C (a–c respectively) and G (d–f respectively) specimens after failure.

mainly driven by the uncracked mortar, which provides the main contribution to the overall stiffness. As expected, coating has little bearing on the stiffness of the uncracked mortar. Successively, once the matrix is fully cracked, the coupon stiffness is governed by the dry fabric's and the contribution of the deposited nano and micro particles is negligible. Nonetheless, the improved interphase is responsible for the higher ultimate tensile strength and elongation of the laminate at failure. In fact, the coupling effect induced by the coating increases the resistance against the sliding mechanisms at the interphase and it promotes the formation of a diffuse crack pattern throughout the length of the laminate. This contribution manifests itself after matrix cracking and gradually disappears at the fully cracked stage. The mean curves are representative of the performance enhancement for both G and C reinforcements. For carbon fibres, these outcomes are consistent with the study carried out by [Nadiv 2017]. They performed double-sided pull-out tests on uncoated, micro- and nanosilica-coated single carbon yarns embedded in a Portland cement mortar. According to Nadiv et al., the presence of pozzolan particles penetrating the bundle of fabric yarns induces a relevant increase in mechanical performance in terms of pull-out force. As anticipated, microsilica coating brings higher beneficial effects when applied to glass rather than carbon fabric. This outcome may be ascribed to the superior compatibility between microsilica and silica-based fibres, as opposed to carbon fibres. Considering nanosilica, a trend similar to that found in a previous study [Signorini 2018b] is observed by which the effectiveness of the nano-coating seems likewise governed by the chemical nature of the fibres. Indeed, when ARG fabric is considered, a double-sided coupling effect is established (i.e. fibres-silica and silica-matrix), thanks to the pozzolanic reactions that are likely to

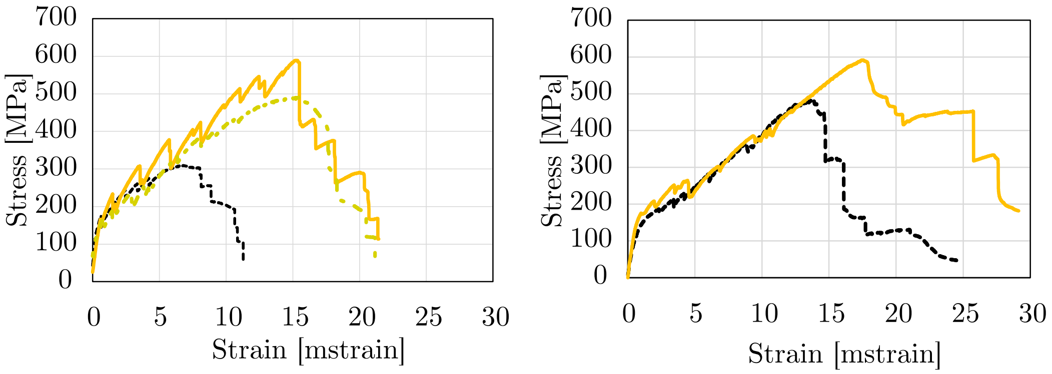

(a) G fabric

(b) C fabric

Figure 3.39: The mean stress-strain curves for G (a) and C (b) samples: uncoated group (black,dotted), NS coated group (green,dash-dotted, only for G samples) and MS coated group (orange, solid)

occur. This coupling promotes a stable interphase layer of silicates that strengthens the composite material. The bar-charts of Fig.3.40 provide characteristic and mean values for the ultimate stress and elongation for G ((a) and (b)) and C ((c) and (d)) fabrics. Data scattering is given through ±1 standard deviation bars. The mean, design (cf. Eqn.(3.9)) and characteristic (cf. Eqn.(4.3)) values for G and C samples are reported in Table 3.11. This table presents the ultimate strength and strain values and their relative increment, referred to as $\Delta(\cdot)$, with respect to the uncoated specimen, alongside the coefficient of variation $\mathrm{CV}(\cdot)$. Looking at the ARG fabric, we observe that the gain in terms of ultimate elongation in the silica group with respect to the uncoated group is almost equal to the benefit achieved with microsilica. This behaviour is due to micro-crack formation on the surface of the coupon, which allows to dissipate a vast amount of mechanical energy[Signorini 2018c]. Despite the undeniable increase of mechanical performance achieved in the coated groups, the ultimate strength of the dry fabric could not be reached and failure of the composite system still occurs through sliding at the interphase. This classical collapse mechanism (well described by the recent CNR Technical Document 215/18 [CNR DT215 2018]) takes place in combination with telescopic failure, namely the differential displacement between the inner (core) and the outer (sleeve) filaments in the yarns. In fact, the internal filaments are poorly bonded to the surrounding matrix and are therefore prone to slide over the external filaments.

3.2.3 Conclusive remarks

An experimental investigation concerning the mechanical performance of coated AR-glass and carbon Textile Reinforced Mortar (TRM) systems is presented. Two sustainable inorganic silica-based coatings, namely micro- and nano-silica (respectively MS and NS), are considered for the reinforcing fabric, which is embedded in a hybrid lime-cement matrix (M15). Coating fosters a concentrated pozzolanic reaction[Nadiv 2017, Jo 2007] at the fabric-to-matrix interphase and thereby pro-

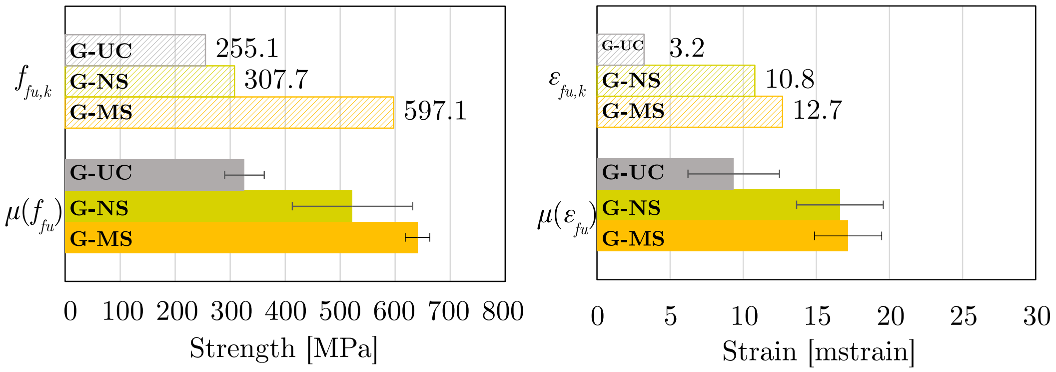

(a) G samples: values of strength (b) G samples: values of strain

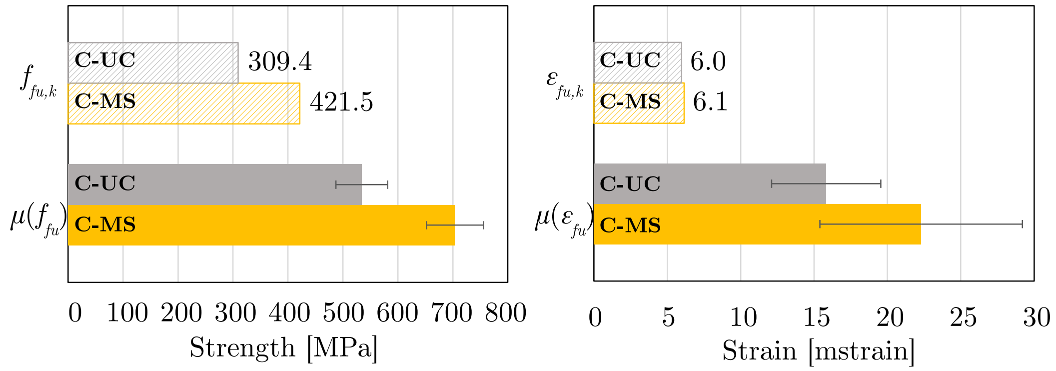

(c) C samples: values of strength (d) C samples: values of strain

Figure 3.40: Mean ultimate values with ±1 standard deviation bands and characteristic values for uncoated (UC, grey), nanosilica-coated (NS, green) and microsilica-coated (MS, orange) specimens for each test group.

Table 3.11: Ultimate tensile strength and design limits for all tested groups

Group	$\mu(f_{fu})$ [MPa]	$\varsigma(f_{fu})$ [MPa]	CV(f_{fu}) [%]	$\Delta(f_{fu})$ [%]	$f_{fu,k}$ (Eqn.3.12) [MPa]	$f_{f,d}$ (Eqn.3.11) [MPa]	$\Delta(f_{fu,k})$ [%]
G-UC	325.8	36.1	11.1	—	255.1	178.5	—
G-NS	522.3	109.4	21.0	+60.3	307.7	215.4	+20.7
G-MS	640.8	22.3	3.5	+96.7	597.1	418.0	+134.1
C-UC	534.3	47.1	8.8	—	442.0	309.4	—
C-MS	703.8	51.9	7.4	+31.7	602.1	421.5	+36.2
Group	$\mu(\varepsilon_{fu})$ [mstrain]	$\varsigma(\varepsilon_{fu})$ [mstrain]	CV(ε_{fu}) [%]	$\Delta(\varepsilon_{fu})$ [%]	$\varepsilon_{fu,k}$ (Eqn.4.3) [mstrain]	$\varepsilon_{f,d}$ (Eqn.3.9) [mstrain]	$\Delta(\varepsilon_{fu,k})$ [%]
G-UC	9.3	3.1	33.4	—	3.2	2.3	—
G-NS	16.6	3.0	17.9	+77.7	10.8	7.6	+235.1
G-MS	17.2	2.3	13.4	+83.8	12.7	8.9	+293.5
C-UC	15.8	3.7	23.5	—	8.5	6.0	—
C-MS	22.3	6.9	30.9	+40.9	8.8	6.1	+2.9

motes chemical bond formation. The role of the coating is assessed qualitatively through optical and electron microscopy and quantitatively in uni-axial tensile tests, according to the ICC AC434 guidelines. Design considerations are given in terms of ultimate strength and elongation. Both MS and NS coatings appear to effectively address the poor bond formation issue that affects inorganic matrix composites. Indeed, they impart remarkable strength improvement over the uncoated specimens, especially when applied to glass fabric. Besides, in contrast to epoxy coating, this technology retains the important advantages connected with an inorganic agent, namely high-temperature resistance[Trapko 2013, Donnini 2017], compatibility and durability, water vapour permeability[Garmendia 2011]. With respect to other available technologies, such as impregnation with partially organic primers at the lamination stage[Nobili 2017b], it affords standardization and industrialization and consequently a reliable and consistent performance. In summary, the following conclusions can be drawn:

- Nano- and micro-silica particles induce a substantial increase in terms of ultimate strength and elongation for textile reinforced mortar (TRM);

- The remarkable improvement in mechanical performance can be ascribed to pozzolanic activity, concentrated at the interphase between the fabric and the matrix.

- on the uncracked modulus, that is dominated by the inorganic matrix stiffness, as well as on the cracked modulus, that is related to the dry fabric stiffness.

- Both coatings convey the advantages connected to an inorganic material alongside the ease of application of a "pre-preg" technology. Indeed, dry coating is prone to industrialization as opposed to on-site treatments with primers or resins;

- Silica coating appears more performing in connection to glass fabric, as a consequence of the superior chemical affinity with glass and of the related two-way connection at the interphase. This strong bridging impacts on data scattering, which is highest for C-MS as compared to G-NS and G-MS specimens;

- Compared to uncoated specimens, surface modification produces a remarkable reduction of data scattering, which, in turn, markedly improves the design limits. Indeed, a more than two-fold increase in terms of design elongation is achieved for the coated specimens and this outcome is mainly ascribed to the sharp reduction in terms of standard deviation. In fact, the coefficient of variation decreases from 33% for G-UC to 18% for G-NS and to 13% for G-MS.

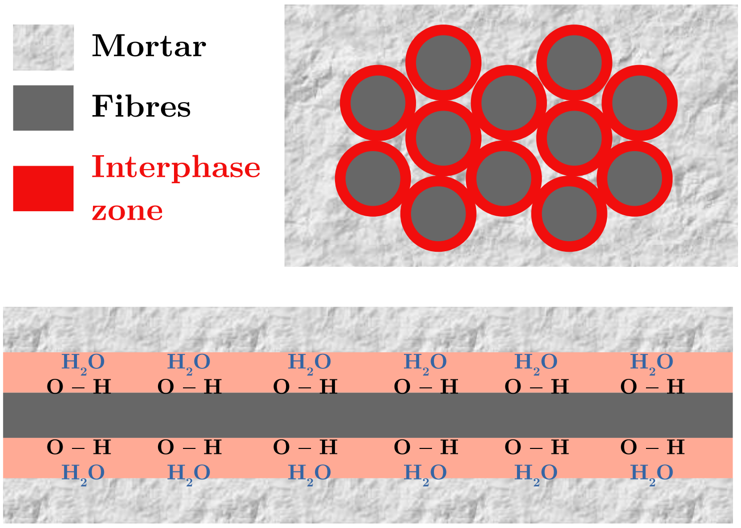

Figure 3.41: Schematic for the interphase zone in TRM composites in the case of silica coating, where hydroxyl groups establish hydrogen bonding with the water of the conglomerate.

3.3 Dispersed multi-walled carbon nanotubes (MWCNT) in nano-silica coating

From the experimental outcomes presented in the previous sections, the importance of the interphase layer in the composite system in the overall mechanical response has arisen. We intend the interphase layer as the contact area between the reinforcing fabric and the embedding medium, as well as the thin layer of mortar immediately surrounding the fibre. This transition zone is responsible for the bond between the two main phases. Bond is crucial for the development of the crack pattern during loading and therefore for the energy dissipation capacity of the composite. Silica (both amorphous nano- and micro-) interphase layer is proven to provide an outstanding enhancement of the bond. Primarily, acting as a functionalization agent of the fibre's surface, where the functional hydroxyl groups are able to interact with the water molecules and then increasing the roughness of the surface (Fig.3.41). By reinforcing the coating with nano-materials as filler, one can attempt to provide the interphase layer of a further strengthening agent. Fillers may have again the combined effects of increasing the surface roughness and exploit their peculiar mechanical properties. In this section, an amorphous nano-silica coating filled with multi-walled carbon nanotubes (MW-CNT) is proposed on AR-glass and carbon fabrics and the effects are evaluated for two kinds of lime-based mortars, namely M15 and HM5 (with the nomenclature proposed in Table 2.1).

3.3.1 Carbon nanotubes

Carbon nanotubes (CNTs) are tubes characterized by a diameter of few nanometres ($0.7 \div 10$ nm) and a high shape-factor ($\sim 10^4$) and therefore CNTs may be considered as unidirectional nanostructures, with attractive peculiar properties. The discovery of CNTs is traditionally ascribed to Sumio Iijima, researcher at NEC Corporation in Japan in 1991 [Iijima 1991], even if several papers documenting the study of cave carbon nano fibres can be found in a pioneering paper in 1952, by Russian scholars L. V. Radushkevich and V. M. Lukyanovich, who published clear images of 50 nanometer diameter tubes made of carbon [Radushkevich 1952]. Anyway, this crucial discovery has remained largely unnoticed in the Western research community due to the Cold War. Later, other scientists provided evidence of the existence of CNTs, in the early Eighties, produced with different techniques, like during arc discharge on carbon anodes, properly characterized only 20 years later [Abrahamson 1999] and thermocatalytical disproportionation of carbon monoxide. In 1987 a U.S. patent was released about the manufacturing of "cylindrical discrete carbon fibrils" with a "constant diameter between about 3.5 and about 70 nanometers [...], length 10^2 times the diameter, and an outer region of multiple essentially continuous layers of ordered carbon atoms and a distinct inner core" [Tennent 1987].

3.3.1.1 Synthesis of CNTs

Several techniques have been developed to produce CNTs in large quantity and with controlled dimensional properties. Advances in the catalysis methods are progressively making CNTs more commercially viable [Takeuchi 2014, Ebbesen 1992].

Arc discharge The arc discharge technique led to the discovery of CNTs, and therefore it was the most adopted at the early stage. Arc discharge process is based on the sublimation of the carbon contained in the anode due to the high-discharge temperatures. Arc discharge procedure allows to produce both single-walled (SW) and multi-walled CNTs, exploiting up to 30% by weight of the raw material. The purity of CNTs obtained by this technique is high, since extremely high temperatures are reached for synthesis (more than 1700 °C) and CNTs characterized by a maximum length of 50 μm can be obtained [Collins 2000].

Laser ablation Another technique to produce a massive amount of CNTs was studied by the team led by Dr. Richard Smalley at Rice University. It consists of a pulsed laser vaporizing a graphite target in a high-temperature reactor within an inert gas atmosphere. Nanotubes grow on the cooler surfaces of the reactor after vaporized carbon condensation. Both SW- and MW-CNTs can be produced varying the composition of the target employed (namely graphite+metal catalyst and graphite only, respectively) [Guo 1995a]. The yield of laser ablation technique is assessed around the 70% (when a mixture of cobalt and nickel is used as metallic catalyser [Guo 1995b]) and the process temperature governs the diameter of the nano-particles. The major drawback lies in the elevated cost.

Plasma torch The thermal plasma method was introduced and patented by Olivier Smiljanic in 2000, to produce SW-CNTs [Smiljanic 2009]. The carbon precursor is supplied by a carbon-containing gas instead of graphite, adopting the beneficial features of the arc discharge and laser ablation techniques. In this case, the yield of the process is enhanced since energy consumption and cost are reduced substantially. A microwave plasma torch is charged with a gaseous mixture of argon, ethylene and ferrocene. The gases are atomized by the atmospheric pressure plasma. The fumes contain SW-CNTs, metallic and carbon nanoparticles and amorphous carbon [Smiljanic 2002]. An evolution of the process is the induction thermal plasma method introduced by scholars from the University of Sherbrooke and the National Research Council of Canada [Kim 2007]. Plasma is obtained by high frequency oscillating currents in an environment saturated by inert gas. Ionized gas is used to reach the elevated temperatures required for vaporizing carbon-containing substances and the metal catalysts that trigger nanotube growth, in line with the arc discharge method. However, induction plasma torch is more efficient in terms of quantity of CNTs produced with respect to the previously mentioned techniques ($\leq$ 2g/min).

Chemical vapour deposition (CVD) The CVD method has been adopted to produce CNTs since 1993, even if the same technique for carbon was documented in the Fifties [Radushkevich 1952, Walker Jr 1959]. The method was subsequently upgraded in 2007 by a team of researchers at the University of Cincinnati [Beckman 2007]. Nowadays, CVD is the most widespread protocol for manufacturing CNTs [Kumar 2010]. Essentially, a metallic substrate (generally made of nickel, cobalt, iron as well as their combinations) is heated at 700 °C. Then, two gases are inserted within the reactor, among which a carbon-containing gas (like acetylene, ethylene, ethanol or methane). CNTs deposit and grow on the sites of the metal catalyst, transported after the dissolution of the precursor gas. Thermal catalytic decomposition of hydrocarbon has recently become an increasing research branch and can lead to a promising route for the bulk production of CNTs. The major issue concerning CVD is due to the necessity of removing the catalyst particles from the CNTs, by means of acid treatment. This additional treatment might modify the original structure of the nanotubes.

3.3.1.2 Mechanical properties

Because the carbon–carbon sp^2 bond observed in graphite is one of the strongest in nature, carbon nanotubes are excellent candidates for the stiffest and strongest material ever synthesized. CNTs exert the main mechanical properties in the axial direction, where the covalent bonds lie. Along the axial axis, CNTs present elastic Young's modulus around 270 GPa to 950 GPa and a tensile strength ranging from 11 000 MPa to 63 000 MPa, according to several experimental studies and theoretical prediction models available in the literature [Yu 2000]. The most impressive property of CNTs regards their specific strength. Indeed, the extremely high ultimate strength experimentally measured by [Peng 2008] ($\approx$ 100 GPa) should be related to CNTs low density (1.3 g/cm^3 to 1.4 g/cm^3). As a result, CNTs' specific strength reaches the value of 48 MNm/kg, up to 311 times more than the specific strength of high-carbon steel. In compression, the high aspect ratio induces buckling effects, as well as when subjected to bending and torsion. Instead, along the radial direction, Van der Waals interaction forces are able to deform adjacent CNTs, as shown in the pioneering study by [Ruoff 1993], through transmission electron microscope (TEM) investigation. Radial elastic modulus was found to span between 9 and 57 GPa, as a function of the diameter of CNT, by means of an atomic force microscope (AFM) [Palaci 2005, Yang 2011]. As far as multi-walled CNTs are concerned, interactions between internal shells are found to reduce the strength of the nanotube. Like all crystalline materials, also CNTs may present structural defects (i.e. Stone Wales effect). Such atomic vacancies within the trussed internal structure may induce a substantial reduction to mechanical properties of CNTs, up to the 85%, since the overall mechanical behaviour of the tube is leaded by the weakest link in the chain. Other important properties that CNTs take advantage of are an extremely high hardness and customizable wettability. Indeed, the latter is the key for several application fields of CNTs, since can range from a super-hydrophobic to a super-hydrophilic nature, just applying a low voltage around 1.3 V, or performing a variety of chemical or physical treatments [Bekou 2011, Rodrigues 2016].

3.3.1.3 Main application fields

In the 2010s, CNTs production have been consisting in several thousands of tons per year and scientific papers and patents focused on CNTs has triplicate with respect to the beginning of the 21th century [De Volder 2013]. Individual CNT walls can be metallic or semiconducting depending on chirality. This interesting feature has arisen an increasing interest in using CNTs in the electronic engineering field. But several other applications have been studied, comprising energetic field, device modelling, automotive, aeronautic, sports, water filters, coatings, actuators and scaffolding for bone growth in biomedical engineering [Zanello 2006]. Current uses of CNTs is limited to their unorganized bulk form, whose properties, albeit notably inferior than individual tubes, are often acceptable for practical purposes, like for example nano-fillers in polymeric composites. Indeed, the higher drawback associated to CNT production is still given by their elevated cost. In polymeric composite materials, bulk CNTs generally act as a conductive filler (MWNT-polymer composites reach conductivity up to 10 kS/m at 10 wt.% ratio), but also exploiting their mechanical performance to increase stiffness, strength and toughness, as well as damping properties to enhance resin-based mixtures.

3.3.1.4 Multi-walled CNTs

Multi-walled nanotubes (MW-CNTs) consist of multiple concentric rolled layers of graphene, brought together through out-of-plane Van der Waals forces. The interlayer distance is approximately 3.4 , very close to the layers in the graphite structure. Due to their peculiar shape, MW-CNTs present a telescopic motion ability, which is a particularly interesting property in the field of upcoming nano-metric mechanical devices. The structure schematic is displayed in Fig.3.42.

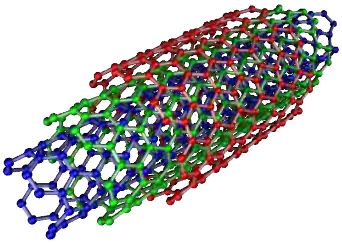

Figure 3.42: Schematic for the trussed structure of a multi-walled CNT. Courtesy of Eric Wieser (Own work, CC BY-SA 3.0, https://commons.wikimedia.org/w/index.php?curid=12453670)

Table 3.12: Multi-walled carbon nanotubes properties

Characteristic	Unit	Value
Density (at 25 °C)	g/cm^3	2.1
Bulk density	g/cm^3	0.06 ÷ 0.08
Outside diameter	nm	10
Inside diameter	nm	4
Length	nm	4000
Aspect ratio	—	350 ÷ 550
Walls	No.	6 ÷ 8
Surface area (BET)	m^2/g	280 ÷ 350
Surface resistivity	Ω/sq	700 ÷ 900
Melting point	°C	3652 ÷ 3697

3.3.2 Experimental: Coating procedure and testing program

Mortars M15 and HM5, whose properties are declared in Table 2.1, are employed as the embedding media for the laminates. Indeed, mortar M15 is characterized by a higher strength due to the presence of a lime-cement blend as the binder, while HM5 is mainly hydraulic lime-based, and therefore its ultimate compressive strength is lower. Fabrics utilized as the reinforcing phase are both alkali resistant glass (ARG) and uni-axial carbon (C2), according to the properties already pointed out in Table 2.2 in Section 2. Multi-walled carbon nanotubes (Sigma Aldrich, Merck Group) properties are gathered in Table 3.12.

3.3.2.1 The issue of CNT dispersion

Carbon nanotubes main issue is their attitude to form bundles and aggregates, due to their nano-scale dimensions and hence their surface area is sensibly high and it triggers attractive forces (van der Waals energy of 500 eV/µm [Girifalco 2000, Shvartzman-Cohen 2004]) and facilitates entanglement of tubes in ropes [Thess 1996]. One of the challenges is to successfully obtain a stable dispersion of CNT in water and organic media. This is often required whenever CNTs are employed for industrial applications, since sub-micron/nanometre-sized particles are involved. To this aim, several additional reactants are used, the so-called *surfactants*

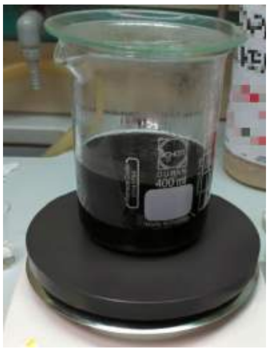

Figure 3.43: The stabilized CNT dispersion in the silica sol before gelification.

[Vaisman 2006]. Surfactants have the property of accumulating on the surfaces of the nano-particles and thus tend to separate them. This effect is due to the typical structure of surfactants, which have a polar (i.e. hydrophilic) head region and an apolar (i.e hydrophobic) tail region, the latter usually made of hydrocarbon groups. Many kinds of surfactants can be used, depending on the chemistry of the solvent and the particles.

3.3.2.2 Coating procedure and mechanical testing

CNT dispersion is obtained taking advantage of the excess water required to accommodate hydrolysis of the acid-catalysed silica sol-gel. A stable CNT aqueous dispersion is obtained by adding sodium dodecyl benzene sulfonate (NaDBS) as surfactant, as reported in the research by [Haghgoo 2014]. In a covered beaker, a 3.3%wt solution (with respect to deionized water) of CNTs is mixed with NaDBS powder in a 2:3 CNT/NaDBS weight ratio. The suspension is stirred on a magnetic plate for 5 minutes and then sonicated for 60 minutes, in order to allow the surfactant to distribute within the nanotubes interstices and favour disaggregation [Rastogi 2008] (see Fig.3.43). The suspension is added to TEOS/isopropyl alcohol solution together with nitric acid in stoichiometric ratio to trigger sol-gel transition, see also [Signorini 2019a]. The silica solution, with an overall CNT weight ratio of 0.5%, is stirred on a magnetic plate for 2 hours at 50°C and then sonicated in a water for further 15 minutes before fibres' dip-coating. Cut-to-size textiles are then briefly immersed in the suspension for 5 minutes and consequently left drying at laboratory conditions for a few minutes and finally in a muffle at 110°C for 15 minutes. Uni-axial tensile tests are performed out of 1-ply coupons. Laminates are produced following the protocol detailed in Section 2.3.1 and mechanical tests performed complying with the settings reported in Section 2.3.2. At least four specimens are tested for each group (namely uncoated (UC) and silica+CNT (S-CNT) coated). The chosen widths for the coupons' cross-section are 36 mm and 35 mm for ARG (accommodating 3 strands) and C2 (the interphase layer 7 strands), respectively.

Table 3.13: Tensile tests results for G-TRM laminates.

M	**UC**				**S-CNT**				**Δ**	
	$\mu(f_u)$ [MPa]	$\varsigma(f_u)$ [MPa]	CoV [%]	$f_{u,k}$ [MPa]	$\mu(f_u)$ [MPa]	$\varsigma(f_u)$ [MPa]	CoV [%]	$f_{u,k}$ [MPa]	Δf_m [%]	$\Delta f_{u,k}$ [%]
HM5	256	123	48	54	511	78	15	383	+100	+600
M15	317	43	14	246	947	23	2	909	+198	+270
	$\mu(\varepsilon_u)$ $[\cdot 10^{-3}]$	$\varsigma(\varepsilon_u)$ $[\cdot 10^{-3}]$	CoV [%]	$\varepsilon_{u,k}$ $[\cdot 10^{-3}]$	$\mu(\varepsilon_u)$ $[\cdot 10^{-3}]$	$\varsigma(\varepsilon_u)$ $[\cdot 10^{-3}]$	CoV [%]	$\varepsilon_{u,k}$ $[\cdot 10^{-3}]$	$\Delta\varepsilon_m$ [%]	$\Delta\varepsilon_{u,k}$ [%]
HM5	13.5	3.0	23	8.6	19.7	4.8	24	11.8	+46	+38
M15	8.6	2.7	31	4.2	27.0	1.8	7	24.0	+214	+476
	$\mu(W_u)$ [J/mm^3]	$\varsigma(W_u)$ [J/mm^3]	CoV [%]	$W_{u,k}$ [J/mm^3]	$\mu(W_u)$ [J/mm^3]	$\varsigma(W_u)$ [J/mm^3]	CoV [%]	$W_{u,k}$ [J/mm^3]	ΔW_m [%]	$\Delta W_{u,k}$ [%]
HM5	2.10	1.11	53	0.28	5.93	1.15	19	4.0	+183	+1346
M15	2.65	0.60	22	1.67	16.1	0.91	6	14.6	+508	+777

3.3.3 Results and discussion

3.3.3.1 Glass fabrics

At least four specimens for each group are tested and the mean curves are reported in Figure 3.44 (a) and (b) for M15 and HM5 mortars, respectively. An almost perfectly trilinear trend is consistently observed across the S-CNT coated groups. Indeed, elastic behaviour holds until first cracking strength is attained and it is followed by a short regime characterized by the opening of several sequential cracks and finally by a post-cracking branch, more compliant (i.e. less stiff) than in the elastic regime. Remarkably, the formation of new cracks in coated specimens during testing is accompanied by many small stress drops which account for the formation of a diffuse cracking pattern. This leads to high levels of mechanical energy being dissipated at failure [Mobasher 2006]. Conversely, crack formation in the uncoated specimens induces irreversible damage to the interphase, as a consequence of the large burst of mechanical energy that is suddenly released. Accordingly, the detachment between the fabric and the embedding mortar at the interphase caused by cracking induces sliding of the fibres and internal delamination, thus achieving lower bearing capacity. For such reasons, CNT-coating provides remarkable improvement both in terms of strength and of deformability, that is particularly effective for the hybrid lime-cement mortar (namely, M15).

Bar-chart comparison of the mean ultimate strength and elongation of G-TRM composites at failure is given in Figure 3.45 and 3.46, respectively for HM5 and M15 mortars. It is also observed that coating effectively decreases data scattering, especially for G mortar, thus strongly improving design limits [Signorini 2019c]. In Table 3.13 the beneficial effect of coating on the mechanical behaviour of G-TRM can be appreciated. Ultimate strength (f_u), strain (ε_u) and dissipated energy (W_u) are compared across the uncoated and coated groups, together with their relevant standard deviation. Here, $\mu\cdot$, $\varsigma\cdot$ and CoV$\cdot$ represent the mean value, the standard

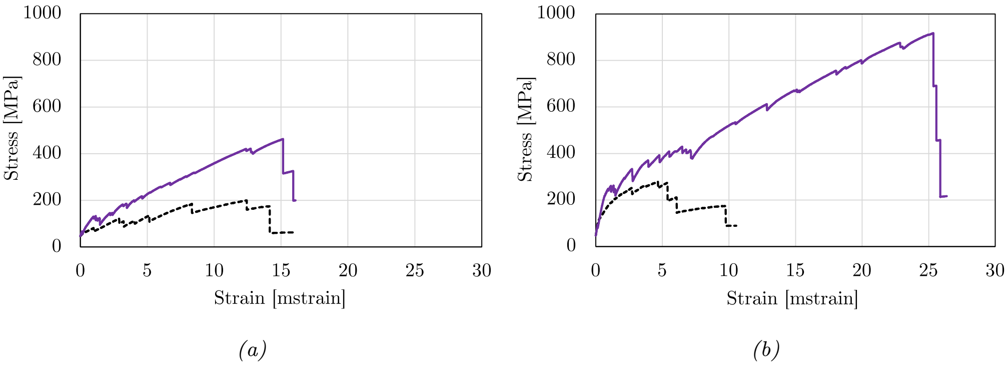

(a)

(b)

Figure 3.44: Mean stress-strain curves for uncoated (UC, black/dotted) and (silica+CNT)-coated (S-CNT, violet/solid) for G-TRM with HM5 hydraulic lime (a) and M15 hybrid lime/cement (b) mortar.

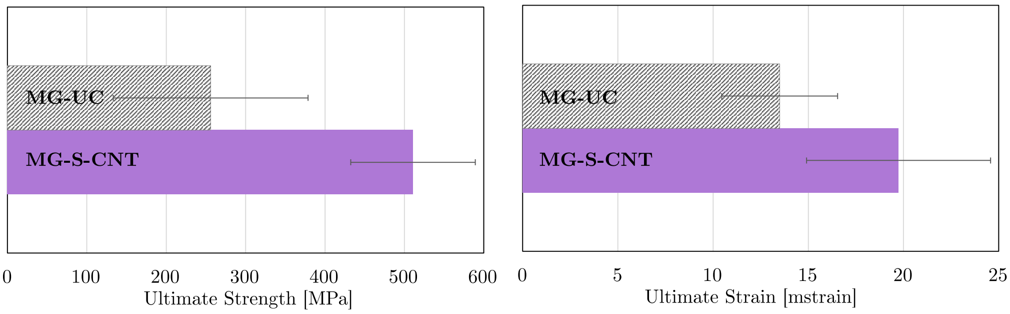

(a)

(b)

Figure 3.45: Ultimate strength (a) and strain (b) with ±1 standard deviation band for uncoated (UC, grey) and (silica+CNT)-coated (S-CNT, violet) for G-TRM with HM5 hydraulic lime mortar.

deviation and the coefficient of variation of the sample, respectively; $\Delta(\cdot)_m$ provides the percent variance of the relevant mean for the coated against the uncoated group. In order to take into account data scattering, characteristic values (5%–fractile) are computed through Eqn.(3.13), assuming that data are normally distributed [Mandel 2012].

$$(\cdot)_k = \mu(\cdot) - 1.64\,\varsigma(\cdot) \tag{3.13}$$

The corresponding percent variance of the coated vs the uncoated group is denoted by $f_{u,k}$. We observe a striking five-fold increase in the mean dissipated energy for the M15 mortar, as a combination of enhanced ultimate strength (+198%) and elongation (+214%). For the HM5 mortar, the corresponding result is also important, albeit not quite so impressive (+183%). Data scattering is also significantly reduced by CNT-coating: for strength we move from 48% CV in the UC group to 15% for HM5 mortar and from 14% to 2% for M15 mortar. Consistency in ultimate performance is strictly connected to the suppression of telescopic failure and of intralaminar textile's sliding occurrence. Indeed, such mechanisms are intrinsically inconsistent.

Stereo-microscopic images are shown in Fig. 3.47 and 3.48 that provide clear ev-

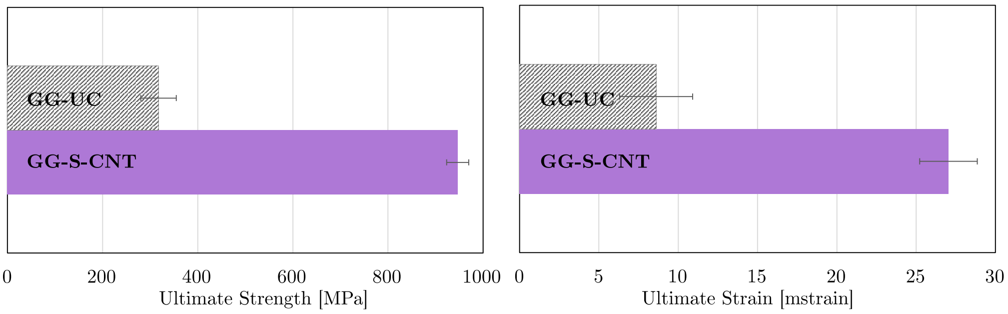

(a) *(b)*

Figure 3.46: Ultimate strength (a) and strain (b) with ±1 standard deviation band for uncoated (UC, grey) and (silica+CNT)-coated (S-CNT, violet) for G-TRM with M15 hydraulic lime mortar.

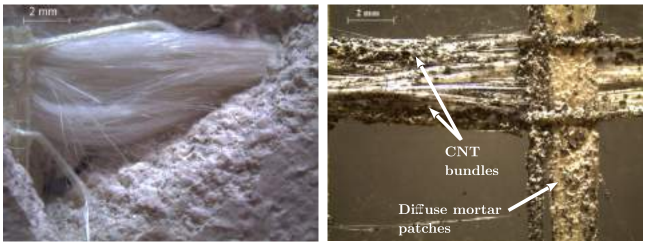

(a) Uncoated *(b) Silica/CNT-coated*

Figure 3.47: 8x magnification microscopy image for failed AR Glass-TRM

idence of interphase compatibility improvement. Indeed, while UC strands are clean and “pulled-out” as a result of telescopic sliding (unfolding generates misalignment of the filaments of a single yarn), fibres in the S-CNT group maintain good alignment and to them many mortar patches and CNT bundles are diffusely attached. MW-CNT distribution appears not uniform over the fibre surface whence micro-roughness is enhanced and so is grip with the mortar at the interphase. In addition to providing a functionalizing dispersing medium, silica enhances the chemical interlocking with the mortar and bonds fibres together [Signorini 2019a]. To these benefits, the contribution of CNT is superposed and it consists of strengthening the interphase zone and the fibre-to-matrix adhesion capability. x-axis displacement colour maps obtained post-processing DIC data along the loading process are shown in Figure 3.49 in correspondence of the strain level $\bar{\varepsilon} = 1.5\,\mathrm{mstrain}$. As anticipated, uncoated samples present a coarse crack pattern, with few large cracks spanning the direction y orthogonal to the loading. In contrast, coated samples are characterized by many fine cracks with the distinctive feature of them being tilted with respect to the loading direction. This behaviour is associated to enhanced adhesion, consistently to the findings presented in previous papers and related to plain nano-silica coating (cf. Sect.3.1) and to epoxy coating (cf. Chapter 4). Crack inclination, however, is a novel feature that is most likely connected to partial occurrence of telescopic failure, whereupon a non-symmetric stress state ensues.

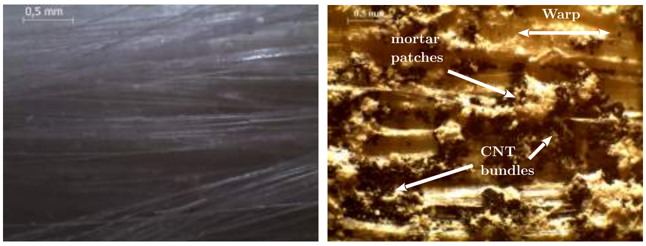

(a) Uncoated *(b) Silica/CNT-coated*

Figure 3.48: 35x magnification microscopy image for failed AR Glass-TRM

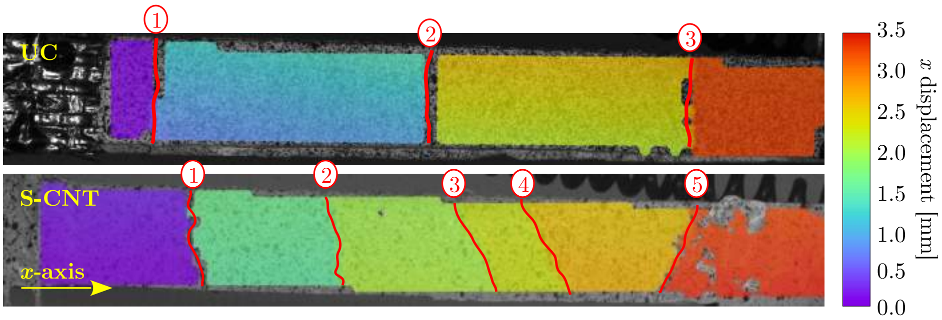

Figure 3.49: Longitudinal displacement colour map for uncoated (UC) and silica+CNT coated (S-CNT) textile reinforced M15 mortar coupon reinforced with ARG fabric

3.3.3.2 Carbon fabrics

Analogous considerations are put forward for TRM reinforced with uniaxial carbon fabric: As already pointed out in Section 3.1, nano-silica coating applied on carbon fabric is less effective when compared to AR-glass. This can be ascribed to the lower chemical affinity of the silica-carbon system, as compared to silica-glass. Indeed, the latter is expected to be extremely high as a result of the chemical composition of the coating and of the substrate being essentially the same. Consistent outcome is evidenced also when carbon nanotubes are added as high-strength interphase nanofillers. Figure 3.50 presents the mean stress-strain curve in uni-axial tension obtained for HM5 and M15 mortars. Very remarkably, coating fabric embedded in the M mortar is found to impair performance, although this negative outcome is compensated by significant benefits in terms of ductility.

For comparison, bar-charts are given which illustrate ultimate performance alongside standard deviation bands for the HM5 and M15 mortars, respectively in Fig.3.51 and 3.52. Ultimate strength, elongation and specific energy dissipated at failure are gathered in Table 3.14, where the percentage variance is also given.

This seems partly in contrast with the observations drawn in Section 3.1.6, according to which best performance is associated to higher lime content in the binder. However, differently to the present experimental set, in Section 3.1.6 a mortar with higher compressive strength is adopted and whose composition comprises glass microfibers. Indeed, the benefit of adding dispersed microfibres to the mortar in terms

Table 3.14: Tensile tests results for C-TRM laminates.

M.	**UC**				**S-CNT**				**Δ**	
	$\mu(f_u)$ [MPa]	$\varsigma(f_u)$ [MPa]	CoV [%]	$f_{u,k}$ [MPa]	$\mu(f_u)$ [MPa]	$\varsigma(f_u)$ [MPa]	CoV [%]	$f_{u,k}$ [MPa]	Δf_m [%]	$\Delta f_{u,k}$ [%]
HM5	713	58	8	618	540	24	5	501	-24	-19
M15	756	150	20	510	911	266	29	475	+20	-7
	$\mu(\varepsilon_u)$ [mstrain]	$\varsigma(\varepsilon_u)$ [mstrain]	CoV [%]	$\varepsilon_{u,k}$ [mstrain]	$\mu(\varepsilon_u)$ [mstrain]	$\varsigma(\varepsilon_u)$ [mstrain]	CoV [%]	$\varepsilon_{u,k}$ [mstrain]	$\Delta\varepsilon_m$ [%]	$\Delta\varepsilon_{u,k}$ [%]
HM5	11.3	0.8	7	10	15.7	2.8	18	11.1	+40	+11
M15	13.3	3.7	27	7.2	17.7	3.3	18	12.3	+33	+70
	$\mu(W_u)$ [J/mm^3]	$\varsigma(W_u)$ [J/mm^3]	CoV [%]	$W_{u,k}$ [J/mm^3]	$\mu(W_u)$ [J/mm^3]	$\varsigma(W_u)$ [J/mm^3]	CoV [%]	$W_{u,k}$ [J/mm^3]	ΔW_m [%]	$\Delta W_{u,k}$ [%]
HM5	3.94	0.40	10	3.28	4.91	1.05	21	3.19	+25	-3
M15	8.74	3.06	35	3.72	23.54	11.64	49	4.45	+169	+20

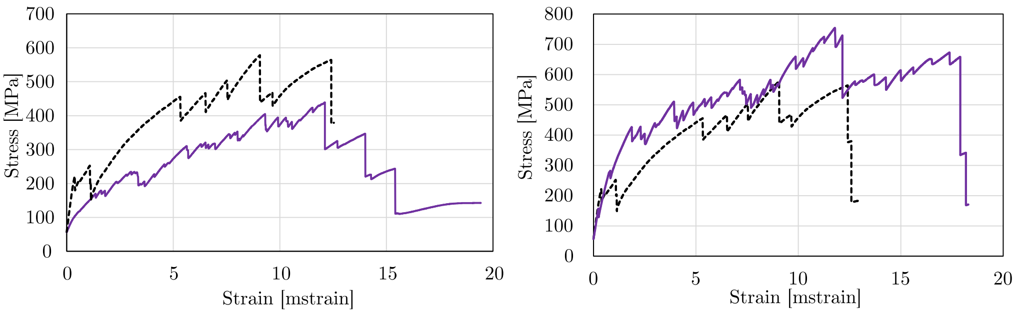

(a) *(b)*

Figure 3.50: Mean stress-strain curves for uncoated (UC, black/dotted) and (silica+CNT)-coated (S-CNT, violet/solid) for C-TRM with HM5 hydraulic lime (a) and M15 hybrid lime/cement (b) mortar.

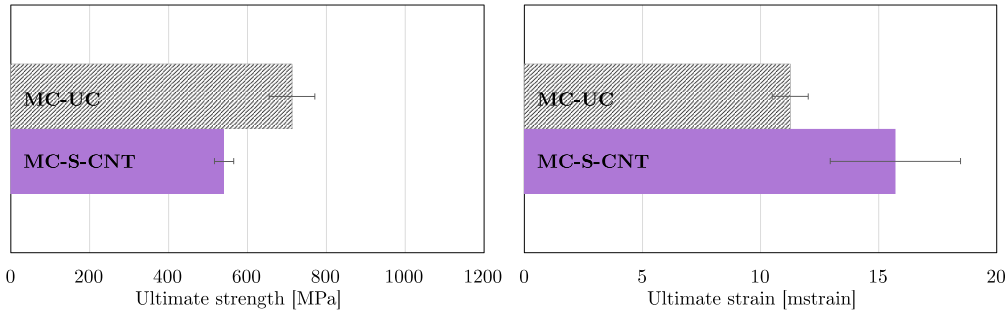

(a) *(b)*

Figure 3.51: Ultimate strength (a) and strain (b) with ±1 standard deviation band for uncoated (UC, grey) and (silica+CNT)-coated (S-CNT, violet) for C-TRM with HM5 hydraulic lime mortar.

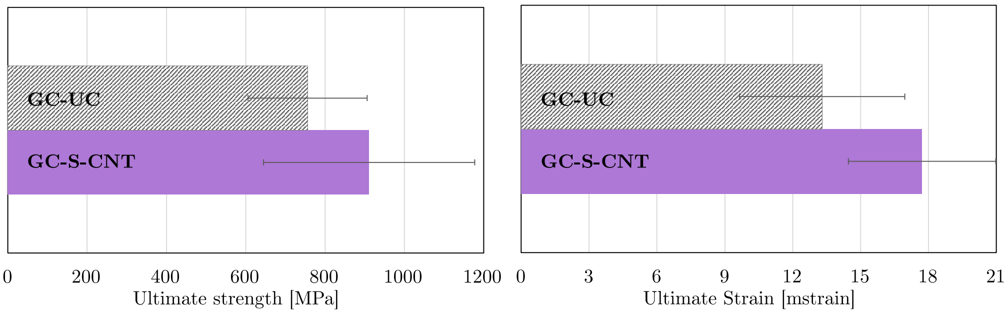

(a) (b)

Figure 3.52: Ultimate strength (a) and strain (b) with ±1 standard deviation band for uncoated (UC, grey) and (silica+CNT)-coated (S-CNT, violet) for C-TRM with M15 hydraulic lime mortar.

(a) Uncoated (b) Silica/CNT-coated

Figure 3.53: 8x magnification microscopy image for failed carbon-TRM

of tensile response is well-documented in the literature [De Santis 2015a, Shu 2015]. Therefore, we conclude that mechanical performance in traction of the embedding mortar plays a crucial role in the overall tensile response of the laminates.

In the case of either mortar, a significant increase in the mean ultimate elongation is brought by coating, respectively +40% for HM5 and +33% for M15. In terms of ultimate strength, coating induces an unexpected 24% loss for mortar HM5. This detrimental effect is outweighed by enhanced ductility and results in a 25% improvement in terms of toughness (i.e. energy dissipation) and still much lower than what is obtained for M15 mortar specimens (+169%). In general, coating unfavourably impacts strength while ductility is consistently improved, it being 70% higher for M15 mortar; the combined effect is still on the positive side for dissipated energy at failure (+20%).

Optical microscopy depicts a scenario that is consistent with the findings coming from mechanical testing. Fig.3.53 and 3.54 show magnified images of failed C-TRM fabric embedded into G mortar at 8X and 35X, respectively. Indeed, despite good impregnation of the coated yarn, supported by the presence of diffuse mortar patches on the surface, wide clean zones exist where CNT-coating is not attached to the mortar (see detail in Figure 3.54(b)). These areas suggest that lack of adhesion still occurs. The random placement of the portions of fabric uncovered by the coating is likely the principal cause of a more scattered failure mode and behaviour in traction tests, which is no longer trilinear.

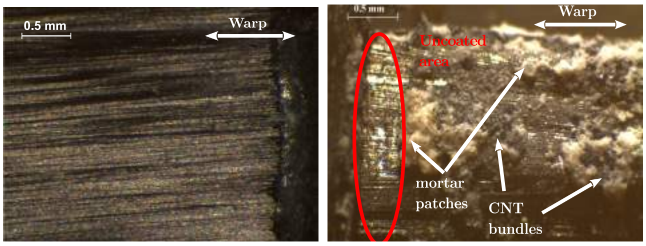

(a) Uncoated *(b) Silica/CNT-coated*

Figure 3.54: 35x magnification microscopy image for failed carbon-TRM

3.4 Conclusive remarks

This chapter deals with the application of sustainable mineral coatings based on silica with the aim of enhancing the mechanical and chemical adhesion at the fibres-to-matrix interphase. Design considerations are also conducted, in the perspective of a possible inclusion of the coated textiles in the technical practice. Comparisons between inorganic and partially organic coatings are presented in Section 3.1. All the proposed coatings take advantage of the triggering of pozzolanic reactivity concentrated within the first mortar layer just surrounding the fabrics' yarn (i.e. interphase transition zone [Amraei 2019]). The main attractive features of these treatments consist in the chance of including the manufacturing process within an industrial controlled chain, having a final product with repeatable properties and composition. Furthermore, coatings allow to preserve the fully inorganic nature of the binder, thus maintaining the attractive properties thank to which TRM is preferred to FRPs. Glass fibres appear to be the best candidate to be coupled with silica, with respect to carbon, albeit the coatings evidenced a positive effect for both materials. Detailed considerations for each coating type are discussed in the relevant sections. Figure 3.55 compares the mean stress-strain curves in tension separately encountered in the previous sections for ARG fabric and M15 mortar, while the relevant mean strength, strain and dissipated energy values are reported in the summarizing bar-chart in Figure 3.56. Silica coating on glass fabrics induces a clear enhancement of the mechanical behaviour in tension of TRM laminates, both in the

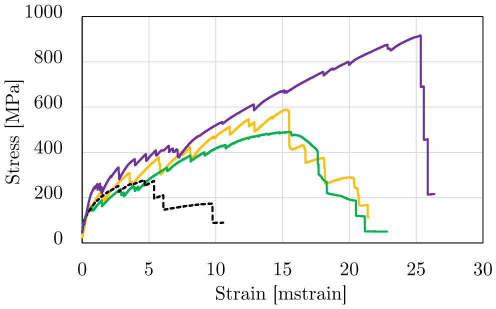

Figure 3.55: Mean strength curves for all tested groups: uncoated (UC, grey), nano-silica coated (NS, green), micro-silica coated (MS) and nano-silica with CNT (S-CNT)

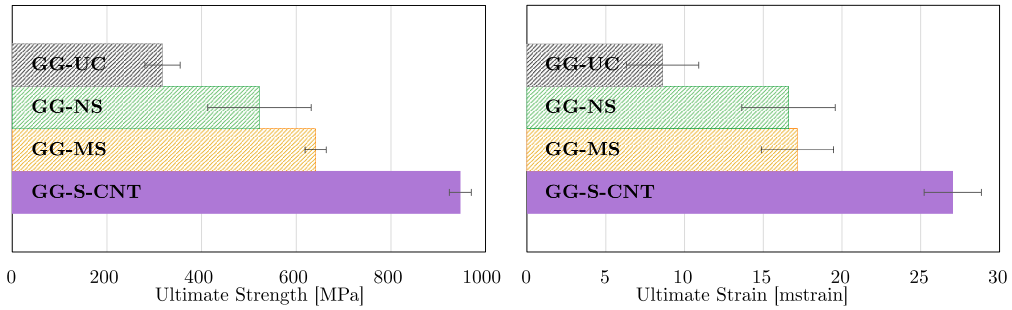

(a) Ultimate strength *(b) Ultimate strain*

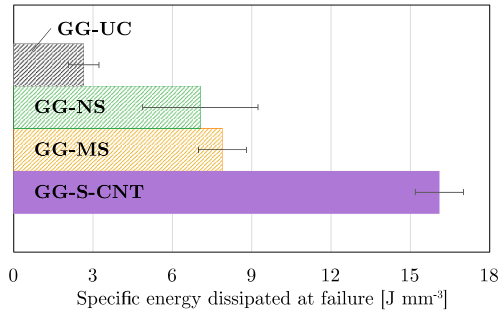

(c) Specific dissipated energy

Figure 3.56: Mean values comparison for ARG fabric in M15 mortar across all groups dealt with in this Chapter: uncoated (UC, grey), nano-silica coated (NS, green), micro-silica coated (MS) and nano-silica with CNT (S-CNT)

form of silica fume dispersion and of amorphous nano-silica. Remarkably, the addition of a 0.5%wt. amount of well-dispersed carbon nanotubes in the silica sol-gel produces a two-fold increase in terms of strength than the plain nano-silica coating, attaining an ultimate value slightly lower than the tensile strength of the glass fibres (i.e. around 1200 MPa). A notable ductility improvement is also achieved, which results in a reinforcing technique with a highly dissipative attitude. This can be ascribed to the reinforcement of the interphase zone around the fibres with high specific strength nano-fillers, which act by enhancing roughness and thus offering more grip, and by effectively bridging micro-cracks at the interphase, making possible the triggering of a capillary crack pattern.

Chapter 4

Epoxy-based coatings for synthetic fibres

Contents

In this chapter two novel epoxy coatings are fully characterized in order to enhance the mechanical performance of G-TRM composite materials. In Section 4.1, a preliminary treatment is proposed to enhance compatibility between fibres and epoxy resin. Then in Section 4.2, the two different coatings are proposed and characterized. The thermal stability of these epoxy coating is assessed in Section 4.3. Indeed, response to high temperatures is one of the main parameters to preserve when polymeric coatings are proposed in the context of inorganic composites for structural purposes. Finally, the optimization of the more promising coating is presented by finding the optimal dilution degree to improve the fabric impregnation

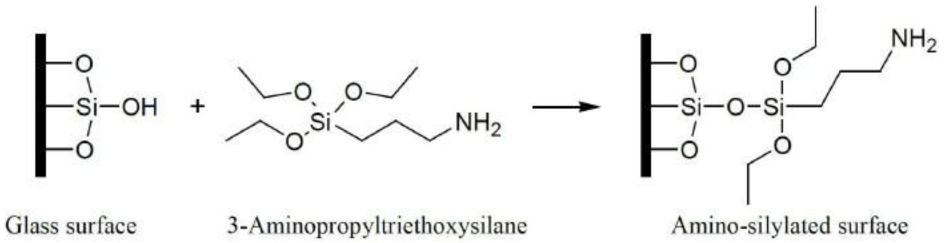

Figure 4.1: Schematic of the functionalization of glass surfaces through 3-Aminopropyltriethoxysilane.

and thus the overall mechanical performance. Tensile and bending tests are adopted to characterize the coated TRM.

4.1 Silanization

Glass fabric is preliminary treated to enhance chemical bond formation with the organic coating (functionalization). To this aim, a distilled water solution of 3-Aminopropyltriethoxysilane ($C_9H_{23}NO_3Si$, hereafter ”silane”) is chosen as coupling agent. The functioning schematic is reported in Fig.4.1. The functional group NH_2 is affine to epoxy groups while the triethoxysilane group cross-links with the hydroxyl group of the glass surface of the fibres. The choice of water as solvent is due to the strong chemical aggression of alcohols (i.e. ethanol [Matinlinna 2009] and acetone [Garg 2016]) on the thermoplastic resin of the thermo-welding joints of the fibreglass net. The coupling agent is diluted with distilled water until a 2% vol. solution is obtained, that is stirred for 15 mins at room temperature. Glass fabric is immersed in this solution for 40 s, carefully rinsed with distilled water and then left to dry at room temperature. Distilled water has been preferred to organic solvents, such as ethanol or acetone, to preserve the integrity of the stitches connecting warp/waft yarns in the fabric mesh.

4.2 Epoxy coating formulation

In this section, the mechanical performance of AR-glass fabric reinforced mortar-based composite is assessed. Two epoxy micro coatings are considered for the reinforcing fabric, which differ only by the hardening agent. Coating is applied by liquid deposition on fibres previously treated with the silane coupling sizing. Thus, uniform coating thickness is attained on the yarn, although liquid tends to lump on the fabric stitches. Coating thickness stands in the range of 300 µm depending on the specific epoxy formulation and plays a relevant role in affecting the overall performance. Besides, coating thickness has a strong bearing on fabric flexibility for it affects its capacity to closely follow irregular surfaces.

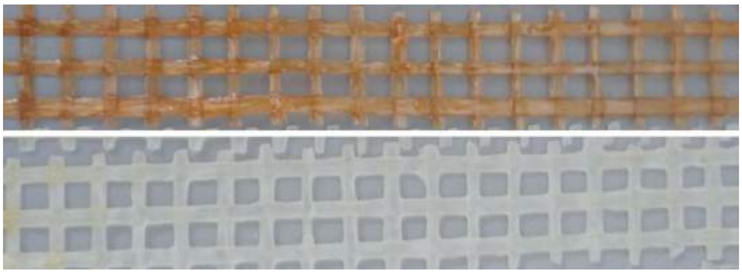

Figure 4.2: Coated ARG fabric after cross-linking: G-ER (lower) and G-EW (upper)

4.2.1 Materials and methods

The bi-directional commercially available alkali-resistant (AR) multifilament fabric mentioned in Table 2.2, is used as reinforcement fabric.

Once functionalized, the ARG fabric is coated with epoxy resin. To this aim, high-purity bisphenol A diglycidylether resin ($C_{21}H_{24}O_4$, D.E.R. 332, DOW Chemicals, hereafter "DER") is reacted with two different curing agents: either the aromatic hardener m-phenylenediamine (hereafter "m-PDA"), also called 1,3-diaminobenzene ($C_6H_4(NH_2)_2$), or the organic aliphatic hardener diethylenetriamine ($HN(CH_2CH_2NH_2)_2$, hereafter "DETA"), also known as 2,2-Iminodi(ethylamine). DER is pre-heated at 50°C in a magnetic stirrer and mixed, in stoichiometric ratio, with m-PDA flakes or liquid DETA until complete homogenization [Zobg 2009]. Glass fabric is bathed in either solution for 10 s, extracted and squeezed out to remove the excess of resin and then left to crosslink at room temperature. Accordingly, the following sample groups are investigated:

- uncoated ARG fabric (coded G-UC);
- silane functionalized ARG fabric coated with epoxy resin and m-PDA as hardening agent (G-ER);
- silane functionalized ARG fabric coated with epoxy resin and DETA as hardening agent (G-EW).

The two families of coated fabric are shown in Fig.4.2.

4.2.1.1 Inorganic matrix

A pre-mixed natural hydraulic lime (NHL) mortar, aimed at structural purposes is employed for all specimens (see Table 2.1, mortar “M15”). This fine aggregate matrix, endowed with superior ductility compared to Portland cement and good workability, promotes specimen reproducibility and diffuse cracking at failure [Nobili 2016, Signorini 2018c].

4.2.1.2 Specimen preparation

A minimum of five 1-ply ARG-TRM specimens (coupons) for each test group are manufactured according to the ICC Guidelines [ICC AC434 2013], as detailed in

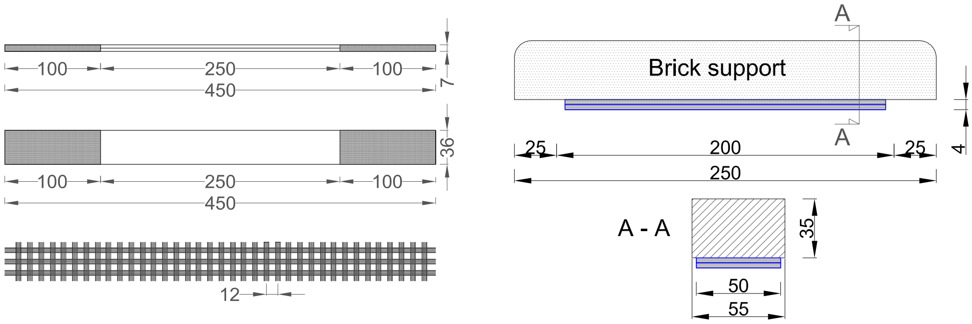

(a)

(b)

Figure 4.3: Specimen geometry (dimensions in mm*): (a) rectangular coupons for uni-axial traction test and (b) three-point bending of laminated bricks*

Section 2.3.1. As detailed in [Nobili 2016], specimen manufacture is carried out on an individual basis, to avoid cutting from a larger sheet, in a polyethylene formwork specially designed to warrant thickness uniformity of the matrix layers and consistent placing of the fabric at mid-plane. Coupon geometry is illustrated in Fig.4.3(a).

Laminated clay brick supports have been tested in three-point (3-P) bending, as illustrated in Fig.4.3(b). Although no provision against delamination is taken, the design anchoring length $L_a = 100\,\mathrm{mm}$ warrants that failure initiates in the composite and delamination only occurs eventually [Nobili 2017a].

4.2.2 Experimental investigation

The experimental part consists of mechanical tests and microscopy investigation aimed at assessing the quality of interphase bond formation.

4.2.2.1 Mechanical tests

Uni-axial tensile tests are performed using a universal testing machine (UTM) Instron 5567, equipped with a 30 kN load cell and pneumatic wedge clamps, according to the procedure described in Section 2.3.2. Fig.4.4 reports the mean linear trends that are used to compute the actual displacement rate for each coated group.

Three-point bending tests are carried out using the same UTM equipped with a knife acting at midspan of a twin point-support clamp. Support spacing is set at 200 mm. Flexural test takes place under displacement control of the acting knife with a displacement rate $\dot{\delta} = 1\,\mathrm{mm/min}$ (see also Section 2.4.2).

4.2.2.2 ESEM microscopy investigation

To analyse both epoxy-coated fabrics and failed specimens, the environmental scanning electron microscopy ESEM Quanta-200 is operated without metal coating in low vacuum (pressure 0.68 Torr).

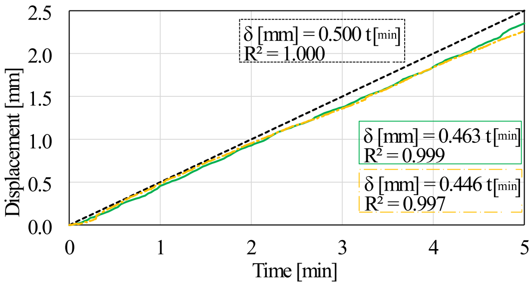

Figure 4.4: Uni-axial test nominal elongation ramp imposed at the UTM cross-head (dotted line, black) and actual elongation rate, as measured by DIC, for G-ER (solid, green) and G-EW (dash-dotted, yellow) specimen groups. Linear fitting expressions are also given alongside the coefficient of determination R^2

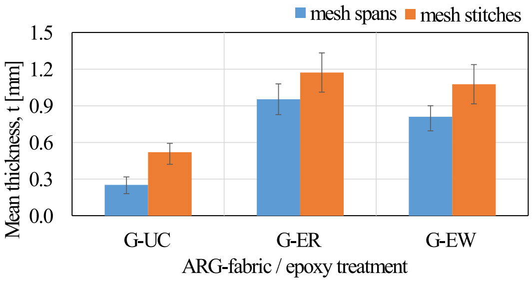

Figure 4.5: Mean fabric thicknesses at the yarns and at the stitches

4.2.3 Results and discussion

4.2.3.1 Coating thickness

The average thickness (i.e. equivalent diameter) of the ARG fabric is shown in Fig.4.5 for the uncoated and coated groups. Thickness measures are taken at several different positions both on the yarns and on the stitches, where the coating solution tends to lump. The mean thickness of the reinforcement fabric sits below 300 µm for the yarn and it is almost twice as large at the stitches. The mean thickness of the epoxy coating is $t_{ER} = 338\,\mu$m in the G-ER group and $t_{EW} = 279\,\mu$m in the G-EW group, with standard deviation $\varsigma(t_{ER}) = 17\,\mu$m and $\varsigma(t_{EW}) = 1\,\mu$m, respectively. For interphase modification, mesh flexibility and response homogeneity, coating thickness should be as small as possible, while higher thickness proves beneficial for durability and defect-healing purposes. Although G-ER coating is only 21% thicker than G-EW, the corresponding specimens can be easily told apart in light of their greater stiffness.

4.2.3.2 Failure analysis

Fig.4.6 (a) shows the typical failure mode taking place in the G-ER and G-EW groups and involving fabric rupture. In contrast, G-UC specimen failure always occurs in telescopic fashion and indeed the same mechanism is encountered in bending (Fig.4.6 (b)). Bending test of coated specimens ends by delamination failure, that is an expected consequence of the lack of shear strengthening provisions (Fig.4.6

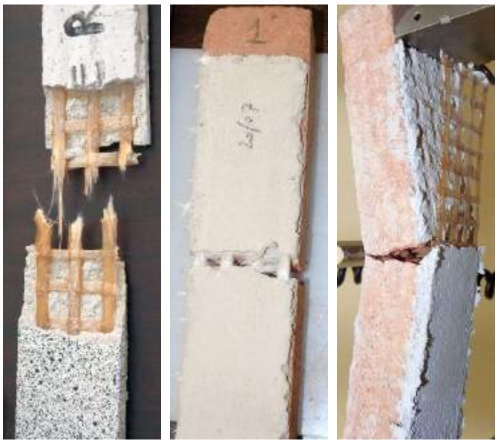

(a) *(b)* *(c)*

Figure 4.6: Failure modes for laminates in bending: Fabric rupture is the typical failure mode in the G-ER and G-EW groups (a), typical telescopic failure mode for brick bending in the G-UC specimen group (b) and typical delamination failure mode for brick bending in the G-ER and G-EW groups (c)

(c)). However, strength curves clearly show the positive effect of coating on the mechanical response prior to failure (see Sec.4.2.3.6).

4.2.3.3 ESEM investigation of failed specimens

Figs.4.7 and 4.8 show ESEM magnification of the matrix-to-fabric interface of failed specimens. In particular, it appears that telescopic failure wipes the matrix off the multifilament yarns whenever the chemical bond is weak enough, as it is the case for G-UC specimens, see Fig.4.7(a). In contrast, both epoxy coatings provide enough substrate adhesion for the matrix to resist failure, as in Figs.4.7(b) and (c). Furthermore, in Fig.4.7(a) multifilaments stand well separated and identifiable in the yarn, while Figs.4.7(b-c) reveal only a few external filaments emerging from the epoxy coating. Indeed, at higher magnification, the latter appears as a solid block embedding the multifilaments. In Fig.4.8(a), small matrix particles occasionally stain the surface of full-round individual multifilaments, whereas in Fig.4.8(b) coated specimen strands appear embedded in solid resin. Moreover, it is clear that large and widespread patches of mortar are still well bonded to the solid resin, in contrast to multifilaments that support very few.

4.2.3.4 Uni-axial tensile test

Fig.4.9 plots the mean strength curve for each specimen group alongside the corresponding one-standard-deviation band, where the same scaling is adopted for the axes to better appreciate performance comparison. As customary, strain is conventionally reported to the fabric cross-sectional area A_f. Looking at these curves, it is immediately clear that coated specimens exhibit remarkable ductility and strength gains over the uncoated group and, in this respect, the G-EW group performs best.

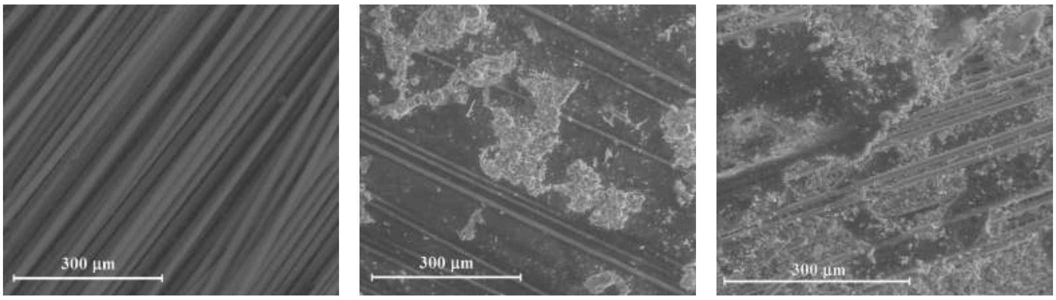

(a) *(b)* *(c)*

Figure 4.7: ESEM micrography at 400X magnification of G-UC (a) G-ER (b) and G-EW (c) failed specimens

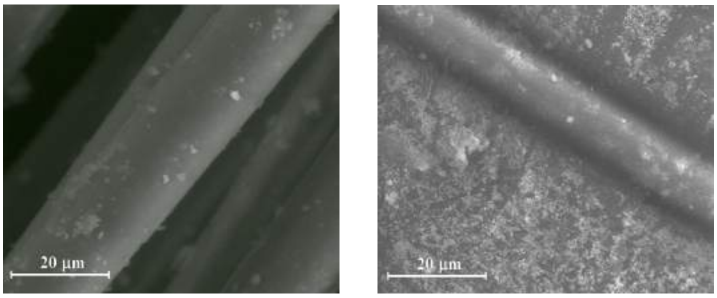

(a) *(b)*

Figure 4.8: ESEM micrography at 4000X magnification of G-UC (a) and G-ER (b) failed specimens.

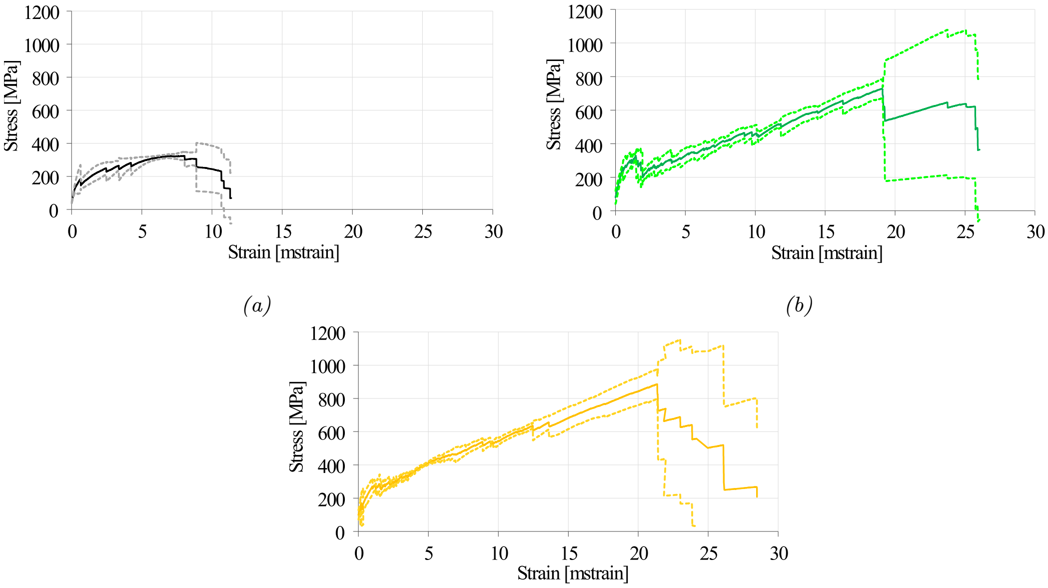

(a) *(b)*

(c)

Figure 4.9: Mean stress-strain curve with ±1 standard deviation band for uni-axial traction of (a) G-UC, (b) G-ER and (c) G-EW specimen groups

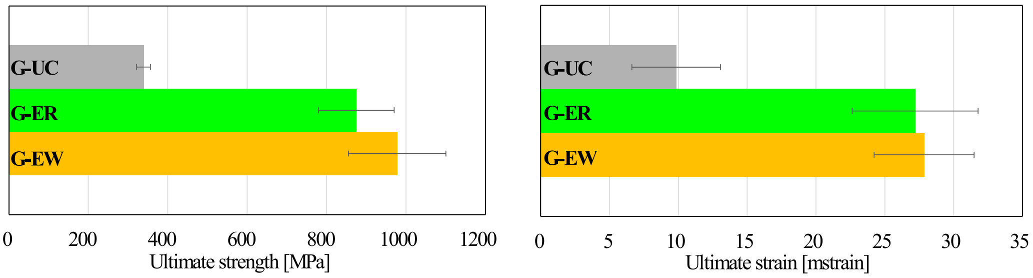

(a) (b)

Figure 4.10: Mean ultimate stress (a) and mean ultimate strain (b) evaluated in uni-axial traction for all specimen groups

Table 4.1: Mean ultimate tensile strength $\mu(f_{fu})$ and elongation $\mu(\varepsilon_{fu})$, with corresponding standard deviation ς and coefficient of variation CV, for all specimen groups, as derived by uni-axial tension tests

Group	**Tensile strength**			**Tensile elongation**		
	$\mu(f_{fu})$ [MPa]	ς_f [MPa]	CV_f [%]	$\mu(\varepsilon_{fu})$ [mstrain]	ς_ε [mstrain]	CV_ε [%]
G-UC	339	17	5.1	9.8	3.2	32.7
G-ER	875	95	10.9	27.2	4.6	16.8
G-EW	978	123	12.6	27.9	3.6	13.0

Comparing this picture with Fig.6 in [Dvorkin 2013], obtained for carbon fabric in Portland cement, we see similar ductility levels (ultimate strength at about $\varepsilon = 20\,\text{mstrain}$) and yet remarkably superior mean performance increments over the uncoated fabric. A bar chart comparison of ultimate strength and strain values is presented in Fig.4.10.

Tab.4.1 collects the mean ultimate strength and strain values, together with the corresponding standard deviation ς and coefficient of variation CV, for all specimen groups. It appears that G-ER and G-EW coated specimens present a 158% and 188% increment in the mean ultimate strength $\mu(f_{fu})$ over the uncoated group G-UC, respectively. However, as expected, this remarkable strength gain comes at a significant cost in terms of data scattering, which is due to the well-known positive covariance effect [Nobili 2017b]. To better assess the actual performance gain, design values should be compared instead. According to the minimum acceptable design criteria proposed in [ICC AC434 2013], a 3-sigma rule is adopted to evaluate the ultimate strain ε_{fu} and the ultimate design strain ε_{fd} therefrom

$$\varepsilon_{fu} = \mu(\varepsilon_{fu}) - 3\varsigma_\varepsilon, \quad \varepsilon_{fd} = 0.7\varepsilon_{fu} \leq 1.2\%.$$

The design strength (at failure) may be evaluated from the design strain by multiplication by the crack longitudinal modulus E_f

$$f_{fd} = 0.85 E_f \varepsilon_{fd}, \tag{4.1}$$

or from experimental data, which is largely more realistic [Nobili 2017b].

Table 4.2: Design tensile strength, f_{fd}, characteristic ultimate strength, f_{fuk}, ultimate elongation ε_{fu} and design elongation ε_{fd} for all specimen groups, as derived from uni-axial tension tests. Δ expresses the coated/uncoated ratio for the relevant characteristic.

Group	**Strength**				**Elongation**	
	f_{fd} [MPa]	Δ [%]	f_{fuk} [MPa]	Δ [%]	ε_{fu} [mstrain]	ε_{fd} [mstrain]
G-UC	288	-	311	-	0.2	0.14
G-ER	590	105	719	131	13.4	9.4
G-EW	609	111	776	150	17.1	12.0

Tab.4.2 presents design values for strength and elongation as determined from the experimental results through a 3-sigma rule, together with the ultimate characteristic strength f_{fuk} (this is obtained from the 1.64-sigma rule and it is really the characteristic value provided that a Gaussian distribution for the data is assumed). Data analysis supports some of the conclusions already discussed in [Nobili 2017b] and it confirms that the 3-sigma rule is very conservative for it produces a very unfavourable design strain in the presence of the data scattering characteristic of brittle matrix composite materials. As a consequence, evaluation of the design strength from the design strain according to Eq.(4.1) produces a strong under-estimation of the experimental evidence. Indeed, in the uncoated group, design strain is drastically reduced by the comparatively large data scattering associated with telescopic failure. When experimental data are employed instead, the design and the characteristic strength associated with either coated group exceeds a two-fold increase over the uncoated group, almost independently of the coating type. In this respect, G-ER and G-EW appear almost equivalent and this conclusion seems to support the common action mechanism associated with epoxy coating, whose role is to prevent telescopic failure. However, results change significantly when elongation is considered. Although the mean ultimate elongation associated with the G-ER and G-EW groups is almost identical, i.e. $\mu(\varepsilon_{fu}) \approx 27\,\text{mstrain}$, the standard deviation ς_ε is 22% smaller for G-EW compared to G-ER. This reduction in data scattering translates into a 28% improvement of the ultimate and design elongation. It is remarkable that data scattering in the G-EW group is close to that connected with the uncoated group G-UC and yet the design elongation is 85-times greater. Furthermore, the design elongation of the G-EW group reaches the allowable maximum value 1.2% and, in this respect, it is an optimum value.

4.2.3.5 Crack pattern analysis

Determination of the crack pattern brings a significant contribution to the assessment of the energy dissipation capability associated with the failure mechanism. Fig.4.11 shows a colour map representation of the axial displacement field for the three specimen groups at a common elongation value $\varepsilon = 15\,\text{mstrain}$. As expected, specimen displacement mainly occurs in a discrete fashion, through crack widening,

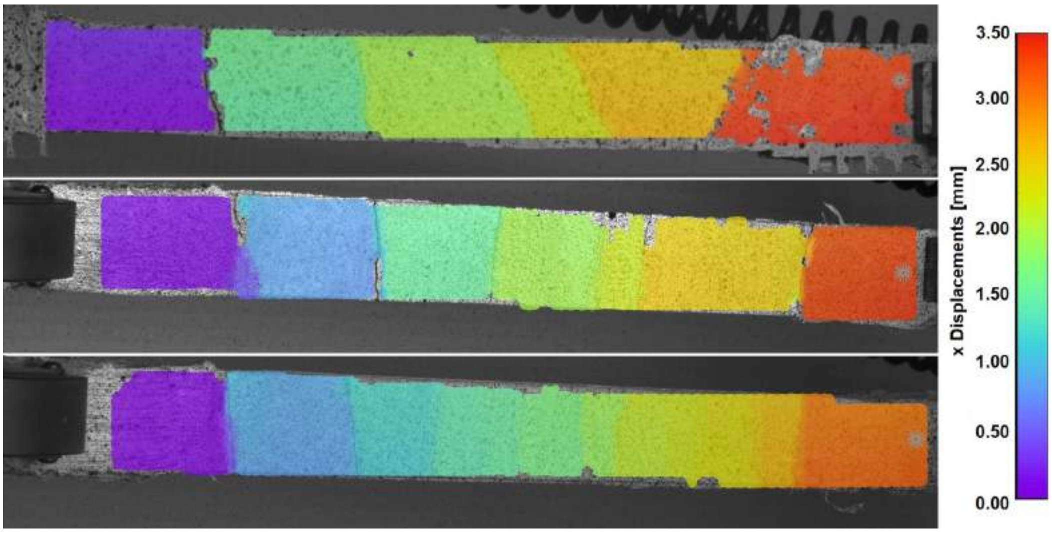

Figure 4.11: Longitudinal displacement field for ARG coupons at $\varepsilon = 15\,\mathrm{mstrain}$ *(from top to bottom: G-UC, G-ER and G-EW specimens)*

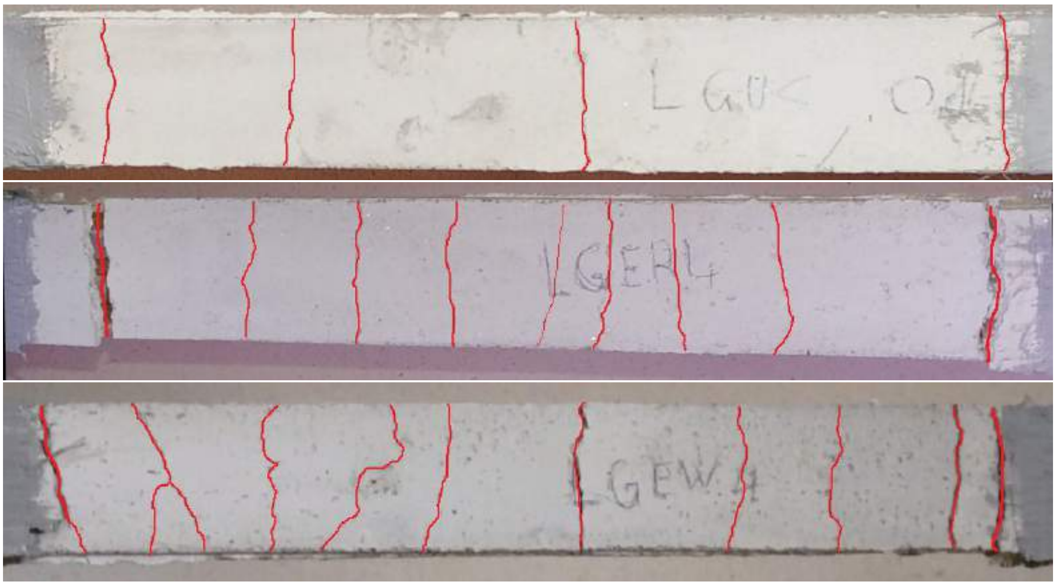

Figure 4.12: Near failure crack pattern in G-UC (top), G-ER (middle) and G-EW (bottom) specimens

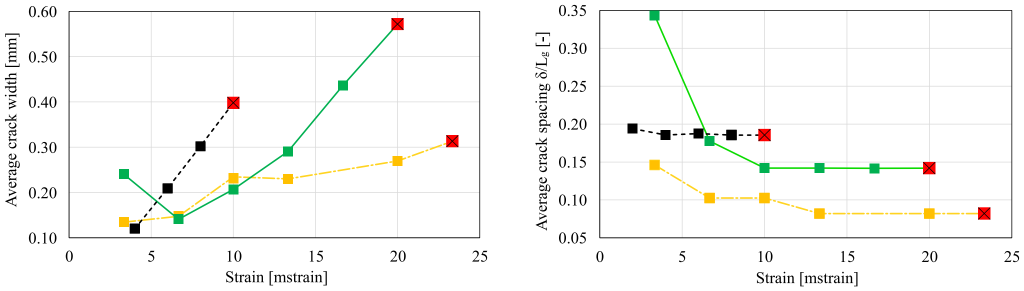

(a) *(b)*

Figure 4.13: Mean crack width (a) and dimensionless crack mean spacing (b) vs. strain for G-UC (dotted, black), G-ER (solid, green) and G-EW (dash-dotted, orange)

and the number of cracks is a good indication of the specimen ductility and energy dissipation capability. In this respect, the G-UC specimen features fewer cracks with larger displacement jumps compared to coated specimens. Fig.4.12 compares the near-failure crack pattern for G-ER and G-EW specimens, with the latter exhibiting better damage distribution and diffusion.

Estimation of the number of cracks and of the crack width is obtained from DIC data at different elongation values in uni-axial test. Figs.4.13(a) and (b) plot the average crack width and the crack average spacing as a function of the strain up to failure, respectively. The crack average spacing is normalized to the gauge length $L_g = 250\,\text{mm}$. The failure point is denoted by a red square marker at the end of each curve. Curves support the qualitative conclusion that, at the same strain level, the uncoated specimen exhibits fewer cracks located at larger distance and those cracks are wider than those in the coated groups, with the partial exception of very low strain levels for which cracking is mainly induced by curing. Fig.4.13(a) shows that crack width increases with strain in an almost linear fashion with similar slope for all specimens (cf.[Nobili 2017b]). However, the G-EW specimen closely follows the G-ER specimen until $\varepsilon = 10\,$mstrain, that is the failure strain for the uncoated specimen, beyond which point it acquires a far smaller slope. Thus, it appears that the G-EW specimen features a strongly enhanced crack pattern diffusion, with several thin cracks located at short distance, which seems to be the result of an apparently stiffer fabric, i.e. fabric telescopic slippage lowers the apparent elastic modulus. Indeed, Fig.4.13(b) shows that the crack average spacing for G-EW is about half as much as that for the uncoated specimen, the G-ER specimen faring in between. Crack spacing quickly plateaus for all groups and, in fact, the corresponding limit can be considered as a good indication of the coating effectiveness [Nobili 2017b]. It is worth observing that, in contrast to the uncoated specimen for which crack average spacing is almost flat throughout, coated specimens exhibit decreasing curves, the decrease rate being most pronounced at small strain. It can be deduced that in coated specimens new cracks are able to open, especially at low strain levels, whereas in the uncoated specimen the number of cracks rest the same and the sliding mechanism of the embedded fabric brings the sole contribution to

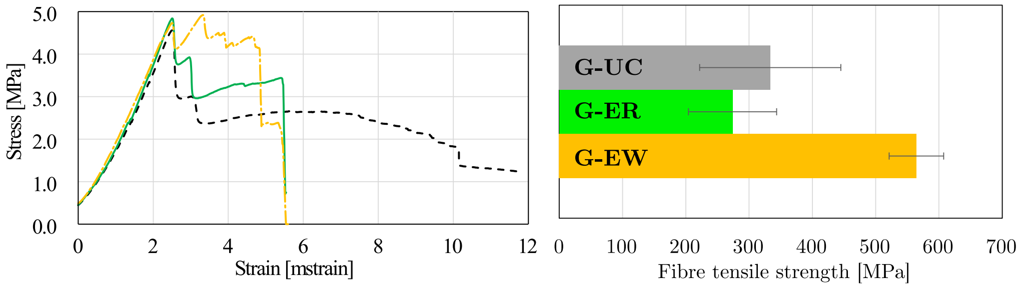

(a) *(b)*

Figure 4.14: Mean stress-strain curves for three-point bending of clay bricks laminated with G-UC (dotted, black), G-ER (solid, green) and G-EW (dash-dotted, yellow) composite (a). Besides, maximum axial stress attained by the fibres is reported and compared across all the groups (b).

deformation through crack widening.

4.2.3.6 Three-point bending test

The strength curves of laminated clay bricks in three-point bending are presented in Fig.4.14, together with the relevant maximum axial stress attained by the fibres once the brick support cracked (for the computation of this values, see Eqn.(2.3)). Conversely, stress in Fig.4.14(a) is conventionally reported to the resistant cross-section

$$\sigma_{zz} = \frac{M_{xx}}{W_x},$$

where W_x is the resistance modulus. The stress peak is consistently reached at brick failure and it is the same regardless of the lamination type. Nonetheless, the post-peak behaviour is strongly affected by the composite capacity to resist telescopic slippage and delamination. In this respect, it is clearly seen that G-EW specimens present an almost constant post-peak strength (plastic behaviour), whereas G-ER perform in between uncoated and G-EW (softening behaviour). Since support adhesion is independent on the coating and no provision was taken against delamination, a superior performance in terms of strength inevitably leads to anticipated delamination, i.e. less ductility. Indeed, failure strain in the G-ER and in the G-EW group is virtually identical ($\varepsilon = 5.4\,\text{mstrain}$) and it is located about halfway to the failure strain of G-UC. An upgrade of the present work may consist in performing flexural tests with larger beams, having care to ensure an adequate bonding length for the fabric, avoiding premature failure caused by detachment induced by the presence of high peeling stresses [ACI 549.4R-13 2013].

4.2.4 Conclusive remarks

The mechanical performance of epoxy coated AR-glass fabric composite has been considered. Preliminary functionalization of the fabric surface is adopted to enhance chemical bond formation with the coating. Two epoxy coatings are employed in a mortar matrix, which only differ in terms of hardening agent. Mechanical performance is assessed in uni-axial traction of rectangular specimens (coupons) and in three-point bending of laminated clay bricks. Failure mode analysis, crack pattern development and microscopy investigation are presented. As expected, coated specimens largely over-perform uncoated ones, for telescopic failure is averted and fabric rupture is reached. Somewhat surprisingly, a relatively small difference in the coating thickness (G-EW coating is 17% thinner than G-ER owing to reduced viscosity in the liquid phase) produces a strong effect in the final performance. Indeed, although mechanical performance appears very similar when mean failure strength is considered, and in fact almost identical in terms of mean elongation at failure, coating thickness has a strong bearing on data scattering and results take on a different perspective when looked under the viewpoint of design limits. This conclusion is indeed supported by failure analysis, which shows that fabric rupture is consistently met in the thin coated group (G-EW), while mixed results are encountered for thick coating (G-ER). Along the same line is crack pattern assessment and again best performance, in terms of crack diffusion and energy dissipation, is reached in the thin coated group. Three-point bending tests suggest that the post-peak behaviour of the stress-strain curve is deeply affected by coating thickness and in fact the thin coated group presents a plastic behaviour, as opposed to the thick coated group which demonstrates softening. This preliminary study aims at drawing attention on the coating strategy rather than on the coating material, given that only the latter seems to have been investigated in the literature.

4.3 Thermal stability assessment of epoxy coatings

The possibility of high temperature exposure poses a serious limitation to the applicability of organic matrix reinforcing systems, such as fibre-reinforced polymers (FRPs). Indeed, exposing FRP systems to temperatures in excess of or even close to the glass transition temperature T_g produces a substantial and sudden drop in the mechanical response [Foster 2005, Chowdhury 2011]. This behaviour, that rapidly leads to delamination and failure, is all the more undesired in consideration of the fairly low transition temperature $T_g \approx 80\,°\mathrm{C}$ characterizing most organic resins. In this respect, Textile Reinforced Mortar/Cement (TRM/TRC) and Fabric Reinforced Cementitious Matrix (FRCM) composite materials exhibit vastly superior thermal stability, in light of the adoption of an inorganic matrix. On the other hand, the bond strength between the fabric and the inorganic matrix is generally weak and this leads to poor mechanical performance and a generally inconsistent failure pattern [Badanoiu 2003, Nobili 2017a]. Improvement in the matrix-to-fabric bond may be obtained by adopting inorganic [Homoro 2018, Signorini 2019c] or organic [Scheffler 2009, Donnini 2017, Messori 2018] coatings. Consequently, investigation of the effect of temperature exposure on TRM is complicated by the need to consider the whole composite package, which consists of the matrix, the fabric and the coating. A large body of literature is devoted to the characterization of FRP systems subjected to elevated temperature, see, for instance, [Foster 2005, CNR TD200-R1 2013, Cao 2009, Saafi 2002, Li 2017, Jarrah 2018] and references therein. Conversely, a limited number of studies is available concerning the effect of high temperature exposure on TRM and FRCM and these are mainly focused on carbon and PBO fabrics [Ombres 2017, Xu 2014]. In this framework, a crucial issue that requires careful investigation is the role played by high temperature exposure on the adhesive behaviour of the laminates at the mortar-to-substrate interphase, as discussed by [Ombres 2015] and [Maroudas 2017] for concrete and masonry structures, respectively. The former study presents single-lap shear tests on PBO-FRCM laminates applied on concrete supports and reports that conditioning at 50 °C and 100 °C affects not only the load-bearing capacity of the composite, which decreases from 25 to 40% depending on the number of layers, but also the failure and the delamination modes. Indeed, failure statistically changes from matrix-to-fabric slippage for the unconditioned samples to debonding at matrix-to-concrete interphase for the conditioned ones. Analogously, in the contribution by [Maroudas 2017], single-lap shear tests are conducted on G-TRM thin laminates applied to brick panels and exposed to temperatures up to 300 °C. It is shown that, if the temperature exceeds 100 °C, failure is mainly triggered by adhesive debonding at the masonry-to-mortar interphase and strongly affected by the deterioration of the ultimate strength of the bare glass fabric. Furthermore, [Raoof 2017] and [Bisby 2013] assess the response in bending of TRM and FRP reinforcing systems subjected to high temperatures, while [Tetta 2016] considers jacketing. [Trapko 2013] compares FRP and FRCM confined concrete elements exposed to temperatures up to 80 °C for 24 h. Already at 40 °C compressive strength of FRP jacketed elements is reduced by 20% and at 80 °C ductility drops by 50%, as opposed to a 11% loss encountered for FRCM. [de Andrade Silva 2014] investigate double-sided pull-out strength of an epoxy coated carbon yarn after 120 min exposure at 100 °C, 150 °C, 200 °C, 400 °C and 600 °C. Maximum pull-out force and pull-out work are computed and compared with the dry yarn. Interestingly, an increase in mechanical performance of the coated specimens is observed after heating at temperatures up to 150 °C, that is ascribed to a "polymer interlocking mechanism in the yarn-matrix interface, which is generated during the heating and cooling of the polymer yarn coating". In [Rambo 2015], uni-axial tensile tests of basalt textile reinforced plates are conducted. The basalt fabric is coated with styrene-acrylic latex and refractory concrete is adopted as matrix. Plates are exposed for 60 min at temperatures in the range 75–1000 °C. It is found that performance loss is mild up to 200 °C and it is concluded that "the presence and the type of coating can become a deterministic factor in the tensile response of the composite submitted to elevated temperatures". Recently, [Donnini 2017] present experimental and numerical results on the mechanical performance of dry and epoxy-plus-sand coated carbon FRCM composites under uni-axial tension and double-shear bond test. Beside ambient temperature, 120 min exposure at 80 °C and at 120 °C are considered. It is worth emphasizing that mechanical tests are carried out inside the climatic chamber, where specimens are exposed at high temperature. An impressive 70% drop in

Table 4.3: Hardening agents datasheet

Characteristic	**Unit**	**m-PDA**	**DETA**
Physical form	-	Pellets	Liquid
Formula	-	$C_6H_8N_2$	$C_4H_{13}N_3$
Melting point	°C	63÷65	-40
Flash point	°C	175	94
Boiling point	°C	282÷284	200÷204

the ultimate tensile strength (and a 54% elongation loss) is determined with respect to the ambient condition already at 80 °C. In general, the existing literature lacks from detailing the thermo-physical properties of the coating agent, that is usually adopted taking an out-of-the-box approach. In this work, we focus on the role of epoxy coating on the thermal deterioration of the matrix-to-fabric interface. To this aim, the same pair of epoxy resins considered in [Messori 2018] are adopted, which differ only by the hardening agent. This feature, however, leads to important differences in terms of thermo-physical properties that exert a profound influence on the behaviour upon high temperature exposure [Harper 2003]. To avoid degradation of the lime mortar and restrict attention to the epoxy coating, temperature exposure is limited in the range 20–250 °C and 56-day dry curing is adopted. Mechanical performance is assessed in uni-axial traction of rectangular coupons according to Annex A of the guidelines [ICC AC434 2013]. DSC analysis supports the conclusion that, depending on the resin formulation, high temperature exposure may benefit strength (at the expense of ductility), inasmuch as it promotes cross-linking in a post-curing process. This mechanism is likely to explain the outcome of the double pull-out tests carried out in [de Andrade Silva 2014] and of the uni-axial traction of plates described in [Rambo 2015].

4.3.1 Materials and methods

4.3.1.1 Materials

The same reinforcement-matrix combination adopted for the epoxy coatings developed in Section 4.2 is considered, and the same epoxy coatings are assessed against high temperatures.

Table 4.3 presents the main characteristics of the curing agents as declared by the producers, with particular emphasis on thermal properties.

4.3.1.2 Specimen manufacturing

1-ply ARG-TRM coupons are manufactured on an individual basis by means of a dismountable polyethylene formwork, following a well-established and reliable manufacturing protocol, see Section 2.3.1 and [Signorini 2018c, Nobili 2017b]. A minimum of four specimens is considered for each test group. 7-day moist curing is followed by dry curing at room temperature for 56 days in total. The specimen ge-

Table 4.4: High temperature exposure conditions in the literature

Ref.	**Temp.** [°C]	**Exp. time** [min]	**Composite**	**Test**
[Xu 2014]	120, 200	30, 90	CFRCM+epoxy	3-point bending
[Donnini 2017]	20, 80, 120	100	CFRCM+epoxy	uni-axial traction, double shear bond
[de Andrade Silva 2014]	100, 150, 200, 400, 600	120	CFRCM+epoxy	double sided pull-out
[Trapko 2013]	40, 60, 80	1440	CFRCM	compression of confined cylinders
[Rambo 2015]	75, 150, 200, 300, 400, 600, 1000	60	basalt+latex+FRCM	traction of plates
[Ombres 2015]	20, 50, 100	480	PBO-FRCM	single-lap shear
[Ombres 2017]	20, 50, 100, 150, 200, 250	1200	PBO-FRCM	compression on confined cylinders
[Maroudas 2017]	20, 100, 200, 300	1200	GFRCM	single-lap shear

ometry (coupon) is schematically drawn in Fig.4.3(a) alongside the fabric mesh size. After heating and natural cooling, a pair of externally bonded 100-mm G-FRP tabs is glued at both ends of each specimen to accommodate the clamps of the testing machine.

4.3.1.3 High temperature exposure

After curing, coupons undergo a heating treatment in a Binder WTC oven. A 4 °C/min heating ramp is applied until either of four different target temperatures is reached, namely 100, 150, 200 or 250 °C. The set of target temperatures is chosen to induce coating degradation only. Indeed, according to [Çavdar 2012], fabric composites in a cement-based matrix perform well up to 450 °C. Once the target temperature is attained, isothermal conditions are maintained for 120 min. It should be observed that heating time and target temperature are not standard and indeed they vary greatly across the relevant literature, as summarized in Tab.4.4. Specimens are then moved to room temperature (20 ± 2°C) and left to cool down in a natural cooling process, as in [de Andrade Silva 2014].

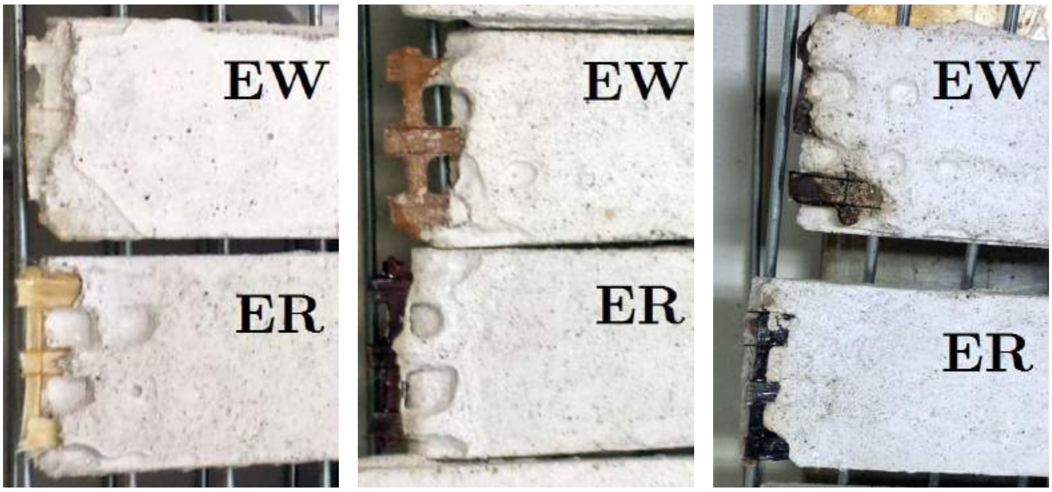

(a) 150° C (b) 200° C (c) 250° C

Figure 4.15: Mortar and fabric after temperature exposure: it clearly appears that both epoxy coatings oxidise above 150 °C

4.3.2 Experimental characterization

4.3.2.1 Optical investigation

Preliminary visual investigation of the specimens after heating is illustrated in Fig.4.15. In particular, both epoxy coatings, when exposed to temperatures higher than 150 °C, appear oxidized and blackened (compare with the uncoated fabric shown in Fig.4.2), while little to no effect is visible at lower temperature. Mortar appears unaffected by any temperature.

4.3.2.2 Differential Scanning Calorimetry

A Differential Scanning Calorimetry (DSC) analysis (TA DSC 2010, TA Instruments, New Castle, DE, USA) is performed on both epoxy resins, EW and ER, in a single heating ramp, starting from 0 °C up to 250 °C, with a heating rate of 10 °C/ min, under nitrogen flow. The analysis is conducted at two different stages, namely immediately after resin preparation ("as mixed" condition) and after two-week curing at ambient temperature. Comparing the heating enthalpy developed in the two conditions yields the *conversion degree*, that measures the extent to which cross-linking may occur at ambient temperature.

4.3.2.3 Uni-axial monotonic tensile test

Uni-axial tensile tests are carried out as described in Section 2.3.2, according to the guidelines [ICC AC434 2013]. The correct determination of elastic moduli, transition points and of the strain evolution during testing, the sliding displacement occurring in the wedge clamps needs is subtracted from the nominal elongation ramp, according by means of DIC device (see Section 2.3.2).

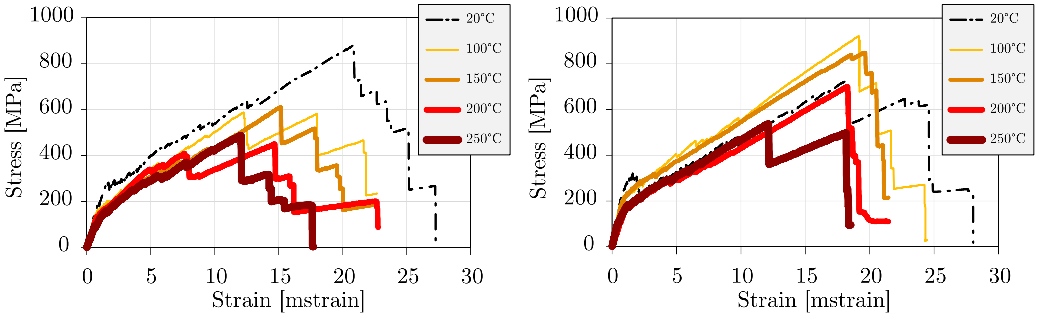

(a) EW groups

(b) ER groups

Figure 4.16: Mean stress-strain curve for the control (black, dashed-dotted line) and the exposed groups (solid lines with increasing thickness in dependence of the temperature exposure), namely 100 °C *(yellow),* 150 °C *(orange),* 200 °C *(red) and* 250 °C *(amaranth)*

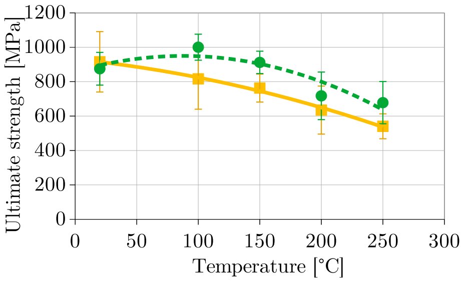

Figure 4.17: Mean ultimate tensile strength as a function of the exposure temperature for ER (circles, green) and EW (squares, yellow). ±1 *standard deviation bars and parabolic curve-fits are also presented*

4.3.3 Results

4.3.3.1 Mechanical performance

Fig.4.16 presents the mean strength curve for all test groups. As customary, strength is reported to the coated fabric cross-section and strain is normalized against the gauge length L_g. It immediately appears that the EW group performance is significantly impaired by the heating conditioning at any temperature, while the ER groups exhibit a mixed response. Results in terms of first cracking strength, ultimate tensile strength (UTS), cracked and uncracked moduli are summarized in Tab.4.5 for EW and in Tab.4.6 for ER. This behaviour is better illustrated by the curves of Fig.4.17, which compare the mean ultimate tensile strength (UTS) across the two groups. Indeed, while the mean UTS across the EW group decreases monotonically with the exposure temperature, it increases significantly in the ER-100 group and marginally in the ER-150 group, before it starts to decay. Data scattering for elastic moduli is presented in Fig.4.18 as a function of the conditioning temperature. Parabolic curve-fitting shows that scattering decreases upon temperature exposure up to a critical temperature that is connected to a post-curing phenomenon, as discussed in Sect.4.3.3.2.

In general, even for EW, heat conditioning has a surprisingly limited effect on the

Table 4.5: Mean first cracking strength (FCS), ultimate tensile strength (UTS), uncracked and cracked moduli for the EW group as a function of the exposure temperature. CV is the coefficient of variation

T	**FCS**		**UTS**		E_f^*		E_f	
[°C]	$\mu(f_{cr})$ [MPa]	CV [%]	$\mu(f_u)$ [MPa]	CV [%]	$\mu(E_f^*)$ [GPa]	CV [%]	$\mu(E_f)$ [GPa]	CV [%]
20	271.0	23.1	915.6	19.2	249.7	20.5	30.8	23.1
100	163.1	14.0	816.3	21.6	190.9	12.6	37.4	14.0
150	154.2	15.0	762.7	10.7	193.8	38.1	34.7	1.5
200	165.1	42.0	634.8	22.0	162.8	21.7	39.0	42.0
250	168.8	51.2	540.7	13.4	160.8	41.0	29.8	51.8

Table 4.6: Mean first cracking strength (FCS), ultimate tensile strength (UTS), uncracked and cracked moduli for the ER group as a function of the exposure temperature. CV is the coefficient of variation

T	**FCS**		**UTS**		E_f^*		E_f	
[°C]	$\mu(f_{cr})$ [MPa]	CV [%]	$\mu(f_u)$ [MPa]	CV [%]	$\mu(E_f^*)$ [GPa]	CV [%]	$\mu(E_f)$ [GPa]	CV [%]
20	192.4	24.4	875.0	10.9	319.7	21.1	31.0	15.0
100	183.3	16.4	1000.3	7.6	286.1	18.6	40.1	7.2
150	225.5	5.9	912.0	7.1	250.9	10.1	35.3	10.2
200	135.4	30.3	717.6	19.3	156.4	1.8	32.4	22.2
250	124.5	29.5	678.0	18.1	187.4	18.7	37.2	6.8

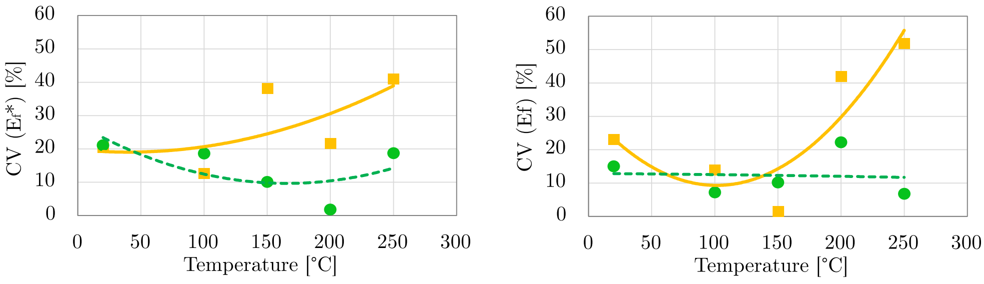

(a) E_f^*

(b) E_f

Figure 4.18: Coefficient of Variance (CV) for the uncracked (a) and cracked (b) secant moduli as a function of the exposure temperature for EW (orange) and ER (green) alongside its parabolic curve-fit. It is seen that post-curing positively affects data scattering as well as absolute performance

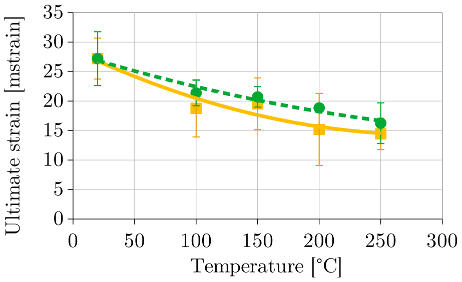

Figure 4.19: Mean ultimate strain values as a function of the exposure temperature for ER (circles, green) and EW (squares, yellow). ±1 standard deviation bars and parabolic curve-fits are also presented

performance decay of the coated fabric, especially when results are compared with the existing literature. In fact, although the performance pattern of ER is similar to that observed in [de Andrade Silva 2014, Fig.5] in the context of a double-sided pull-out test of a epoxy coated carbon multi-filament yarn, it should be remarked that, in the absence of a DSC analysis, the polymer coating adopted there seems exceptionally thermostable, for it cross-links at 160 °C and "the polymer film remained stable at temperatures up to 200 °C".

Fig.4.19 presents a similar comparison of the mean ultimate strain at failure and it shows that ductility decreases with temperature through a similar trend for both coatings.

4.3.3.2 Thermal analysis

Table 4.7: Specific enthalpy associated to curing (H_{curing}) of as-mixed and two-week-cured EW and ER resins and corresponding conversion degree.

Resin	H_{curing} [J/g] as mixed	 two-week cured	**Conversion degree** [%]
EW	387	15	96
ER	379	123	67

The DSC analysis reveals an exothermic peak for both resins, associated to two-week post-curing in ambient conditions. In order to estimate the conversion degree that could be achieved, the specific enthalpy measured from the DSC thermograms of Fig.4.20 in the two-week-cured group is compared to the corresponding value obtained in the "as-mixed" group, as summarized in Table 4.7. For EW, the specific enthalpy associated to curing is located at 387 J/g in the as-mixed condition and plunges to 15 J/g (corresponding to less than 4%) after two-week curing at ambient temperature. Consequently, two-week curing lends a conversion degree of about 96% when DETA is employed as curing agent. The same procedure applied to ER (that is when m-PDA acts as curing agent) reveals that the conversion degree achieved after two week curing at ambient temperature is much lower: about 67%.

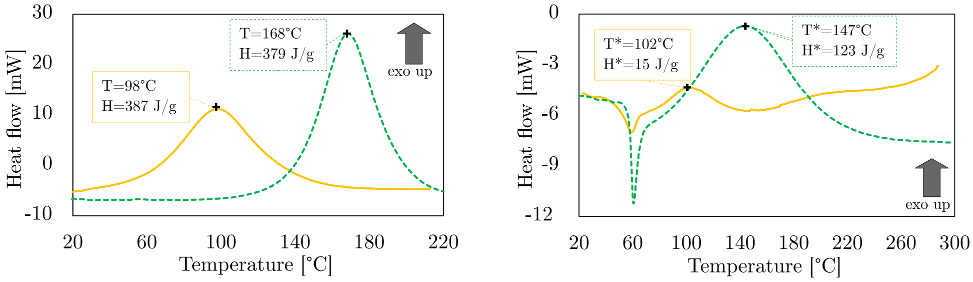

(a) Resins "as mixed"

(b) Two-week cured resins

Figure 4.20: Differential scanning calorimetry (DSC) of EW resin (solid, yellow) and ER resin (dashed, green) right after mixing (a) and after two-week curing (b)

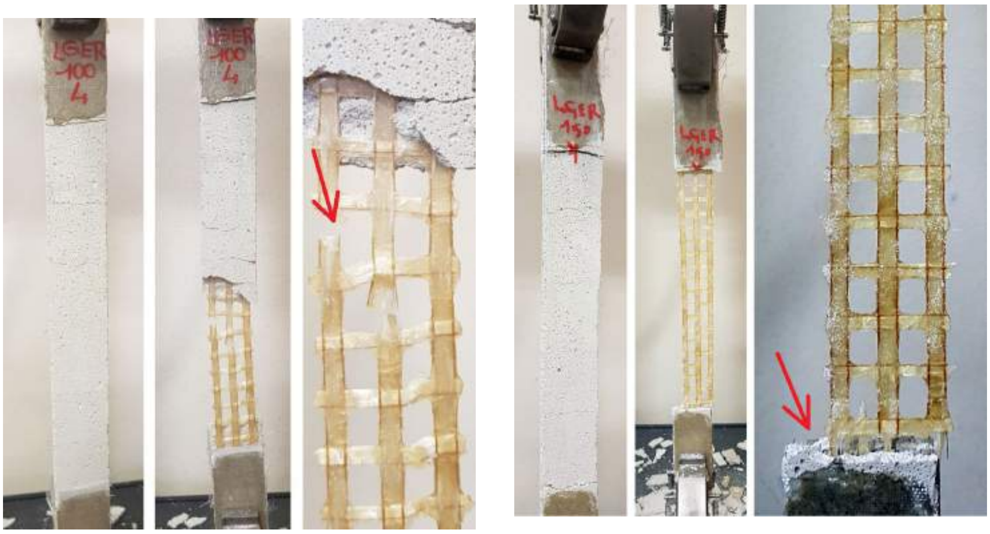

(a) Fabric failure

(b) Fabric slippage within the matrix and near the clamps

Figure 4.21: Typical failure modes observed for all groups

In fact, aliphatic amines allow curing at room temperature, whereas aromatic amines usually require a high-temperature treatment to achieve full conversion. However, aromatic amine-cured systems can be applied at temperatures sensibly higher than those which are compatible with aliphatic amine-cured resins [Harper 2003, p.168]. The completion of the curing process and the high thermal stability that is typical of amine-cured epoxy resins are likely responsible for the increase in mechanical properties (elastic modulus and strength) that is observed in the epoxy-coated G-TRM composite materials that were treated at temperatures not exceeding 150 °C. At higher temperature, degradative phenomena are likely to outweigh the benefit conveyed by post-curing.

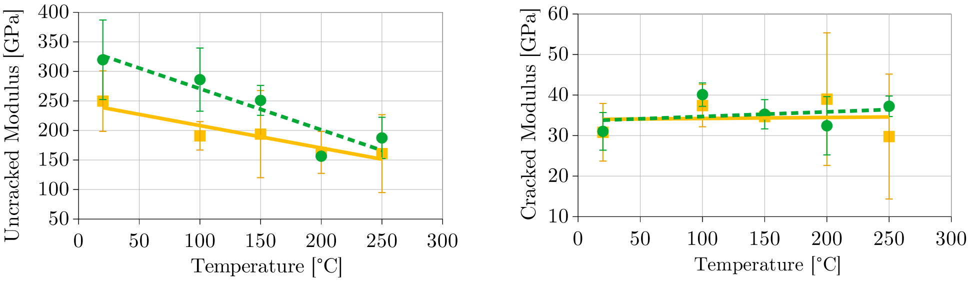

Figure 4.22: Uncracked (left) and cracked (right) modulus as a function of the exposure temperature for ER (circles, green) and EW (squares, yellow). ±1 standard deviation bands and linear curve-fits are also given

4.3.3.3 Failure analysis

Fig.4.21 illustrates progression to the two typical failure modes: either fabric rapture (a) or fabric slippage inside the matrix (b). Although, generally, both of them occur in mixed proportion in all test groups, fabric failure is far more frequent in the control group, while fabric slippage prevails in the specimens exposed to high temperature.

4.3.4 Discussion

Fig.4.22 illustrates the effect of temperature on the uncracked modulus E_f^* and on the cracked modulus E_f in the EW and in the ER group (see [ICC AC434 2013, Arboleda 2014a] for the details of moduli definition and evaluation). It may be observed that temperature exposure strongly impairs the uncracked modulus E_f^*, while the cracked modulus E_f remains statistically unaltered. This is compatible with the expectation that temperature affects the coating performance, whose bearing is mostly relevant when the matrix is still collaborating with the fabric and thereby uncracked. Furthermore, although ER coating performs significantly better than EW, line fitting suggests that this advantage decreases with temperature until equal performance is met at T =250 °C. Conversely, the cracked modulus E_f reflects the modulus of the glass fabric, which is little affected by temperature. In fact, the cracked modulus is about the same across all groups.

Transition points (TPs) conventionally mark a sudden stiffness loss and a regime shift, in light of the fact that the cracked matrix ceases to contribute to the composite rigidity. Their location is shown in Fig.4.23 at different temperatures. This figure indicates that the transition stress nearly halves on high temperature exposure, irrespectively of the temperature value, in the EW group. Conversely, the ER group presents a similar transition point location for ER-100 and, remarkably, higher transition stress and strain for ER-150, with respect to the control group. Temperature adverse influence starts to manifest itself at 200 °C, when stress is impaired (−37.5%) and yet strain is still higher than in the control group. Finally, at 250 °C, strain drops and it reaches the value for the control group. It is concluded that temperature generally decreases transition stress but it may improve transition strain.

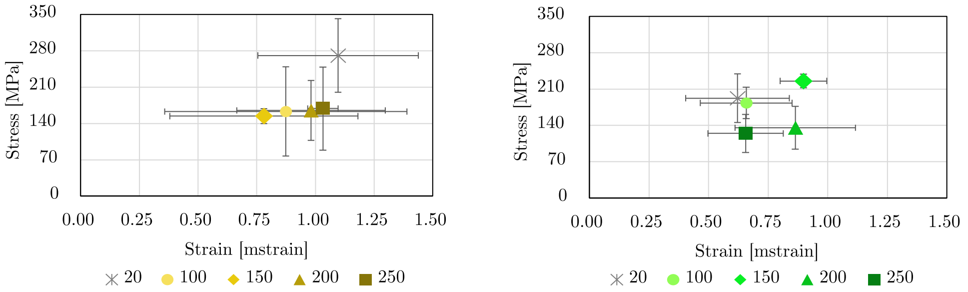

(a) EW group *(b) ER group*

Figure 4.23: Mean transition point location and ±1 standard deviation bars as a function of temperature for all test groups

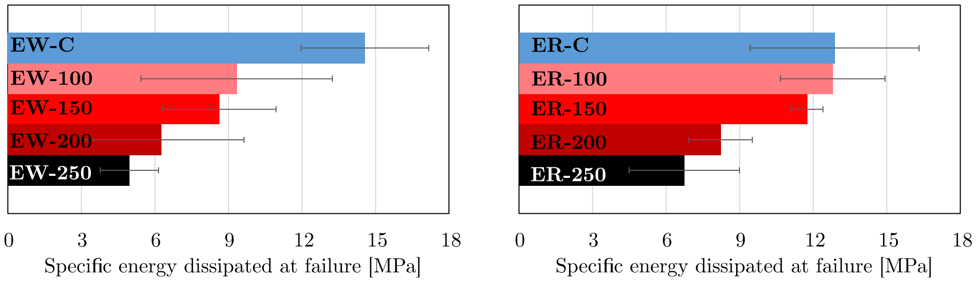

(a) EW groups *(b) ER groups*

Figure 4.24: Mean specific energy dissipated at failure W and ±1 standard deviation bars for the control (C, blue) and the heat treated groups at 100 °C (light red), 150 °C (red), 200 °C (dark red) and 250 °C (black).

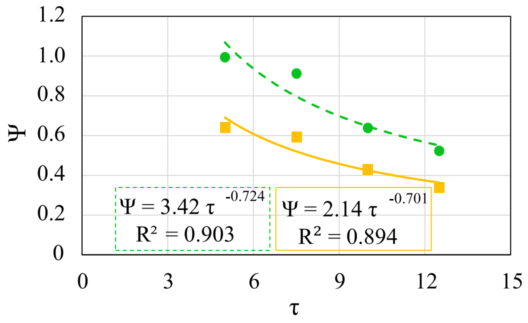

Figure 4.25: Normalized specific energy dissipated at failure $\Psi = W/W_0$ against normalized exposure temperature $\tau = T/T_0$ for ER (circles, green) and EW (squares, yellow) and power-law curve fit. $T_0 =$ 20 °C is the ambient temperature and $W_0 = W(T_0)$ is the corresponding dissipated energy.

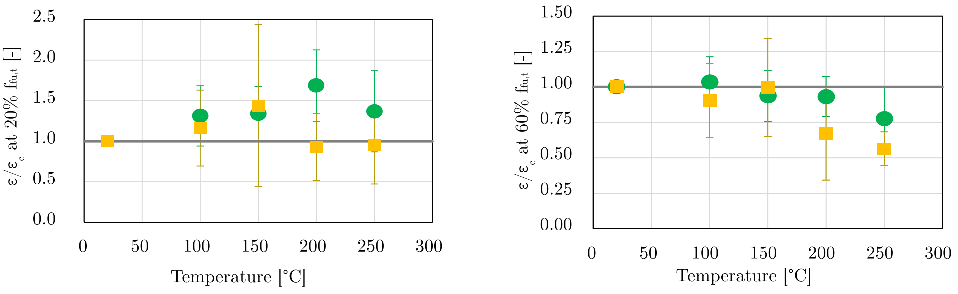

(a) 20% of UTS

(b) 60% of UTS

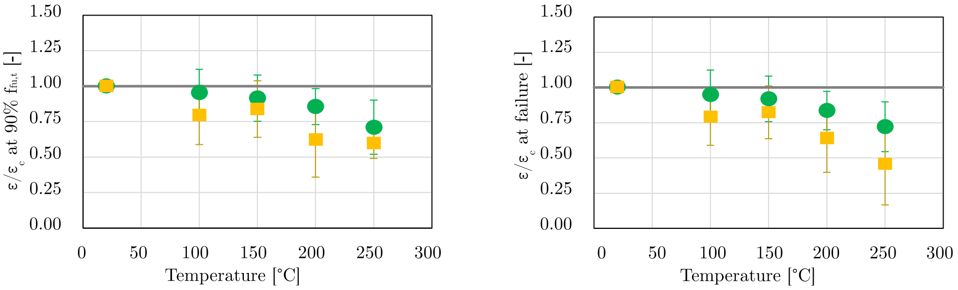

(c) 90% of UTS

(d) 100% of UTS

Figure 4.26: Ratio of the group mean elongation ε to the relevant control group elongation ε_C at a fraction of the corresponding UTS as a function of temperature for ER (circles, green) and EW (squares, yellow)

Comparison in terms of specific (per unit fabric volume) dissipated energy W is carried out in Fig.4.24. It appears that high temperature impairs energy dissipation in all test groups, with the possible exception of ER-100 which behaves similarly to the relevant control group. Remarkably, both coatings decay with an almost identical power-law rule, as illustrated in Fig.4.25 in terms of normalized quantities with respect to the ambient conditions. This finding is compatible with a cumulative Weibull distribution for the relaxing and breaking of the intermolecular bonds in the resin, as described in the model proposed by [Mahieux 2001], and it suggests that mechanical performance is indeed impaired by the mechanism of resin degradation. Conversely, hyperbolic tangent models, as in [Gibson 2006, Eq.(5)], do not seem to fit well experimental data.

Fig.4.26 presents the behaviour of the relative ductility across all test groups against temperature at different fraction of the UTS. Relative ductility is expressed as the ratio of the mean group strain $\varepsilon_i(f)$, $i \in \{\text{ER,EW}\}$ over the mean control group strain $\varepsilon_C(f)$, when specimens are subjected to a traction force f which is a fraction of $f_{ui}, i \in \{\text{ER,EW}\}$, that is the UTS for the relevant group. It is clearly seen that the higher the temperature of conditioning, the more brittle specimens behave, with the single exception of 20% loading, see Fig.4.26(a). However, for any temperature and loading fraction, ER outperforms EW in a statistically significant manner. It is worth emphasizing that the EW group is connected to superior energy dissipation capability in the control group, as compared to the ER group. This advantage at ambient temperature can be traced back to the EW coating layer being significantly thinner [Messori 2018]. Therefore, it may be argued that coating thickness is unfavourable in terms of ambient temperature mechanical performance, yet it is advantageous when high temperature exposure is envisaged.

4.3.5 Conclusive remarks

This section reports on the influence of the epoxy coating thermo-physical properties on the mechanical performance of AR-glass textile reinforced mortar (TRM) after exposure to high temperature. As in [Messori 2018], two epoxy coatings are considered, which differ by the hardening agent alone. Nonetheless, this difference brings about distinct thermo-physical properties. Since focus is set on the epoxy coating, exposure temperatures are limited to 250 °C to prevent thermal effects from extending to the lime mortar and, eventually, to the glass fabric. Mechanical performance is assessed according to AC434 through uni-axial tensile tests of rectangular coupons. The effect of temperature exposure in terms of first cracking strength and strain, ultimate strength and elongation, cracked and uncracked moduli, transition point location and energy dissipation capability is illustrated. It is found that temperature exposure may increase strength at the expense of ductility, and this outcome parallels similar findings obtained in the context of pull-out [de Andrade Silva 2014] and tensile [Rambo 2015] tests. DSC analysis reveals that temperature exposure may trigger competing processes: on the one side further cross-linking is favoured in a post-curing process, on the other side thermal degradation occurs. The final outcome strongly depends on the considered epoxy coating and its post-curing capability. Indeed, in contrast to the findings reported in [Donnini 2017], mild degradation is documented, especially when compared to FRP systems. Temperature induces a monotonic decay in the energy dissipation capability and, remarkably, the decay law, that is the same for both coatings, complies with a cumulative Weibull distribution (power-law rule). This behaviour is typical of models accounting for the relaxing and breaking of molecular bonds in resins, as in [Mahieux 2001, Gibson 2006]. Therefore, this observation supports the understanding that the resin degradation mechanism at the fabric-to-matrix interface governs mechanical performance for both coatings.

4.4 Design of epoxy viscosity for optimal mechanical performance

In this section, following a simplest possible approach, we consider coating by a single epoxy resin with different degrees of dilution in acetone. The aim is to resolve the effect of interphase strengthening as opposed to yarn penetration. Finally, a simple cost effectiveness analysis is presented according to which the optimal epoxy dilution places coated G-TRM alongside FRP in terms of cost-to-performance ratio [Signorini 2020a].

Table 4.8: Epoxy coating composition (normalized to 100 g *of DER + acetone), alongside polymer content by weight, w_r, with respect to the matrix, w_m*

Dilution degree	**D.E.R.**[g]	**Acetone** [g]	**DETA** [g]	**Resin** [g]	w_r/w_m [%]
0%	100	0	11.9	111.9	4.68
10%	90	10	10.7	100.7	4.31
25%	75	25	8.9	84.9	3.50
50%	50	50	6.0	56.0	1.33
75%	25	75	3.0	28.0	0.62
90%	10	90	1.2	11.2	0.23

4.4.1 Materials and methods

4.4.1.1 Materials

For better comparison, the same mortar and reinforcing fabric as in Sections 4.2 and 4.3 are considered. A commercially available premixed lime-based mortar (mortar M15, see Table 2.1) is considered as the embedding medium for the reinforcing fabric. Mortar characterization, through flexural and compression tests, is described in Section 2.2. A thermo-welded balanced open-square grid AR-glass woven fabric is employed as the reinforcing phase (see properties in Table 2.2). The zirconium oxide (ZrO_2) sizing of the fibres ensures stability in the alkaline environment.

Fabric coating As reported in detail in Section 4.1, AR-glass fabric is preliminarily treated with a coupling agent to enhance chemical compatibility with the epoxy coating. A 2% vol. aqueous solution of (3-Aminopropyl) triethoxysilane (99%, Sigma-Aldrich) is adopted. Successively, the functionalized fabric is coated with epoxy resin obtained from high-purity bisphenol A diglycidylether (D.E.R. 332, DOW Chemicals). The aliphatic hardener diethylenetriamine (DETA 99%, Alfa-Aesar) is adopted as curing agent (cf. labelled as "EW" in Section 4.2). Alongside the undiluted epoxy, 6 dilution degrees are considered for the epoxy precursor and, to this purpose, technical acetone ($(CH_3)_2CO$, Incofar Srl) is adopted at 10, 25, 50, 75 and 90% weight ratios. To reduce the viscosity of the solution, D.E.R. is mixed with acetone on a magnetic stirrer at 50 °C. The solution is subjected to ultrasonication for 5 min to promote homogenization. Finally, the curing agent is added and the solution is mixed for at least 15 min or until complete homogenization is reached. Successively, fabric sheets are immersed in the epoxy resin and than laid to harden for 7 days on a polypropylene support at ambient temperature. Fabric sheets are weighted before and after coating, in order to determine the polymer-to-matrix weight fraction w_r/w_m. Results are presented in Table 4.8, which gathers the dilution degrees investigated in the present work. It is noteworthy that the polymer weight fraction never exceeds the 5% threshold (see also the guidelines [ACI 549.4R-13 2013]). Besides, polymer content decays exponentially with dilution, which result is in accordance with the findings of Section 4.4.3.2.

Figure 4.27: Rheometer test set-up

Specimen manufacturing Following Annex A of ICC AC 434 [ICC AC434 2013], 1-ply rectangular coupons are cast on an individual basis (see. Section 2.3.1).

4.4.2 Experimental investigation

4.4.3 Uni-axial tensile tests

Uni-axial tensile tests are performed according to ICC AC434 [ICC AC434 2013], as detailed in Section2.3.2. As in standard practice, stress and strain obtained from the test are referred to the fabric cross-section, A_f, and to the gauge length, $L_g = 230\,\mathrm{mm}$,

$$\sigma = \frac{P}{A_f}, \quad \varepsilon = \frac{\delta}{L_g}. \tag{4.2}$$

Here, P and δ are the load and the corresponding displacement, as measured by the UTM and corrected by DIC to eliminate wedge grip elongation [Nobili 2016].

4.4.3.1 Optical and electron scanning microscopy

Optical investigation at 35x magnification is performed in a Leica EZ4D stereo-microscope to qualitatively assess the coating distribution and its effect on inter-phase adhesion. A scanning electron microscope (SEM) Quanta-200 (Fei Company, The Netherlands) is also employed.

4.4.3.2 Rheometer analysis

Resin viscosity is measured, for different dilution degrees, through a HAAKE RS100 Rheostress rheometer (Fig.4.27), that applies to the fluid a nominal tangential stress, τ, at constant temperature (37 ± 1)°C. This temperature is chosen as to represent the actual conditions of fabric impregnation. The test program consists of an ascending ramp plus a descending ramp for the applied torque.

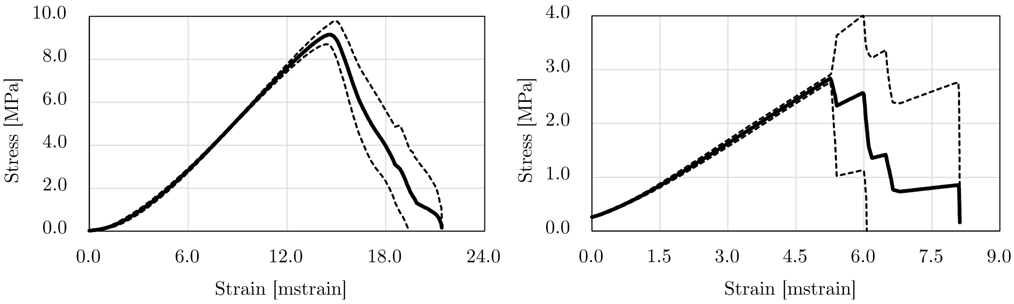

(a) *(b)*

Figure 4.28: Mean stress-strain curve with ±1 standard deviation bands for compression (a) and bending (b) of lime mortar prisms

Table 4.9: Mechanical characterization of the lime mortar according to [UNI EN 1015-11 2007]. $\mu(f)$, $\varsigma(f)$ and $(f)_k$ are the mean, the standard deviation and the characteristic value of the (assumed normally distributed) stochastic variable f and they are connected through Eq.(4.3). $CV = \varsigma/\mu$ is the coefficient of variation

Characteristic **Unit**	$\boldsymbol{\mu(\cdot)}$ [MPa]	$\boldsymbol{\varsigma(\cdot)}$ [MPa]	$\boldsymbol{CV(\cdot)}$ [%]	$\boldsymbol{(\cdot)_k}$ (Eq.(4.3)) [MPa]
Compressive strength, f_c	9.2	0.5	5.4	8.2
Young Modulus, $E_{c,s}$ (Eq.(4.4))	802	41	5.1	723
Flexural strength, f_f	3.4	0.6	17.6	2.3
Flexural modulus, $E_{f,s}$ (Eq.(4.4))	539	13	2.4	512

4.4.4 Results and discussion

4.4.4.1 Mortar characterization

The mean stress-strain curves for compression and bending of lime mortar prisms are reported in Figs.4.28(a) and (b), respectively. Data scattering is provided by ±1 standard deviation bands and it appears remarkably narrow for both compression and bending. Table 4.9 gathers the mean value of the mortar ultimate strength, $\mu(f)$, as well as of the secant modulus, $\mu(E)$, together with the relevant standard deviation, $\varsigma(\cdot)$, and coefficient of variation, $CV(\cdot)$. The characteristic value $(\cdot)_k$ is evaluated as for a normal distribution (with the so-called "2-sigma-rule", used in conjunction with a 95% confidence interval [Fisher 1925])

$$(\cdot)_k = \mu(\cdot) - 1.96\ \varsigma(\cdot). \tag{4.3}$$

The elastic modulus is determined from the stress-strain curve as the slope of the secant line passing through $(\sigma_{0.6}, \varepsilon_{0.6})$ and $(\sigma_{0.9}, \varepsilon_{0.9})$, that are the stress-strain points at 60% and 90% of the ultimate strength [Arboleda 2014a]

$$E = \frac{\sigma_{0.9} - \sigma_{0.6}}{\varepsilon_{0.9} - \varepsilon_{0.6}}. \tag{4.4}$$

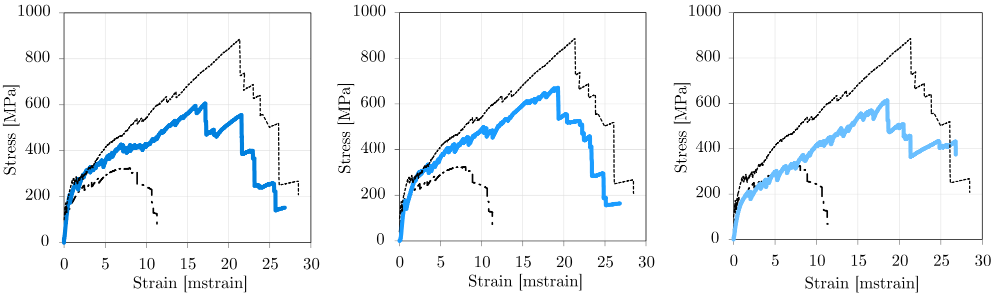

(a) 10%

(b) 25%

(c) 50%

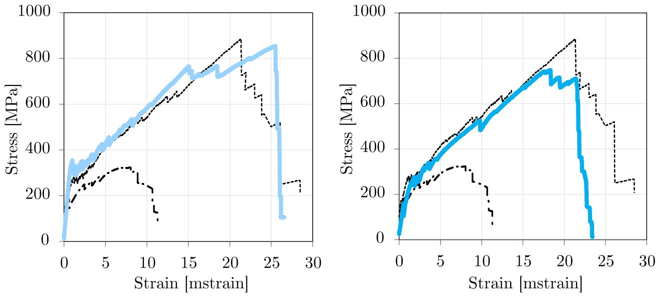

(d) 75%

(e) 90%

Figure 4.29: Mean stress-strain curves obtained in uni-axial tension of epoxy-coated G-TRM coupons for different dilution degrees (blue, solid lines), compared to the uncoated (black, dash-dotted lines) and to the undiluted (black, fine dashed lines) groups [Signorini 2019b]

4.4.4.2 Uni-axial tensile tests

Fig.4.29 presents the mean stress-strain curve for each coating group alongside two reference curves expressing the mean performance in the uncoated and in the undiluted (alias 0% diluted) epoxy group (the latter is taken from [Messori 2018]). Remarkably, it appears that epoxy dilution in acetone little impairs the mean mechanical performance, which remains way superior to that of the uncoated group, particularly in terms of ductility. Further, most unexpectedly, performance is not a monotonic decreasing function of the dilution degree and, after an initial descending trend, it raises again and it reaches or even exceeds the undiluted performance.

To take a better insight into this unexpected behaviour, Fig.4.30(a-b) presents the mean ultimate tensile strength (UTS) and strain for all groups alongside ±1 standard deviation bars. Looking at this figure, two interesting observations can be made:

1. the mean ultimate performance is a decreasing/increasing/decreasing function of epoxy dilution, which attains a local minimum at $10 \div 25\%$-dilution and then raises up to a local maximum that occurs at 75% for strength and at 50% for strain;
2. strikingly, this maximum strength appears best performing (i.e. it is an absolute maximum), although it occurs in the presence of wider scattering when compared to the undiluted group;

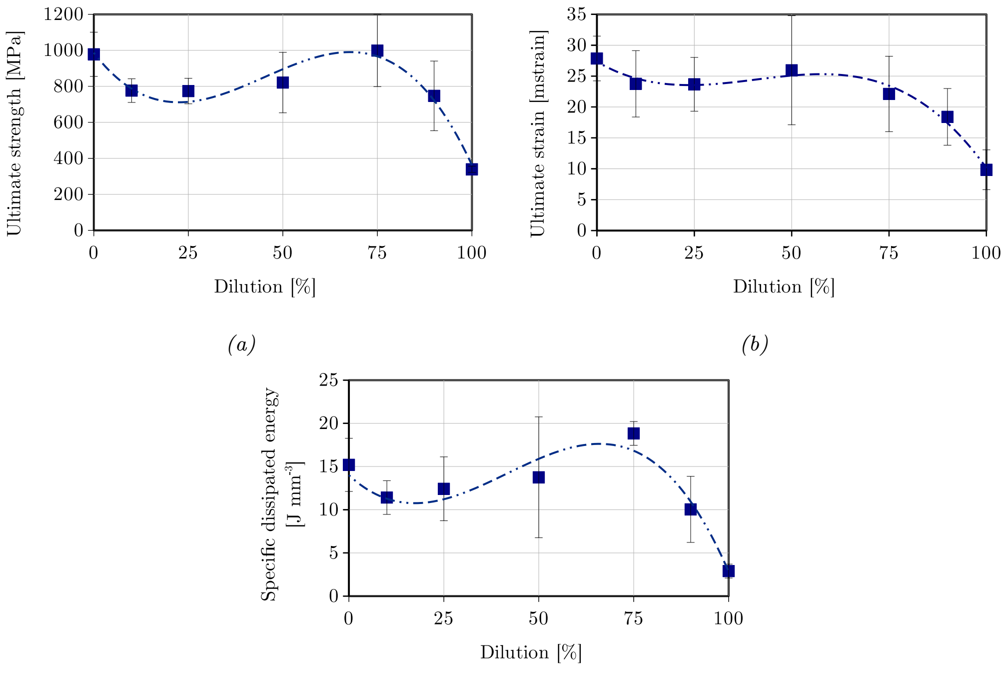

(a) *(b)*

(c)

Figure 4.30: Mean ultimate strength (a), strain (b) and energy dissipation per unit volume (c) as a function of the dilution degree. ±1 standard deviation bars and cubic curve-fits are also plotted

3. data scattering is not monotonic increasing either and it is relatively stable across the groups.

It is important to emphasize that dilution affects strength and strain in a similar manner, which fact is a good indication that an underlying phenomenon is consistently being captured. Indeed, the same trend is confirmed by looking at the dissipated energy at failure, that is evaluated as the mean, within each group, of the area under the stress-strain curve. In this respect, 4.30(c) is even more surprising, for best performance is again associated with 75% dilution and yet it now exceeds by more than 30% that of the undiluted group, while possessing remarkably narrow data scattering. This behaviour seems to suggest that a threshold dilution exists which triggers a beneficial effect on performance and scattering. This effect competes against and eventually overcomes the expected degradation of the epoxy coating associated with resin dilution.

Fig.4.31 plots the first cracking strength (FCS) and strain and once more it supports the assumption that dilution has a mixed bearing on mechanical performance. Here, however, the picture is less clear cut, owing to the uncertainty that is associated with the identification of the transition point. Indeed, transition point location is charted in Fig.(4.32) and it is interesting to observe that the highest stress and the least scattering again occurs at 75% dilution. Fig.4.33 shows the uncracked and the cracked elastic moduli, which reflects the matrix (see Tab.4.9) and the fabric moduli, respectively. As expected, little dependence on the dilution

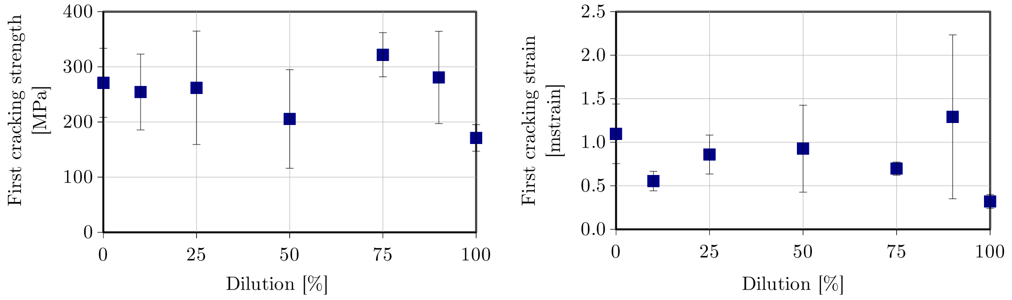

(a) FCS

(b) Cracking strain

Figure 4.31: Mean first cracking strength (a) and strain (b) as a function of the dilution degree, with ±1 standard deviation bars

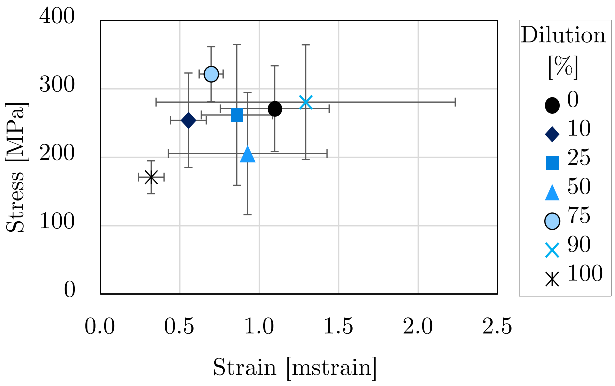

Figure 4.32: Transition points (TP) location as a function of the dilution degree with ±1 standard deviation bars

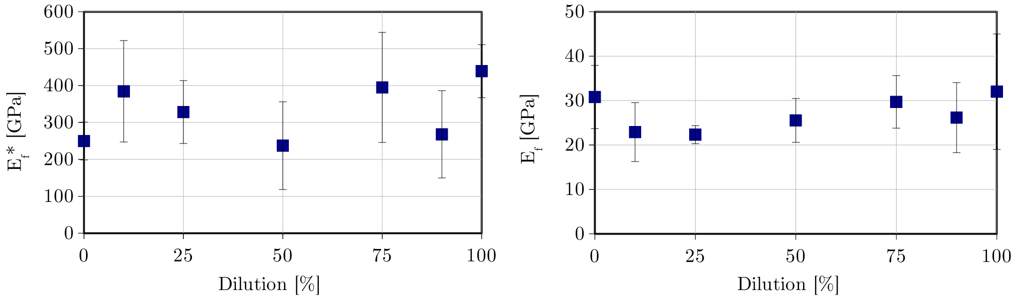

(a) Uncracked modulus

(b) Cracked modulus

Figure 4.33: Mean uncracked (a) and cracked (b) moduli as a function of the dilution degree with ±1 standard deviation bars

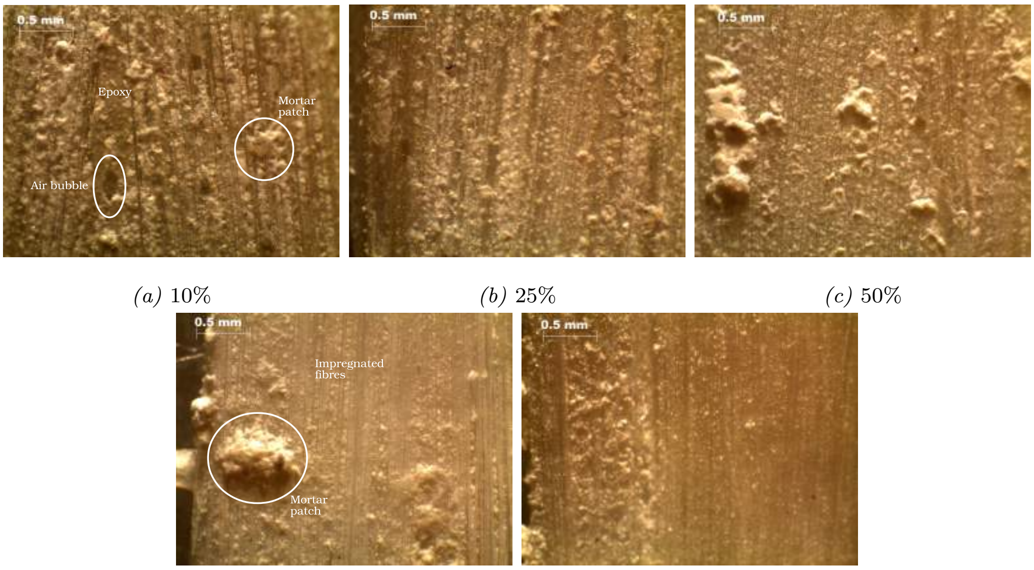

(a) 10% *(b)* 25% *(c)* 50%

(d) 75% *(e)* 90%

Figure 4.34: Optical microscopy of the fabric after failure at 35x magnification

grade is demonstrated and yet the underlying trend can still be appreciated.

4.4.4.3 Optical and Scanning Electron Microscopy

Fig.4.34 presents the outcome of optical investigation of failed specimens at 35x. The effect of dilution emerges with great clarity in that individual fibres within the fabric yarn can only be appreciated at high dilution degrees, and to these fibres large mortar patches adhere. In contrast, at low dilution, fibres are deeply embedded in a sizeable lump of epoxy resin (that traps several air bubbles) to which only small mortar patches can adhere. Evidently, mortar adhesion occurs mainly at 50% and 75% dilution.

Along the same line and yet with greater detail, Fig.4.35 displays the outcome of SEM microscopy at 1000x. Indeed, at low dilution, scanty fibres emerge from the resin block which mainly surrounds the external filaments of the yarn, the so-called sleeve. To this block, scattered mortar patches adhere. In contrast, dilution reveals the glass fibres within the yarn, that the epoxy is eventually capable of penetrating. The coating thickness is substantially reduced to a thin layer to which mortar patches are diffusely attached. This adhesion is perhaps of poorer quality, yet it extends well inside the core of the fabric yarn and the surface area involved is greatly enlarged (Fig.**??**, right sketch). Besides, telescopic failure, that is failure by sleeve filaments sliding over the core, is prevented. The dilution degree that triggers filaments penetration is the threshold level that significantly enhances mechanical response. Competing with this positive effect is the reduction of the epoxy content due to dilution, that weakens interphase adhesion and negatively affects performance. Of course, a mixed response is exhibited for intermediate dilution

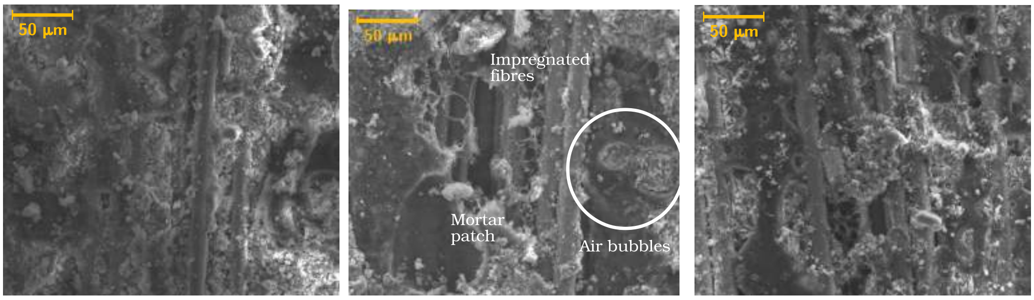

(a) 10% *(b)* 25% *(c)* 50%

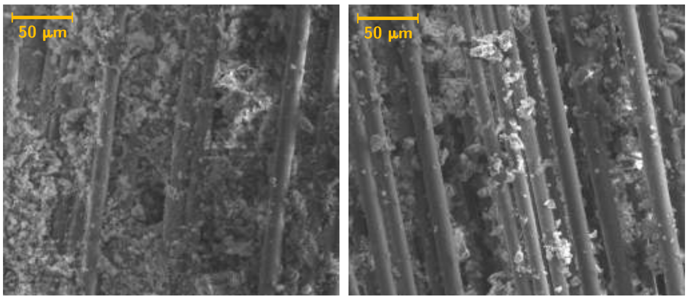

(d) 75% *(e)* 90%

Figure 4.35: SEM of the fabric after failure at 1000x magnification

degrees.

4.4.4.4 Viscosity curve

It is most striking that the beneficial effect of epoxy resin penetration in the yarn core occurs almost suddenly and at an unexpectedly large dilution degree. Indeed, the dilution threshold is located around 3 : 1 acetone to epoxy weight ratio. This outcome may be traced back to the exponential decay of epoxy viscosity as a function of acetone dilution d. Fig.4.36 plots the mean viscosity, $\mu(\eta)$, normalized to acetone viscosity η_1, superposed onto the exponential fit (logarithmic scale)

$$\mu(\eta) = \eta_1 \exp\left[-6.613(d-1)\right], \tag{4.5}$$

where $0 \leq d \leq 1$ is the dilution degree. The viscosity at $d = 1$ (i.e. the uncoated group) is let equal to acetone viscosity, namely $\eta_1 = 0.28\,\mathrm{mPa}\cdot\mathrm{s}$ [Kaye 1966]. The fit shows good correlation ($R^2 = 0.9518$).

4.4.5 Resampling analysis

We begin by considering the question whether the different behaviour that we see across the test groups is due to sampling or rather reflects some intrinsic variance. For this, we carry out a permutation test on the total count [Good 2013] and results are given in Tab.4.10. The permutation test works as follows: we compare two dilution groups, namely 0%, that is the reference group, and y% and for this we

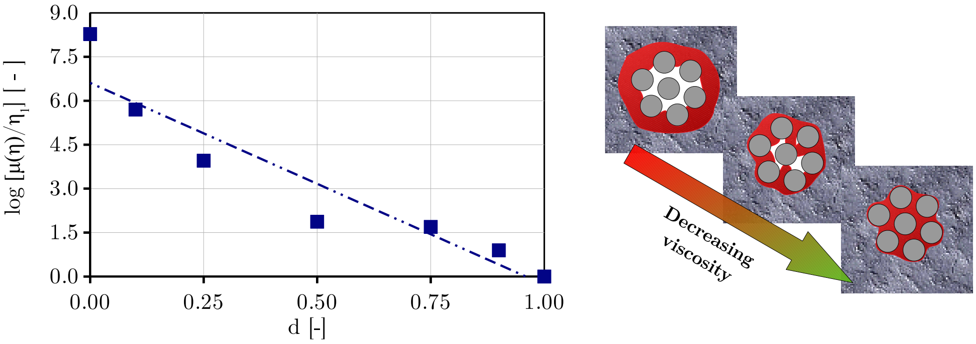

Figure 4.36: Viscosity measurement in logarithmic scale at 37 °C *as a function of the dilution degree. An exponential curve-fit is also proposed* ($R^2 = 0.95$)*. On the right side, schematic of the penetration of epoxy resin (red) in the voids between the filaments (gray) within the fabric yarn.*

Table 4.10: Permutation test results

Dilution	probability of exceedance [%]		
$100d$ [%]	UTS	Strain	Energy
10	1.0	7.8	1.8
25	0.4	9.8	8.4
50	8.2	30.6	31.2
75	53.6	46.2	89.2
100	4.0	0	4.2

bring them together in the set A_y. Then, we form $N = 500$ permutations with repetition of 5 elements of A_y and, for each of these, we compute the total count (sum of the elements) s_k, $k = 1, \dots, 500$. We count the number of permutations whose total count exceeds that of the reference group 0% and divide by N. We expect that, when difference is due to sampling, the total count of any permutation is located above/below the reference count 50% of the times. We see that this is never really the case for any group, although it may occasionally occur for a single characteristic. For instance, considering UTS and ultimate strain, we see that the reference group and $y = 75\%$ dilution are statistically equivalent, yet the latter still dissipates significantly more energy than the former. We conclude that results are statistically meaningful and an underlying process is being captured.

Next, we carry out a resampling analysis for each dilution group and consider the statistics of 5000 permutations with repetition of the original dataset. Fig.4.37 plot the mean UTS and ultimate elongation, normalized to the corresponding mean of the original sampling in the undiluted group, respectively f_0 and ε_0, superposed onto a cubic curve fit of the form (likewise for strain)

$$\mu(f) = f_0 \left[1 + (f_1 - 1)x + a_2 x(x-1) - a_3 x(x^2 - 1)\right], \tag{4.6}$$

where f_1 is the mean of the resampled uncoated group. A cubic curve-fit is chosen because $d \leq 1$ and any curve-fit turns into a polynomial in a Taylor sense. Remark-

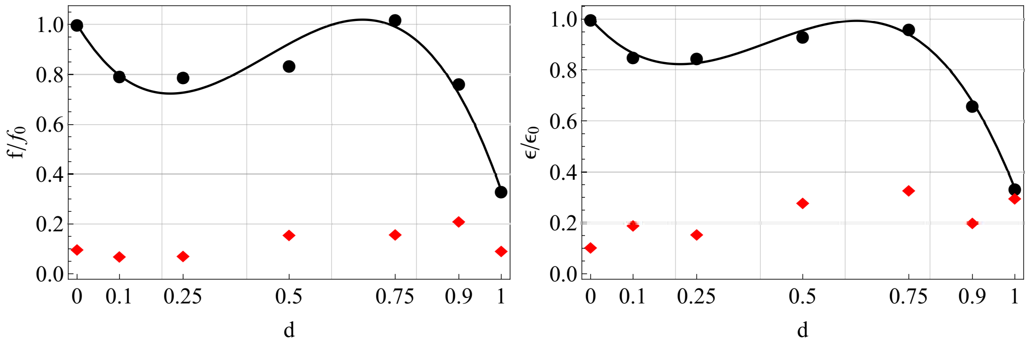

(a) UTS f

(b) ultimate elongation ε

Figure 4.37: Resampled mean tensile ultimate strength and elongation (black, circles) with mean CV (red, diamonds) as a function of the dilution degree d, normalized to the corresponding mean of the original sample for the undiluted group, respectively f_0 and ε_0. The cubic curve fit (4.6) *is also shown*

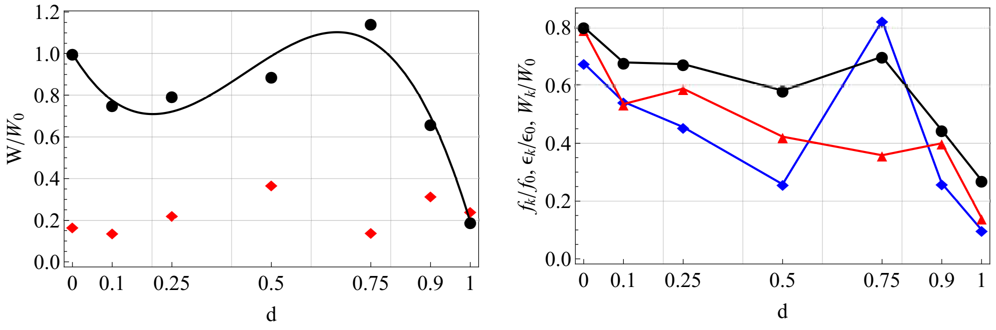

(a)

(b)

Figure 4.38: Resampled mean dissipated energy at failure W (black, circles) and mean CV (red, diamonds) (a) and characteristic ultimate strength (black, circles), strain (red, triangles) and dissipated energy (blue, diamonds) (b) as a function of the dilution degree, normalized to the original sample mean dissipated energy of the undiluted group, W_0

ably, upon normalization, strength and elongation follow a very similar trend, whose resemblance supports the fact that a physical process is being portrayed. Besides, unless a very large dilution degree is adopted, performance rests above 80% of the uncoated group, before falling off steeply beyond 75% dilution.

Figs.4.38(a) presents the resampled dissipated energy at failure W, normalized to the mean dissipated energy W_0 in the original undiluted sampling, and it shows that a 14% performance gain over the undiluted group is achieved at 75% dilution, that is accompanied by a very small CV. This behaviour, that seems to contrast that observed for strength and strain, may be explained noting that these are contravariant statistical variables, in the sense that when one increases, the other decreases and yet their ”product” (i.e. the energy) remains the same.

With the resampling size $N = 5000$, the population distribution is close to normality and we may safely consider characteristic values according to Eq.(4.3). Fig.4.38(b) presents the characteristic ultimate strength, strain and dissipated energy, normalized with respect to the corresponding *mean* value in the original sample

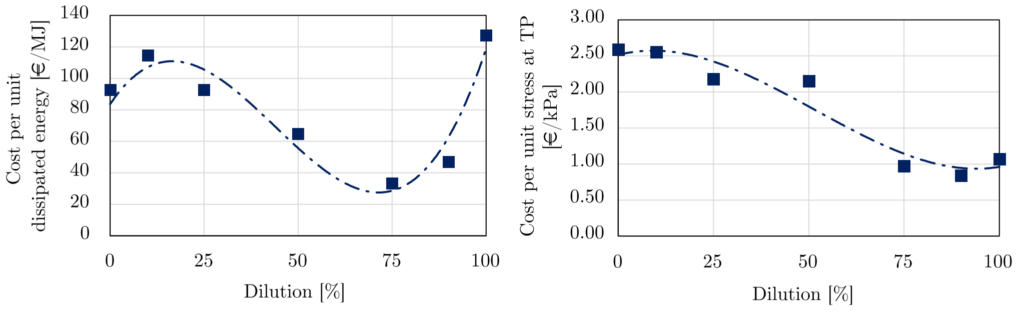

(a) *(b)*

Figure 4.39: Mean cost per unit dissipated energy at failure (a) and per FCS (b) as a function of the dilution degree. A third-order polynomial curve-fit is also proposed.

of the undiluted group. We see that dilution has a significant negative effect on the characteristic ultimate strain, which drops in monotonic fashion. This is due to increasing standard deviation, see Fig.4.37(b). Conversely, strength and energy recover significantly at 75% dilution to the point that they behave almost as or better than the undiluted group. Such results support the idea that optimizing epoxy dilution and epoxy viscosity conveys remarkable benefit in terms of performance-to-cost efficiency.

4.4.6 A simple cost-effectiveness analysis

Fig.4.39(a) shows the total cost of raw materials per unit dissipated energy at failure. The material cost is a decreasing function of dilution, for acetone is far cheaper than epoxy, yet performance loss produces a competing trend. As expected, an absolute optimal point is met in correspondence of 75% dilution, where a 64% (74%) reduction in the cost-to-performance ratio is achieved, with respect to the undiluted (uncoated) group. Within this comparison, the undiluted group is only 37% better performing than the uncoated group, despite the vastly superior mechanical performance, see Fig.4.38. Unexpectedly, cost normalization in terms of FCS leads to a monotonic decreasing function, i.e. the cost reduction associated with dilution outweighs the performance decay in terms of FCS, see Fig.4.39(b). This result, among others, may justify the marginal diffusion of epoxy coating in the current TRM technology landscape.

Fig.4.40 presents an all-around cost-to-performance comparison among different strengthening and retrofitting technologies, in terms of mean material cost per unit dissipated energy. Costs for FRP and steel mesh are taken from 2018 data officially provided in [Camera di Commercio di Modena 2018]. FRP dissipated energy is obtained referring to the mean ultimate stress-strain values, as given by [CNR TD200-R1 2013], and restricting the analysis to the linear regime. Mechanical response of steel is assumed to follow a bilinear model, with an initial elastic response until yield, followed by a linear hardening plastic phase until failure. Data for high-tenacity (HT) carbon (C) and basalt (B)-TRC are taken from [Signorini 2018a].

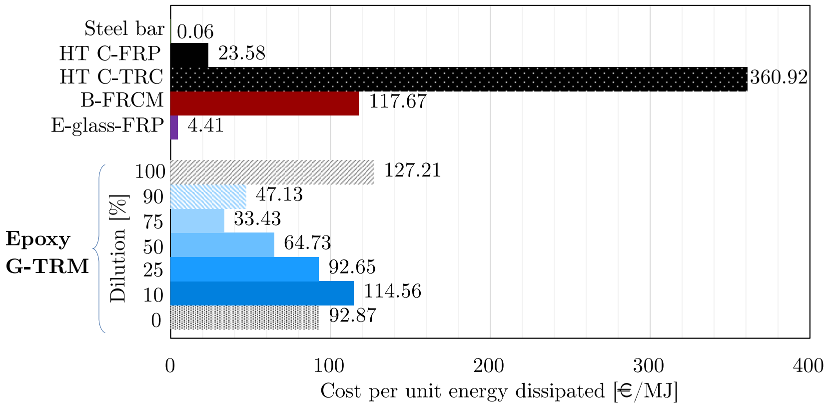

Figure 4.40: Comparison among strengthening and retrofitting technologies in terms of cost per unit dissipated energy (HT : high-tenacity, C : carbon, B : basalt, FRCM : fabric reinforced cementitious mortar)

According to Fig.4.40, strengthening technologies may be ranked as follows. First, steel appears to be the best performing by far, manly in consideration of its marginal cost. This obvious result, which accounts for the large adoption of reinforced concrete, should be weighed against other design constraints, such as durability and feasibility. Then, FRP follows, in light of its low cost compared to the outstanding mechanical performance. Glass TRM comes third and we see that dilution is capable of dramatically reducing the cost-to-performance ratio to an extent that is comparable with high tenacity carbon FRP. In fact, 75% dilution produces an outstanding three-fold reduction in the cost-to-performance index compared to the undiluted group. Of course, different performance indices may be considered and costs greatly vary across countries, but the general idea that diluted epoxy coating may significantly increase the interest in TRM composites still holds. Basalt and carbon FRCM come last, although they score similarly to epoxy coated TRM. However, mechanical performance is generally little reliable in the absence of interphase strengthening [Nobili 2017a].

4.4.7 Conclusive remarks

The results of mechanical uni-axial traction tests on epoxy coated AR-glass Textile Reinforced Mortar (TRM) specimens are presented. Spotlight is set on the role of the epoxy coating and its ability to penetrate the glass filaments within the yarn. To this aim, epoxy is diluted with acetone at $10, 25, 50, 75$ and 90% weight ratios and performance is compared to that of undiluted and uncoated fabric. It is found that the effect of dilution is two-fold: on the one hand it decreases the interphase strength and yet, on the other hand, it decreases viscosity exponentially and therefore enhances the epoxy penetration capability. These two effects are competing and, as a result, an optimal formulation is defined. Most remarkably, filament penetration occurs at a unexpectedly high dilution degree and it takes place through a rapid surge of mechanical performance. This burst is so intense that it compensates interphase weakening, to the extent that performance gets close to or even exceeds that of the undiluted specimens. This trend consistently emerges in the first cracking strength and strain, in the energy dissipation capability, in the cracked and uncracked moduli and in the turning point location alike. Besides, a simple cost-effectiveness analysis shows that dilution leads to a very substantial material cost reduction, which places this technology on an efficiency level comparable to that of FRPs. It is concluded that careful engineering of the epoxy coating can significantly contribute to the improvement of the overall performance of glass TRM composites.

Chapter 5

Durability of inorganic matrix composites

Contents

5.1 The issue of durability in fibre-reinforced inorganic composites

Inorganic matrix composite materials, such as Fabric Reinforced Cementitious Matrix (FRCM) or Textile Reinforced Concrete/Mortar (TRC/TRM), are a new class of composite systems that is gaining grounds for structural rehabilitation and retrofitting [Brameshuber 2006, Koutas 2019].

After two decades of extensive research, the role of FRCM/TRC as strengthening systems is currently shifting from R&D to the application stage. This evolution is supported by the appearance of new code guidelines, such as the recently approved Italian specifications [CNR DT215 2018] and acceptance criteria

[Consiglio Superiore dei Lavori Pubblici 2019], which follow upon the already established [ICC AC434 2013] and [ACI 549.4R-13 2013]. One important issue, that is discussed in these guidelines, concerns the performance decay associated to exposure to aggressive environments. In fact, following [Mobasher 2011], ”a major challenge is in incorporating durability test methods into a standard acceptance test protocol”. Although ACI and Italian guidelines agree on the conditioning regimes to be considered for durability assessment (see [Donnini 2019]), they take a different stance on how to move from test data to design values. Beside experimentation, ACI does not provide specific prescriptions for taking into account performance reduction as a result of aggressive environment exposure. In contrast, the Italian regulation introduces a *environmental conversion factor* η_a for reducing design values [CNR DT215 2018, §3.2], in analogy with the approach already proposed for FRP [CNR TD200-R1 2013, §3.5.1]. In fact, in the lack of specific tests, it provides the one-fits-them-all coefficient $\eta_a = 70\%$, common to all aggressive environments. Interestingly, this is precisely the factor attached to exposure to aggressive environments of aramid/epoxy FRP and should be confronted with $\eta_a = 85\%$ assumed for carbon/epoxy FRP [CNR TD200-R1 2013, Table 3-2]. Consequently, according to the Italian regulation, FRCM/TRC are no better performing than FRPs in aggressive environments in general. This is particularly remarkable if one considers that ”better long-term durability” is credited among the major assets of FRCM/TRC systems [Nanni 2012]. In this work, we show that this stance is not always justified in terms of design values.

Only a small number of papers have appeared in the literature discussing the performance decay of FRCM/TRC systems associated to exposure to aggressive environments. Indeed, according to the recent review by [Koutas 2019], ”Future work in this field should be directed at [..] understanding the durability of the strengthening system”. Furthermore, opposing results are sometimes encountered.

In her interesting dissertation, [Arboleda 2014a] investigates the tensile strength of PBO and carbon FRCM 1-ply coupons after immersion in alkaline and saline solutions, and after exposure to water vapour and freeze-thaw cycles. Unexpectedly, performance appears consistently unaffected by exposure, if not enhanced. In fact, [Arboleda 2014b] write ”Results indicate there are no significant degradation concerns for the environments cited. On the contrary, strength improvements are noted on most exposures probably due to continued hydration after 28 days”. [Nobili 2016] considers tensile performance of AR-glass FRCM coupons after immersion in a saline or alkaline solution. Consideration of the effect on the isolated components, namely dry fabric and lime mortar, shows that exposure little affects AR-glass. Indeed, this result parallels the findings of [Purnell 2000], for glass reinforced cement (GRC), of [De Santis 2015b] and [Micelli 2019] for dry fabric in alkaline environment. In fact, exposure mainly impairs the lime mortar and this, in turn, promotes delamination failure and large data scattering. Exposed specimens present a residual strength that is roughly 75% of that pertaining to the control group, *in the mean.* Although this appears in line with the conversion factor given by the Italian regulation, consideration of *design values* offers a different perspective. Recently, [Donnini 2019] presented a durability analysis of AR-glass FRCM after immersion for 1000 hours in a saline solution or in water at 60 °C. Single shear-bond tests show that adhesion to a fire clay support is reduced by more than 20% (surprisingly, relative data scattering is decreased in the exposed groups) and the hydraulic mortar is little affected by exposure. Indeed, dry glass fabric performance is reduced by more than 30% in the mean. A likely explanation of this result may be traced to the exposure temperature, that is sensibly higher than that suggested by the guidelines (namely 23 °C). In fact, [Micelli 2019] point out that ”a maximum temperature should be individuated in conditioning protocols, otherwise unreal detrimental effects could be produced”. In their work, they assess the tensile strength of E- and AR-glass, carbon, basalt, PBO and steel strands extracted from dry fabrics after exposure to different alkaline environments at various temperatures, the latter designed as to simulate different service life spans. They find that ”E-glass fibres and basalt fibres confirmed to be highly sensitive to the alkaline environments”, while ”carbon and steel fibres did not exhibit a chemical vulnerability”. The protective role of a polymeric coating is also investigated. [De Santis 2015a] consider immersion for 15, 30 and 41.6 days of dry steel textiles in Substitute Ocean Water (SOW), presumably at laboratory temperature. They report that exposure produces negligible effect on the stress-strain curves and therefore propose $\eta_a = 95.5\%$ for the longest immersion. From this literature review, it clearly appears that durability is a complex function of fabric coating, matrix composition and curing time. Besides, to the best of the author’s knowledge, no all-around durability investigation is available concerning SRG. To conclude, only in the very last period, adequate building code provisions have been delivered and the incompleteness of them greatly hinders large scale project application of FRCM strengthening, which manly rely on ad-hoc experimental validation [D’Ambrisi 2013b, Pellegrino 2013, Stratford 2004, De Felice 2014, Nobili 2017a].

The effect of curing time and aggressive environment exposure on the mechanical performance in uni-axial tensile test of CFRCM coupons according to ICC indications is investigated. Indeed, while much work has been devoted to developing a sound knowledge of fabric bonding and pullout mechanisms [Banholzer 2006, D’Ambrisi 2013a, Carozzi 2015], limited data are currently available in the literature concerning FRCM durability [Butler 2009, Hempel 2007, Butler 2010, Arboleda 2014b, Nobili 2016]. Spotlight is set on assessing the composite design limits according to ICC design criteria for all test environments and curing times and on comparing such results with some established design protocol for FRP systems.

5.2 Materials and methods

5.2.1 Materials

All specimens considered in this analysis are manufactured according to Annex A of [ICC AC434 2013] using a commercially available pozzolan-based mortar, corresponding to mortar M5 of Table 2.1 and mortar B of [Nobili 2016]. As pointed

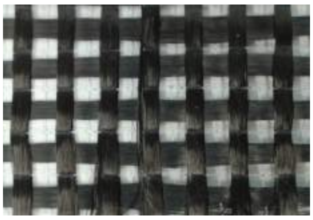

Figure 5.1: Carbon fabric grid

out in the introductory section, this semi-hydraulic lime provides excellent synergy with the impregnation agent and still good “breathability”. Besides, its fairly low-modulus makes it especially compatible with clay or masonry support [Nobili 2017a]. Reinforcement is provided by a square-grid carbon fabric (bi-axial reinforcing, Fig.5.1) whose main mechanical properties are given in Tab.2.2, labelled as "C1". While no dry polymer content is introduced in the matrix, bond formation is enhanced by fabric impregnation with a partially organic adhesion promoter [Nobili 2016, Signorini 2018b]. The same hybrid two-component adhesion promoter is adopted as a reference in Section 3, to be compared with totally inorganic silica nano-coating. As suggested by the presence of a polymeric binder, the adhesion at the fibre-to-matrix interphase is proven to be remarkably enhanced and telescopic failure hindered. The major drawback lies in its difficult application procedure. Indeed, the hybrid primer should be applied at the fresh state on the multifilament fabric just before lamination on the substrate. For this reason, in combination with its low viscosity, application can be a severe issue, especially when large surfaces or horizontal structures are to be strengthened (e.g. slabs, roofs concrete beams).

5.2.2 Composite material configuration and test procedure

Composite 1-ply carbon fabric reinforced mortar are manufactured as described in Section 2.3.1 and subjected to monotonic uni-axial tensile tests. The set-up and the parameters of the testing protocol are reported in detail in Section 2.3.2.

5.2.3 Test environments

Tab.5.1 describes the environments considered in this analysis. Coupons, that have been cured for either 28-days or 60-days in the laboratory environment, are immersed in an alkaline or saline solution and then stored at constant temperature for 1000 hours ($\approx$ 42 days) in a Memmert HPP110 climatic chamber [ICC AC434 2013]. The alkaline environment is a sodium hydroxide (NaOH) aqueous solution with 10 pH level. The saline environment (saltwater resistance) is a 3.5% weight sodium chloride (NaCl) aqueous solution, which amounts to the world’s ocean seawater average salinity [ASTM D 1141 2013]. Following [Kajorncheappunngam 2002], to better contrast the effect of the alkaline environment, immersion in 1-molar hydrogen chloride acid solution (diluted from hydrochloric acid HCl 37% RPE Carlo Erba) at room temperature is also considered (PH 2.5). Similarly, to better dis-

Table 5.1: Tested environments; room temperature is $21 \pm 2°C$ (70 ± 3.6 F)

Environment	**Curing** [days]	**Time of exposure**	**Temperature** °C	F
Control (CC28/CC60)	28/60	-	room	
Saline (SW28/SW60)	28/60	1000 hrs	23 ± 1	73 ± 2
Alkaline (AK28/AK60)	28/60	1000 hrs	23 ± 1	73 ± 3
Acid (HA28)	28	1000 hrs	room	
Distilled water (DW28)	28	1000 hrs	room	
Freeze-Thaw (FT)	28	20 cycles	$-18/37.7$	$0/100$

(a) *(b)* *(c)*

Figure 5.2: Optical microscopy investigation at 35x magnification: (a) control (b) saline (c) alkaline

tinguish between the detrimental effect of low/high-PH solutions and water immersion, the effect of distilled water at room temperature has also been investigated [ASTM D 2247 2002, ICC AC434 2013]. For the latter two types of environments, plain water and 1 M HCl, only 28-day cured specimens are employed. Furthermore, freeze-thaw cycles are also considered, according to which conditioned specimens are stored for 12 hours at constant temperature (37.7°C) and 100% relative humidity in the climatic chamber (thaw) and then moved into a freezer (−18°C) for at least 4 hours (freeze). A total of 20 freeze-thaw cycles have been performed [ICC AC434 2013, §4.4.1], after which specimens are stored at room temperature to complete the 28-day curing period. A minimum number of 5 replicates is considered for each test environment [ICC AC434 2013, Table 1]. Besides, temperature and humidity data recording was carried out at 0.2 sample/min rate for all test environments so that relevant prescribed oscillation bands could be verified.

5.3 Experimental investigation

5.3.1 Conditions of acceptance

Following [ICC AC434 2013, §4.5.2], control and exposed specimens have been visually examined at 5x magnification and little surface damage could be found. However, Fig.5.2 shows the effect of the aggressive environments on the specimen surface as it appears at 35x magnification. Indeed, the control specimen's clean and polished surface may be contrasted with the crystallized deposits and the grooves (erosion)

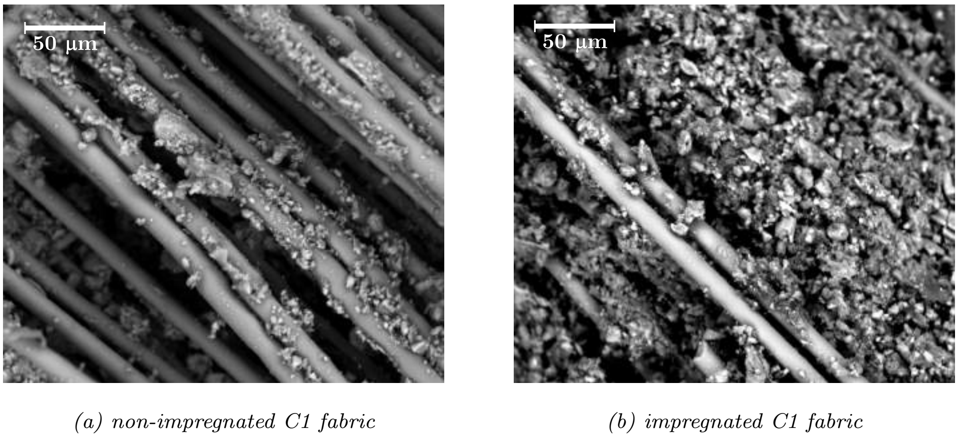

(a) non-impregnated C1 fabric *(b) impregnated C1 fabric*

Figure 5.3: SEM investigation: non-impregnated (a) vs. impregnated (b) carbon fabric

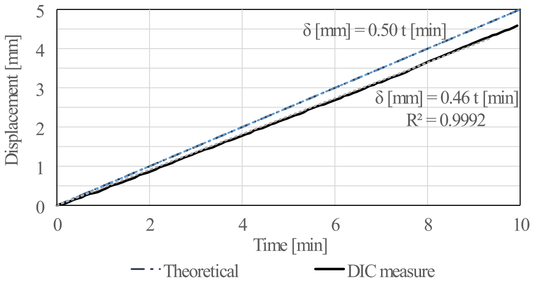

Figure 5.4: DIC vs imposed specimen end displacement

appearing in the saline and the alkaline environments. A scanning electron microscopy (SEM) investigation brings along the important role of the impregnation agent and shows that, while impregnated fabric is mostly embedded in the matrix and only a few strands emerge from it, non-impregnated fabric rests clearly separated from the matrix (Fig.5.3).

5.3.2 Uni-axial tensile test

Since no substantial deviation from this pattern could be found in the tested specimens, in the worst scenario (that is for ductile specimens, such as control's), the ultimate displacement (and strain accordingly) is overestimated by, roughly, 10%. This correction, which is often well outside the one-standard-deviation error band, is hereinafter considered when computing the ultimate strain of the specimens and it is relevant for the correct assessment of the design limits (see §5.4.6).

Fig.5.5 compares the mean strength curve, evaluated from averaging the single specimen results from any specific aggressive environment, with the relevant control group's, i.e. either 28 or 60-day curing. The sharpness of the mean stress-strain curve is indicated by embedding it in a ±1 standard deviation band; the fact that this band appears remarkably narrow indicates that good reproducibility was achieved. It is remarked that, according to [ICC AC434 2013, A7.0], the stress mea-

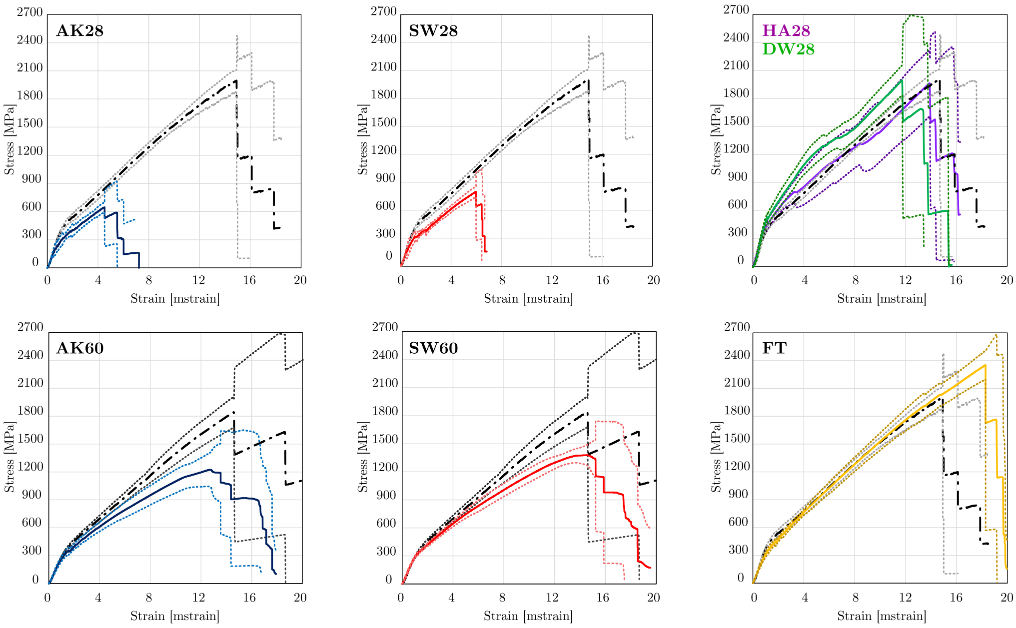

Figure 5.5: Mean stress-strain curves for any aggressive environment compared to the relevant control curve

sure is conventional, inasmuch it is obtained from scaling the applied force P by the fabric net area $A_f w_s$ (see formula (A3) of [ICC AC434 2013]). Similarly, the strain ε is obtained reporting the displacement to the coupon gauge length ($L_g = 250$ mm) [ICC AC434 2013, A4]. Tab.4.1 gathers the mean ultimate tensile strength, $\mu(f_{fu})$, and elongation, $\mu(\varepsilon_{fu})$, with the corresponding absolute and relative standard deviation (RSD also named coefficient of variation, CV), respectively ς and $CV = \varsigma/\mu$, for all test environments.

5.4 Results and discussion

5.4.1 Longitudinal elastic moduli and first cracking strength

Elastic moduli (namely uncracked and creacked) are determined from the single strength curves by linear-fitting of the conventional points given in Eqn.(2.1) in Section 2.3.3. Fig.5.6 shows that the longitudinal elastic moduli E_f^* and E_f, evaluated from the *mean* strength curve, provide a very accurate description of the composite stress-strain behaviour before and after the cracking of the brittle matrix, respectively (see the coefficient of determination r^2 given in Tab.5.3 for the cracked regime). The transition from the uncracked to the cracked regime occurs at the so-called transition point T, whence its ordinate is often named *first cracking resistance*. Tab.5.3 gathers the mean μ and the coefficient of variation CV for the elastic moduli and for the transition point location when they are calculated for each experimental stress-strain curve within a given environment. It is emphasized that, in the lack of specific indication from the guidelines, moduli and transition point

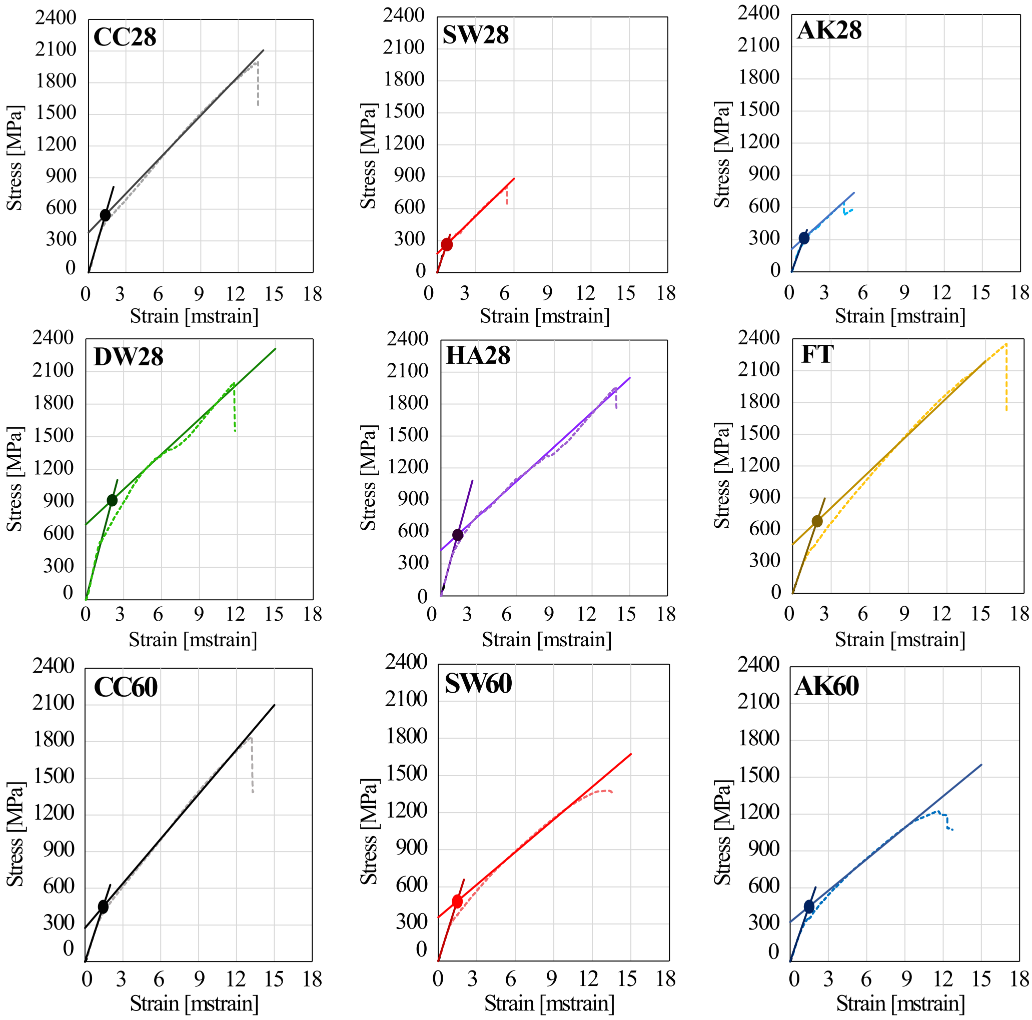

Figure 5.6: Location of the transition point T, evaluated from the mean stress-strain curve, for 28- and 60-day cured specimens

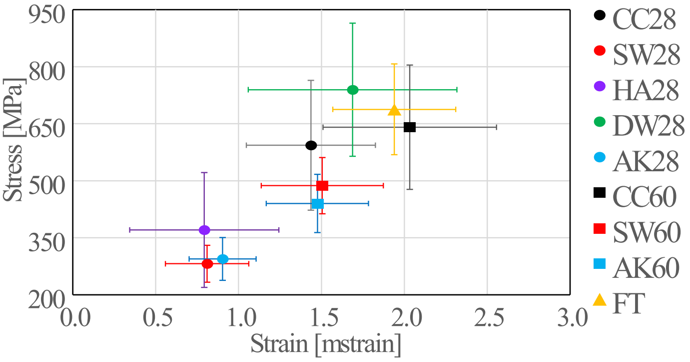

Figure 5.7: Transition point location and one-standard-deviation bars for stress and strain

Table 5.2: Mean ultimate tensile strength $\mu(f_{fu})$ and elongation $\mu(\varepsilon_{fu})$, with respective standard deviations, ς, and coefficient of variation, CV, for all test environments (Envs) of Tab.5.1

Envs	$\mu(f_{fu})$ [MPa]	ς_f	CV_f	$\mu(\varepsilon_{fu})$ [%]	ς_ε	CV_ε
CC28	2117	92	4.3	1.52	0.19	12.6
SW28	827	51	6.2	0.58	0.03	4.5
AK28	742	89	12.0	0.52	0.09	17.0
AK28	2210	281	12.7	1.34	0.15	10.9
HA28	2118	276	13.0	1.52	0.11	7.3
FT	2400	148	6.2	1.73	0.05	2.9
CC60	2162	337	15.6	1.92	0.44	23.1
SW60	1445	106	7.4	1.41	0.12	8.4
AK60	1313	220	16.8	1.27	0.22	17.2

location determined from the mean strength curve are to be preferred over taking the average of the corresponding quantities calculated for each experimental curve. Indeed, the former procedure is less sensitive to experimental error, in consideration of the conventional nature of the definitions of E_f, E_f^* and T which make use of single points on the stress-strain curve. Fig.5.7 shows the uncertainty connected with the determination of the transition point for each stress-strain curve within the considered environment in terms of one standard deviation bars. In contrast to the results obtained for glass fabric composites [Nobili 2016], the corrected uncracked elastic modulus E_1^* largely underestimates the matrix elastic modulus of Tab.2.1. In a similar manner and similarly to the results for glass fabric composites, the cracked modulus E_f underestimates the carbon fabric elastic modulus. However, moduli and transition point location for the control environment closely resemble the analogous results presented in [Carozzi 2015, Tab.8], despite a stronger (yet more brittle) matrix was there considered.

5.4.2 Effect of the curing time

To better illustrate the important role of curing time in affecting the aggressive environment resistance, ultimate tensile strength and elongation values are illustrated in the bar charts of Fig.5.8 for the control, saline and alkaline environments, for which 28- and 60-day curing times are available. Although the small increment in the ultimate strength and elongation which is seen in the control group at 60-day with respect to 28-day curing time appears of little statistical significance (cf.[Mobasher 2011, §13]), the corresponding improvement in the saline and in the alkaline environment is truly remarkable. Indeed, it appears that early-stage exposure to the aggressive environment determines a 60% and 65% decay in the ultimate strength, respectively for the saline and alkaline environments, as opposed to a 32% and 39% decay for later-stage exposure. Similar results attain the ultimate elonga-

Table 5.3: Mean moduli E_1^*, E_f^*, E_f and transition point (T) location (CV and r^2 are the coefficient of variation and of determination, respectively) evaluated from each stress-strain curve within a given environment

Envs	E_1^*	E_f^*		E_f			ε_T		f_T	
	μ [GPa]	μ [GPa]	CV %	μ [GPa]	CV [%]	R^2 [-]	μ [%]	CV [%]	μ [MPa]	CV [%]
CC28	3.8	413	8.1	117	17.8	0.929	0.14	27.1	593	28.8
SW28	3.4	364	21.7	114	13.6	1.022	0.08	31.0	282	17.2
AK28	3.1	332	16.1	110	7.7	0.915	0.09	22.3	295	19.1
DW28	4.2	456	17.2	123	16.1	0.867	0.17	37.3	739	23.7
HA28	4.0	435	13.0	120	12.4	0.995	0.08	56.8	371	40.7
FT	3.3	357	10.5	115	9.1	0.961	0.19	19.1	688	17.3
CC60	2.9	316	3.8	98	25.5	0.952	0.20	25.7	641	25.5
SW60	3.1	331	11.8	88	6.8	0.981	0.15	24.5	487	15.2
AK60	2.8	303	14.8	87	10.9	0.957	0.15	20.9	440	17.4

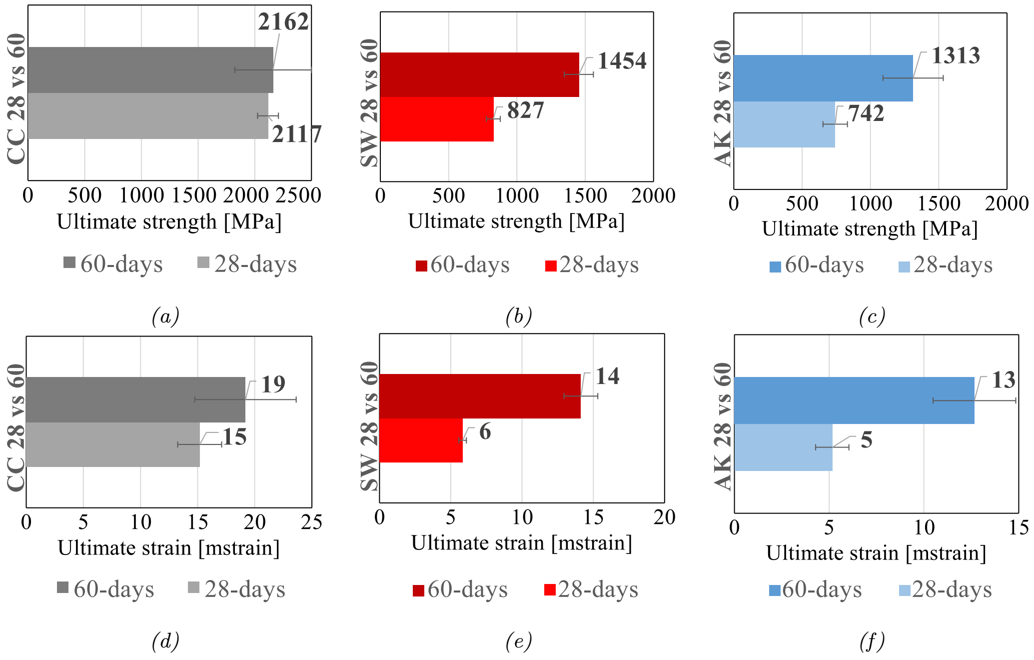

(a) (b) (c)

(d) (e) (f)

Figure 5.8: Ultimate strength (left) and elongation (right panel) 28- vs. 60-day-curing-time bar chart comparison: (a,d) control (b,e) saline (c,f) alkaline environments

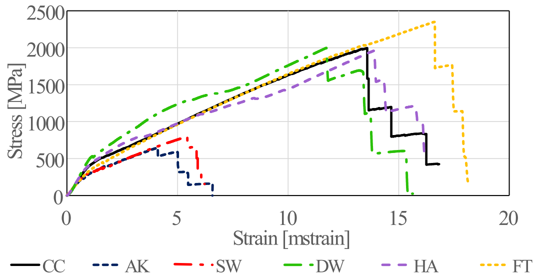

Figure 5.9: Mean stress-strain curve of the control, alkaline, saline, distilled water, HCl-acid environments and freeze-thaw cycles for 28-day cured specimens

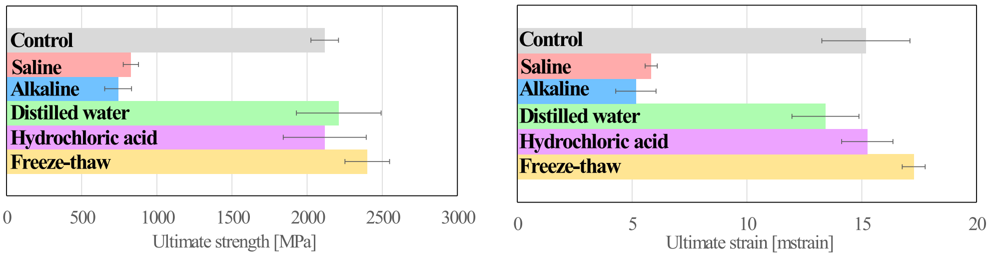

Figure 5.10: Mean ultimate stress (left) and ultimate strain (right) for 28-day cured specimens

tion, with a reduction in the order of 64% for both environments, to be compared with 28% and 33% at later-stage. These results follow in the wake of a vast body of literature confirming the important role of curing time on concrete porosity and resistance to penetration of aggressive agents [Gowripalan 1990, Zhutovsky 2012]. It is worth mentioning that curing time appears to have little effect on the relative standard deviation for the ultimate strength in the aggressive environments (while the same no longer holds true for the ultimate elongation, whose determination, however, is generally less accurate).

5.4.3 Aggressive environments comparison

Fig.5.9 shows the mean stress-strain curves for all environments at 28-day curing time. The effect of the different aggressive environments on the specimen ultimate stress and ultimate strain is better illustrated through the bar charts of Fig.5.10 and 5.11, respectively for 28- and 60-day cured specimens. It clearly appears that a sub-

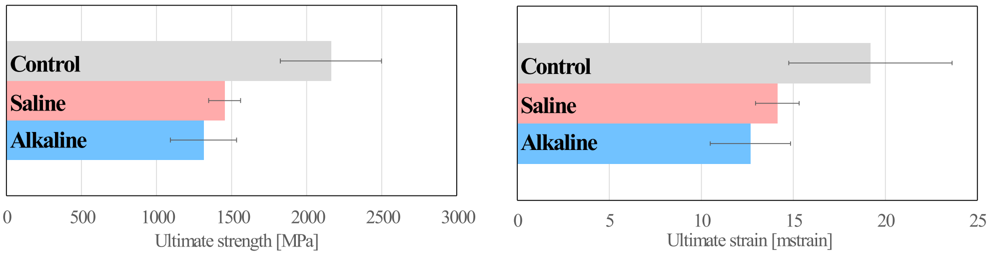

Figure 5.11: Mean ultimate stress (left) and ultimate strain (right) for 60-day cured specimens

stantial strength reduction is produced by the saline and the alkaline environments, which is particularly pronounced for 28-day cured specimens. This is in agreement with the corresponding results obtained for ar-glass fabric reinforced composites [Nobili 2016] and particularly for the alkaline environment, wherein performance degradation is attributed to formation of a new solid phase at the matrix/fabric interface and not to glass fabric deterioration [Hempel 2007, Butler 2009, Butler 2010]. Indeed, the mean ultimate tensile strength for the saline and alkaline environments for glass as well as carbon fabric reinforced composites are very similar, which suggests that the composite's performance decay is mostly due to matrix/fabric bond degradation and it is little responsive to the nature of the reinforcement. As a result, owing to its superior mechanical property in the control environment, carbon fabric composite performance degradation appears much greater than glass fabric composite's. It is further observed that an opposite trend is described in [Arboleda 2014a, Appendix D], wherein the alkaline and the saline environments appear to have a beneficial or neutral effect on the first cracking resistance, f_T, and on the ultimate tensile strength, f_{fu}, as compared to the control group's. Immersion in distilled water, hydrochloric acid and freeze-thaw cycles seem to have little effect on the strength curve, the statistical significance of which is assessed through a one-way ANalysis of Variance (ANOVA) [Mandel 2012, Nobili 2016]. ANOVA assumes a normal distribution in the specimen groups and a Behrens-Fisher distribution for the corresponding variance evaluated within the groups. Tab.5.4 shows the Fisher-Snedecor ratio, F, as well as the probability confidence, P, that different specimens really belong to the same population (this is the null hypothesis, which is associated with $P > 1$). It appears that some statistical support, albeit weak, is attached to a real influence of these aggressive environments on the composite performance. In particular, the performance enhancement obtained for freeze-thaw exposed specimens with respect to the control group possesses statistical significance. On the other hand, inasmuch as ultimate strength is concerned, ANOVA suggests that control, distilled water and hydrochloric acid exposed specimens really belong to the same population. This outcome is especially interesting with respect to the HCl-acid solution, which exhibits a highly detrimental influence on the mechanical performance of FRP composite [Kajorncheappunngam 2002]. Conversely, the neutral effect of distilled water immersion is compatible with the semi-hydraulic nature of the adopted mortar.

5.4.4 Crack pattern and failure mechanism

The specimen displacement field gives good indications on crack progression to failure. Fig.5.12 shows the crack opening pattern at the same elongation level $\varepsilon = 0.55\%$ for all the considered environments. It may be seen that control, acid, distilled water and freeze-thaw exposed specimens are characterized by several multiple small cracks developing across the specimen, so that numerous uniformly-coloured bands appear along the specimen length, each expressing the displacement of a fragment of uncracked mortar. In contrast, alkaline and saline specimens show fewer and bigger

Table 5.4: ANOVA test results: F – Fisher-Snedecor ratio, P – Probability confidence, s.p.– same population. The null hypothesis is rejected whenever $F > 1$

Null hypothesis for the ultimate strength	F	P
CC28, DW28, HA28, FT $\in$ s.p.	1.6629	21.9%
CC28, DW28, HA28 $\in$ s.p.	**0.2378**	79.2%
DW28, HA28, FT $\in$ s.p.	1.484	27.3%
Null hypothesis for the ultimate strain	F	P
CC28, DW28, HA28, FT $\in$ s.p.	5.005	1.5%
CC28, DW28, HA28 $\in$ s.p.	1.905	19.5%
DW28, HA28, FT $\in$ s.p.	11.870	0.2%

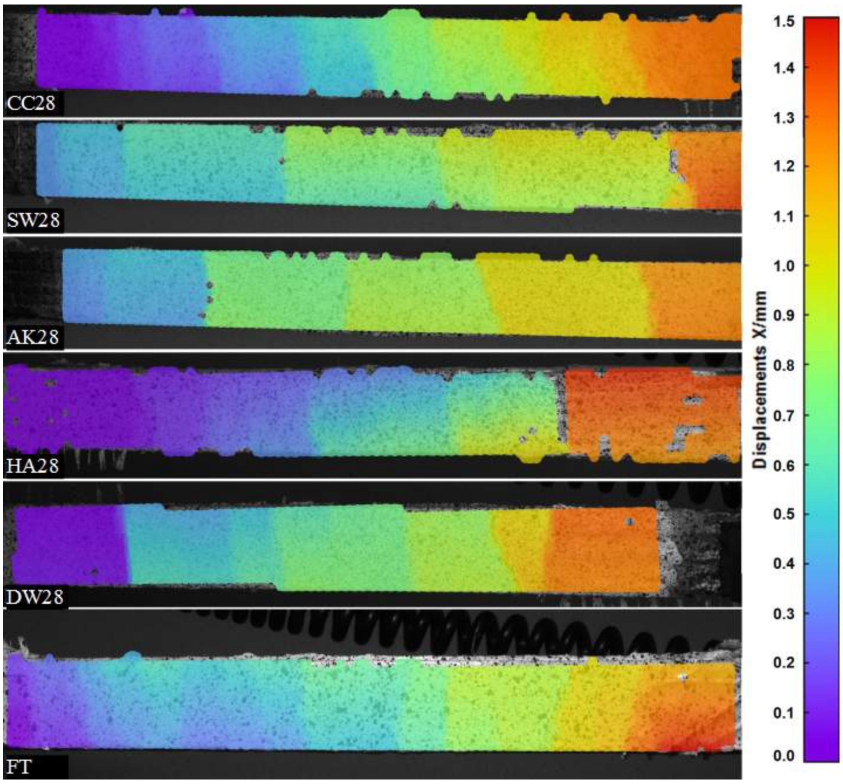

Figure 5.12: Crack opening pattern at $\varepsilon = 0.55\%$

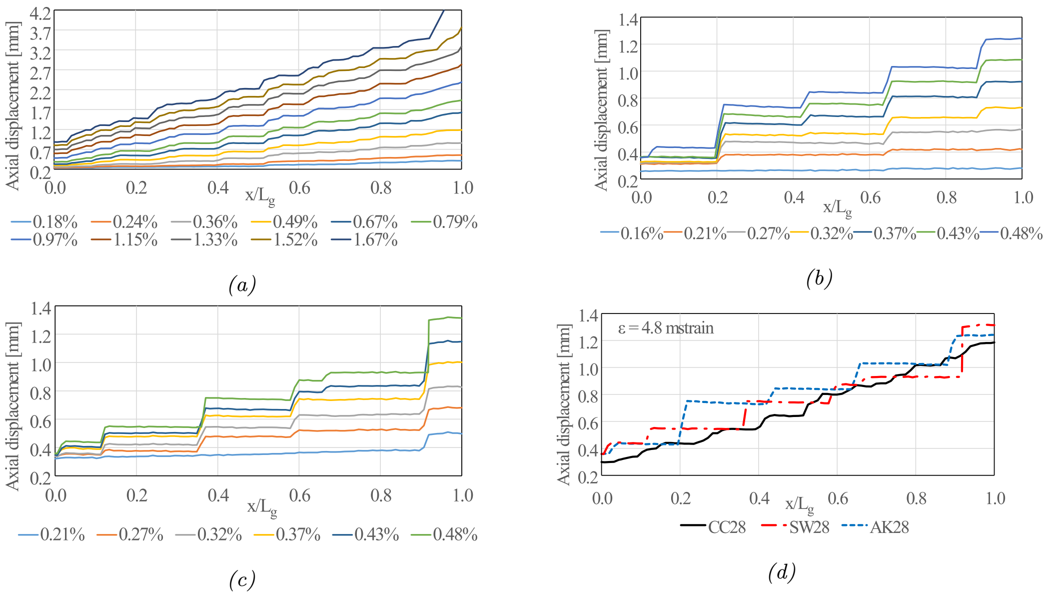

(a) (b)

(c) (d)

Figure 5.13: Longitudinal displacement at the coupon axis at different strain levels for CC28 (a), SW28 (b), AK28 (c) and comparison at $\varepsilon = 0.48\%$ *(d)*

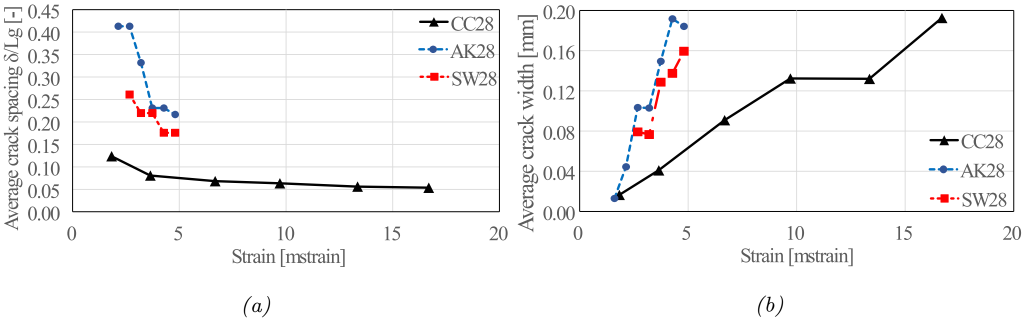

(a) (b)

Figure 5.14: Dimensionless mean crack spacing (a) and width (b) vs. strain

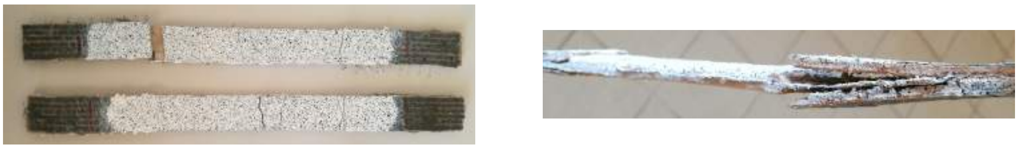

Figure 5.15: Failure mechanism (left) and fabric slippage (right)

Table 5.5: Average crack width at failure for CC, SW and AK groups

28-day curing	$w_{cr,u}$ [μm]	**60-day curing**	$w_{cr,u}$ [μm]
CC28	193	CC60	161
SW28	184	SW60	180
AK28	176	AK60	217

cracks marking the limits of 5 or 6 uniformly-coloured bands. This behaviour is better illustrated in Fig.5.13 which compares the longitudinal displacement along the coupon axis at different elongations for the control, saline and alkaline environments. In Fig.5.13, displacement jumps amount to crack openings. As it is well known, a diffused cracking texture is generally desirable for it warrants ductility and energy absorption capability.

A measure of (dimensionless) average crack spacing vs. strain is given in Fig.5.14 (a), which illustrates the different levels of crack saturation attained by the exposed specimens compared to the control ones. Crack spacing is indirectly related to matrix/fabric bond strength, to the composite stiffness and to durability aspects [Mobasher 2011]. Besides, digital image analysis allows plotting the average crack width against strain (Fig.5.14(b)). This plot is remarkable in that it shows that, unlike crack spacing, the mean crack width increases with the strain until it reaches a maximum value (saturation) which is independent of the environmental exposure.

In all cases, failure is due to delamination as a result of crack spacing saturation, whereby a dominant crack (usually but not always located near the end of any one tab) propagates inside the specimen at the fabric/mortar interface [Mobasher 2006]. Fabric failure could never be reached (Fig.5.15).

5.4.5 Degradation law for crack pattern

Crack analysis is carried out to relate mechanical properties to the failure mechanism and to matrix deterioration. Indeed, crack spacing provides indirect evidence of interphase bond strength and it affects the apparent composite stiffness [Falope 2018]. A nice introduction to the significance and application of crack spacing measurement is given in [Mobasher 2011, Chap.13]. It is important to observe that crack spacing may be adopted as a design parameter. Besides, crack widening and diffusion clearly affects durability.

This qualitative picture is given a quantitative description in Fig.5.16, that plots the average crack spacing as well as the average crack width as a function of strain for AK, SW and CC and it compares 28-day with 60-day curing. In general, crack spacing is a decreasing function of strain, until a saturation level is reached. Crack spacing data may be interpolated according to the decay law [Mobasher 2006, Eq.(1)] and [Signorini 2018c].

$$S(\varepsilon) = S_1 + S_0 \exp\left[-\alpha(\varepsilon - \varepsilon_1)\right], \quad \varepsilon \geq \varepsilon_1, \tag{5.1}$$

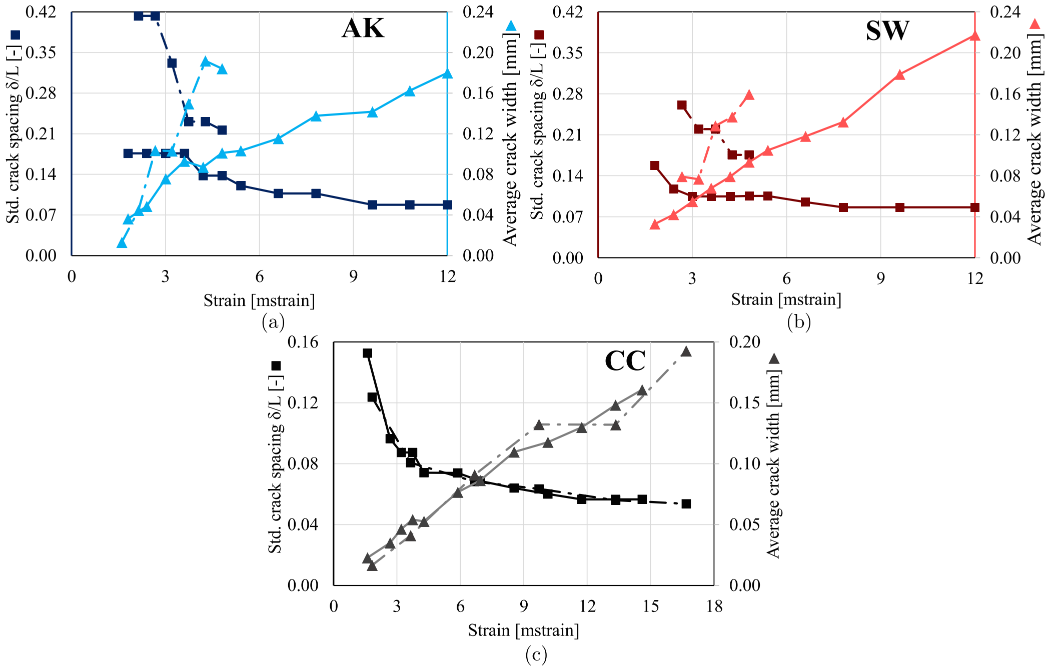

(a) (b) (c)

Figure 5.16: Crack pattern development during uni-axial traction for AK (a), SW (b) and CC (c) at 28-day (line-dot) and 60-day (solid) curing time. Crack spacing (left scale, triangles) and crack width (right scale, squares) is plotted vs strain

where S_1 is the saturation crack spacing, ε_1 the first elongation in the data set and $S_0 = S(\varepsilon_1) - S_1$. S_1 and α are fitted to the available data sets and results are presented in Tab.5.6. Best performance is attached to a small saturation spacing S_1 and a large spacing decay α, for this combination brings significant energy dissipation at small deformation. In this respect, the control group performs best and results are consistent for 28 and 60 day curing. Conversely, SW performs very poorly and curing appears strongly beneficial. The AK group stands in between, for it features a surprisingly small saturation spacing and yet a very small decay rate. It is observed that results appear qualitatively consistent with what is shown in [Mobasher 2006, Tab.4]

Crack width is found to almost linearly increase with strain. Remarkably, the

Table 5.6: Fitting parameter S_1 and α for the exponential law (5.1) for crack spacing data and coefficient of determination R^2

Group	S_1 [mm]	α [mstrain^{-1}]	R^2
CC28	13.33	0.51	0.998
CC60	14.04	0.71	0.997
SW28	30.39	0.54	0.998
SW60	21.76	1.27	0.996
AK28	13.31	0.30	0.991
AK60	12.47	0.13	0.993

crack pattern development in the control group for 28- and 60-day curing time almost coincide. Conversely, AK and SW specimens display a marked contrast between 28- and 60-day curing, with the crack spacing being almost uniformly twice as large for the former compared to the latter and the crack width increasing at a much slower rate. However, despite this different evolution, the ultimate mean crack width $w_{cr,u}$ attained at failure appears similar for all test groups, as reported in Table 5.5. Such saturation crack width is located around the mean value $\mu(w_{cr,u}) = 185\,\mu\text{m}$ with narrow standard deviation $\varsigma(w_{cr,u}) = 18\,\mu\text{m}$, that corresponds to a unexpectedly limited coefficient of variation, $CV \approx 10\%$. Thus, it appears that the saturation crack width is a characteristic parameter of this composite system [Nobili 2017a, Signorini 2018b].

5.4.6 Design considerations

[ICC AC434 2013, §8.0] provides minimum acceptable design criteria for the design of FRCM strengthening which allow assessing the mechanical bearing capacity of the composite system. When failure of the composite system is due to tensile rupture of the FRCM material, the flexural strength enhancement to both masonry and reinforced concrete (RC) members is limited by the design tensile strain

$$\varepsilon_{fd} = 0.7\varepsilon_{fu} \leq 1.2\% \tag{5.2}$$

wherein ε_{fu} is the ultimate tensile strain of the composite material. The latter is obtained through the so-called three-sigma rule, namely

$$\varepsilon_{fu} = \mu(\varepsilon_{fu}) - 3\varsigma$$

and it cannot exceed the 5% fractile of the capacities obtained experimentally, i.e. the characteristic value, which, for normally distributed populations, is given by

$$\varepsilon_{fuk} = \mu(\varepsilon_{fu}) - 1.96\varsigma. \tag{5.3}$$

The effective tensile stress level in the composite follows through the cracked longitudinal modulus E_f as

$$f_{fe} = 0.85E_f\varepsilon_{fe}, \tag{5.4}$$

where $\varepsilon_{fe} \leq \varepsilon_{fd}$ and equality holds at failure. From a methodological viewpoint, this approach can be confronted with the strength design protocol [International Code Council 2012], as coded in [CNR TD200-R1 2013] for FRP materials, which makes use of the characteristic value of the material strength further divided by the material partial factor γ_m (also known as *safety factor* or *strength reduction factor*), i.e.

$$R_d = \eta\frac{f_{fck}}{\gamma_m}, \tag{5.5}$$

where $\eta = \eta_a\eta_l$ is the conversion factor which comprises the effect of environmental exposure and long-term effects, respectively. Partial factors γ_m for FRP material

Table 5.7: Ultimate tensile elongation ε_{f_u} and design values for all test environments

Envs	ε_{fu} [%]	$\varepsilon_{f_{uk}}$ [%]	ε_{fd} [%]	γ'_m [-]	f_{fe} [MPa]	f_T [MPa]	f_{fek} [MPa]	γ_m [-]
CC28	0.94	1.35	0.66	2.06	619	554	2022	3.27
SW28	0.50	0.55	0.35	1.58	316	265	788	2.49
AK28	0.26	0.43	0.18	2.38	149	316	622	4.18
DW28	0.90	1.19	0.63	1.89	524	573	1872	3.57
HA28	1.19	1.40	0.83	1.68	714	912	1750	2.45
FT	1.58	1.67	1.10	1.51	985	682	2225	2.26
CC60	0.58	1.40	0.41	3.43	385	437	1864	4.84
SW60	1.08	1.30	0.76	1.71	516	483	1302	2.52
AK60	0.57	0.98	0.40	2.44	267	448	1090	4.09

depend on the limit state under consideration and, in the case of the ultimate limit state (ULS), they vary with the envisioned rupture mechanism in the range 1.10–1.50 [CNR TD200-R1 2013, Tab.3-2]. For the serviceability limit state (SLS), it is taken $\gamma_m = 1$. A similar approach is described in [Machida 1997] in the more general context of Continuous Fiber Reinforcing Materials (CFRM) to which FRCM composite belongs, although specific reference is there restricted to organic binders (epoxy or vinyl-ester resin) typical of FRP.

Tab.5.7 gathers the ultimate tensile strain along with the characteristic and the design ultimate strain as well as the ultimate and characteristic strength at failure. It may be seen that consideration of the ultimate design strain ε_{fd} to determine the design strength at failure, according to (5.4), greatly underestimates the experimental mean $\mu(f_{fu})$, to the extent that the design strength often falls in the proximity of or even prior to the first cracking resistance f_T. This result, which comes about despite the design strain limit at failure, ε_{fd}, being much greater than the first cracking strain, ε_T, entails from considering only the cracked modulus E_f in Eq.(5.4) and neglecting the initial contribution of the uncracked modulus E_f^*. In this respect, the bi-linear behavior characteristic of FRCM materials (the tri-linear behavior advocated in [Carozzi 2015] is not matched in our results) is really replaced with a linear law, which is the typical behavior assumed for FRP (see, for instance, [Machida 1997, §3.4.3] and [CNR TD200-R1 2013, §2.3.1]). Besides, we remark that the three-sigma rule is a very cautionary provision when applied to the ultimate strain, for its determination is often connected to a bigger experimental uncertainty as compared to the ultimate strength (see, for instance, the dispersion of the experimental results presented in [Nobili 2016, Carozzi 2015]). As a result, the ultimate design strength, as evaluated on the basis of the ultimate design strain, for the control environment and for 60-day cured specimens, is 37.8% smaller than the corresponding strength deduced from 28-day cured specimens, whereas the corresponding comparison on the characteristic values yields a mere 7.8% reduction.

It is remarked that this outcome, although specific to this experimental sample, is believed to be general, as bigger relative standard deviation bands usually accompany higher-mean samples (the same experimental trend is casually observed in [Carozzi 2015]). This phenomenon, called positive covariance, occurs because small imperfections, which are ineffective in weak specimens, tend to play an important role in the failure of tougher specimens [Mandel 2012]. Indeed, no exception to this rule may be found in our data. The same considerations carry over, with little modification, when considering a deformation limit, for then the design strain limit is [CNR TD200-R1 2013, §4.2.2]

$$\varepsilon_{fd} = \eta'_a \frac{\varepsilon_{fuk}}{\gamma'_m} \tag{5.6}$$

where γ'_m and η'_a are really equal to, respectively, γ_m and η_a in the codes.

Tab.5.7 lists the partial factors γ'_m and γ_m for all the test environments. γ_m is determined as the partial factor which reduces the material resistance, R_d, to the design strength f_{fe}, as obtained from Eqs.(5.5) and (5.4), respectively (take $\eta = 1$). It is straightforward to see that operating on the basis of the characteristic strength yields the same result as operating from the design strain inasmuch as exceedingly large values (compared with those introduced for FRP materials) for the partial factor γ_m are assumed, falling in the range 2.26–4.84. Likewise, the partial factor γ'_m, which makes the design ultimate strain ε_{fd} evaluated according to (5.6) correspond to the limit given by (5.2), lies in the range 1.51–3.43 and its maximum is attained for 60-day cured specimens in the control environment. It may be argued that this is a consequence of the adoption of a brittle matrix, which requires bigger safety factors to avert the danger of sudden failure. However, characteristic value design applies equally well to brittle failure, such as it occurs in shear induced collapse, and, generally, FRP materials undergo fragile rupture.

When exposure to aggressive environments is envisaged, such is the case in seafront constructions, bridge decks and quays, industrial plants, storage tanks etc., and in the absence of experimental data on the exposed FRCM system, the design procedure illustrated in [ICC AC434 2013] is no longer available. This shortcoming can be amended by the knowledge of the environmental conversion factors η_a, η'_a of interest, through which the design parameters of the standard composite material may be safely reduced to accommodate for the detrimental effect of the environment. The available experimental data allows determining the environmental conversion factor $\eta \leq 1$ for the test environments by two formally different methods. They are illustrated with reference to the ultimate strength (resistance):

(a) By the first procedure, conversion factors are determined in the spirit of [CNR TD200-R1 2013, §3.5.1] as the ratio between the characteristic strength in the environment of interest and the characteristic strength in the control environment for the same curing time

$$\gamma_m^{(a)} = \frac{f_{fek,\,\text{exposed}}}{f_{fek,\,\text{control}}}.$$

Table 5.8: Environmental conversion factors for the test environments calculated according to method (a) and (b). Numbers in parenthesis are to be ceiled at the maximum allowed value of 1

Envs	Curing [days]	η_a (a)	η_a (b)	η'_a (a)	η'_a (b)
SW28	28	0.39	0.35	0.41	0.32
AK28		0.31	0.28	0.32	0.26
DW28		0.93	0.84	0.88	0.72
HA28		0.87	0.77	(1.03)	0.80
FT		(1.10)	(1.02)	(1.24)	0.95
SW60	60	0.70	0.53	0.93	0.55
AK60		0.84	0.45	0.70	0.42

From a statistical standpoint, this method guarantees that the 5%-fractile of the *population sample* strength is retrieved. However, it should be remarked that here the considered population sample is restricted to the exposed specimens.

(b) The second procedure treats all possible strength ratios between the exposed and the control environment specimens (for the same curing time) as a new population sample, whose 5%-fractile is then determined, i.e.

$$\gamma_m^{(b)} = 5\%\text{-fractile of } \left\{ \frac{f_{fe,\,i}}{f_{fe,\,j}} \right\} \quad \text{for any pair } (i,j) \in N \times N.$$

Conceptually, this method is more sound as it provides the 5%-fractile of a bigger population sample, which consists of all possible permutations of the performance decay ratios. In this sense, according to this method, γ_a is a *covariant* quantity of two population samples. As a result of considering a bigger sample size, this method provides smaller factors.

By analogy, the same procedure may be applied to determine the conversion factor for the design strain, $\eta'_a \leq 1$. The environmental conversion factors, as calculated according to both methods, are gathered in Tab.5.8. For the sake of comparison, they can be confronted with $\eta_a = 85\%$ proposed in [CNR TD200-R1 2013] for resistance of carbon/epoxy in a general aggressive environment and with the 70% strength loss reported in [Kajorncheappunngam 2002] for ar-glass FRP composites in acid and alkali solutions (see also [Kootsookos 2004] for FRP long-term seawater resistance). Remarkably, the conversion factors for strength and strain are very similar when calculated according to method (b). Similarly to strength ratios, which provide a measure of structural safety, they furnish a very convenient indication of the FRCM system vulnerability to a given aggressive environment. Finally, some word of caution should be spent on the identification of the characteristic quantities, usually obtained from Eq.(5.3), with the 5%-fractile of the population distribution, for this is indeed the case for *normally distributed* populations only. As it can be seen from the frequency bar charts of [Carozzi 2015], experimental data are often far from being normally distributed. In this sense, simply referring to the two-sigma rule would be more appropriate.

5.5 Conclusive remarks

In this study, the effect of the aggressive environment and of the curing time on the mechanical performance of impregnated carbon-FRCM prismatic coupons is assessed according to the ICC guidelines. Specimens have been subjected to 5 aggressive environments, namely seawater, alkaline, distilled water, hydrochloric acid and freeze-thaw cycles, and two curing times: 28 and 60 days. Emphasis is placed on determining the design limits for all test environments from the experimental data and following ICC minimum design criteria. The following results are especially worthy of consideration:

- aggressive environments may significantly reduce the design limits and should be carefully considered; in particular, the seawater and the alkaline environments are especially demanding in terms of performance degradation, while distilled water and hydrochloric acid produce no statistically significant effect (under ANOVA test); finally, freeze-thaw cycles induce a small beneficial effect.

- These results set some interesting application ranges for FRCM in contrast to FRP, the latter being more suitable for seawater conditions, the former for acid environments, both suffering in alkali [Kajorncheappunngam 2002];

- compared to 28-day cured samples, 60-day curing time produces little effect on the limit properties of the unexposed specimen, yet it is capable of greatly mitigating the impact of the aggressive environments with a beneficial effect close to 30% of the unexposed value;

- consequently, early-stage protection of the composite material should be always considered in an aggressive environment;

- the crack pattern (spacing) measured along tensile uni-axial testing provides strong evidence of the mechanical performance of the matrix and of the matrix/fabric bond: in degraded specimens, the closely-spaced array of tiny cracks typical of the control environment is replaced by a coarse arrangement of bigger cracks and this markedly different behavior is evident at all stages of the test. In this sense, uni-axial testing of composite samples may represent a good test candidate for material qualification.

- Conversely, mean crack width is a monotonic increasing function of strain whose maximum, attained at failure, appears independent of environmental exposition.

- Design limits determined by the two-sigma rule and subsequent application of a safety factor, as prescribed in several codes dealing with FRP strengthening, are to be preferred over limits determined by the three-sigma rule, for the latter is strongly based by the positive covariance effect;
- as a result, design limits evaluated according to the three-sigma rule for longer-term-cured specimens substantially differ from and indeed are smaller than the corresponding limits evaluated from shorter-term-cured specimens.

Environmental conversion factors are introduced following two statistically different procedures, named (a) and (b), as a mean to easily and safely assess the detrimental effect of an aggressive environment on the mechanical properties of the composite. Indeed, they allow reducing the unexposed composite design limits to the corresponding ones pertaining to the exposed material at the same curing time. In this sense, environmental conversion factors should be given for different aggressive environments, specimen curing time and design limit. In particular, method (b) proves to be safest and yields almost equal results for stress and strain limits. Finally, we emphasize that the experimental results presented in this analysis should be regarded as a qualitative guideline for further experimentation, as they are specific to a single mortar (adopted in the strengthening project illustrated in [Nobili 2017a]). However, allowing for different mortar properties, the qualitative trend should remain the same [Butler 2010], on the grounds that variations in the test set-up, with special regard to gripping, specimen preparation and uni-axial test specifications, may also significantly alter the quantitative results but still preserve the qualitative behaviour.

Part II

Plastic fibres-reinforced concrete (FRC) composite materials with enhanced interphase

CHAPTER 1

Introduction

Fibre Reinforced Concrete (FRC) is an established technology that aims at improving the poor post-cracking tensile strength, namely toughness, of concrete, as well as dissipative properties in case of impact loading [Mindess 1988, Wang 1996]. Fibres used as dispersed phase to brittle materials root very far in time, ranging from straw added to mud bricks for early buildings, to plaster reinforced with horse hair and to pottery with asbestos. As a main difference to reinforcement in the form of continuous fibres, short fibres and other discrete reinforcements require skilled manufacturing workforce [Wafa 1990]. According to ACI 116R, FRC is a "concrete containing randomly dispersed fibres" [ACI 116 R 2000]. Since the 1960s, early applications of FRC have been developed by randomly dispersing short steel fibres, as a natural upgrade of the traditional re-bar with steel rods. FRC reinforced with steel fibres (SFRC) possesses a long history of successful applications and it is now widely employed, often in conjunction with polypropylene (PP) fibres, in Hybrid Fibre Reinforced Concrete (HFRC). Synthetic fibres, such as polypropylene, polyethylene, polyvinyl chloride and many others [Zollo 1997], offer several advantages with respect to steel fibres, especially in consideration of their chemical resistance to aggressive environments [Lanzoni 2012]. Besides, polypropylene fibres impart a positive anti-spalling character to FRC, particularly to high strength concrete, for they sublimate and provide room for water vapour to expand when exposed to high temperature. Synthetic fibres have been used in a variety of applications, ranging from road pavements, to airport runways, industrial floors and many others [Bentur 2006, Mobasher 2011, Nobili 2013]. Qian and Stroeven [Qian 2000] have also developed Hybrid steel-polypropylene fibres, in combination with fly-ash in concrete.

(a) (b)

Figure 1.1: Different cracking behaviour of plain concrete (a) and concrete reinforced with polypropylene wavy fibres

The major drawback associated with synthetic fibres is their lack of hydrophilicity, whereupon they create a weak interface with the concrete matrix [Felekoglu 2009]. As a result, from the mechanical standpoint, mechanical load is hardly transferred from the matrix to the fibres and the premature occurrence of delamination impedes the full exploitation of the fibre strength. This is a typical failure mode of composite materials, including FRC [Bentur 2006]. To remediate such shortcoming, several approaches have been investigated, ranging from fibre shaping to composition design and especially surface treatment.

Several surface treatments have been considered in the literature, such as cold plasma [Denes 1996, Felekoglu 2009], chemical attack (such as etching) [Lovata 1987, Peled 1992], flame treatment [Terlingen 1994] and surface mechanical pitting [Singh 2004]. Improvement of the interfacial bond with the cementitious mortar is obtained in the contribution by [Tu 1998] through oxyfluorination, which increases the free energy of the fibre surface. [López-Buendía 2013] investigates the effect of an unspecified "alkaline surface treatment and alkaline precursors" on the mechanical performance of PP fibres for FRC. Similarly, alkaline and silane treatment of natural and PP fibres is discussed, alongside some durability issues, in the paper by [Park 2008]. Pre-treatment of PP fibres through a microbiological process of microbially induced calcite precipitation is studied by [Hao 2018].

Silica coating has been recently proposed as a viable technique to bridge the fibre-to-matrix interface. In the research by [Di Maida 2015], a base-catalysed sol-gel silica coating was investigated under pull-out tests and, successively, in the following contribution by [Di Maida 2018], the material was tested under notched bending. PP fibres were bathed in the silica solution for a long time (2 hours) to allow for silica nano-spheres to deposit on the fibres' surface. As a result, that mechanical performance was greatly enhanced, presumably due to the increased fibre surface roughness. Finally, in a recent work by [Erdem 2018], nano-silica coating of recycled aggregates has been assessed against traditional concrete with natural aggregates.

1.1 Fibre-reinforced concrete in civil engineering

The ability of randomly dispersed short fibres of providing FRC with a higher degree of isotropy results in an enhanced response after early cracking, hindering indeed the sudden failure that is typical of plain concrete. Besides, high torsional strength, stiffness, ductility, diffused micro-cracking (see Fig.1.1) are other major effects that have promoted the spread usage of FRC [Wafa 1990]. Nowadays, several kinds of FRC can be designed, according to fibres' length. In fact if micro-fibres are added, they stop cracking due to shrinkage, while in the case of macro-fibres, they fulfil a structural response. The most common application of FRC regards the manufacturing of precast elements. The interesting mechanical properties of FRC is combined with an easy and controlled ex-situ production chain. In addition, fibres provide the precast conglomerate with high toughness and resistance to impact, thus lowering the probability of damage during transportation and installation, with higher


(a) (b)

Figure 1.2: Testing of a prestressed SFRC girder (a) and a sewage pipe (b) at the real scale. Courtesy of [Kohoutková 2017]

Figure 1.3: Example of industrial pavement realized with FRC. Courtesy of [Rossi 2006]

durability against aggressive environments and with lower weight than traditional concrete. Weight reduction is of primary importance from the economic standpoint, since reduced cost is required for the transient phases, from production to in-situ application. With reference to steel fibre-reinforced concrete, in particular, traditional steel longitudinal rebar can be highly reduced, as well as shear brackets. In Figure 1.2, a 13.6 m long steel-FRC girder subjected to load-test is shown, taken from the conference paper by [Kohoutková 2017]. In that work, steel fibres having diameter and length equal to 0.8 mm and 60 mm respectively, are embedded in concrete. Traditional reinforcement is present only in the form of pre-stressed rebar [Kohoutková 2012]. Applications for FRC range from manholes, risers or curbs to industrial pavements, tunnels, pipes. In the infrastructural field, FRC can be used to repair existing highway, airfield or industrial pavements. In fact, the use of composite fibrous concrete is useful to design thinner elements with high resistance to impact and smoother upper surface (see an example in Fig.1.3). These features allow to reduce the number of joints in both transversal and longitudinal directions. Moving to hydraulic applications, (see a pipe for mechanical testing in Fig.1.2) FRC offers high resistance to erosion damaging.

Another technique that takes advantage from the addition of dispersed fibres is sprayed concrete, or FRS (fibre-reinforced shotcrete), which consists of spraying cementitious mortar or concrete at very high speed onto a surface by means of a pneumatic device. The system presents the twofold benefit of placing and compacting the conglomerate at the same time, thanks to the high ejection force. It has been traditionally combined with steel grids previously installed on site. FRS exploits all the properties of fibre-reinforced composites in order to stabilise rocks and to build tunnels, dams, mines, bridges arches and dome-shaped structures. It is also applied to restore concrete surfaces subjected to aging and to stabilise slopes to prevent the soil from sliding.

1.1.1 Fibres

With the increasing interest around discrete fibre-reinforced cementitious composites, several kinds of fibres have been studied in the last decades. They can be classified following several criteria. First of all, fibres can be distinguished according to the material they are made of. Common fibres for civil engineering applications are made of steel, since they are cheap and easy to produce. Generally, round and thin fibres are used as the dispersed reinforcing phase. The shape plays an important role in the effectiveness of S-FRC. Fibres can be produced without (straight) or with (crimped, twisted, hooked or ringed) an enhanced adhesion shape and equipped with paddled ends. Steel fibres' diameter range from 250 µm to 760 µm. Besides steel fibres, also glass fibres are very popular. The geometry of glass fibres is straight, the surface is smooth and filaments can be used individually (diameter around 5 µm to 15 µm) or even bonded together to obtain fibres' bundles from 130 µm to 1300 µm. Natural fibres are another important category of reinforcements for FRC. They can be organic and mineral and comprise, for example, wood, asbestos, cotton, bamboo and rock-wool. Natural fibres may present different sizes and surfaces. However, the durability of natural fibres is still an open issue [Larsen 1990, Juarez 2007]. Instead, synthetic fibres benefit from a better resistance to aggressive environments, as is the case for aramid, nylon, polyester and polypropylene. In general, synthetic fibres are manufactured in diameters ranging from 20 µm to 800 µm and among them, polypropylene fibres present high durability and can be plain, twisted or fibrillated, to enhance the mechanical grip with the surrounding matrix. For each kind of fibres, an important parameter is the aspect ratio (L/D), namely the length-to-diameter ratio, which typically spans between 30 to 150. Mechanical properties of the most common fibres are reported in Table 1.1.

Table 1.1: Mechanical properties of some common fibres for FRC [Sharda 2016]

Fibre	**Elastic Modulus** [GPa]	**Tensile Strength** [GPa]	**Ultimate elongation** [mstrain]
Steel	$200 \div 210$	$0.50 \div 2.00$	$5 \div 35$
Glass	$70 \div 80$	$2.00 \div 4.00$	$20 \div 35$
Polypropylene	$5 \div 7$	$0.50 \div 0.75$	80
Nylon	4	0.9	$130 \div 150$
Carbon	$230 \div 250$	2.6	10

Chapter 2

General materials

Contents

2.1 Fibres

Polypropylene (PP) draw-wire fibres [Lanzoni 2012] are used as the dispersed reinforcing phase, Fig.2.1. Table 2.1 lists the main physical and mechanical properties of macro synthetic PP-fibres, as given by the manufacturer. In order to role out any effect due to shape modification and surface treatment, fibres are delivered in the raw state, that is after being drawn and cooled down, but without any further processing.

Table 2.1: PP-fibres characteristics

Characteristic	**Unit**	**Value**
Diameter, φ	mm	0.70
Elastic modulus, E_f	MPa	1500
Density, ρ	kg/m^3	946
Length, L_f[1]	mm	10

[1] This length refers to the fibres dispersed in the cement matrix for bending tests.

Figure 2.1: Polypropylene draw-wire fibres

(a) Compression test (R_c) *(b) Slump test*

Figure 2.2: Characterization of SB concrete

2.2 Mortar

Table 2.2: Properties of adopted cementitious mortars

Characteristic	**Unit**	**Geo**	**SB**
Composition		$CO_3{-}SiO_4$	
w/c	%	20	5
max grain size ϕ	mm	0.5	6.0
Density, ρ_{mix}	$kg\,m^{-3}$	2050	2308*
Consistency (slump)	class	n.a.	S1*
$f_{ck,28}$	MPa	> 50	22*
$f_{tk,28}$	MPa	> 9	6.3*
E_{28}	GPa	20	n.a.

* Values measured on actual concrete batches.
n.a. datum *not available* from the technical sheet of the manufacturer.

Specimens are manufactured by mixing two commercially available cementitious conglomerates (GeoLite, Kerakoll SpA, labelled as “Geo” and SabbiaCemento più, Fornace Sberna Srl, labelled as “SB”), whose properties as declared by the producer are reported in Table 2.2. The exceptions are related to SB concrete, whose mechanical properties and consistency properties are evaluated through three-point bending and compression tests in compliance with [UNI EN 12390-5 2019]. Compression tests are carried out on 150 mm × 150 mm × 150 mm cubic samples (see Figure 2.2(a)) while consistency class is measured through the slump test using a standard Abrams cone, as prescribed by [UNI EN 206 2013] (see Figure 2.2(b)).

CHAPTER 3

Surface treatments of polypropylene Fibre-reinforced Concrete (PP-FRC)

Contents

3.1 Nano-silica coating

In this section, the effect of a rapid acid-catalysed sol-gel silica coating, suitable for industrial processing, is investigated. The effect of the coating is assessed alongside the role of curing time, in an attempt to distinguish interface bond strengthening from matrix enhancement.

Silica nano-particles are deposited on PP-fibres via the sol-gel technique [Brinker 2013]. Following [Hench 1990], method 3 is adopted, which consists of "hydrolysis and polycondensation of alkoxide precursors followed by aging and drying under ambient atmospheres". Indeed, "the surface area of dried gels made by method 3 is very large (> 400 m^2 g^{-1}), and the average pore radius is very small (< 10 nm)". Silicon alkoxide (we recall that an *alkane* is a molecule containing only carbon and hydrogen linked exclusively by single bonds [Brinker 2013]) is used as starting compound (precursor) and it is hydrolysed by mixing with water:

$$\mathrm{Si(OR)_x} + n\mathrm{H_2O} \rightarrow \mathrm{Si(OR)_{n-x}(OH)_n} + nR - \mathrm{OH}, \quad R = \mathrm{C_2H_5}. \tag{3.1}$$

Hydrated silica develops a condensation reaction, that is linking of partly hydrolysed molecules, followed by polycondensation, until the polymeric sol (i.e. a colloidal suspension of solid particles in a liquid) is finally formed. In particular, tetraethyl orthosilicate $C_5H_{26}O_4Si$ (98% TEOS, Sigma-Aldrich Inc.) and isopropyl alcohol C_3H_8O (99.7% , Sigma-Aldrich Inc.) are mixed together in stoichiometric ratio for 15 min on a magnetic stirrer, while heated at 50 °C. Subsequently, deionized water and nitric acid, HNO_3, are added in stoichiometric ratio and the solution is stirred for 2h, still heating at 50 °C. Nitric acid acts as a catalyst and indeed its role is to decrease the pH to prevent colloidal particles from precipitating. Finally, PP-fibres are thoroughly yet briefly immersed in the sol and then they are dried in a muffle oven at 50 degrees, as described in [Signorini 2018b, Signorini 2019a]. Fibre immersion is very rapid, a few minutes, unlike the process described by [Di Maida 2015] where it occurs for 2 hours. This choice is made to allow the scale-up of this technology to an industrial process. In the case of drawn PP fibres, production is economically sustainable because it is very rapid. However, it should be noted that the allotted time is insufficient to grow full-size arrays of silica nano-particles.

3.2 Surface activation with Piranha solution

3.2.1 Piranha solution

Piranha etch is a solution of sulphuric acid (H_2SO_4) and hydrogen peroxide (H_2O_2), generally used to remove organic residues off substrates, like for example in the microelectronics industry, to clean residue from silicon wafers. The peculiar feature exploited in this work is the strong oxidizing potential of the piranha solution. This aspect is attractive to hydroxylate most surfaces (i.e. through the addition of OH groups), making them hydrophilic. Several proportions of the two reactants can be crossed in the literature, as well as a basic variant that substitutes sulphuric acid with ammonia [Long 2004].

Two main stages can be distinguished when the action of the piranha solution is analysed.

- The first one consists of the **dehydration**, mainly conducted by sulphuric acid, which is highly hygroscopic. Dehydration, i.e. the removal of oxygen and hydrogen, occurs very quickly and due to its dramatic reactivity, the solution is traditionally associated to *piranha fish*. After dehydration, common organic materials are carbonized in a few instants.

- Again due to the presence of sulphuric acid, hydrogen peroxide is converted from a relatively mild oxidizing agent into a very aggressive one that dissolves elemental carbon, which is resistant to room-temperature aqueous reactions. This transformation, namely **oxidation**, can be considered as the energetically favourable dehydration of hydrogen peroxide to form hydronium ions, bisulfate ions, and, transiently, atomic oxygen:

  $$2\,SO_4 + H_2O_2 \rightarrow H_3O^+ + HSO_4^- + O$$

  This extremely reactive atomic oxygen species promotes dissolution of elemental carbon. Besides, the highly stable and typically graphite-like bonds typical of carbon allotropes, can be disrupted by an atomic oxygen, which directly attaches to a surface carbon to form a carbonyl group, see the schematic representation of the mechanism in Fig.3.1. In this way, the oxygen atom "steals"

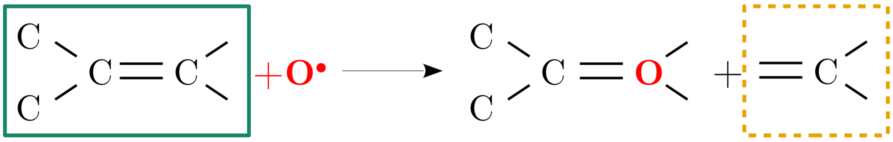

Figure 3.1: Oxidative mechanism that disrupts carbon allotropes' strong graphite covalent bonds

an electron bonding pair from the central carbon, forming the carbonyl group and simultaneously disrupting the bonds of the target carbon atom with one or more of its neighbours. The result is a domino effect in which a single atomic oxygen reaction triggers an unraveling process for the local bonding structure. The carbon removed by piranha solution may be either original residue or char from the dehydration step. The oxidation process is slower than the dehydration process, taking place over a period of minutes. The oxidation of carbon results as a gradual clearing of suspended soot and char left by the initial dehydration.

High purity reactants employed for the piranha solution are:

- Hydrogen peroxide, H_2O_2,
- Sulfuric acid 98%, H_2SO_4.

Sulfuric acid is gradually added to hydrogen peroxide in the 3/1 weight ratio and the solution is mixed for 15 minutes. The solution is mixed on a magnetic stirrer at ambient temperature in a covered beaker. Polypropylene fibres are then immersed for 15 minutes. The ongoing reaction triggered by the reactants of the piranha solution is strongly exothermic as shown by the gasses emanated during the process in Fig.3.2. Then, fibres are carefully rinsed with deionized water and dried in a muffle at 50°C for 24 hours.

Figure 3.2: Reactivity of piranha solution: exothermic reaction

Chapter 4

Testing methods

Contents

4.1 Fibres and PP-FRC chemical characterization

A FTIR (Fourier Transform Infrared Spectroscopy) VERTEX 70, (Bruker Optik GmbH, Ettlingen, Germany) infrared spectrometer (Figure4.1(a)) is employed to analyse the chemical composition of the surface of the PP-fibres, to assess the effects of the treatments discussed in Chapter 3. The test is carried out under Attenuated Total Reflection (ATR) mode, and the IR spectrum is recorded in the mid-infrared 4000–600 cm^{-1} wavenumber range.

Environmental SEM (Quanta FEI company, Eindhoven, The Netherlands (Figure4.1(b)) is used to highlight the presence of SiO_2 nanoparticles on the fibre surface as well as in the fibre-to-mortar interphase. Specimens are observed in low vacuum mode (pressure 0.68 Torr). Chemical element analysis is obtained in the sites of interest by Energy Dispersive X-ray (EDX) microanalysis using Inca software (Oxford Instruments, UK).


(a) (b)

Figure 4.1: E-SEM (a) and FT-IR (b) used for the characterization of the surface of the fibres.

4.2 Specimen manufacturing

4.2.1 Pull-out specimens

Specimens for fibre pull-out tests are manufactured using special formworks designed to align the fibre with the symmetry axis of the cylindrical mortar block, see Figure 4.2. The manufacturing process proceeds as follows:

- ⌀80 mm polyvinyl-chloride tubes are attached onto the bottom plate of the formwork and provide lateral confinement to the mortar; tubes are 30 mm long for this is the embedded length of the fibre;
- Fibre is tied to an anchoring system and pulled through the cylinder through a coaxial hole in the bottom plate; finally, each fibre is tensioned by a weight. Thus, fibres are aligned with the axis of the cylinders;
- After lubricating the formwork, cement mortar is poured in the cylinders and thoroughly compacted.

Specimens are cured for 8 days under ambient conditions (20 °C and 60−75% relative humidity) and finally stripped out.

Figure 4.2: Pull-out specimen manufacturing

4.2.2 Three-point bending specimens

To endorse the effective use in the practice for the FRC with enhanced adhesion at the interphase zone, three test set-ups are designed for bending tests, characterized by scaled dimensions. The actual dimensions of the specimens are mutually proportional, to warrant the consistency in terms of flexural behaviour. The length of the fibres is scaled accordingly. Effects of the surface treatments on PP fibres are therefore assessed from a small to a medium and eventually to a real scale.

4.2.2.1 Small-scale specimens

40 mm × 40 mm × 160 mm prismatic formworks are used to manufacture specimens for three-point (3-P) bending test. Formworks are sprayed with a silicone lubricant

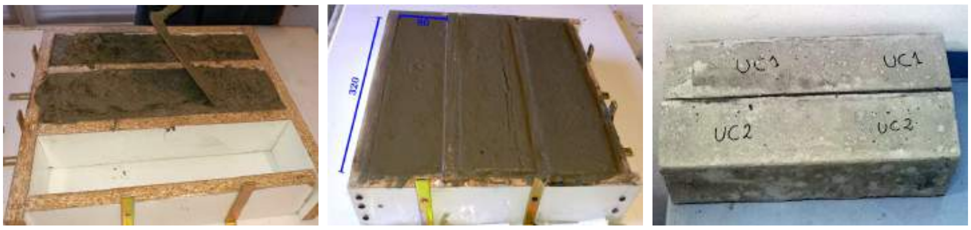

(a) Casting *(b) Specimens before curing* *(c) Specimens after stripping*

Figure 4.3: Medium-scale prismatic specimens manufacturing.

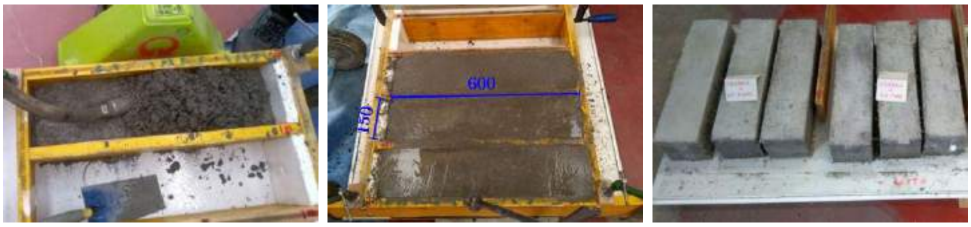

(a) Vibration of an intermediate concrete layer *(b) Specimens before curing* *(c) Specimens after stripping*

Figure 4.4: Large-scale prismatic specimens manufacturing.

to ease stripping. 3% vol. of 10-mm polypropylene fibres are mixed in the mortar powder and gently incorporated by means of low rotational speed mechanical stirrer, to warrant a randomly uniform distribution within the conglomerate. Then water was added and the mortar uniformly stirred. Curing is carried out under ambient conditions (20 °C and 60 − 75% relative humidity) for either 8 or 28 days.

4.2.2.2 Medium-scale specimens

80mm × 80mm × 320mm prismatic beams are cast in a plywood dismountable formwork. The surfaces of the formworks in contact with the cementitious paste are preliminarily laminated with resin and then sprayed with an hydrophobic coating to reduce water adsorption. The pre-mixed cementitious mortar (Geolite, Kerakoll) is stirred together with 20-mm-long PP fibres. As before, fibres/matrix volume ratio is 3%. Water is then added and the conglomerate is properly mixed with a mechanical stirrer, till a homogeneous mixture is obtained. Specimens are left to cure for 28 days before mechanical assessment. Of these 28 days, stripping is performed after the first 7 days, when specimens remain wrapped in a tight polypropylene bag to avoid any humidity exchange with the environment. The process is displayed in Figure 4.3.

4.2.2.3 Large-scale specimens

The large scale beams are manufactured accroding to the specifications of UNI guidelines, which prescribe a standard size of 150mm × 150mm × 600mm

(a) Pullout test *(b) 3-P bending test*

Figure 4.5: Setups of the mechanical tests

to assess the flexural behaviour of hardened concrete [UNI EN 12390-5 2019, Constantinescu 2016]. However, while the standards prescribe a 4-point configuration, the bending tests in the present contribution are conducted with the 3-point configuration in order to have consistent results with the small- and medium-size specimens. 4-mm long macro-fibres are now mixed with a sand-cement pre-mixed concrete, commonly used in screeds (Sabbiacemento Più, Sberna). Fibres are randomly distributed by means of a 25 dm^3 cement mixer. Prismatic specimens are cast in a wooden formwork, previously lubricated to ease stripping. The conglomerate is applied in three times and progressively vibrated to remove air bubbles that may induce the formation of bulk discontinuities in the concrete at the hardened stage (see Figure 4.4(a)). Specimens are stripped after three days (Figure 4.4(b)) and then are left to cure at 100% humidity for further 25 days (28 days total curing time). Three FRC beams are manufactured for each group (Figure 4.4(c)).

4.3 Mechanical characterization for FRC composites

4.3.1 Pull-out tests

Pull-out tests provide a measure of fibre resistance to being extracted from the matrix. Specimens are tested in an Instron 5567 electromechanical universal testing machine (UTM), under displacement control. The prescribed elongation rate is 1 mm/ min. The testing machine is equipped with a 1 kN load cell and pneumatic wedge clamps connected to the crosshead through a spherical hinge. The top clamping device is constituted by a special disk around which the fibre emerging from the specimen is wound and eventually blocked with a screw. The bottom clamp constraints the mortar cylinder in which the fibre is embedded. The test set-up is shown in Figure 4.5(a). At least five specimens are considered for each group/treatment.

4.3.2 Three-point bending tests

For the small and the medium scale tests, three-point (3P) bending tests are carried out in the same UTM adopted for pull-out tests, now equipped with a steel two-point support with knifes placed 10 cm and 20 cm apart, respectively (Figure4.6(a-b)).

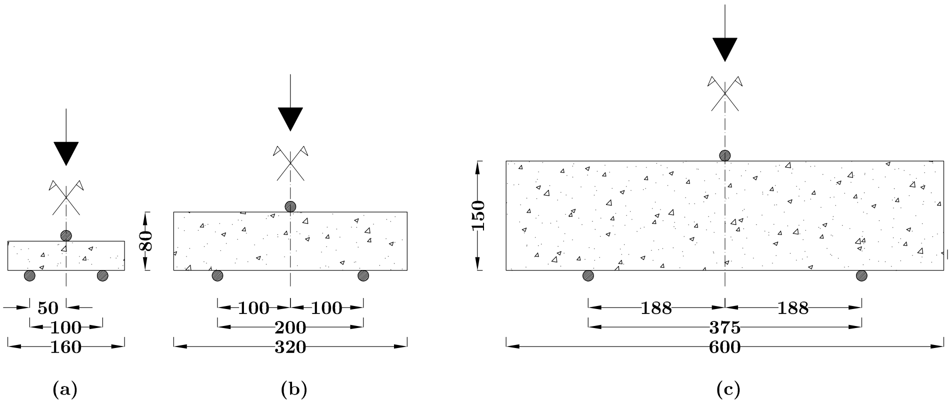

Figure 4.6: Three-point bending test set-ups

Table 4.1: Designed bending tests activity for PP-FRC composite materials with treated fibres

Scale	UTM	Load cell [kN]	A_c [cm^2]	L_s [mm]	L_f [mm]	Specs [no.]	CT [days]	$\dot{\delta}$ $[\frac{mm}{min}]$
Small	Instron	30	16	100	10	5	8-28	1
Medium	Instron	30	64	200	20	5	28	1
Large	Metrocom	300	225	375	40	3	28	1

A_c Cross-section of the beams;
L_s Span length;
L_f Length of the fibres;
CT Curing Time
$\dot{\delta}$ displacement rate of the test

Specimens are loaded at mid-span. Tests occur under displacement control at the nominal rate of 1 mm/ min. The test set-up is shown in Figure 4.5(b). Specimens are cured for either 8 or 28 days and 5 specimens are taken within each group. Large scale samples are tested at the Materials Laboratory of the San Marino University (RSM) by means of a Metrocom UTM equipped with a 300 kN load cell at the same displacement rate of the other tests. The dimensions of the specimens and of the experimental set up are displayed in Figure 4.6(c). A summary of the bending tests is outlined in Table 4.1.

CHAPTER 5

Results

Contents

5.1 Fibre surface investigation

Figures 5.1 and 5.2 compare the IR spectra of the silica coated fibres and of the piranha treated ones to the spectrum of the untreated group. IR-spectra mainly differ in the typical bands of carboxyl $-C{=}O$ and hydroxyl $O{-}H$ ligand stretching (in general, an alkyl, that is a ligand formed by removing an hydrogen from an alkane), that is in the wavenumber ranges $[3700 - 3000]$ and $[1800 - 1500]$ cm^{-1}. Such findings are consistent with those reported by [López-Buendía 2013, §3.1]. Etching with piranha solution induces a strong oxidation peak around $[3400 - 3300]$ cm^{-1}, consistently with the findings by [Ahsani 2015]. Indeed, intense absorption peaks in this interval correspond to the stretching of $O{-}H$ bond, which indicative of the formation of functional groups on the fibre's surface [Pavia 2008]. Accordingly, the oxidation process induces a reduction of the $C{-}H$ peak detected around $[2950 - 2700]$ as a consequence of the partial replacement of $-CH_3$ functional groups of the polymer with hydroxyl ones. Alongside the typical bands of PP, in the silica coated group only, the IR analysis highlights the presence of the silica-based functional groups $Si{-}O{-}Si$ and $Si{-}OH$, in the range $[1200 - 1000]$ and $[950 - 820]$ cm^{-1}, see also [Ahsani 2015, Wang 1996]. This confirms appears that rapid sol-gel deposition has been effective in modifying the fibre surface.

The fibre surface capability to retain mortar patches after failure is an indication of the interface bond strength. SEM investigation of the failure surface in bending is presented in Fig.5.3 for both the control (a) and the coated/etched groups (b,c). In the control group, the fibre surface appears scarred and scratched, presumably due to slippage and sliding friction, given that grooves are directed along the fibre

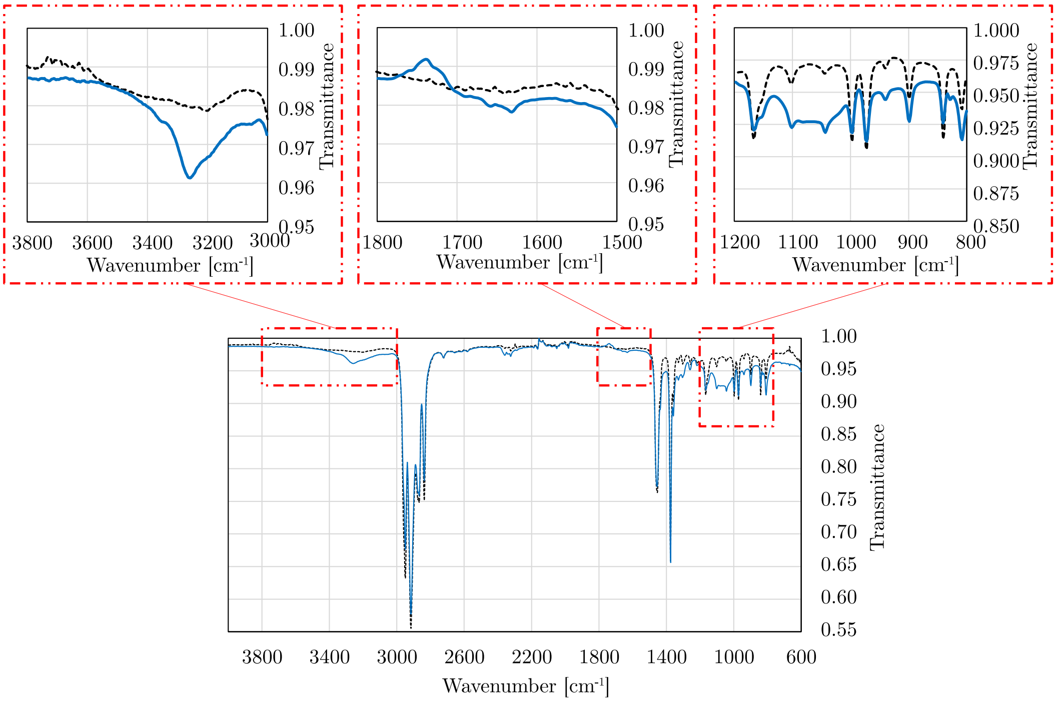

Figure 5.1: IR spectrum of uncoated (black, dashed) and silica coated (blue, solid) fibres

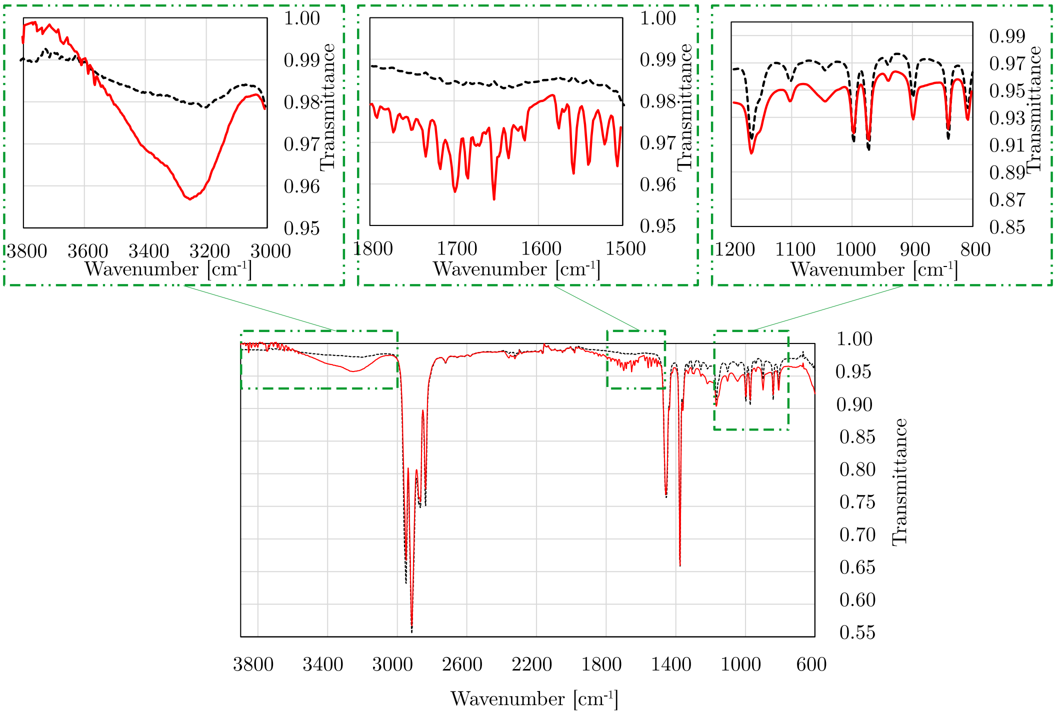

Figure 5.2: IR spectrum of uncoated (black, dashed) and piranha etched (red, solid) fibres

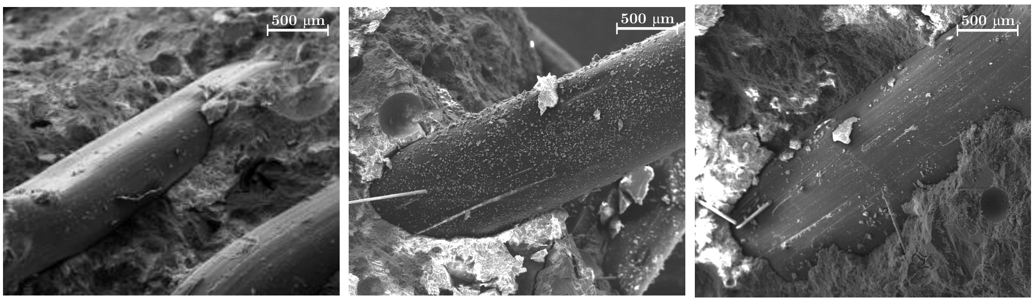

(a) *uncoated/untreated fibre* (b) *silica-coated fibre* (c) *piranha-etched fibre*

Figure 5.3: SEM 100x magnification of the failure surface of a specimen after bending test in the control (a), in the silica coated (b) and in the piranha etched (c) group

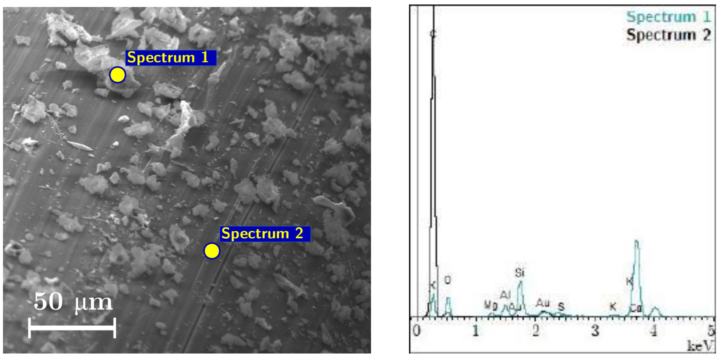

(a) *(b)*

Figure 5.4: SEM 800x magnification of the fibre surface after pull-out in the silica coated specimen: we appreciate diffused mortar grains adhering to the PP surface (a), as confirmed by relevant EDS spectra (b)

axis. Besides, only occasional mortar patches adhere to the surface. Conversely, fine closely-spaced mortar grains stick to the silica-coated specimen, whose smooth surface (with the exception of casual PP filament detachment, see [Bentur 1989] for the role of filaments in a PP yarn) is a good indication that failure now occurs in the "interphase region". This is a thin transition zone within the matrix, originally defined in micromechanics, that conveys the loading from the fibre surface to the outer matrix, the latter being insensitive to the details of the interaction (like fibre roughness or chemical bonds, see also the paper by [Amraei 2019] and references therein). Indeed, higher magnification reveals that the bonding mechanism in the coated specimen is diffused on the surface, see Fig.5.4(a). In fact, the "significant increase in roughness" of the coated group, already observed by [López-Buendía 2013], favours adhesion. EDS spectra of the fibre surface, illustrated in Fig.5.4(b) for silica-coated fibre only, support this picture. Indeed, they reveal that the particles attached to the fibre surface in Fig.5.4(a) are mortar grains. As suggested in [López-Buendía 2013], such grains are most likely originated from hydrated cement mineral nucleation. Focusing on etched fibre, a mixed behaviour is observed: indeed, the several superficial imperfections detected by SEM analysis can be ascribed to the corrosive action of

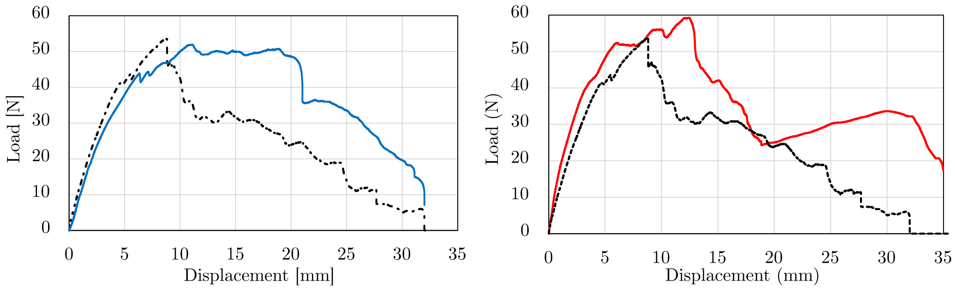

(a) *(a)*

Figure 5.5: Pull-out mean strength curves for the coated (SIL, solid blue) (a) and etched (PIR, solid red) (b) vs. uncoated (UC, dotted black) specimen groups

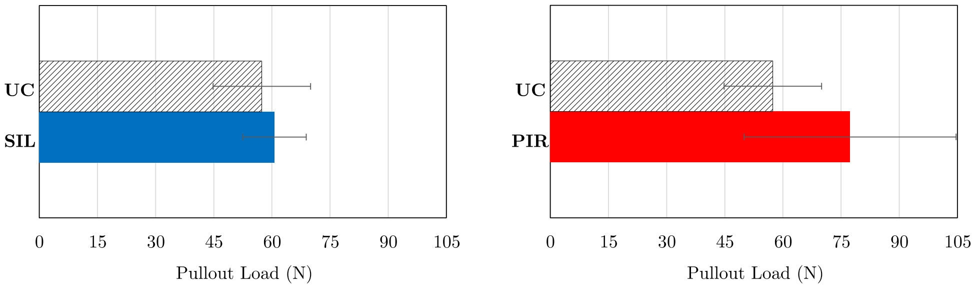

(a) *(b)*

Figure 5.6: Pull-out mean peak-strength for the control (UC, black) and the coated (SIL, blue) (a) and etched (PIR, red) (b) specimen groups

piranha solution. Besides the functionalization aimed to improve hydrophilicity, the increased roughness and the longitudinal holes generated by etching are adhesion poles for the embedding medium, which attaches to the fibres, even if the qualitative effect is not as clear as it is for the silica-coated group.

5.2 Mechanical performance

Both pull-out and 3-P bending tests are carried out according to the protocols reported in Section 4.3 and results are presented in the following section. With regard to bending tests, two slants are proposed to read the experimental outcome. First, since small scale tests are conducted at 8 and 28 days of curing time, the failure mechanisms as a function of the mortar strength are investigated [Signorini 2020b]. Furthermore, the effect of coupled scaling of test set-up and fibres' length is investigated and on the improvements in the mechanical behaviour correlated to the bridging effect that fibres achieve through the mid-span crack is analysed.

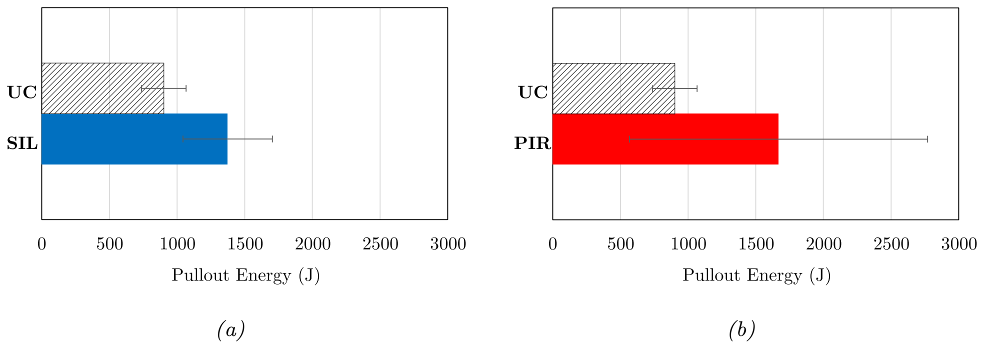

(a) *(b)*

Figure 5.7: Pull-out mean dissipated energy for coated (SIL, blue) (a) and etched (PIR, red) (b) vs. control (UC, black) specimen groups

Table 5.1: Mean pull-out load $\mu(P_{p,max})$ and dissipated energy $\mu(W_p)$ for the uncoated (UC), the silica-coated (SIL) and the piranha-etched (PIR) groups, with relevant standard deviation $\varsigma(\cdot)$, coefficient of variation (CoV) and relative variation across groups, Δ

Group	$P_{p,max}$				W_p			
	μ [N]	ς [N]	CoV [%]	Δ [%]	μ [N]	ς [N]	CoV [%]	Δ [%]
UC	57.4	12.6	21.9	—	939	239	25.4	—
SIL	60.7	8.2	13.5	+5.75	1365	344	25.2	+45.37
PIR	77.3	21.2	27.4	+34.7	1668	1101	66.0	+77.64

5.2.1 Pull-out tests

Mean pull-out strength curves are given in Fig.5.5, which shows a significant improvement of the silica-coated group over the uncotaed group, although the strengthening effect is not as strong as that reported for long bathing times, cfr.[Di Maida 2015]. In the uncoated group, a sudden strength loss occurs at the first cracking strength (FCS), followed by a softening behaviour. In contrast, similarly to the findings reported in [Di Maida 2015], a mild strength loss followed by a plastic-hardening behaviour is generally met in the coated group. Indeed, the strength curve of the coated group expresses a significant perfect-plastic behaviour followed by softening, while the control group is strongly softening (cfr.[Di Maida 2015, Fig.10] that shows hardening). A different behaviour is observed for FRC reinforced with piranha-etched fibres (PIR). Indeed, the treatment induces a higher pullout load than both uncoated (UC) and silica-coated (SIL) fibres. However, this beneficial effect is balanced by a scattered post-peak behaviour, which moves from softening (especially for specimens that attain the highest pullout load values) to plastic-hardening (especially for specimens that attain the lower pullout load values). As a result, mechanical parameters are characterized by high fluctuation, i.e. standard deviation. The important role of the post-cracking performance is well illustrated by the bar chart of Fig.5.7, which describes the mean dissipated energy at pull-out, and shows that a 45% and 77% improvements over the control (uncoated) group is achieved for SIL and PIR, respectively (see also Tab.5.1). Most impor-

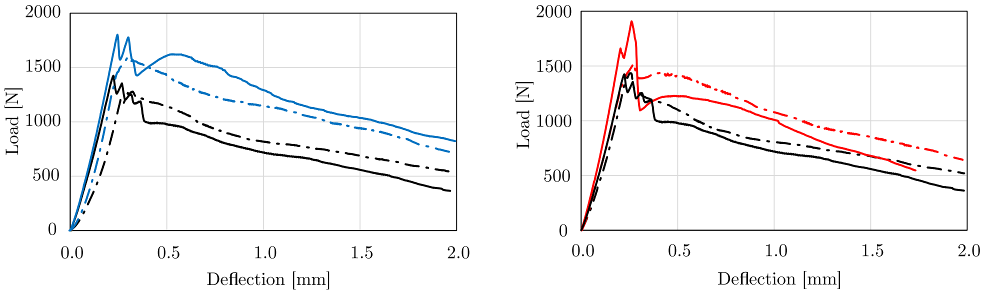

(a) silica-coated groups

(b) piranha-etched groups

Figure 5.8: 3P bending test mean strength curves. Uncoated (black), silica coated (blue) and piranha-etched (red) for each curing time (8 days, dash-dotted lines and 28 days, solid lines)

tantly, for SIL group, this benefit is obtained while retaining the same coefficient of variation, whence it translates directly (i.e. linearly) in terms of design values [Signorini 2019c]. A different outcome is obtained for the PIR group, which presents a high data fluctuation, as already pointed out. This can be ascribed to the higher pre-peak energy release after triggering the debonding stage, which damages fibre-to-matrix interphase [Zia 2017]. Fig.5.6 indicates that, as expected, the peak strength, that is related to the fibre breaking free from the matrix and starting to slip, is little affected by the nano-coating. On the other hand, etching highly affects the peak load, due to a better interlocking, both chemically and mechanically, at the interface [Felekoglu 2009]. However, it also shows that standard deviation is greatly reduced for SIL, whence slippage begins at a consistent threshold, while as expected, the higher peak strength for PIR corresponds to a higher deviation in its value, even if slightly. Tab.5.1 gathers the main mechanical performance indices obtained in pull-out testing.

5.2.2 Bending tests: effect of curing time on failure mechanism in flexure

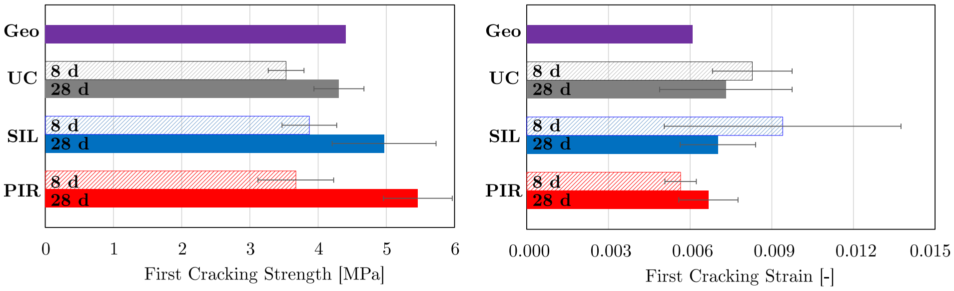

Figure 5.9: First cracking strength and strain in 3P bending for all test groups: plain mortar (GEO, violet), control at 8 and 28 day curing (UC8 and UC28, grey), silica coated at 8 and 28 day curing (SIL8 and SIL28, blue) and piranha-etched at 8 and 28 day curing (PIR8 and PIR28, red)

The mean strength curve in 3P bending is presented in Fig.5.8 for all test groups and shows that the addition of fibres mainly contributes to improve toughness. In

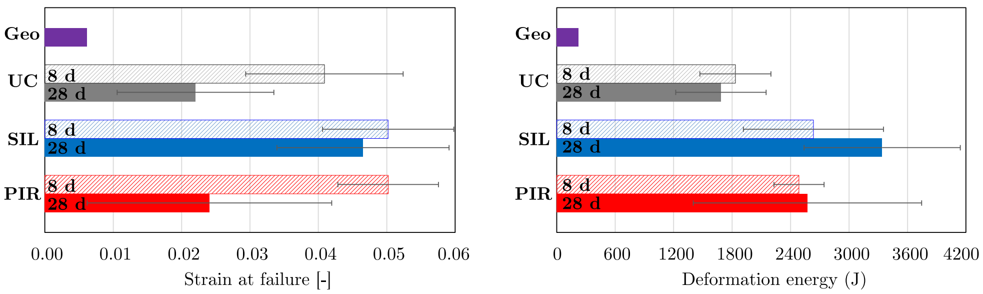

(a) *(b)*

Figure 5.10: 3P bending strain (a) and energy dissipated at failure (b) across all test groups: plain mortar (GEO, violet), control at 8 and 28 day curing (UC8 and UC28, grey), silica coated at 8 and 28 day curing (SIL8 and SIL28, blue) and piranha-etched at 8 and 28 day curing (PIR8 and PIR28, red)

fact, as for pull-out, the post-peak behaviour shifts from fragile (plain mortar) to softening (uncoated fibres) to plastic-softening (coated and etched fibres). It is interesting to compare such results with those given in [Di Maida 2018, Fig.8] for the silica-coated groups, concerning notched beams, that present a steep fall after peak and then rise.

To better elucidate the main performance characteristics, Fig.5.9 presents a bar-chart comparison of the First Cracking Strength (FCS) and strain across all groups. As already observed by [Santos 2005], at low percentage, fibre addition brings only a weakly positive effect on the first cracking strength, as fibres offer tensile strength and yet reduce the mortar resisting cross-section in compression. In particular, the improvement observed for the silica coated group at 28 day curing (SIL28) is in line with the findings in [López-Buendía 2013]. As already noted in the pullout tests, the PIR group at 28-day curing time is characterized by a remarkable and consistent enhancement of the FCS, which strongly delays the crack triggering, dissipating high pre-peak energy. A diverse trend is observed for early cured mortar. A similar behaviour is encountered for the first cracking strain, that is marginally affected by fibres and curing. Indeed, as it might be expected, fibres promote ductility, while curing acts in the opposite direction. The only exception is noted for PIR group, albeit the the difference in the mean values is slight and the standard deviation bands of PIR8 and PIR28 intersect. Such trends are much more pronounced in the post-cracking regime, as the deformation at 40% of FCS shown in Fig.5.10 (a) well illustrates. The improvement is particularly significant at 28 days curing for the silica-coated group, which presents a 110% increase over the uncoated group and a remarkable five-fold improvement over plain mortar, see Tab.5.3. In Tabs.Tabs.5.2 and 5.3, Δ_{SIL}% and Δ_{PIR}% indicate the percentage improvement of the relevant characteristic of SIL and PIR groups over the UC group, respectively. For piranha etched specimens a 23% increase over the UC group is observed at 8 day curing, while a lower benefit appears after 28 days. This effect can be ascribed again to the high FCS achieved (+27% with respect to UC), and consequently a sudden release of mechanical energy which tends to deteriorate the interphase region. Fig.5.10 (b)

Table 5.2: Main mechanical performance indices at 8 day *curing time*

Characteristic	**Unit**	**UC**	**SIL**	$\Delta_{SIL}\%$	**PIR**	$\Delta_{PIR}\%$
Deformation Energy	J	1834	2635	+44%	2486	+36%
1st Cracking Strength	MPa	3.531	3.872	+10%	3.673	+4%
1st Cracking Strain	mstrain	8.3	9.4	+13%	11.6	+40%
Strain at failure	mstrain	41	50	+23%	50	+23%
Elastic Modulus	MPa	662	760	+15%	660	−%

Table 5.3: Main mechanical performance indices at 28 day *curing time*

Characteristic	**Unit**	**UC**	**SIL**	$\Delta_{SIL}\%$	**PIR**	$\Delta_{PIR}\%$
Deformation Energy	J	1685	3340	+98%	2573	+53%
1st Cracking Strength	MPa	4.306	4.967	+15%	5.467	+27%
1st Cracking Strain	mstrain	7.3	7.0	−4%	6.7	−9%
Strain at failure	mstrain	22	47	+110%	24	+9%
Elastic Modulus	MPa	701	745	+6%	832	+19%

presents the deformation energy dissipated at failure (evaluated as the area under the load-deflection curves consistently truncated at a fixed deflection of 2 mm) and shows that silica coating imparts an outstanding 44% and 90% improvement over the uncoated group, respectively at 8 and 28 day curing, in terms of mean values. Accordingly, piranha etching induces a positive effect on toughness around 36% and 53%, for the two curing times. Remarkably, curing exhibits a significant positive effect on energy dissipation only in the treated groups (see Tab.5.4), which fact seems to provide evidence for a shift from a delamination-dominated scenario to a matrix-dominated failure. Again this outcome is clearer for the silica-coated group (+27%) than for the piranha-treated group (+4%). Indeed, the former appears to increase the fibre-to-matrix bond strength beyond the interphase strength, and therefore failure moves from the fibre-to-matrix interface to within the interphase zone, that is sensitive to matrix curing. The reduction in data scattering observed in the silica coated groups appears to point in the same direction, since delamination

Table 5.4: The role of curing time on mechanical performance

Characteristic	Δ% 28 vs. 8 day curing		
	UC	**SIL**	**PIR**
1st Cracking Strength	+22%	+28%	+49%
1st Cracking Strain	−12%	−25%	−42%
Elastic Modulus	+6%	−2%	+18%
Strain at failure	−46%	−7%	−52%
Deformation Energy	−8%	+27%	+4%

is typically inconsistent compared to matrix fracture.

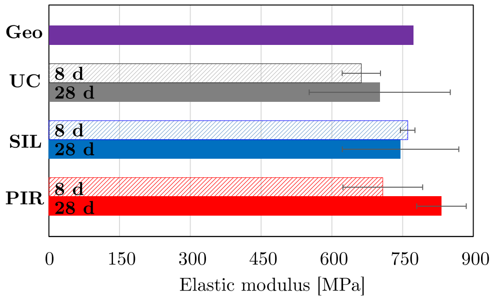

Figure 5.11: 3P bending (secant) elastic modulus, estimated across all test groups: plain mortar (GEO, violet), control at 8 and 28 day curing (UC8 and UC28, grey), silica coated at 8 and 28 day curing (SIL8 and SIL28, blue), and piranha-etched at 8 and 28 day curing (PIR8 and PIR28, red)

Fig.5.11 illustrates the variation of the secant elastic modulus across all groups. As expected, addition of fibres that are softer (i.e. more compliant) than the matrix itself produces a global modulus reduction. However, results indicate that an approach merely based on the Rule of Mixture, which accounts only for the fibre-to-matrix volume fraction, is too simplistic, in consideration of the fact that coating/treatment is capable of restoring the modulus of plain mortar and substantially reduce data scattering. This effect is particularly significant as far as the PIR group is concerned after complete curing of the mortar. Indeed, PIR28 group exhibits a stiffer pre-peak $\sigma - \varepsilon$ branch than the plain mortar, being also more consistent than the other groups at 28-day curing (lower coefficient of variance). For this, the effect of the mortar strength (i.e. direct consequence of curing time) is substantial for piranha treated group (+18% for the secant modulus at 28-day curing with respect to 8-day curing).
Tab.5.4 elucidates the effect of the curing time on the mechanical performance. It is noteworthy that the curing time has the same effect both on the uncoated group and on the coated/etched groups in terms of FCS and of elastic modulus. This suggests that such properties are related to the performance of mortar, that is affected by curing time and unresponsive to fibre coating. In contrast, ultimate deformation and dissipated energy at failure strongly rely on the role of fibres and therefore on the presence of the coating. A mixed condition occurs for the first cracking deformation.

5.2.3 Bending tests: bridging effects at different scales

The study of the crack and in particular the control of crack width in cementitious materials is still a debated research topic, despite several attempts to provide promising technological solutions and predictive models. In unreinforced concrete members, cracks trigger at the final part of the elastic branch of the constitutive law, before failure (around $0.7 f_{ct}$) [Cedolin 1987]. In this case we generally deal with microcracks, which soften the overall tensile behaviour of the conglomerate. When microcracks join together in the more loaded section, a major crack triggers and failure is procrastinated till the bridging effect of grains acted through mutual locking is able to support the applied loading. Generally, this extreme contribution to resistance is quite modest and it is as more important as the conglomerate is weaker (i.e. high strength concretes exhibit lower ductility). Some analytical models are proposed to take into account this effect [Stang 1992]. Oriented fibres distributed in the zone in traction may provide a further contribution to concrete as crack bridging elements and even produce a strain-hardening behaviour after the tensile strength is reached. Hence, fibres act in the post-peak stage in FRC, increasing the carried stress through the main crack [Stang 1995]. The overall effect is given by combining the grain interlocking and the fibre bridging action [Li 1993, Fig.6]. According to the studies by [Brincker 1997] in pure tensile tests, the combination of the brittle nature of the conglomerate combined with the pull-out ductile behaviour of fibres in the debonding stage results in a plastic law.

In this section, we compare the results obtained in 3P bending tests in medium and large scale with the reference outcomes provided in the previous sections. In Figures 5.13 and 5.14 the mean strength curves for SIL and PIR groups are compared with the uncoated group (UC) at medium (M) and large (L) scale, respectively. This experimental activity is carried out to evaluate the possible scale effect that may influence the mechanical behaviour of FRC beams in bending. Indeed, since the cracking phenomenon is discrete in nature, the changing in the fibres' length and grain size may affect the overall response in a non-trivial way [Kim 2010]. For this reason, as already described in Chapter 2, three different scales for bending tests are considered among which the medium scale considers FRC beams where fibres are scaled accordingly to the dimensions of the beams, but mortar aggregates are maintained as fine as in the small (S) scale. Besides, the large scale comprises FRC beams with both fibres and average grain size scaled accordingly. Analysing the mean curves, the treatments on the fibres produce a remarkable effect in all the tests. Shifting from S to L scale, a different behaviour, in general, is observed. Indeed, the higher length of the fibres offers a more effective bridging effect for the mid-span crack and an enhanced stress transfer (see Figure 5.12). This effect results in a more pronounced strain-hardening branch after the first cracking peak, independently of the fibres' treatment. S scale curves consistently present a softening (or in the best case, plastic) post-peak branch. Contrarily, for M and L scales it is possible to define as ultimate strength or load (US or UL) the maximum strength (load) reached in the hardening post-peak stage, being higher than FCS. In Tables 5.5 and 5.6 the toughness and strength are reported for M and L scale, respectively.

Table 5.5: Main mechanical performance indices at the medium scale (MS)

Characteristic	**Unit**	**UC**	**SIL**	$\Delta_{SIL}\%$	**PIR**	$\Delta_{PIR}\%$
Specific deformation Energy	J/cm^3	229	332	+45%	280	+22%
1st Cracking Strength	MPa	3.27	3.49	+7%	3.08	−6%
Ultimate Strength	MPa	3.65	5.07	+39%	4.66	+28%

Table 5.6: Main mechanical performance indices at the large scale (LS)

Characteristic	Unit	UC	SIL	$\Delta_{SIL}\%$	PIR	$\Delta_{PIR}\%$
Specific deformation Energy	J/cm^3	199	233	+17%	255	+28%
1st Cracking Strength	MPa	4.22	4.45	+5%	5.34	+27%
Ultimate Strength	MPa	4.37	5.24	+20%	5.58	+28%

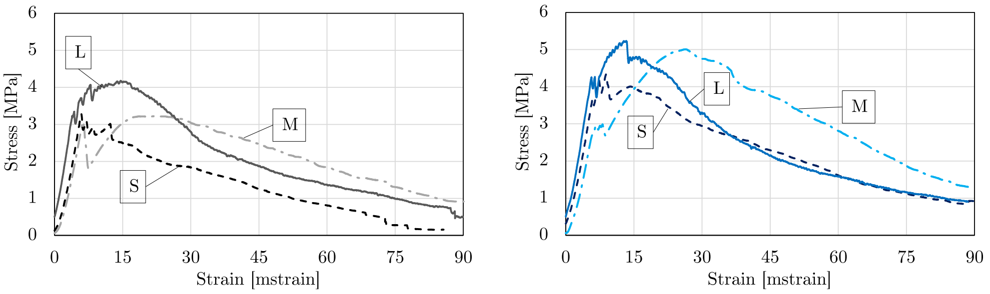

(a) Uncoated/untreated

(b) Silica coated

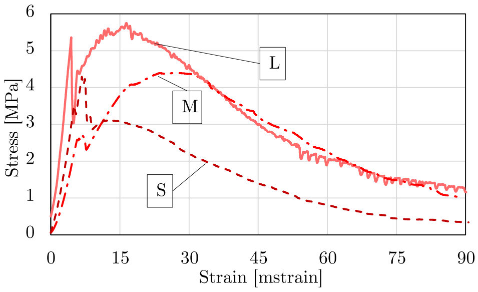

(c) Piranha etched

Figure 5.12: Mean stress-strain curves in 3P bending tests at different scales for the tested groups. Small (S), medium (M) and large (L) scale are plotted.

Contrarily to what shown in the Section 5.2.2, where the actual dissipated energy is provided (i.e. area under the load-displacement curve [J]) it is now computed the *specific* dissipated energy, which represents the area under the stress-strain curve, namely energy per unit volume [J/m^3]. In other words, values in Tables 5.5 and 5.6 are calculated in the following way:

$$W = \sum_{i=1}^{N} \left(F_i + F_{i+1}\right) \hat{\eta} \cdot \frac{\left(\delta_i - \delta_{i+1}\right)}{2} \hat{\gamma} \tag{5.1}$$

In Eqn.(5.1), W is the specific energy, N is the number of acquired data up to 2 mm of displacement, $(\delta_i; F_i)$ and $(\delta_{i+1}; F_{i+1})$ are the i-th and the $(i+1)$-th couple of measured values of displacement and load, respectively. The coefficients $\hat{\eta}$ and $\hat{\gamma}$ derive from the classical Navier theory and comprise geometrical parameters which refer to the specific test set-up. Namely:

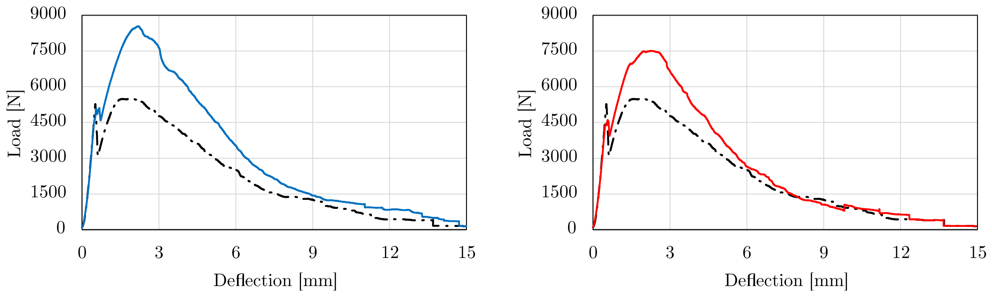

(a) SIL vs. UC

(b) PIR vs. UC

Figure 5.13: 3P bending test mean strength curves at medium (M) scale. Uncoated (black), silica coated (blue) and piranha-etched (red)

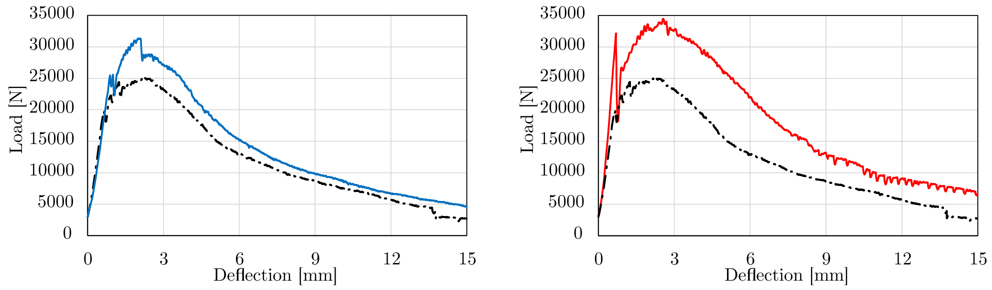

(a) SIL vs. UC

(b) PIR vs. UC

Figure 5.14: 3P bending test mean strength curves at large (L) scale. Uncoated (black), silica coated (blue) and piranha-etched (red)

$$\hat{\eta} = \frac{2}{3}\frac{bh^2}{L_s} \qquad \hat{\gamma} = \frac{L_s^2}{6h} \tag{5.2}$$

where b and h are the cross-section dimensions and L_s is the span length (recalling nomenclature adopted Table 4.1).

Bar-charts in Fig. 5.15(a) present the energy dissipation capability for the three groups of specimens across the three test scales. Within each scale, fibre treatments remarkably improve the toughness of the beams, and apart from L scale where the effects of the treatments are almost equivalent, SIL appears to be the more effective solution, also taking into account the average reduced data scattering. Scale effect seems to have an impact on toughness moving from small to medium scale. A minor difference is observed instead moving from medium to large scale.

5.3 Conclusive remarks

The effect of a rapid acid-catalysed silica coating obtained by sol-gel deposition and an effective etching treatment are considered. These treatments are applied to draw-wire polypropylene fibres to be dispersed in Fibre Reinforced Concrete (FRC). Silica coating in particular is very effective to improve the fibre-to-matrix bond

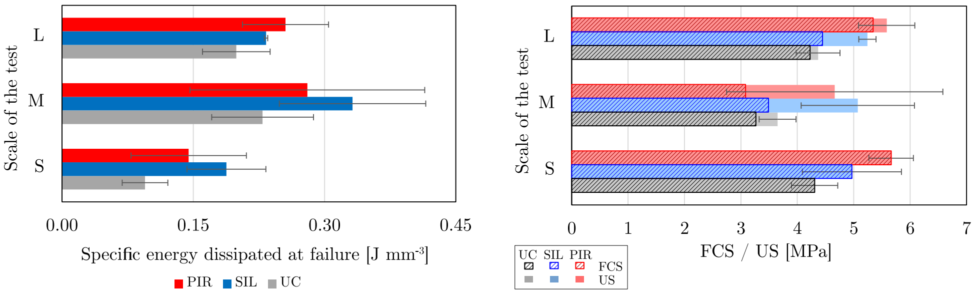

(a) Dissipated energy

(b) FCS and US

Figure 5.15: Mechanical parameters bar-charts as a function of the length of the scale of the test.

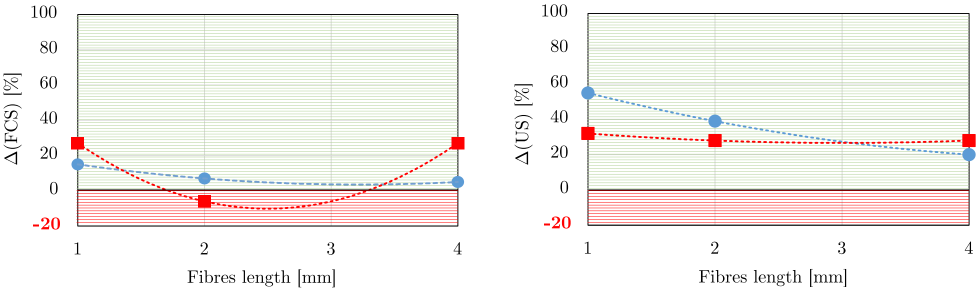

(a) First cracking strength

(b) Ultimate (residual) strength

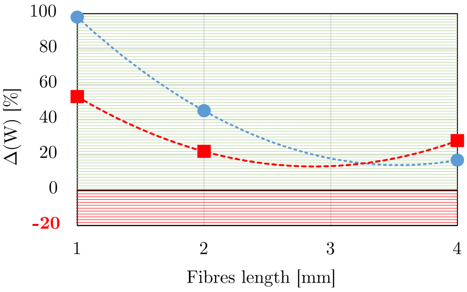

(c) Dissipated energy

Figure 5.16: Enhancement of mechanical parameters as a function of the length of the fibres, namely the scale of the test.

strength, through the deposition of an inhomogeneous surface layer, which increases the specific area of the fibre and functional groups deposited on the surface enhance hydrophilicity. Piranha etching is proven to modify the fibre surface through a highly oxidative action. Besides, surface is also slightly roughened and hence a mechanical interlocking is promoted. As a result, the long softening post-peak behaviour, that is typical of FRC at mid/low fibre dosage (including the case of steel fibres), turns into a plastic-softening response (or, possibly, hardening), when short (1 mm) fibres are adopted. In this context, the role of curing time is assessed for the first time, in an attempt to elucidate the failure mechanism. In general terms, it is found that curing acts in standard way, for it reduces ductility and increases strength. However, most interestingly, curing is found to play little role in the energy dissipation capability of uncoated FRC, because strength gain compensates ductility loss. On the other hand, curing has a favourable effect on silica-coated FRC for it enhances energy dissipation, while it little impairs ductility. This result, together with the observation that data scattering is significantly reduced, suggests that the failure mechanism moves from the stronger fibre-to-matrix interface, to the weaker interphase zone. Indeed, the former mechanism takes the form of interface delamination, which is inconsistent by nature and little sensitive to curing, while the latter is interphase failure, which depends on the matrix performance. This analysis indicates that further interface bond enhancement may be irrelevant to the global mechanical behaviour. Instead, efforts should be directed towards improving the interphase/matrix performance, for example by reducing porosity. A different impact of curing is observed for piranha etched fibres in FRC. Enhanced adhesion promoted by both mechanical and chemical bond induces an astonishing gain in terms of pre-peak mechanical performance, which at 28-day curing presents a 49% increase with respect to 8-day curing FCS. However, this effect is compensated by a notable ductility decrease (-42% and 52% for first cracking strain and strain at 0.4 FCS, respectively). Therefore, curing time has a little global effect on dissipated energy. Nevertheless, this etching technique provides beneficial effects, if compared to FRC samples with uncoated fibres, and its effectiveness is comparable to silica coating. Therefore, a combined investigation of interface and matrix strengthening (here studied acting on curing time) appears to be an interesting methodology to better understand the failure mechanism. If focus is set on the scale effect induced by the fibre length and by the average grain size of the embedding medium, it is observed that fibres provide a remarkable bridging action when longer than 2 mm. Indeed, a substantial modification in the constitutive law in bending for FRC is detected, since a pronounced hardening post-peak branch is obtained. The maximum load measured in the post-peak branch is almost equal (for UC) or even notably higher (for SIL and PIR) than the first cracking strength. On the other hand, small scale specimens exhibit a post-peak ultimate strength that is lower than FCS, and therefore it can be more properly labelled as *residual strength (RS)*. Figure 5.16 shows the enhancements for the main mechanical performance, $\Delta(\cdot)$ as a function of the scale (i.e. the fibres length), achieved with SIL and PIR surface treatments. W is the specific dissipated energy. A quadratic curve-fit is also reported. As expected, across all the test scales treatments have a little effect on the

FCS, which is dominated by the matrix quality, even if a fairly promising increase around 30% is obtained for PIR, consistently for S and L scale, and unexpectedly not confirmed in the M scale. For SIL a slightly decreasing trend is observed, when scale increase. When US (RS) is considered across all groups, a more repetitive trend is observed, but contrarily to FCS, the enhancement is significant and SIL has a more effective impact for S scale, than PIR. This can be ascribed to the post-peak enhancement action supplied by SIL coating, which is transversally observed through all test scales. For this reason, where post-peak branch is strongly softening (i.e. small scale, UC) the relative contribution of silica is prominent, because it switch the constitutive law from softening to plastic-hardening, thus increasing the area under the curve. Contrarily, in M and L scale, the hardening behaviour is mainly given by the fibres bridging action itself, and secondly due to the treatment, which provides an increase of US but its relative impact is lower. The descending trend is also evident for the dissipated energy. SIL prevails over PIR for small and medium scale, while at real scale the increase in toughness is quite similar, assessed around 20 % to 30 %, which is a very interesting result for practical applications. The lower enhancement generally observed for L scale tests, can be also argued observing that differently to S and M scales, mortar grains have a significantly higher mean diameter. This may produce an increasing interlocking effect supplied by concrete grains, which is common to all groups, independently of the surface functionalization.

Bibliography

[Abrahamson 1999] John Abrahamson, Peter G Wiles and Brian L Rhoades. *Structure of carbon fibres found on carbon arc anodes.* Carbon, vol. 11, no. 37, pages 1873–1874, 1999. (Cited on page 61.)

[ACI 116 R 2000] ACI 116 R. *Cement and concrete terminology.* Technical report, American Concrete Institute, 2000. (Cited on page 137.)

[ACI 549.4R-13 2013] ACI 549.4R-13. Guide to design and construction of externally bonded fabric-reinforced cementitious matrix (FRCM) systems for repair and strengthening concrete and masonry structures. American Concrete Institute, 2013. (Cited on pages 6, 15, 86, 100 and 114.)

[Ahsani 2015] Mina Ahsani and Reza Yegani. *Study on the fouling behavior of silica nanocomposite modified polypropylene membrane in purification of collagen protein.* Chemical engineering research and design, vol. 102, pages 261–273, 2015. (Cited on page 153.)

[Amraei 2019] Jafar Amraei, Jafar E Jam, Behrouz Arab and Roohollah D Firouz-Abadi. *Effect of interphase zone on the overall elastic properties of nanoparticle-reinforced polymer nanocomposites.* Journal of Composite Materials, vol. 53, no. 9, pages 1261–1274, 2019. (Cited on pages 72 and 155.)

[Arboleda 2014a] Diana Arboleda. *Fabric Reinforced Cementitious Matrix (FRCM) Composites for Infrastructure Strengthening and Rehabilitation: Characterization Methods.* PhD thesis, University of Miami, 2014. Open Access Dissertation. Paper 1282. (Cited on pages 23, 24, 46, 96, 102, 114 and 124.)

[Arboleda 2014b] Diana Arboleda, Saman Babaeidarabad, CDL Hays and Antonio Nanni. *Durability of Fabric Reinforced Cementitious Matrix (FRCM) Composites.* In Proceedings of the 7th International Conference on FRP Composites in Civil Engineering. International Institute for FRP in Construction (IIFC), 2014. Vancouver, 20-22 August 2014. (Cited on pages 24, 114 and 115.)

[Arduini 2010] Marco Arduini, Andrea Nicoletti and Paolo Corrado. Il rinforzo con materiali compositi fibrosi frp per strutture in cemento armato, muratura, legno: esempi di calcolo, modalita operative, prescrizioni tecniche. Maggioli, 2010. (Cited on page 14.)

[Ascione 2018] Francesco Ascione, Marco Lamberti, Annalisa Napoli and Roberto Realfonzo. *SRP/SRG Strips Bonded to Concrete Substrate: Experimental Characterization.* Special Publication, vol. 326, pages 110–1, 2018. (Cited on page 5.)

[ASTM C 947-03 2003] ASTM C 947-03. *Standard Test Method for Flexural Properties of Thin-Section Glass-Fiber-Reinforced Concrete (Using Simple Beam With Third-Point Loading).* Technical report, American Society for Testing and Materials International, 2003. (Cited on pages 24 and 26.)

[ASTM D 1141 2013] ASTM D 1141. *Standard Practice for the Preparation of Substitute Ocean Water.* Technical report, American Society for Testing and Materials International, 2013. (Cited on page 116.)

[ASTM D 2247 2002] ASTM D 2247. *Standard Practice for Testing Water Resistance of Coatings in 100% Relative Humidity.* Technical report, American Society for Testing and Materials International, 2002. (Cited on page 117.)

[Babaeidarabad 2013] Saman Babaeidarabad, Francisco De Caso and Antonio Nanni. *URM walls strengthened with fabric-reinforced cementitious matrix composite subjected to diagonal compression.* Journal of Composites for Construction, vol. 18, no. 2, page 04013045, 2013. (Cited on page 11.)

[Babaeidarabad 2014] Saman Babaeidarabad, Giovanni Loreto and Antonio Nanni. *Flexural strengthening of RC beams with an externally bonded fabric-reinforced cementitious matrix.* Journal of Composites for Construction, vol. 18, no. 5, page 04014009, 2014. (Cited on page 13.)

[Badanoiu 2003] Alina Badanoiu and Jonas Holmgren. *Cementitious composites reinforced with continuous carbon fibres for strengthening of concrete structures.* Cement and Concrete Composites, vol. 25, no. 3, pages 387–394, 2003. (Cited on page 87.)

[Balsamo 2016] Alberto Balsamo, Domenico Asprone, Ivano Iovinella, Gennaro Maddaloni, Costantino Menna, Andrea Prota, Francesca Ceroni and Alberto Zinno. *Effectiveness of inorganic matrix–grid composites for strengthening masonry walls.* In Brick and Block Masonry, pages 2013–2020. CRC Press, 2016. (Cited on page 11.)

[Balsamo 2018] Alberto Balsamo, Alessio Cascardi, Marco Di Ludovico, Maria Antonietta Aiello and Giulio Morandini. *Analytical study on the effectiveness of the FRCM-confinement of masonry columns.* In Construction Pathology, Rehabilitation. Technology and Heritage Management, 2018. (Cited on page 13.)

[Banholzer 2006] Björn Banholzer, Tanja Brockmann and Wolfgang Brameshuber. *Material and bonding characteristics for dimensioning and modelling of textile reinforced concrete (TRC) elements.* Materials and structures, vol. 39, no. 8, pages 749–763, 2006. (Cited on page 115.)

[Barton 2005] B Barton, E Wobbe, Lokeswarappa R Dharani, P Silva, Victor Birman, Antonio Nanni, Tarek Alkhrdaji, J Thomas and G Tunis. *Characterization of reinforced concrete beams strengthened by steel reinforced polymer* *and grout (SRP and SRG) composites.* Materials Science and Engineering: A, vol. 412, no. 1-2, pages 129–136, 2005. (Cited on page 5.)

[Beckman 2007] Wendy Beckman, V Shanov and M Schulz. *UC Researchers Shatter World Records with Length of Carbon Nanotube Arrays.* University of Cincinnati, 2007. (Cited on page 62.)

[Bekou 2011] Sofia Bekou and Davide Mattia. *Wetting of nanotubes.* Current Opinion in Colloid & Interface Science, vol. 16, no. 4, pages 259–265, 2011. (Cited on page 63.)

[Bentur 1989] Arnon Bentur, Sidney Mindess and Gary L. Vondran. *Bonding in polypropylene fibre reinforced concretes.* International Journal of Cement Composites and Lightweight Concrete, vol. 11, no. 3, pages 153–158, 1989. (Cited on page 155.)

[Bentur 2006] Arnon Bentur and Sidney Mindess. Fibre reinforced cementitious composites. CRC Press, 2006. (Cited on pages 6, 15, 137 and 138.)

[Bianchi 2013] Giuseppe Bianchi, Diana Arboleda, Francesca Giulia Carozzi, Carlo Poggi and Antonio Nanni. *Fabric reinforced cementitious matrix (FRCM) materials for structural rehabilitation.* In Proceedings of the 39th IAHS World Congress, Milan, Italy, pages 17–20, 2013. (Cited on page 24.)

[Bisby 2013] Luke Bisby, Tim Stratford, Courtney Hart and Sinead Farren. *Fire performance of well-anchored TRM, FRCM and FRP flexural strengthening systems.* In Advanced Composites in Construction (ACIC), Queen's University Belfast, September 2013. (Cited on page 88.)

[Borri 2015] Antonio Borri, Giulio Castori, Marco Corradi and Emanuela Speranzini. *Durability analysis for FRP and composites in civil applications.* In Key Engineering Materials, volume 624, pages 421–428. Trans Tech Publ, 2015. (Cited on page 17.)

[Bournas 2009] Dionysios A Bournas, Thanasis C Triantafillou, K Zygouris and F Stavropoulos. *Textile-reinforced mortar versus FRP jacketing in seismic retrofitting of RC columns with continuous or lap-spliced deformed bars.* Journal of Composites for Construction, vol. 13, no. 5, pages 360–371, 2009. (Cited on page 6.)

[Brameshuber 2006] Wolfgang Brameshuber. Report 36: Textile reinforced concrete-state-of-the-art report of RILEM TC 201-TRC, volume 36. RILEM publications, 2006. (Cited on page 113.)

[Brincker 1997] Rune Brincker, J Simonsen and W Hansen. *Some aspects of formation of cracks in FRC with main reinforcement.* Nordic Concrete Research, no. 20, pages 1–15, 1997. (Cited on page 162.)

[Brinker 2013] C Jeffrey Brinker and George W Scherer. Sol-gel science: the physics and chemistry of sol-gel processing. Academic press, 2013. (Cited on page 143.)

[Brunauer 1938] Stephen Brunauer, Paul Hugh Emmett and Edward Teller. *Adsorption of gases in multimolecular layers.* Journal of the American chemical society, vol. 60, no. 2, pages 309–319, 1938. (Cited on page 29.)

[Bunsell 2005] Anthony Roland Bunsell and Jacques Renard. Fundamentals of fibre reinforced composite materials. CRC Press, 2005. (Cited on page 10.)

[Butler 2009] Marko Butler, Viktor Mechtcherine and Simone Hempel. *Experimental investigations on the durability of fibre–matrix interfaces in textile-reinforced concrete.* Cement and Concrete Composites, vol. 31, no. 4, pages 221–231, 2009. (Cited on pages 115 and 124.)

[Butler 2010] Marko Butler, Viktor Mechtcherine and Simone Hempel. *Durability of textile reinforced concrete made with AR glass fibre: effect of the matrix composition.* Materials and structures, vol. 43, no. 10, pages 1351–1368, 2010. (Cited on pages 16, 115, 124 and 134.)

[Butler 2011] Marko Butler, Simone Hempel and Viktor Mechtcherine. *Modelling of ageing effects on crack-bridging behaviour of AR-glass multifilament yarns embedded in cement-based matrix.* Cement and Concrete Research, vol. 41, no. 4, pages 403–411, 2011. (Cited on page 15.)

[Camera di Commercio di Modena 2018] Camera di Commercio di Modena. *Building materials price datasheet 2018 (Prezziario opere edili 2018).* https://www.mo.camcom.it/tutela-del-mercato/prezzi/prezzi-informativi-delle-opere-edili-in-modena, 2018. (Cited on page 110.)

[Cao 2009] Shenghu Cao, WU Zhis and Xin Wang. *Tensile properties of CFRP and hybrid FRP composites at elevated temperatures.* Journal of Composite Materials, vol. 43, no. 4, pages 315–330, 2009. (Cited on page 88.)

[Carozzi 2015] Francesca Giulia Carozzi and Carlo Poggi. *Mechanical properties and debonding strength of Fabric Reinforced Cementitious Matrix (FRCM) systems for masonry strengthening.* Composites Part B: Engineering, vol. 70, pages 215–230, 2015. (Cited on pages 115, 121, 130, 131 and 133.)

[Carozzi 2017] Francesca Giulia Carozzi, Alessandro Bellini, Tommaso D'Antino, Gianmarco de Felice, Francesco Focacci, Łukasz Hojdys, Luca Laghi, Emma Lanoye, Francesco Micelli, Matteo Panizza*et al.* *Experimental investigation of tensile and bond properties of Carbon-FRCM composites for strengthening masonry elements.* Composites Part B: Engineering, vol. 128, pages 100–119, 2017. (Cited on page 24.)

[Cascardi 2016] Alessio Cascardi, Francesco Micelli and Maria Antonietta Aiello. *Analytical model based on artificial neural network for masonry shear walls strengthened with FRM systems.* Composites Part B: Engineering, vol. 95, pages 252–263, 2016. (Cited on page 11.)

[Cascardi 2017] Alessio Cascardi, Maria Antonietta Aiello and Thanasis Triantafillou. *Analysis-oriented model for concrete and masonry confined with fiber reinforced mortar.* Materials and Structures, vol. 50, no. 4, page 202, 2017. (Cited on page 13.)

[Cascardi 2018] Alessio Cascardi, Francesco Micelli and Maria Antonietta Aiello. *FRCM-confined masonry columns: experimental investigation on the effect of the inorganic matrix properties.* Construction and Building Materials, vol. 186, pages 811–825, 2018. (Cited on page 13.)

[Çavdar 2012] Ahmet Çavdar. *A study on the effects of high temperature on mechanical properties of fiber reinforced cementitious composites.* Composites Part B: Engineering, vol. 43, no. 5, pages 2452–2463, 2012. (Cited on page 90.)

[Cedolin 1987] Luigi Cedolin, Sandro Dei Poli and Ivo Iori. *Tensile behavior of concrete.* Journal of engineering mechanics, vol. 113, no. 3, pages 431–449, 1987. (Cited on page 161.)

[Cherian 2015] Chinchu Cherian and Dali Naidu Arnepalli. *A critical appraisal of the role of clay mineralogy in lime stabilization.* International Journal of Geosynthetics and Ground Engineering, vol. 1, no. 1, page 8, 2015. (Cited on page 55.)

[Chowdhury 2011] EU Chowdhury, R Eedson, Luke A Bisby, Mark F Green and Noureddine Benichou. *Mechanical characterization of fibre reinforced polymers materials at high temperature.* Fire Technology, vol. 47, no. 4, pages 1063–1080, 2011. (Cited on page 87.)

[CNR DT215 2018] CNR DT215. *Istruzioni per la Progettazione, l'Esecuzione ed il Controllo di Interventi di Consolidamento Statico mediante l'utilizzo di Compositi Fibrorinforzati a Matrice Inorganica.* Technical report, Consiglio Nazionale delle Ricerche, 2018. (Cited on pages 12, 13, 14, 15, 57, 113 and 114.)

[CNR TD200-R1 2013] CNR TD200-R1. *Guide for the design and construction of an externally bonded FRP system for strengthening existing structures.* Technical report, Italian National Research Council, 2013. (Cited on pages 7, 14, 88, 110, 114, 129, 130, 131 and 132.)

[Cohen 2012] Zvi Cohen and Alva Peled. *Effect of nanofillers and production methods to control the interfacial characteristics of glass bundles in textile fabric cement-based composites.* Composites Part A: Applied Science and Manufacturing, vol. 43, no. 6, pages 962–972, 2012. (Cited on pages 15 and 17.)

[Collins 2000] Philip G Collins and Phaedon Avouris. *Nanotubes for electronics.* Scientific American, vol. 283, no. 6, pages 62–69, 2000. (Cited on page 61.)

[Consiglio Superiore dei Lavori Pubblici 2019] Consiglio Superiore dei Lavori Pubblici. *Linea Guida per la identificazione, la qualificazione ed il controllo di accettazione di compositi fibrorinforzati a matrice inorganica (FRCM) da utilizzarsi per il consolidamento strutturale di costruzioni esistenti.* Italian standard for the qualification of frcm composite systems for externally bonded reinforcement of existing structures, Consiglio Superiore dei Lavori Pubblici, 8 Jan 2019. (Cited on page 114.)

[Constantinescu 2016] Horia Constantinescu, Oana Gherman, Camelia Negrutiu and Sosa Pavel Ioan. *Mechanical Properties of Hardened High Strength Concrete.* Procedia Technology, vol. 22, pages 219–226, 2016. (Cited on page 150.)

[D'Ambrisi 2013a] Angelo D'Ambrisi, Luciano Feo and Francesco Focacci. *Experimental analysis on bond between PBO-FRCM strengthening materials and concrete.* Composites Part B: Engineering, vol. 44, no. 1, pages 524–532, 2013. (Cited on page 115.)

[D'Ambrisi 2013b] Angelo D'Ambrisi, Francesco Focacci and Andrea Caporale. *Strengthening of masonry–unreinforced concrete railway bridges with PBO-FRCM materials.* Composite Structures, vol. 102, pages 193–204, 2013. (Cited on page 115.)

[D'Antino 2017] Tommaso D'Antino and Catherine Papanicolaou. *Mechanical characterization of textile reinforced inorganic-matrix composites.* Composites Part B: Engineering, vol. 127, pages 78–91, 2017. (Cited on pages 6 and 15.)

[de Andrade Silva 2014] Flávio de Andrade Silva, Marko Butler, Simone Hempel, Romildo Dias Toledo Filho and Viktor Mechtcherine. *Effects of elevated temperatures on the interface properties of carbon textile-reinforced concrete.* Cement and Concrete Composites, vol. 48, pages 26–34, 2014. (Cited on pages 88, 89, 90, 94 and 99.)

[De Felice 2014] Gianmarco De Felice, Stefano De Santis, Leire Garmendia, Bahman Ghiassi, Pello Larrinaga, Paulo B Lourenço, Daniel V Oliveira, Fabrizio Paolacci and Catherine G Papanicolaou. *Mortar-based systems for externally bonded strengthening of masonry.* Materials and Structures, vol. 47, no. 12, pages 2021–2037, 2014. (Cited on page 115.)

[De Santis 2015a] Stefano De Santis and Gianmarco de Felice. *Steel reinforced grout systems for the strengthening of masonry structures.* Composite Structures, vol. 134, pages 533–548, 2015. (Cited on pages 71 and 115.)

[De Santis 2015b] Stefano De Santis and Gianmarco de Felice. *Tensile behaviour and durability of mortar-based strengthening systems with glass-aramid textiles.*

In Key Engineering Materials, volume 624, pages 346–353. Trans Tech Publ, 2015. (Cited on page 114.)

[De Volder 2013] Michael FL De Volder, Sameh H Tawfick, Ray H Baughman and A John Hart. *Carbon nanotubes: present and future commercial applications.* science, vol. 339, no. 6119, pages 535–539, 2013. (Cited on page 63.)

[Denes 1996] Ferencz Sandor Denes, Dorel Feldman, ZQ Hua, Zhihong Zheng and Raymond A. Young. *Cementitious-matrix composites from SiCl4-plasma-activated polypropylene fibres.* Journal of Adhesion Science and Technology, vol. 10, no. 1, pages 61–77, 1996. (Cited on page 138.)

[Di Maida 2015] Pietro Di Maida, Enrico Radi, Corrado Sciancalepore and Federica Bondioli. *Pullout behavior of polypropylene macro-synthetic fibers treated with nano-silica.* Construction and Building Materials, vol. 82, pages 39–44, 2015. (Cited on pages 138, 144 and 157.)

[Di Maida 2018] Pietro Di Maida, Corrado Sciancalepore, Enrico Radi and Federica Bondioli. *Effects of nano-silica treatment on the flexural post cracking behaviour of polypropylene macro-synthetic fibre reinforced concrete.* Mechanics Research Communications, vol. 88, pages 12–18, 2018. (Cited on pages 138 and 159.)

[Donnini 2016] Jacopo Donnini, Valeria Corinaldesi and Antonio Nanni. *Mechanical properties of FRCM using carbon fabrics with different coating treatments.* Composites Part B: Engineering, vol. 88, pages 220–228, 2016. (Cited on pages 17 and 23.)

[Donnini 2017] Jacopo Donnini, Francisco De Caso y Basalo, Valeria Corinaldesi, Giovanni Lancioni and Antonio Nanni. *Fabric-reinforced cementitious matrix behavior at high-temperature: Experimental and numerical results.* Composites Part B: Engineering, vol. 108, pages 108–121, 2017. (Cited on pages 59, 87, 88, 90 and 99.)

[Donnini 2019] Jacopo Donnini. *Durability of glass FRCM systems: Effects of different environments on mechanical properties.* Composites Part B: Engineering, page 107047, 2019. (Cited on page 114.)

[Dvorkin 2013] D Dvorkin, Amir Poursaee, Alva Peled and William Jason Weiss. *Influence of bundle coating on the tensile behavior, bonding, cracking and fluid transport of fabric cement-based composites.* Cement and Concrete Composites, vol. 42, pages 9–19, 2013. (Cited on pages 17 and 82.)

[D'Ambrisi 2011] Angelo D'Ambrisi and Francesco Focacci. *Flexural strengthening of RC beams with cement-based composites.* Journal of Composites for Construction, vol. 15, no. 5, pages 707–720, 2011. (Cited on page 13.)

[D'Antino 2019] Tommaso D'Antino, Francesco Focacci, Lesley H Sneed and Carlo Pellegrino. *Shear Strength Model for RC Beams with U-Wrapped FRCM Composites.* Journal of Composites for Construction, vol. 24, no. 1, page 04019057, 2019. (Cited on page 14.)

[Ebbesen 1992] Thomas W Ebbesen and Pulickel M Ajayan. *Large-scale synthesis of carbon nanotubes.* Nature, vol. 358, no. 6383, page 220, 1992. (Cited on page 61.)

[Erdem 2018] Savaş Erdem, Serap Hanbay and Zeynel Güler. *Micromechanical damage analysis and engineering performance of concrete with colloidal nanosilica and demolished concrete aggregates.* Construction and Building Materials, vol. 171, pages 634–642, 2018. (Cited on page 138.)

[Faella 2010] Ciro Faella, Enzo Martinelli, Emidio Nigro and Sergio Paciello. *Shear capacity of masonry walls externally strengthened by a cement-based composite material: An experimental campaign.* Construction and Building Materials, vol. 24, no. 1, pages 84–93, 2010. (Cited on page 11.)

[Falope 2018] Federico Oyedeji Falope, Luca Lanzoni and Angelo Marcello Tarantino. *Modified hinged beam test on Steel Fabric Reinforced Cementitious Matrix (SFRCM).* Composites Part B: Engineering, vol. 146, pages 232–243, 2018. (Cited on page 127.)

[Felekoglu 2009] Burak Felekoglu, Kamile Tosun and Bulent Baradan. *A comparative study on the flexural performance of plasma treated polypropylene fiber reinforced cementitious composites.* Journal of Materials Processing Technology, vol. 209, no. 11, pages 5133–5144, 2009. (Cited on pages 138 and 158.)

[Feo 2016] Luciano Feo, Raimondo Luciano, Giulia Misseri and Luisa Rovero. *Irregular stone masonries: Analysis and strengthening with glass fibre reinforced composites.* Composites Part B: Engineering, vol. 92, pages 84–93, 2016. (Cited on page 5.)

[Fisher 1925] Ronald Aylmer Fisher. Statistical methods for research workers. Oliver and Boyd, Edinburgh, 1925. (Cited on page 102.)

[Fitzer 2000] Erich Fitzer, Rudolf Kleinholz, Hartmut Tiesler, Martyn Hugh Stacey, Roger De Bruyne, Ignace Lefever, Andrew Foley, Wilhelm Frohs, Tilo Hauke, Michael Heine*et al. Fibers, 5. Synthetic Inorganic.* Ullmann's Encyclopedia of Industrial Chemistry, 2000. (Cited on page 10.)

[Forster 2014] Alan M Forster, Ewan M Szadurski and Phillip FG Banfill. *Deterioration of natural hydraulic lime mortars, I: Effects of chemically accelerated leaching on physical and mechanical properties of uncarbonated materials.* Construction and Building Materials, vol. 72, pages 199–207, 2014. (Cited on page 43.)

[Foster 2005] SK Foster and Luke A Bisby. *High temperature residual properties of externally bonded FRP systems.* In Proceedings of the 7th international symposium on fiber reinforced polymer reinforcement for reinforced concrete structures (FRPRCS-7), SP-230-70, pages 1235–52, 2005. (Cited on pages 87 and 88.)

[Fu 1996] Xuli Fu, Weiming Lu and DDL Chung. *Improving the bond strength between carbon fiber and cement by fiber surface treatment and polymer addition to cement mix.* Cement and concrete research, vol. 26, no. 7, pages 1007–1012, 1996. (Cited on page 16.)

[Galano 1998] Luciano Galano and Vittorio Gusella. *Reinforcement of masonry walls subjected to seismic loading using steel X-bracing.* Journal of Structural Engineering, vol. 124, no. 8, pages 886–895, 1998. (Cited on page 11.)

[Gao 2007] Shanglin Gao, Edith Mäder and Rosemarie Plonka. *Nanostructured coatings of glass fibers: improvement of alkali resistance and mechanical properties.* Acta Materialia, vol. 55, no. 3, pages 1043–1052, 2007. (Cited on page 17.)

[Garg 2016] Mohit Garg, Shruti Sharma and Rajeev Mehta. *Processing of Functionalized and Pristine Carbon Nanotube Epoxy Composites with Silane-Treated Glass Fiber.* Materials and Manufacturing Processes, vol. 31, no. 15, pages 2044–2056, 2016. (Cited on page 76.)

[Garmendia 2011] Leire Garmendia, José Tomás San-José, David García and Pello Larrinaga. *Rehabilitation of masonry arches with compatible advanced composite material.* Construction and Building Materials, vol. 25, no. 12, pages 4374–4385, 2011. (Cited on page 59.)

[Gibson 2006] Arthur Geoff Gibson, Yongshu Wu, John Terry Evans and Adrian P Mouritz. *Laminate theory analysis of composites under load in fire.* Journal of Composite Materials, vol. 40, no. 7, pages 639–658, 2006. (Cited on pages 98 and 99.)

[Girifalco 2000] Louis A Girifalco, Miroslav Hodak and Roland S Lee. *Carbon nanotubes, buckyballs, ropes, and a universal graphitic potential.* Physical Review B, vol. 62, no. 19, page 13104, 2000. (Cited on page 64.)

[Goldstein 2017] Joseph I Goldstein, Dale E Newbury, Joseph R Michael, Nicholas WM Ritchie, John Henry J Scott and David C Joy. Scanning electron microscopy and x-ray microanalysis. Springer, 2017. (Cited on page 44.)

[Gonzalez-Libreros 2017] Jaime H Gonzalez-Libreros, Cristian Sabau, LH Sneed, Carlo Pellegrino and Gabriel Sas. *State of research on shear strengthening of RC beams with FRCM composites.* Construction and Building Materials, vol. 149, pages 444–458, 2017. (Cited on page 14.)

[Good 2013] Phillip Good. Permutation tests: a practical guide to resampling methods for testing hypotheses. Springer Science & Business Media, 2013. (Cited on page 107.)

[Gowripalan 1990] Nadarajah Gowripalan. *Effect of curing on durability.* Concrete International, vol. 12, no. 2, pages 47–54, 1990. (Cited on page 123.)

[Guo 1995a] Ting Guo, Pavel Nikolaev, Andrew G Rinzler, David Tomanek, Daniel T Colbert and Richard E Smalley. *Self-assembly of tubular fullerenes.* The Journal of Physical Chemistry, vol. 99, no. 27, pages 10694–10697, 1995. (Cited on page 61.)

[Guo 1995b] Ting Guo, Pavel Nikolaev, Andreas Thess, Daniel T Colbert and Richard E Smalley. *Catalytic growth of single-walled manotubes by laser vaporization.* Chemical physics Letters, vol. 243, no. 1-2, pages 49–54, 1995. (Cited on page 61.)

[Gürdal 1999] Zafer Gürdal, Raphael T. and Prabhat Hajela. Design and optimization of laminated composite materials. John Wiley & Sons, 1999. (Cited on page 53.)

[Haghgoo 2014] Majid Haghgoo, Ali Akbar Yousefi, Mohammad Jalal Zohouriaan Mehr, Alain Celzard, Vanessa Fierro, Angélique Léonard and Nathalie Job. *Characterization of multi-walled carbon nanotube dispersion in resorcinol–formaldehyde aerogels.* Microporous and Mesoporous Materials, vol. 184, pages 97–104, 2014. (Cited on page 65.)

[Hao 2018] Yifei Hao, Liang Cheng, Hong Hao and Mohamed A Shahin. *Enhancing fiber/matrix bonding in polypropylene fiber reinforced cementitious composites by microbially induced calcite precipitation pre-treatment.* Cement and Concrete Composites, vol. 88, pages 1–7, 2018. (Cited on page 138.)

[Harper 2003] Charles A Harper and Edward M Petrie. Plastics materials and processes: a concise encyclopedia. John Wiley & Sons, 2003. (Cited on pages 89 and 95.)

[Hartig 2012] J Hartig, Frank Jesse, K Schicktanz and Ulrich Häußler-Combe. *Influence of experimental setups on the apparent uniaxial tensile load-bearing capacity of textile reinforced concrete specimens.* Materials and Structures, vol. 45, no. 3, pages 433–446, 2012. (Cited on pages 23 and 31.)

[Hashemi 2012] Siavash Hashemi and R Al-Mahaidi. *Experimental and finite element analysis of flexural behavior of FRP-strengthened RC beams using cement-based adhesives.* Construction and Building Materials, vol. 26, no. 1, pages 268–273, 2012. (Cited on page 13.)

[Hempel 2007] R Hempel, Marko Butler, Simone Hempel and H Schorn. *Durability of textile reinforced concrete.* Special Publication, vol. 244, pages 87–108, 2007. (Cited on pages 115 and 124.)

[Hench 1990] Larry L Hench and Jon K West. *The sol-gel process.* Chemical reviews, vol. 90, no. 1, pages 33–72, 1990. (Cited on page 143.)

[Hommer 2009] Herbert Hommer. *Interaction of polycarboxylate ether with silica fume.* Journal of the European Ceramic Society, vol. 29, no. 10, pages 1847–1853, 2009. (Cited on page 54.)

[Homoro 2018] Omayma Homoro, Marie Michel and Thouraya Nouri Baranger. *Pull-out response of glass yarn from ettringite matrix: Effect of pre-impregnation and embedded length.* Composites Science and Technology, vol. 170, pages 174–182, 2018. (Cited on page 87.)

[Huang 2005] X Huang, Victor M Birman, Antonio Nanni and George Tunis. *Properties and potential for application of steel reinforced polymer and steel reinforced grout composites.* Composites Part B: Engineering, vol. 36, no. 1, pages 73–82, 2005. (Cited on page 5.)

[ICC AC434 2013] ICC AC434. *Acceptance criteria for masonry and concrete strengthening using fiber-reinforced cementitious matrix (FRCM) composite systems.* Technical report, International Code Council, 2013. (Cited on pages 6, 15, 21, 22, 23, 30, 31, 33, 34, 47, 54, 77, 82, 89, 91, 96, 101, 114, 115, 116, 117, 118, 119, 129 and 131.)

[Iijima 1991] Sumio Iijima. *Helical microtubules of graphitic carbon.* Nature, vol. 354, no. 6348, page 56, 1991. (Cited on page 61.)

[International Code Council 2012] International Code Council. International building code. International Code Council: Washington DC, United States, 2012. (Cited on page 129.)

[Jarrah 2018] Majid Jarrah, Esmaeil Pournamazian Najafabadi, Mohammad Houshmand Khaneghahi and Asghar Vatani Oskouei. *The effect of elevated temperatures on the tensile performance of GFRP and CFRP sheets.* Construction and Building Materials, vol. 190, pages 38–52, 2018. (Cited on page 88.)

[Jo 2007] Byung-Wan Jo, Chang-Hyun Kim, Ghi-ho Tae and Jong-Bin Park. *Characteristics of cement mortar with nano-SiO2 particles.* Construction and building materials, vol. 21, no. 6, pages 1351–1355, 2007. (Cited on page 57.)

[Juarez 2007] Cesar Juarez, Alejandro Duran, Pedro Valdez and Gerardo Fajardo. *Performance of "Agave Lecheguilla" natural fiber in Portland cement composites exposed to severe environment conditions.* Building and environment, vol. 42, no. 3, pages 1151–1157, 2007. (Cited on page 140.)

[Kajorncheappunngam 2002] Somjai Kajorncheappunngam, Rakesh K Gupta and Hota VS GangaRao. *Effect of aging environment on degradation of glass-reinforced epoxy.* Journal of Composites for Construction, vol. 6, no. 1, pages 61–69, 2002. (Cited on pages 116, 124, 132 and 133.)

[Kaye 1966] George William Clarkson Kaye and Thomas Howell Laby. Tables of physical and chemical constants and some mathematical functions. Longmans, London, 1966. (Cited on page 107.)

[Kim 1998] Jang-Kyo Kim and Yiu-Wing Mai. Engineered interfaces in fiber reinforced composites. Elsevier, 1998. (Cited on page 16.)

[Kim 2007] Keun Su Kim, German Cota-Sanchez, Christopher T Kingston, Matej Imris, Benoît Simard and Gervais Soucy. *Large-scale production of single-walled carbon nanotubes by induction thermal plasma.* Journal of physics D: Applied physics, vol. 40, no. 8, page 2375, 2007. (Cited on page 62.)

[Kim 2010] Dong Joo Kim, Antoine E Naaman and Sherif El-Tawil. *Correlation between tensile and bending behavior of FRC composites with scale effect.* In Proceedings of FraMCoS-7, 7th international conference on fracture mechanics of concrete and concrete structures. Jeju Island, South Korea, 2010. (Cited on page 162.)

[Kirkman 1996] Thomas W Kirkman. *Statistics to Use.* http://www.physics.csbsju.edu/stats/anova.html, 1996. (Cited on page 47.)

[Kohoutková 2012] A Kohoutková and I Broukalová. *Concrete Behaviour and Crack Control of Prestressed Concrete Beams with Fibres.* In Fibre Reinforced Concrete: challenges and opportunities, pages 299–300. RILEM Publications, 2012. (Cited on page 139.)

[Kohoutková 2017] A Kohoutková and I Broukalová. *Structural Applications of Fibre Reinforced Concrete in the Czech Republic.* In IOP Conference Series: Materials Science and Engineering, volume 246, page 012001. IOP Publishing, 2017. (Cited on page 139.)

[Kootsookos 2004] Alex Kootsookos and Adrian P Mouritz. *Seawater durability of glass- and carbon-polymer composites.* Composites Science and Technology, vol. 64, no. 10, pages 1503–1511, 2004. (Cited on page 132.)

[Koutas 2018] Lampros N Koutas and Dionysios A Bournas. *Out-of-plane strengthening of masonry-infilled RC frames with textile-reinforced Mortar Jackets.* Journal of Composites for Construction, vol. 23, no. 1, page 04018079, 2018. (Cited on page 14.)

[Koutas 2019] Lampros N. Koutas, Zoi Tetta, Dionysios A. Bournas and Thanasis C. Triantafillou. *Strengthening of Concrete Structures with Textile Reinforced*

Mortars: State-of-the-Art Review. Journal of Composites for Construction, vol. 23, no. 1, page 03118001, 2019. (Cited on pages 113 and 114.)

[Kumar 1997] Satish Kumar and VB Gupta. *Manufactured fibres for high performance, industrial and non-conventional applications.* In Manufactured fibre technology, pages 514–559. Springer, 1997. (Cited on page 9.)

[Kumar 2010] Mukul Kumar and Yoshinori Ando. *Chemical vapor deposition of carbon nanotubes: a review on growth mechanism and mass production.* Journal of nanoscience and nanotechnology, vol. 10, no. 6, pages 3739–3758, 2010. (Cited on page 62.)

[Lanzoni 2012] Luca Lanzoni, Andrea Nobili and Angelo Marcello Tarantino. *Performance evaluation of a polypropylene-based draw-wired fibre for concrete structures.* Construction and Building Materials, vol. 28, no. 1, pages 798–806, 2012. (Cited on pages 6, 137 and 141.)

[Larsen 1990] Erik Stoklund Larsen and Herbert Krenchel. *Durability of FRC-materials.* MRS Online Proceedings Library Archive, vol. 211, 1990. (Cited on page 140.)

[Li 1993] Victor C Li, Henrik Stang and Herbert Krenchel. *Micromechanics of crack bridging in fibre-reinforced concrete.* Materials and Structures, vol. 26, no. 8, pages 486–494, 1993. (Cited on page 162.)

[Li 1996] Victor C Li, Hwai-Chung Wu and Yin-Wen Chan. *Effect of plasma treatment of polyethylene fibers on interface and ementitious composite properties.* Journal of the American Ceramic Society, vol. 79, no. 3, pages 700–704, 1996. (Cited on page 16.)

[Li 1997] Victor C Li and Henrik Stang. *Interface property characterization and strengthening mechanisms in fiber reinforced cement based composites.* Advanced Cement Based Materials, vol. 6, no. 1, pages 1–20, 1997. (Cited on page 16.)

[Li 2017] Yue Li, Xiongfei Liu and Miaoke Wu. *Mechanical properties of FRP-strengthened concrete at elevated temperature.* Construction and Building Materials, vol. 134, pages 424–432, 2017. (Cited on page 88.)

[Lignola 2009] Gian Piero Lignola, Andrea Prota and Gaetano Manfredi. *Nonlinear analyses of tuff masonry walls strengthened with cementitious matrix-grid composites.* Journal of Composites for Construction, vol. 13, no. 4, pages 243–251, 2009. (Cited on page 11.)

[Lignola 2019] Gian Piero Lignola, Antonio Bilotta and Francesca Ceroni. *Assessment of the effect of FRCM materials on the behaviour of masonry walls by means of FE models.* Engineering Structures, vol. 184, pages 145–157, 2019. (Cited on page 11.)

[Loewenstein 1973] Klaus Leopold Loewenstein. The manufacturing technology of continuous glass fibers. Elsevier Science Ltd, 1973. (Cited on page 9.)

[Long 2004] Xiang-Li Long, Zhi-Ling Xin, Hong-Xin Wang, Wen-De Xiao and Wei-Kang Yuan. *Simultaneous removal of NO and SO2 with hexamminecobalt (II) solution coupled with the hexamminecobalt (II) regeneration catalyzed by activated carbon.* Applied Catalysis B: Environmental, vol. 54, no. 1, pages 25–32, 2004. (Cited on page 144.)

[López-Buendía 2013] Angel M López-Buendía, María Dolores Romero-Sánchez, Verónica Climent and Celia Guillem. *Surface treated polypropylene (PP) fibres for reinforced concrete.* Cement and Concrete Research, vol. 54, pages 29–35, 2013. (Cited on pages 138, 153, 155 and 159.)

[Lovata 1987] Norbert L Lovata and MF Fahmy. *Interfacial bond study of a chemically treated polypropylene fibre-reinforced concrete.* Construction and Building Materials, vol. 1, no. 2, pages 83–87, 1987. (Cited on page 138.)

[Lubin 1975] George Lubin. Handbook of fiberglass and advanced plastics composites. RE Krieger Publishing Company, 1975. (Cited on page 9.)

[Machida 1997] Atsuhiko Machida and Taketo Uomoto. Recommendation for design and construction of concrete structures using continuous fiber reinforcing materials. Japan Society of Civil Engineers, 1997. (Cited on page 130.)

[Mahieux 2001] CA Mahieux, Kenneth L Reifsnider and Scott W Case. *Property modeling across transition temperatures in PMC's: Part I. Tensile properties.* Applied Composite Materials, vol. 8, no. 4, pages 217–234, 2001. (Cited on pages 98 and 99.)

[Majumdar 1974] Amal J Majumdar. *The role of the interface in glass fibre reinforced cement.* Cement and Concrete Research, vol. 4, no. 2, pages 247–268, 1974. (Cited on page 16.)

[Mandel 2012] John Mandel. The statistical analysis of experimental data. Dover Publishing Inc, 2012. (Cited on pages 67, 124 and 131.)

[Maroudas 2017] Spyros R Maroudas and Catherine Corina G Papanicolaou. *Effect of high temperatures on the TRM-to-masonry bond.* In Key Engineering Materials, volume 747, pages 533–541. Trans Tech Publication, 2017. (Cited on pages 88 and 90.)

[Matinlinna 2009] Jukka P Matinlinna, Jon E Dahl, Stig Karlsson, Lippo VJ Lassila and Pekka K Vallittu. *The effect of the novel silane system on the flexural properties of E-glass fiber-reinforced composites for dental use.* Silanes and other coupling agents, vol. 5, pages 107–121, 2009. (Cited on page 76.)

[Mayrhofer 2002] Christoph Mayrhofer. *Reinforced masonry walls under blast loading*. International Journal of Mechanical Sciences, vol. 44, no. 6, pages 1067–1080, 2002. (Cited on page 11.)

[Mechtcherine 2013] Viktor Mechtcherine. *Novel cement-based composites for the strengthening and repair of concrete structures*. Construction and Building Materials, vol. 41, pages 365–373, 2013. (Cited on page 15.)

[Menna 2015] Costantino Menna, Domenico Asprone, Massimo Durante, Alberto Zinno, Alberto Balsamo and Andrea Prota. *Structural behaviour of masonry panels strengthened with an innovative hemp fibre composite grid*. Construction and Building materials, vol. 100, pages 111–121, 2015. (Cited on page 12.)

[Messori 2018] Massimo Messori, Andrea Nobili, Cesare Signorini and Antonella Sola. *Mechanical performance of epoxy coated AR-Glass fabric Textile Reinforced Mortar: Influence of coating thickness and formulation*. Composites Part B: Engineering, vol. 149, pages 135–143, 2018. (Cited on pages 87, 89, 99 and 103.)

[Mezrea 2016] Pelin E Mezrea, Irem A Yilmaz, Medine Ispir, Ergün Binbir, Ihsan E Bal and Alper Ilki. *External jacketing of unreinforced historical masonry piers with open-grid basalt-reinforced mortar*. Journal of Composites for Construction, vol. 21, no. 3, page 04016110, 2016. (Cited on page 13.)

[Micelli 2019] Francesco Micelli and Maria Antonietta Aiello. *Residual tensile strength of dry and impregnated reinforcement fibres after exposure to alkaline environments*. Composites Part B: Engineering, vol. 159, pages 490–501, 2019. (Cited on pages 17, 114 and 115.)

[Mindess 1988] Sindney Mindess and Gary Vondran. *Properties of concrete reinforced with fibrillated polypropylene fibres under impact loading*. Cement and Concrete Research, vol. 18, no. 1, pages 109–115, 1988. (Cited on page 137.)

[Mobasher 2006] Barzin Mobasher, Alva Peled and Jitendra Pahilajani. *Distributed cracking and stiffness degradation in fabric-cement composites*. Materials and structures, vol. 39, no. 3, pages 317–331, 2006. (Cited on pages 5, 40, 66, 127 and 128.)

[Mobasher 2011] Barzin Mobasher. Mechanics of fiber and textile reinforced cement composites. CRC press, 2011. (Cited on pages 7, 8, 9, 15, 114, 121, 127 and 137.)

[Nadiv 2017] Roey Nadiv, Alva Peled, Viktor Mechtcherine, Simone Hempel and Christof Schroefl. *Micro-and nanoparticle mineral coating for enhanced properties of carbon multifilament yarn cement-based composites*. Composites Part B: Engineering, vol. 111, pages 179–189, 2017. (Cited on pages 6, 15, 17, 56 and 57.)

[Nanni 2012] Antonio Nanni. *A new tool for concrete and masonry repair*. Concrete international, vol. 34, no. 4, pages 43–49, 2012. (Cited on page 114.)

[Nikkanen 2015] Juha Pekka Nikkanen, Elina Huttunen-Saarivirta, Turkka Salminen, Leo Hyvärinen, Mari Honkanen, Elisa Isotahdon, Saara Heinonen and Erkki Levänen. *Enhanced photoactive and photoelectrochemical properties of* TiO_2 *sol–gel coated steel by the application of* SiO_2 *intermediate layer*. Applied Catalysis B: Environmental, vol. 174, pages 533–543, 2015. (Cited on page 28.)

[Nobili 2013] Andrea Nobili, Luca Lanzoni and Angelo Marcello Tarantino. *Experimental investigation and monitoring of a polypropylene-based fiber reinforced concrete road pavement*. Construction and Building Materials, vol. 47, pages 888–895, 2013. (Cited on page 137.)

[Nobili 2016] Andrea Nobili. *Durability assessment of impregnated Glass Fabric Reinforced Cementitious Matrix (GFRCM) composites in the alkaline and saline environments*. Construction and Building Materials, vol. 105, pages 465–471, 2016. (Cited on pages 15, 17, 23, 35, 46, 47, 50, 77, 78, 101, 114, 115, 116, 121, 124 and 130.)

[Nobili 2017a] Andrea Nobili and Federico O Falope. *Impregnated Carbon Fabric–Reinforced Cementitious Matrix Composite for Rehabilitation of the Finale Emilia Hospital Roofs: Case Study*. Journal of Composites for Construction, vol. 21, no. 4, page 05017001, 2017. (Cited on pages 6, 15, 17, 19, 24, 30, 78, 87, 111, 115, 116, 129 and 134.)

[Nobili 2017b] Andrea Nobili and Cesare Signorini. *On the effect of curing time and environmental exposure on impregnated Carbon Fabric Reinforced Cementitious Matrix (CFRCM) composite with design considerations*. Composites Part B: Engineering, vol. 112, pages 300–313, 2017. (Cited on pages 17, 33, 34, 40, 46, 49, 54, 59, 82, 83, 85 and 89.)

[Ombres 2015] Luciano Ombres. *Analysis of the bond between fabric reinforced cementitious mortar (FRCM) strengthening systems and concrete*. Composites Part B: Engineering, vol. 69, pages 418–426, 2015. (Cited on pages 88 and 90.)

[Ombres 2017] Luciano Ombres. *Structural performances of thermally conditioned PBO FRCM confined concrete cylinders*. Composite Structures, vol. 176, pages 1096–1106, 2017. (Cited on pages 88 and 90.)

[Palaci 2005] Ismael Palaci, Stephan Fedrigo, Harald Brune, Christian Klinke, Michael Chen and Elisa Riedo. *Radial elasticity of multiwalled carbon nanotubes*. Physical review letters, vol. 94, no. 17, page 175502, 2005. (Cited on page 63.)

[Papanicolaou 2008] Catherine Corina G Papanicolaou, Thanasis C Triantafillou, Myrto Papathanasiou and Kyriakos Karlos. *Textile reinforced mortar (TRM) versus FRP as strengthening material of URM walls: out-of-plane cyclic loading.* Materials and Structures, vol. 41, no. 1, pages 143–157, 2008. (Cited on page 6.)

[Park 2008] Joung-Man Park, Pyung-Gee Kim, Jung-Hoon Jang, Zuojia Wang, Byung-Sun Hwang and Kenneth Lawrence DeVries. *Interfacial evaluation and durability of modified Jute fibers/polypropylene (PP) composites using micromechanical test and acoustic emission.* Composites Part B: Engineering, vol. 39, no. 6, pages 1042–1061, 2008. (Cited on page 138.)

[Pavia 2008] Donald L Pavia, Gary M Lampman, George S Kriz and James A Vyvyan. Introduction to spectroscopy. Cengage Learning, 2008. (Cited on page 153.)

[Peled 1992] Alva Peled, Hilda Guttman and Arnon Bentur. *Treatments of polypropylene fibres to optimize their reinforcing efficiency in cement composites.* Cement and Concrete Composites, vol. 14, no. 4, pages 277–285, 1992. (Cited on page 138.)

[Peled 2003] Alva Peled and Barzin Mobasher. *The pultrusion technology for the production of fabric-cement composites.* In Brittle Matrix Composites 7, pages 505–514. Elsevier, 2003. (Cited on page 11.)

[Pellegrino 2013] Carlo Pellegrino and Tommaso D'Antino. *Experimental behaviour of existing precast prestressed reinforced concrete elements strengthened with cementitious composites.* Composites Part B: Engineering, vol. 55, pages 31–40, 2013. (Cited on pages 13 and 115.)

[Peng 2008] Bei Peng, Mark Locascio, Peter Zapol, Shuyou Li, Steven L Mielke, George C Schatz and Horacio D Espinosa. *Measurements of near-ultimate strength for multiwalled carbon nanotubes and irradiation-induced crosslinking improvements.* Nature Nanotechnology, vol. 3, no. 10, page 626, 2008. (Cited on page 62.)

[Prota 2006] Andrea Prota, Giancarlo Marcari, Giovanni Fabbrocino, Gaetano Manfredi and Corina M Aldea. *Experimental in-plane behavior of tuff masonry strengthened with cementitious matrix–grid composites.* Journal of Composites for Construction, vol. 10, no. 3, pages 223–233, 2006. (Cited on page 11.)

[Purnell 2000] Phil Purnell, Neil R Short, Christopher L Page and Amal J Majumdar. *Microstructural observations in new matrix glass fibre reinforced cement.* Cement and concrete research, vol. 30, no. 11, pages 1747–1753, 2000. (Cited on page 114.)

[Qian 2000] Chunxiang Qian and Piet Stroeven. *Development of hybrid polypropylene-steel fibre-reinforced concrete.* Cement and Concrete Research, vol. 30, no. 1, pages 63–69, 2000. (Cited on page 137.)

[Qing 2007] Ye Qing, Zhang Zenan, Kong Deyu and Chen Rongshen. *Influence of nano-SiO2 addition on properties of hardened cement paste as compared with silica fume.* Construction and building materials, vol. 21, no. 3, pages 539–545, 2007. (Cited on page 55.)

[Radushkevich 1952] LV Radushkevich and VM Lukyanovich. *O strukture ugleroda, obrazujucegosja pri termiceskom razlozenii okisi ugleroda na zeleznom kontakte (On a structure of carbon formed during the thermal decomposition of carbon monoxide on an iron catalyser).* Soviet Journal of Physical Chemistry, vol. 26, pages 88–95, 1952. (Cited on pages 61 and 62.)

[Rambo 2015] Dimas Alan Strauss Rambo, Flávio de Andrade Silva, Romildo Dias Toledo Filho and Otávio da Fonseca Martins Gomes. *Effect of elevated temperatures on the mechanical behavior of basalt textile reinforced refractory concrete.* Mater Design, vol. 65, pages 24–33, 2015. (Cited on pages 88, 89, 90 and 99.)

[Raoof 2016] Saad M Raoof, Lampros N Koutas and Dionysos A Bournas. *Bond between textile-reinforced mortar (TRM) and concrete substrates: Experimental investigation.* Composites Part B: Engineering, vol. 98, pages 350–361, 2016. (Cited on pages 6 and 15.)

[Raoof 2017] Saad M Raoof and Dionysios A. Bournas. *TRM versus FRP in flexural strengthening of RC beams: Behaviour at high temperatures.* Construction and Building Materials, vol. 154, pages 424–437, 2017. (Cited on page 88.)

[Rastogi 2008] Richa Rastogi, Rahul Kaushal, SK Tripathi, Amit L Sharma, Inderpreet Kaur and Lalit M Bharadwaj. *Comparative study of carbon nanotube dispersion using surfactants.* Journal of colloid and interface science, vol. 328, no. 2, pages 421–428, 2008. (Cited on page 65.)

[RILEM 232-TDT 2016] RILEM 232-TDT. *Test methods and design of textile reinforced concrete.* Technical report 12, International Union of Laboratories and Experts in Construction Materials, Systems and Structures, 2016. (Cited on pages 15, 23 and 31.)

[Rodrigues 2016] Bruno VM Rodrigues, Aline S Silva, Gabriela FS Melo, Luana MR Vasconscellos, Fernanda R Marciano and Anderson O Lobo. *Influence of low contents of superhydrophilic MWCNT on the properties and cell viability of electrospun poly (butylene adipate-co-terephthalate) fibers.* Materials Science and Engineering: C, vol. 59, pages 782–791, 2016. (Cited on page 63.)

[Rossi 2006] Bruno Rossi. *Calcestruzzo fibrorinforzato: caratteristiche generali e comportamento chimico-fisico.* In Advanced Engineering Project Network, pages 1–6, 2006. (Cited on page 139.)

[Ruoff 1993] Rodney S Ruoff, J Tersoff, Donald C Lorents, Shekhar Subramoney and Bryan Chan. *Radial deformation of carbon nanotubes by van der Waals forces.* Nature, vol. 364, no. 6437, page 514, 1993. (Cited on page 63.)

[Saafi 2002] Mohamed Saafi. *Effect of fire on FRP reinforced concrete members.* Composite Structures, vol. 58, no. 1, pages 11–20, oct 2002. (Cited on page 88.)

[Sanchez 2010] Florence Sanchez and Konstantin Sobolev. *Nanotechnology in concrete–a review.* Construction and building materials, vol. 24, no. 11, pages 2060–2071, 2010. (Cited on page 55.)

[Santos 2005] A García Santos, J Ma Rincón, Maximina Romero and R Talero. *Characterization of a polypropylene fibered cement composite using ESEM, FESEM and mechanical testing.* Construction and Building Materials, vol. 19, no. 5, pages 396–403, 2005. (Cited on page 159.)

[Scheffler 2009] Christina Scheffler, Shanglin Gao, Rosemarie Plonka, Edith Mäder, Simone Hempel, Marko Butler and Viktor Mechtcherine. *Interphase modification of alkali-resistant glass fibres and carbon fibres for textile reinforced concrete I: Fibre properties and durability.* Composites Science and Technology, vol. 69, no. 3, pages 531–538, 2009. (Cited on pages 16, 17 and 87.)

[Sharda 2016] Shashwat Sharda, Manvendra Singh and S Singh. *A review on Properties of Fibre Reinforced Cement-based materials.* IOSR Journal of Mechanical and Civil Engineering, vol. 13, no. 05, pages 104–112, 2016. (Cited on page 140.)

[Shu 2015] Xiang Shu, Ryan K Graham, Baoshan Huang and Edwin G Burdette. *Hybrid effects of carbon fibers on mechanical properties of Portland cement mortar.* Materials & Design (1980-2015), vol. 65, pages 1222–1228, 2015. (Cited on page 71.)

[Shvartzman-Cohen 2004] Rina Shvartzman-Cohen, Einat Nativ-Roth, Ezhil Baskaran, Yael Levi-Kalisman, Igal Szleifer and Rachel Yerushalmi-Rozen. *Selective dispersion of single-walled carbon nanotubes in the presence of polymers: the role of molecular and colloidal length scales.* Journal of the American Chemical Society, vol. 126, no. 45, pages 14850–14857, 2004. (Cited on page 64.)

[Signorini 2018a] Cesare Signorini and Andrea Nobili. *Effect of aggressive environment exposure on mechanical performance of Steel-FRCM and Textile Reinforced Concrete (TRC).* In ICCS21 – 21st International Conference on Composite Structures, page 160, 2018. (Cited on page 110.)

[Signorini 2018b] Cesare Signorini, Andrea Nobili, Erika Iveth Cedillo González and Cristina Siligardi. *Silica coating for interphase bond enhancement of carbon and AR-Glass Textile Reinforced Mortar (TRM).* Composites Part B: Engineering, vol. 141, pages 191–202, 2018. (Cited on pages 17, 19, 27, 47, 49, 54, 56, 116, 129 and 144.)

[Signorini 2018c] Cesare Signorini, Andrea Nobili and Federico Oyedeji Falope. *Mechanical performance and crack pattern analysis of aged Carbon Fabric Cementitious Matrix (CFRCM) composites.* Composite Structures, vol. 202, pages 1114 – 1120, 2018. Special issue dedicated to Ian Marshall. (Cited on pages 57, 77, 89 and 127.)

[Signorini 2019a] Cesare Signorini, Andrea Nobili and Cristina Siligardi. *Sustainable mineral coating of alkali-resistant glass fibres in textile-reinforced mortar composites for structural purposes.* Journal of Composite Materials, vol. 53, no. 28–30, pages 4203–4213, 2019. (Cited on pages 19, 65, 68 and 144.)

[Signorini 2019b] Cesare Signorini, Andrea Nobili, Antonella Sola and Massimo Messori. *Diluted epoxy-coatings for TRM composites: tensile tests raw data.* http://dx.doi.org/10.17632/kbg7dz3yhx.3, 2019. , Mendeley Data, v3. (Cited on page 103.)

[Signorini 2019c] Cesare Signorini, Antonella Sola, Andrea Nobili and Cristina Siligardi. *Lime-cement textile reinforced mortar (TRM) with modified interphase.* The Journal of Applied Biomaterials and Functional Materials, vol. 17, no. 1, 2019. (Cited on pages 19, 66, 87 and 158.)

[Signorini 2020a] Cesare Signorini, Andrea Nobili, Antonella Sola and Massimo Messori. *Designing epoxy viscosity for optimal mechanical performance of coated Glass Textile Reinforced Mortar (GTRM) composites.* Construction and Building Materials, vol. 233, page 117325, 2020. (Cited on page 99.)

[Signorini 2020b] Cesare Signorini, Antonella Sola, Beatrice Malchiodi, Andrea Nobili and Andrea Gatto. *Failure mechanism of silica coated polypropylene fibres for Fibre Reinforced Concrete (FRC).* Construction and Building Materials, vol. 236, page 117549, 2020. (Cited on page 156.)

[Singh 2004] Sehaj Singh, Arun Shukla and Richard Brown. *Pullout behavior of polypropylene fibers from cementitious matrix.* Cement and Concrete Research, vol. 34, no. 10, pages 1919–1925, 2004. (Cited on page 138.)

[Smiljanic 2002] Olivier Smiljanic, BL Stansfield, J-P Dodelet, A Serventi and S Désilets. *Gas-phase synthesis of SWNT by an atmospheric pressure plasma jet.* Chemical Physics Letters, vol. 356, no. 3-4, pages 189–193, 2002. (Cited on page 62.)

[Smiljanic 2009] Olivier Smiljanic and Barry L Stansfield. *Method and apparatus for producing single-wall carbon nanotubes*, September 22 2009. US Patent 7,591,989. (Cited on page 61.)

[Stang 1992] Henrik Stang and Tine Aarre. *Evaluation of crack width in FRC with conventional reinforcement.* Cement and Concrete Composites, vol. 14, no. 2, 1992. (Cited on page 162.)

[Stang 1995] Henrik Stang, Victor C Li and Herbert Krenchel. *Design and structural applications of stress-crack width relations in fibre reinforced concrete.* Materials and Structures, vol. 28, no. 4, pages 210–219, 1995. (Cited on page 162.)

[Stratford 2004] Tim Stratford, Giovanni Pascale, Odine Manfroni and Barbara Bonfiglioli. *Shear strengthening masonry panels with sheet glass-fiber reinforced polymer.* Journal of Composites for Construction, vol. 8, no. 5, pages 434–443, 2004. (Cited on page 115.)

[Takeuchi 2014] K Takeuchi, T Hayashi, YA Kim, K Fujisawa and M Endo. *The state-of-the-art science and applications of carbon nanotubes.* Nanosystems: physics, chemistry, mathematics, vol. 5, no. 1, 2014. (Cited on page 61.)

[Tennent 1987] Howard G Tennent. *Carbon fibrils, method for producing same and compositions containing same*, May 5 1987. US Patent 4,663,230. (Cited on page 61.)

[Terlingen 1994] Johannes Gijsbertus Antonius Terlingen. *Introduction of functional groups at polymer surfaces by glow discharge techniques.* PhD thesis, , Universiteit Twente (The Netherlands), 1994. (Cited on page 138.)

[Tetta 2016] Zoi C Tetta and Dionysios A Bournas. *TRM vs FRP jacketing in shear strengthening of concrete members subjected to high temperatures.* Composites Part B: Engineering, vol. 106, pages 190–205, 2016. (Cited on page 88.)

[Thermou 2015] Georgia E Thermou, Konstantinos Katakalos and George Manos. *Concrete confinement with steel-reinforced grout jackets.* Materials and Structures, vol. 48, no. 5, pages 1355–1376, 2015. (Cited on page 5.)

[Thess 1996] Andreas Thess, Roland Lee, Pavel Nikolaev, Hongjie Dai, Pierre Petit, Jerome Robert, Chunhui Xu, Young Hee Lee, Seong Gon Kim, Andrew G Rinzler*et al. Crystalline ropes of metallic carbon nanotubes.* Science, vol. 273, no. 5274, pages 483–487, 1996. (Cited on page 64.)

[Trapko 2013] Tomasz Trapko. *The effect of high temperature on the performance of CFRP and FRCM confined concrete elements.* Composites Part B: Engineering, vol. 54, pages 138–145, 2013. (Cited on pages 59, 88 and 90.)

[Triantafillou 1998] Thanasis C Triantafillou. *Composites: a new possibility for the shear strengthening of concrete, masonry and wood.* Composites Science and Technology, vol. 58, no. 8, pages 1285–1295, 1998. (Cited on page 6.)

[Triantafillou 2016] Thanasis Triantafillou. Textile fibre composites in civil engineering. Woodhead Publishing, 2016. (Cited on page 8.)

[Tu 1998] Lai Tu, D Kruger, JB Wagener and PAB Carstens. *Surface modified polypropylene fibres for use in concrete.* Magazine of Concrete Research, vol. 50, no. 3, pages 209–217, 1998. (Cited on page 138.)

[UNI EN 1015-11 2007] UNI EN 1015-11. *Methods of test for mortar for masonry – Part 11: Determination of flexural and compressive strength of hardened mortar.* Technical report, British Standards Institution-BSI and CEN European Committee for Standardization, 2007. (Cited on pages 19 and 102.)

[UNI EN 12390-5 2019] UNI EN 12390-5. *Testing hardened concrete–Part 5: Flexural strength of test specimens.* Technical report, British Standards Institution-BSI and CEN European Committee for Standardization, 2019. (Cited on pages 142 and 150.)

[UNI EN 15422 2008] UNI EN 15422. *Precast concrete products: Specification of glass fibres for reinforcement of mortars and concretes.* British Standards Institution-BSI and CEN European Committee for Standardization, 2008. (Cited on page 10.)

[UNI EN 206 2013] UNI EN 206. *Concrete – Specification, performance, production and conformity.* Technical report, British Standards Institution-BSI and CEN European Committee for Standardization, 2013. (Cited on page 142.)

[Vaisman 2006] Linda Vaisman, H Daniel Wagner and Gad Marom. *The role of surfactants in dispersion of carbon nanotubes.* Advances in colloid and interface science, vol. 128, pages 37–46, 2006. (Cited on page 65.)

[Veniale 2001] Fernando Veniale, Massimo Setti, Carlos Rodriguez-Navarro and Stefania Lodola. *Role of clay constituents in stone decay processes.* Materiales de Construcción, vol. 51, no. 263-264, pages 163–182, 2001. (Cited on page 43.)

[Wafa 1990] Faisal Fouad Wafa. *Properties & applications of fiber reinforced concrete.* Engineering Sciences, vol. 2, no. 1, 1990. (Cited on pages 137 and 138.)

[Walker Jr 1959] Phillip L Walker Jr, JF Rakszawski and GR Imperial. *Carbon formation from carbon monoxide-hydrogen mixtures over iron catalysts. I. Properties of carbon formed.* The Journal of Physical Chemistry, vol. 63, no. 2, pages 133–140, 1959. (Cited on page 62.)

[Wang 1996] Nianzhi Wang, Sidney Mindess and Keith Ko. *Fibre reinforced concrete beams under impact loading.* Cement and concrete research, vol. 26, no. 3, pages 363–376, 1996. (Cited on pages 137 and 153.)

[Winnefeld 2006] Frank Winnefeld and Karl Georg Böttger. *How clayey fines in aggregates influence the properties of lime mortars.* Materials and Structures, vol. 39, no. 4, pages 433–443, 2006. (Cited on page 43.)

[Wobbe 2004] Elsbeth D Wobbe, Pedro Silva, Bryce L Barton, Lokeswarappa R Dharani, Victor Birman, Antonio Nanni, Tarek Alkhrdaji, Jay Thomas and George Tunis. *Flexural capacity of RC beams externally bonded with SRP and SRG.* In Proceedings of Society for the Advancement of material and Process Engineering 2004 Symposium, pages 16–20, 2004. (Cited on page 5.)

[Xu 1999] Yunsheng Xu and DDL Chung. *Carbon fiber reinforced cement improved by using silane-treated carbon fibers.* Cement and concrete research, vol. 29, no. 5, pages 773–776, 1999. (Cited on page 16.)

[Xu 2014] Shi-lang Xu, Ling-hua Shen, Ji-yang Wang and Ye Fu. *High temperature mechanical performance and micro interfacial adhesive failure of textile reinforced concrete thin-plate.* Journal of Zhejiang University SCIENCE A, vol. 15, no. 1, pages 31–38, 2014. (Cited on pages 88 and 90.)

[Yang 2011] Yuehai Yang and Wenzhi Li. *Radial elasticity of single-walled carbon nanotube measured by atomic force microscopy.* Applied Physics Letters, vol. 98, no. 4, page 041901, 2011. (Cited on page 63.)

[Yu 2000] Min-Feng Yu, Oleg Lourie, Mark J Dyer, Katerina Moloni, Thomas F Kelly and Rodney S Ruoff. *Strength and breaking mechanism of multiwalled carbon nanotubes under tensile load.* Science, vol. 287, no. 5453, pages 637–640, 2000. (Cited on page 62.)

[Zanello 2006] Laura P Zanello, Bin Zhao, Hui Hu and Robert C Haddon. *Bone cell proliferation on carbon nanotubes.* Nano letters, vol. 6, no. 3, pages 562–567, 2006. (Cited on page 63.)

[Zhutovsky 2012] Semion Zhutovsky and Konstantin Kovler. *Effect of internal curing on durability-related properties of high performance concrete.* Cement and Concrete Research, vol. 42, no. 1, pages 20–26, 2012. (Cited on page 123.)

[Zia 2017] Asad Zia and Majid Ali. *Behavior of fiber reinforced concrete for controlling the rate of cracking in canal-lining.* Construction and Building Materials, vol. 155, pages 726–739, 2017. (Cited on page 158.)

[Zobg 2009] Liming Zobg, Martin C Hawley, Rensheng Sun and Leo C Kempel. *Dielectric relaxation of curing DGEBA/mPDA system at 2.45 GHz.* Journal of Thermoplastic Composite Materials, vol. 22, no. 3, pages 249–257, 2009. (Cited on page 77.)

[Zollo 1997] Ronald F Zollo. *Fiber-reinforced concrete: an overview after 30 years of development.* Cement and Concrete Composites, vol. 19, no. 2, pages 107–122, 1997. (Cited on page 137.)